

# Spectrally Efficient Beacons for Aeronautical Applications

Vom Fachbereich 18  
Elektrotechnik und Informationstechnik  
der Technischen Universität Darmstadt  
zur Erlangung der Würde eines  
Doktor-Ingenieurs (Dr.-Ing.)  
genehmigte Dissertation

von  
Dipl.-Ing. Nico Franzen  
geboren am 13.04.1982 in Weingarten

Referent:	Prof. Dr.-Ing. Anja Klein
Korreferent:	Univ.-Prof. Dr. rer. nat. Friedrich K. Jondral
Tag der Einreichung:	14.04.2015
Tag der mündlichen Prüfung:	16.07.2015

D 17  
Darmstädter Dissertation  
Darmstadt 2015



# Vorwort

Die vorliegende Arbeit entstand während meiner Tätigkeit als wissenschaftlicher Mitarbeiter am Institut für Kommunikation und Navigation des Deutschen Zentrums für Luft- und Raumfahrt (DLR) in Oberpfaffenhofen. Besonderer Dank gilt meinem Abteilungsleiter Prof. Uwe-Carsten Fiebig, der mir im Forschungsprojekt Air2Air die Möglichkeit gab, die im Folgenden vorgestellten Ergebnisse zu erarbeiten. Ebenfalls möchte ich meinem Gruppenleiter Dr. Michael Schnell danken, der meine Arbeit stets unterstützt hat und der mir in zahlreichen Diskussionen wertvolle Kommentare zur Verbesserung der vorliegenden Arbeit gab. Genauso danke ich Dr. Dmitriy Shutin, der jederzeit bereit war, über schwierige und komplexe fachliche Fragestellungen zu diskutieren und dabei stets Rat wusste.

Für die Betreuung dieser Arbeit und ihre vielen, wertvollen Kommentare danke ich Prof. Anja Klein von der TU Darmstadt. Darüber hinaus bin ich Prof. Friedrich Jon-dral vom Karlsruher Institut für Technologie dankbar für die Übernahme des Zweitgutachtens.

Essentiell für meine Arbeit war nicht zuletzt auch das kollegiale Arbeitsumfeld beim DLR, für das ich mich bei sämtlichen Kollegen bedanken möchte, insbesondere bei Michael Walter, Ulrich Epple und Nicolas Schneckenburger.

München im August 2015

Nico Franzen



---

## Kurzfassung

Beim aeronautischen Surveillance Beaconing sendet jedes Flugzeug regelmäßig Daten aus, die seine eigene Überwachung (engl., surveillance) ermöglichen, wie z.B. seine eigene Position, Geschwindigkeit und Bewegungsrichtung. Durch den Empfang der von anderen, sich in der Nähe befindlichen Flugzeugen ausgesandten Beacon-Nachrichten wird jedes Flugzeug über den Luftverkehr in seiner Umgebung informiert. Da die Luftverkehrsdichte steigt, muss für die zukünftige Flugverkehrsführung das Situationsbewusstsein gesteigert werden. Aeronautisches Surveillance Beaconing ist eine wichtige Methode, um diese Steigerung des Situationsbewusstseins zu erreichen. Im Gegensatz zu bodengestütztem Radar kann durch aeronautisches Surveillance Beaconing ohne zusätzliche Übertragung von Verkehrsdaten zwischen Boden und Flugzeug ein Bild der Verkehrslage ins Cockpit gebracht werden. Dies funktioniert sogar in ozeanischen sowie entlegenen Gebieten, die nicht durch Radarstationen abgedeckt sind.

In der aeronautischen Kommunikation ist die Knappheit von noch nicht belegtem Frequenzspektrum bereits heutzutage ein limitierender Faktor. Aus diesem Grund ist spektrale Effizienz von zentraler Bedeutung für zukünftiges aeronautisches Surveillance Beaconing. Aktuell gibt es drei aeronautische Surveillance Beaconing Systeme: den auf 1090 MHz ausgestrahlten SSR Mode S Extended Squitter (1090ES), den Universal Access Transceiver (UAT), sowie den VHF Digital Link Mode 4 (VDL4). Es ist bekannt, dass keines der drei existierenden Systeme ausreichend Kapazität bietet, um die Anforderungen des zukünftigen aeronautischen Surveillance Beaconings zu erfüllen. Gleichzeitig sind Verfahren zur Realisierung der physikalischen (PHY) Schicht, sowie der Schicht zur Mediumzugriffskontrolle (engl., medium access control (MAC)) für aeronautisches Surveillance Beaconing bisher nicht genügend erforscht. Es existieren keine ausreichenden Untersuchungen, welche Verfahren auf der PHY- und MAC-Schicht beim aeronautischen Surveillance Beaconing eine hohe spektrale Effizienz erreichen. Ebenfalls wird die gemeinsame Optimierung von Parametern sowohl der PHY- als auch der MAC-Schicht in der Literatur meist vernachlässigt.

In dieser Dissertation werden spektral effiziente Verfahren auf der PHY- und der MAC-Schicht des aeronautischen Surveillance Beaconings untersucht. Zunächst werden die Anforderungen des aeronautischen Surveillance Beaconings beschrieben, der Vielfachzugriffskanal erklärt, sowie eine Definition der spektralen Effizienz des aeronautischen Surveillance Beaconings angegeben. Danach wird ein Überblick über existierende Verfahren zur Umsetzung von PHY- und MAC-Schicht gegeben. Die Verfahren werden hinsichtlich ihrer Eignung für spektral effizientes aeronautisches Surveillance Beaconing bewertet. Basierend auf dieser Bewertung werden die beiden bezüglich ihrer spektralen

Effizienz vielversprechendsten Verfahren ausgewählt. Das erste Verfahren, auf Netzwerkzellen basierendes, selbstorganisierendes TDMA (engl., cell-based self-organizing TDMA (CB-SOTDMA)) verwendet selbstorganisierendes TDMA (engl., time-division multiple-access (TDMA)) innerhalb jeder Zelle eines zellulären Wiederholmusters. Bei CB-SOTDMA werden Übertragungen koordiniert, um Vielfachzugriffsinterferenz zu minimieren. Das zweite Verfahren verwendet Aloha auf der MAC-Schicht, sowie sukzessive Interferenzauslöschung (engl., successive interference cancellation (SIC)) im Empfänger. Aloha mit SIC versucht nicht, Vielfachzugriffsinterferenz zu vermeiden, sondern sie durch Interferenzauslöschung auf der PHY-Schicht tolerieren zu können.

Sowohl für CB-SOTDMA als auch für Aloha mit SIC werden in dieser Dissertation ergänzende Maßnahmen eingeführt, die zur Bewältigung spezieller Herausforderungen beim aeronautischen Surveillance Beaconing nötig sind. Für CB-SOTDMA wird eine neuartige Lösung des Problems vorgeschlagen, dass aus unterschiedlichen Zellen empfangene Signale erhebliche Leistungsunterschiede aufweisen können. Die hierzu existierende Lösungsmöglichkeit funktioniert in der Luftfahrt aufgrund der erheblichen Signallaufzeiten nicht effizient. Für Aloha mit SIC wird gezeigt, wie sich der beim Beaconing mit einem Halbduplex-Funkgerät aufgrund des Empfangsausfalls während eigener Übertragungen entstehende Nachrichtenverlust durch ein Zeitsprungverfahren ausgleichen lässt. Das Zeitsprungverfahren unterteilt jede Nachricht in mehrere Teile, die in Abständen zufälliger Länge übertragen werden.

Unter Berücksichtigung der zuvor eingeführten ergänzenden Maßnahmen werden semi-analytische Modelle sowohl von Aloha mit SIC als auch von CB-SOTDMA entwickelt, um die spektrale Effizienz dieser Verfahren unter vereinfachenden Annahmen zu berechnen. Zusätzlich wird solch ein semi-analytisches Modell von Aloha ohne jegliche Multi-User Detektion oder SIC entwickelt, da dieses Verfahren von den am weitesten verbreiteten existierenden Systemen 1090ES und UAT eingesetzt wird. Durch die semi-analytischen Modelle wird die gemeinsame Optimierung der Parameter von PHY- und MAC-Schicht zur Maximierung der spektralen Effizienz ermöglicht. Diese Optimierung ergibt, dass sich sowohl mit Aloha mit SIC als auch mit CB-SOTDMA eine substantiell höhere spektrale Effizienz erreichen lässt, als mit Aloha ohne SIC. Basierend auf der spektralen Effizienz und weiteren Kriterien kommt die vorliegende Arbeit zu dem Schluss, dass Aloha mit SIC das vielversprechendste Konzept für die PHY- und die MAC-Schicht des aeronautischen Surveillance Beaconings darstellt.

Im semi-analytischen Modell von Aloha mit SIC werden bestimmte Komponenten der PHY-Schicht als ideal angenommen. Um einen realistischeren Systementwurf zu erhalten, wird in dieser Arbeit der Interference Canceling Beacon Transceiver (ICBT) entworfen, ein neuartiges aeronautisches Surveillance Beaconing System basierend auf

Aloha mit SIC und dem zuvor erwähnten Zeitsprungverfahren. ICBT enthält realistische Lösungen für wichtige Komponenten der PHY-Schicht wie z.B. Nachrichtendetektion, Kanalschätzung und Interferenzauslöschung. Der Systementwurf von ICBT setzt keinerlei Synchronizität der empfangenen Nachrichten voraus, wie z.B. Synchronizität zu einem gemeinsamen Symboltakt. Zusätzlich wird die Platzierung von bekannten Synchronisationssymbolen innerhalb einer Nachricht so optimiert, dass sich die Dopplerverschiebung im Empfänger genau schätzen lässt. Die resultierende Struktur der Synchronisationssymbole ermöglicht dabei ebenfalls ein Verfahren zur Nachrichtendetektion mit reduziertem Rechenaufwand.

Schließlich wird die spektrale Effizienz von ICBT durch Monte-Carlo Simulationen der vollständigen PHY- und MAC-Schicht untersucht. Die Ergebnisse stimmen gut mit dem semi-analytischen Modell überein. Ergänzend wird ein Szenario zukünftigen Luftverkehrs basierend auf aus der Literatur bekannten Prognosen für das Jahr 2035 entwickelt. Dieses Szenario beschreibt die Verteilung und Bewegung von Flugzeugen realitätsnäher als die vereinfachenden Annahmen der semi-analytischen Modelle. Monte-Carlo Simulationen von ICBT in diesem Luftverkehrsszenario für das Jahr 2035 zeigen, dass der gesamte Datenverkehr des Surveillance Beaconings innerhalb einer Funkbandbreite transportiert werden kann, die sogar kleiner ist als die existierender Systeme, obwohl bei ICBT sowohl Reichweite als auch Paketgröße erhöht wurden.





# Abstract

In aeronautical surveillance beaconing, each aircraft regularly broadcasts surveillance data such as its own position, speed and heading. By receiving the beacon messages transmitted by other aircraft in vicinity, each aircraft becomes aware of surrounding traffic. Since the density of air traffic is growing, the situational awareness must be increased for future air traffic management. Aeronautical surveillance beaconing is an important method to achieve this increase of situational awareness. In contrast to ground-based radar, aeronautical surveillance beaconing provides situational awareness in the cockpit without any additional ground to air transmission of traffic data, and even works in oceanic and remote areas which are not covered by radar.

In aeronautical communications, the scarcity of unoccupied radio spectrum is a limiting factor already today. For this reason, spectral efficiency is of key importance for future aeronautical surveillance beaconing. Currently, three aeronautical surveillance beaconing systems exist: the SSR Mode S Extended Squitter transmitted on 1090 MHz (1090ES), the Universal Access Transceiver (UAT), and the VHF Digital Link Mode 4 (VDL4). The capacity of all three existing systems is known to be inadequate to fulfill the demands of future aeronautical surveillance beaconing. At the same time, there is a lack of research on physical (PHY) layer and medium access control (MAC) layer schemes for aeronautical surveillance beaconing. It is not sufficiently studied which PHY layer and MAC layer schemes achieve a high spectral efficiency in aeronautical surveillance beaconing. Additionally, the joint optimization of PHY and MAC layer parameters is typically neglected in the literature.

In this thesis, we investigate spectrally efficient PHY layer and MAC layer schemes for aeronautical surveillance beaconing. Initially, the requirements of aeronautical surveillance beaconing are described, the multiple-access channel is explained and a definition of the spectral efficiency of aeronautical surveillance beaconing is given. Subsequently, we review existing PHY layer and MAC layer schemes and assess their suitability for spectrally efficient aeronautical surveillance beaconing. Based on this assessment, we select the two most promising schemes with respect to spectral efficiency. The first scheme, cell-based self-organizing TDMA (CB-SOTDMA), uses self-organizing time-division multiple-access (SOTDMA) within each cell of a cellular reuse pattern. CB-SOTDMA coordinates transmissions such that multiple-access interference is minimized. The second scheme is Aloha MAC with successive interference cancellation (SIC) in the receiver. Aloha with SIC does not attempt to avoid multiple-access interference, but to tolerate it through interference cancellation on the PHY layer.

Both for CB-SOTDMA and for Aloha with SIC, we introduce additional measures needed to overcome challenges specific to aeronautical surveillance beaconing. For CB-SOTDMA, we propose a novel solution to the problem of large power imbalances between signals received from different cells. The existing solution to this problem does not work efficiently in aeronautics due to the long signal propagation delays. For Aloha with SIC, we show that time hopping can mitigate message loss due to received signal outage during the own transmissions of a half-duplex beaconing radio. Time hopping splits up a message into multiple parts which are transmitted with gaps of random length in between.

Considering the additional measures introduced before, we develop semi-analytical models both for Aloha with SIC and for CB-SOTDMA to compute their spectral efficiency under simplifying assumptions. Additionally, we develop such a semi-analytical model for Aloha without any multi-user detection or SIC, since this technique is used by the most common existing systems 1090ES and UAT. The semi-analytical models enable us to jointly optimize PHY and MAC layer parameters for maximum spectral efficiency. This optimization reveals that both Aloha with SIC and CB-SOTDMA can achieve a substantially higher spectral efficiency than Aloha without SIC. Based on the spectral efficiency and on further criteria, we conclude that Aloha with SIC is the most promising PHY and MAC layer concept for aeronautical surveillance beaconing.

In the semi-analytical model of Aloha with SIC, certain PHY layer components are assumed to work ideally. To obtain a more realistic system design, we develop the Interference Canceling Beacon Transceiver (ICBT), a novel aeronautical surveillance beaconing system based on Aloha with SIC and time hopping. ICBT includes realistic solutions for PHY layer components such as message detection, channel estimation and interference cancellation. The design of ICBT does not assume received messages to be synchronous to, e.g., a common symbol clock. Additionally, we optimize the placement of known synchronization symbols in a message such that the Doppler shift can be accurately estimated by the receiver. The resulting structure of synchronization symbols also enables a message detection scheme with reduced computational complexity.

Finally, the spectral efficiency of ICBT is investigated by Monte-Carlo simulations of the complete PHY and MAC layer. The results agree well with the semi-analytical model. Additionally, we derive a scenario of future air traffic based on published predictions for the year 2035. This scenario describes the distribution and movement of aircraft more realistically than the simplifying assumptions of the semi-analytical models. Monte-Carlo simulations of ICBT in the 2035 air traffic scenario demonstrate that the entire beaconing traffic can be handled in a bandwidth which is even smaller

than that of existing systems, although both the beaconing range and the packet size are increased in ICBT.



# Contents

<b>1</b>	<b>Introduction</b>	<b>1</b>
1.1	Beaconing: The Broadcast of State Information . . . . .	1
1.2	Aeronautical Surveillance Beaconing . . . . .	2
1.3	The Need for Spectrally Efficient Aeronautical Surveillance Beaconing . . . . .	3
1.4	State of the Art in Aeronautical Surveillance Beaconing . . . . .	3
1.5	Shortcomings of the State of the Art . . . . .	4
1.5.1	The Capacity Shortage of Existing Aeronautical Surveillance Beaconing Systems . . . . .	4
1.5.2	Existing Research on the Transmission of Surveillance Beacon Messages . . . . .	5
1.6	Open Issues . . . . .	6
1.7	Contents and Contributions . . . . .	8
<b>2</b>	<b>Beaconing Scenario and Requirements</b>	<b>11</b>
2.1	Introduction . . . . .	11
2.2	The Task of Surveillance Beaconing and Required Beaconing Performance . . . . .	11
2.3	Message Error Rates and Scheduling Decisions . . . . .	14
2.4	Channel Model . . . . .	14
2.4.1	Introduction . . . . .	14
2.4.2	Signal Propagation Effects . . . . .	15
2.4.3	Received Signal Outage During Own Transmissions . . . . .	19
2.4.4	Thermal Noise . . . . .	20
2.4.5	Complete Description of the Channel . . . . .	20
2.4.6	Use of Subchannels . . . . .	20
2.5	2-D Aircraft Distribution and Movement Model for the Analysis of Beaconing Schemes . . . . .	22
2.6	Spectral Efficiency as Performance Metric . . . . .	23
2.7	Special Aspects of Aeronautical Surveillance Beaconing . . . . .	24
<b>3</b>	<b>Review and Evaluation of Existing PHY/MAC Layer Techniques</b>	<b>27</b>
3.1	Introduction . . . . .	27
3.2	Uncoordinated MAC . . . . .	28
3.2.1	Unslotted Aloha Designed for Single-User Receivers . . . . .	28
3.2.2	Unslotted Aloha Designed for SIC . . . . .	30
3.2.3	Slotted Aloha Designed for Single-User Receivers . . . . .	31
3.2.4	Slotted Aloha Designed for SIC . . . . .	31
3.3	Coordinated MAC . . . . .	32

3.3.1	Carrier Sense Multiple-Access . . . . .	32
3.3.2	Basic Version of Self-Organizing TDMA . . . . .	34
3.3.3	Cell-Based Self-Organizing TDMA . . . . .	36
3.3.4	Further MAC Strategies Based on Cells . . . . .	37
3.3.5	MAC Strategies Using Implicit Reservations . . . . .	38
3.3.6	Slotmap Propagation to Improve SOTDMA . . . . .	38
3.3.7	Handshake-Based Methods . . . . .	39
3.3.8	Methods Based on Master Node Election . . . . .	41
3.3.9	MAC Scheduling Based on SINR . . . . .	41
3.4	Selection of Beaconing Schemes for Further Investigation . . . . .	42
<b>4</b>	<b>Semi-Analytical Investigation of the Spectral Efficiency of Selected Beaconing Schemes</b> . . . . .	<b>43</b>
4.1	Introduction . . . . .	43
4.2	Assumptions for the Comparison of Beaconing Schemes . . . . .	44
4.3	Unslotted Aloha Designed for Single-User Receivers . . . . .	45
4.4	Cell-Based SOTDMA . . . . .	49
4.4.1	Hexagonal Reuse Patterns . . . . .	49
4.4.2	Reuse Pattern Nesting . . . . .	50
4.4.3	Message Scheduling . . . . .	53
4.4.4	Selection of the Coding and Modulation Rate . . . . .	53
4.4.5	Calculation of the Message Error Rate . . . . .	54
4.4.6	Parameter Optimization for Maximum Spectral Efficiency . . . . .	56
4.5	Unslotted Aloha Designed for SIC . . . . .	59
4.5.1	Message Error Rate as a Function of SINR under Blanking Impairment . . . . .	59
4.5.2	Time Hopping . . . . .	60
4.5.3	Calculation of the Message Error Rate after SIC . . . . .	61
4.5.4	Discretization of Received Power and Message Arrival Time . . . . .	65
4.5.5	Parameter Optimization for Maximum Spectral Efficiency . . . . .	66
4.6	Selection of the Most Promising Beaconing Scheme . . . . .	71
<b>5</b>	<b>Design of the Interference Canceling Beacon Transceiver</b> . . . . .	<b>73</b>
5.1	Introduction . . . . .	73
5.2	Basic System Description . . . . .	73
5.2.1	Beaconing Link . . . . .	73
5.2.2	Receiver Signal Processing . . . . .	76
5.3	Special Challenges in Beaconing with Unslotted Aloha and SIC . . . . .	78
5.3.1	Suitable Structure for Long and Sparse Messages . . . . .	78
5.3.2	Time Hopping . . . . .	80

5.3.3	Hierarchical Synchronization Concept . . . . .	81
5.3.4	Coarse Synchronization . . . . .	82
5.3.5	Fine Synchronization . . . . .	83
5.3.6	Interference Cancellation . . . . .	85
5.4	Implementation Aspects and System Parameter Selection for ICBT . .	87
5.4.1	Introduction . . . . .	87
5.4.2	Symbol Rate and Message Length . . . . .	87
5.4.3	Transmitted Waveform and Receiver Filter . . . . .	88
5.4.4	Coding and Modulation . . . . .	89
5.4.5	Synchronization Structure Optimization . . . . .	91
5.4.6	Initial Detection Threshold for Coarse Synchronization . . . . .	94
5.4.7	ICBT System Parameter Summary . . . . .	96
<b>6</b>	<b>Simulation of ICBT under Real-World Effects</b>	<b>99</b>
6.1	Introduction . . . . .	99
6.2	Extended Semi-Analytical Model of Aloha with SIC . . . . .	99
6.3	Simulation Results in the 2-D Scenario . . . . .	101
6.3.1	Monte-Carlo Simulation of the ICBT Message Error Rate . . . . .	101
6.3.2	Spectral Efficiency of ICBT . . . . .	102
6.3.3	Message Error Rate with ICBT Compared to the Extended Semi-Analytical Model . . . . .	103
6.3.4	Influence of Blanking on the Message Error Rate of ICBT . . . . .	104
6.3.5	Influence of Undetected Messages on the Message Error Rate of ICBT . . . . .	105
6.3.6	ICBT Performance with Reduced Number of Synchronization Symbols . . . . .	106
6.3.7	Interference Suppression Achieved by ICBT . . . . .	107
6.4	Future Air Traffic Scenario . . . . .	107
6.4.1	Air Traffic in Europe 2035 . . . . .	107
6.4.2	Worst-Case Receiver Location . . . . .	109
6.5	Simulation Results in the Future Air Traffic Scenario . . . . .	112
6.5.1	ICBT Message Error Rate . . . . .	112
6.5.2	Bandwidth Required by ICBT in the Future Air Traffic Scenario . . . . .	113
6.6	Summary . . . . .	114
<b>7</b>	<b>Summary and Outlook</b>	<b>115</b>
	<b>Appendix</b>	<b>119</b>
A.1	Derivation of the Message Error Rate Equations . . . . .	119
A.1.1	AWGN Without Blanking . . . . .	119

---

A.1.2	AWGN With Blanking . . . . .	120
A.2	Development of the Europe 2035 Air Traffic Scenario . . . . .	121
A.2.1	Methodology . . . . .	121
A.2.2	Simulation Area . . . . .	121
A.2.3	Flight Database Evaluation . . . . .	122
A.2.4	Air Traffic Upscaling According to Predicted Growth . . . . .	124
A.2.5	Air Traffic Simulation . . . . .	124
A.2.5.1	Aircraft Trajectories . . . . .	124
A.2.5.2	Simulation Procedure and Selection of Time Interval for Beaconing Simulations . . . . .	126
A.2.6	Additional TMA Traffic . . . . .	127
	<b>List of Acronyms</b>	<b>129</b>
	<b>List of Symbols</b>	<b>131</b>
	<b>Bibliography</b>	<b>143</b>
	<b>Lebenslauf</b>	<b>151</b>



---

# Chapter 1

## Introduction

### 1.1 Beacons: The Broadcast of State Information

Recently, a multitude of systems has emerged for radio communication between mobile nodes without any supportive infrastructure such as base stations. An important task in many such systems is the periodical broadcast of messages by each node to any other node in vicinity, a process also known as beacons. In this work, a node refers to any entity in a communication system which either transmits or receives messages. Typical beacons differs from other types of communication in that messages are not routed via intermediate nodes, are not acknowledged by the receiver, and not retransmitted in case of message loss.

Beacons is for example used in mobile ad-hoc networks (MANETs) to transmit control data needed to control the flow of payload data [HBWB07, KAE<sup>+</sup>11]. For geographical routing in a MANET, such control data may include the transmitter's position, as well as the state of its network links [MHRR12]. Another application of beacons is the mutual surveillance of mobile nodes such as vehicles, ships, or aircraft [CVMK11, RG12, Int10, RTC02]. Surveillance beacon messages typically inform the surrounding nodes about the sender's position, speed and heading, which may be summarized as the current state of the sender. This state information increases the situational awareness at each node and is useful for collision avoidance and for the efficient routing of traffic.

A typical surveillance beacons example is shown in Figure 1.1, where the beacons nodes are aircraft. Note, however, that the following description is not specific to aviation, but applies to any type of surveillance beacons. Each aircraft in Figure 1.1 periodically broadcasts surveillance beacon messages. As exemplified by means of the red aircraft in the center, the radio system used for beacons must ensure that the beacon messages transmitted by a certain aircraft can be decoded by any other aircraft within the beacons range  $r_b$  around the transmitter. In this way, each aircraft also regularly receives surveillance beacon messages from any other aircraft within its beacons range, and thus becomes aware of surrounding traffic. The beacons range  $r_b$  is selected as the maximum radius within which awareness about other nodes is required for traffic management.

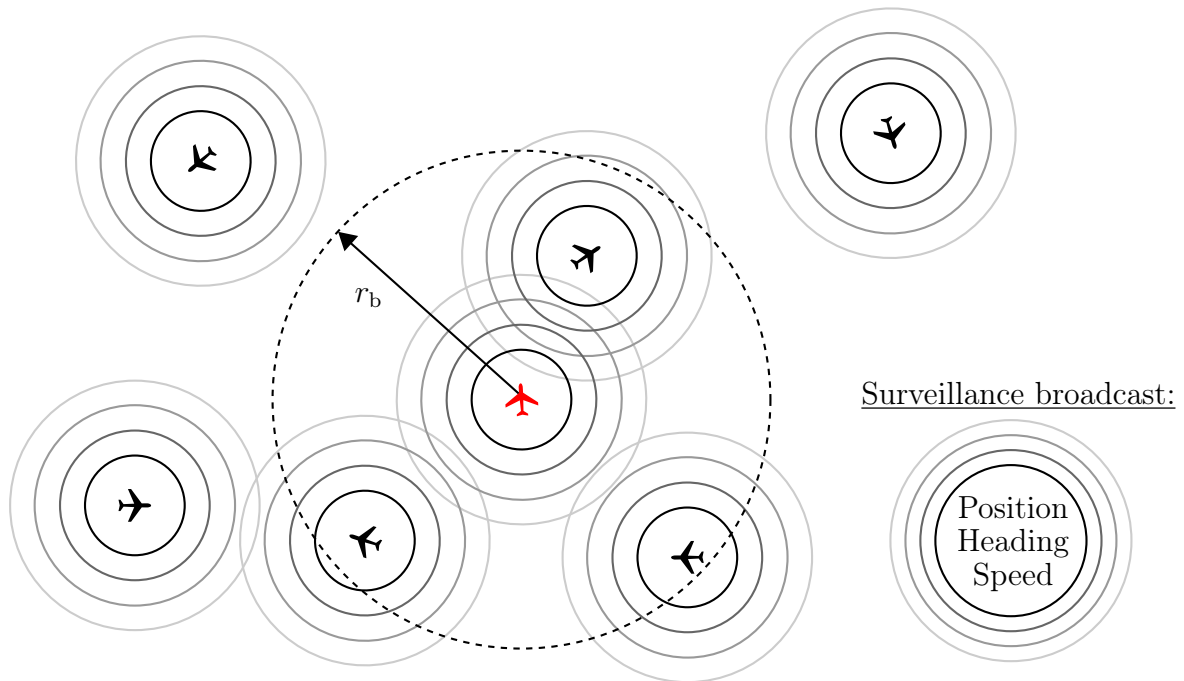


Figure 1.1. Typical surveillance beaconing example. Each aircraft exchanges surveillance beacon messages with all other aircraft in its beaconing range  $r_b$ .

The challenge in the transmission of beacon messages is to share the available radio spectrum in a population of nodes extended over a large area, where each node can only communicate with other nodes within its transmission range. Since no infrastructure is available and the nodes are moving, this situation constitutes a non-trivial multiple-access and radio spectrum reuse problem. The efficient use of radio spectrum for beaconing is made more difficult by the typically small message size and per-node data rate, which increases the impact of any communication overhead such as control data.

## 1.2 Aeronautical Surveillance Beaconing

Aeronautical surveillance beaconing is an important enabler for future air traffic management procedures in civil aviation [Eur07c]. Through increased situational awareness combined with new concepts such as 4-D trajectory coordination, it is expected that the density of air traffic can be increased as needed to meet the growing demand, and that at the same time, safety can be improved. The Automatic Dependent Surveillance Broadcast (ADS-B) standard describes the currently existing aeronautical surveillance beaconing [RTC02]. Note that the standard [RTC02] does not define how beacon messages are transmitted, but only specifies the application, i.e., the data to be broadcast and the communication performance parameters to be achieved.

## 1.3 The Need for Spectrally Efficient Aeronautical Surveillance Beaconing

For aeronautical surveillance beaconing, the efficient use of radio spectrum is a key issue. The spectral efficiency of aeronautical surveillance beaconing can be expressed as the ratio between the maximum aircraft density supported by a beaconing system, and the radio frequency bandwidth it occupies. The importance of spectral efficiency results from the scarcity of both suitable and unoccupied radio spectrum. As a safety-critical air traffic management application, aeronautical surveillance beaconing must operate in specific parts of the electromagnetic spectrum, as determined by international agreements. The frequency bands assigned to air traffic management purposes are listed in the most recent Radio Regulations of the International Telecommunication Union (ITU) [Int12a]. A graphical overview may also be found in [Sta08]. Due to the size of the frequency allocations and the radio wave propagation conditions, the aeronautical frequency allocations in the very high frequency (VHF) band and in the L-band are viable options for beaconing. A joint study by NASA and Eurocontrol surveyed what spectrum could be used for future aeronautical communication systems [Eur07b]. It concluded that the VHF allocations are already congested today by the analogue voice communication system. Therefore, [Eur07b] identified the frequency range from 960 MHz to 1164 MHz in the L-band as the most promising option. However, this frequency range is also already used in large parts, mainly by the navigation system Distance Measuring Equipment (DME) and by secondary surveillance radar (SSR) [ES11, Eur07a]. The importance of spectral efficiency is also recognized by the ADS-B standard [RTC02], which calls it imperative for future systems and suggests to give special attention to it during development. Furthermore, note that surveillance beaconing and similar broadcasts are expected to be the predominant kind of data traffic between aircraft in future air traffic management [Eur07c]. The spectral efficiency of beaconing thus has a large impact on the overall spectral efficiency of air traffic management communication between aircraft.

## 1.4 State of the Art in Aeronautical Surveillance Beaconing

Today, three systems exist for the transmission of ADS-B messages. The SSR Mode S Extended Squitter transmitted on 1090 MHz (1090ES) is an extension of the SSR system used by civil aviation [RTC09]. 1090ES transmits ADS-B messages on the

SSR reply channel at 1090 MHz, in addition to SSR replies. The Universal Access Transceiver (UAT) was developed predominantly for ADS-B and uses dedicated spectrum at 978 MHz [Int09]. The VHF Digital Link Mode 4 (VDL4) standard allows the transmission of ADS-B messages within dedicated, narrowband channels in the VHF band [Int04]. 1090ES and UAT are currently the only two systems in operational use [SSLM14]. 1090ES is the most widespread option, and the only one used internationally, while UAT is permitted for use in the United States by aircraft operating below 18000 ft [Hug14].

In beaconing, multiple-access interference can cause severe message loss [SSLM14, RG12]. Therefore, the physical (PHY) layer, which can be designed to tolerate multiple-access interference, and the medium access control (MAC) layer, which is responsible for controlling multiple-access interference, predominantly determine the spectral efficiency of beaconing. On the PHY layer, all of the existing systems 1090ES, UAT and VDL4 use single-carrier transmission schemes. The typically employed receiver algorithms do not include any multiple-user detection or interference cancellation techniques [RTC09, appendix I.4.1.8]. As MAC layer technology, unslotted Aloha is used by 1090ES and UAT, while VDL4 uses self-organizing time-division multiple-access (SOTDMA). Unslotted Aloha refers to uncoordinated transmissions, which are not synchronized to time slots [Pro01]. In SOTDMA, messages are synchronized to time slots, which are used by the nodes based on a schedule they negotiate using a distributed algorithm [Lan96].

## 1.5 Shortcomings of the State of the Art

### 1.5.1 The Capacity Shortage of Existing Aeronautical Surveillance Beaconing Systems

Using predictions of future air traffic increase, the performance of existing aeronautical surveillance beaconing systems was analyzed already in 2001 by the ADS-B Technical Link Assessment Team (TLAT) led by FAA and Eurocontrol. The TLAT considered all previously mentioned systems, i.e., 1090ES, UAT and VDL4. In its final report, TLAT concluded that none of them would meet all requirements in all considered air traffic scenarios [ADS01]. Those scenarios relied on estimates about future air traffic in the 2015 to 2020 time frame. TLAT considered both the requirements described by the current ADS-B standard [RTC02], and requirements of future surveillance applications. Concerning the latter, it was found that in scenarios of high air traffic density, none

of the assessed technologies would be able to support future autonomous air to air operations with beaconing range requirements of 150 nmi (nautical miles). The main reason for the inadequate performance of the existing systems is that their capacity, i.e., the maximum air traffic density for which acceptable beaconing performance can be achieved, will be insufficient for future, high air traffic densities and future beaconing requirements. Predictions of air traffic growth over the next decades may also be found in [Eur10]. Today, the predominant system 1090ES already suffers from severe message loss due to message collisions [SSLM14].

### 1.5.2 Existing Research on the Transmission of Surveillance Beacon Messages

For the existing aeronautical systems 1090ES, UAT and VDL4 introduced in Section 1.4, simulative studies exist which analyze in how far their performance meets certain requirements in selected air traffic scenarios [RTC09, Int09, ADS01]. However, these studies neither vary the volume of air traffic to determine the exact capacity of the system under consideration, nor do they attempt to optimize PHY or MAC layer parameters in order to maximize the spectral efficiency. Another investigation of VDL4 considers multiple settings of beacon message generation rate and air traffic density, but does not vary any other parameters [SD99]. Furthermore, the air traffic scenarios considered in [RTC09, Int09, ADS01, SD99] represent specific assumptions about the air traffic distribution expected in certain geographical regions at some time in the future. The existence of multiple scenarios in the literature makes it difficult to compare results.

Going beyond the specific design of existing systems, [Ras01] focuses on aeronautical surveillance beaconing and compares two variants of the SOTDMA MAC scheme. Other related works consider surveillance beaconing outside of aviation. In [Ebn05], several MAC schemes, including Aloha and SOTDMA, are compared for surveillance beaconing between road vehicles. For surveillance beaconing between trains, a survey of MAC schemes is available from [RG12]. Although both [Ebn05] and [RG12] develop improved MAC protocols based on SOTDMA, and [RG12] optimizes some MAC parameters, none of the mentioned prior works attempts to optimize the PHY layer. Yet, the interference robustness of the PHY layer determines in how far message collisions lead to message loss, and thus has a large influence on the spectral efficiency. The PHY layer interference robustness is determined by the coding and modulation in the transmitter and the signal processing in the receiver. The assumption used in [Ebn05]

that any message collision results in the loss of all messages involved is an overly simplistic model. Under this assumption, the MAC layer must avoid message collisions at all cost, which is not optimal in cases where the PHY layer would have been able to decode overlapping messages. Assuming a fixed value for the minimum signal to interference and noise ratio (SINR) required for correct decoding, as in [Ras01, RG12], ignores the possibility to take influence on this minimum SINR during system design by appropriately selecting PHY layer parameters.

The previously discussed prior works do not sufficiently analyze the spectral efficiency of aeronautical surveillance beaconing with Aloha MAC. However, this MAC scheme is used by the systems 1090ES and UAT, which are the only ones currently in widespread operational use (cf. Section 1.4). More generally, there is no broader survey of known PHY and MAC layer schemes to identify concepts suitable for achieving a high spectral efficiency in aeronautical surveillance beaconing. It is thus unclear, which PHY and MAC layer scheme should be used for spectrally efficient aeronautical surveillance beaconing. Furthermore, there is a lack of joint PHY and MAC layer parameter optimization for maximum spectral efficiency in beaconing in general. Lastly, note that the shortcomings of existing research discussed in this section apply both to beaconing in dedicated radio spectrum, and to the transmission of beacon messages in spectrum already occupied by another communication or radar system.

## 1.6 Open Issues

Since radio spectrum for aeronautical communications is a scarce resource (cf. Section 1.3) and the capacity of existing aeronautical surveillance beaconing systems is insufficient for future demand (cf. Section 1.5.1), it is necessary to address the shortcomings of existing work discussed in Section 1.5.2. To this end, this work aims at solving the open issues **I1-I9** described in the following. Initially, a review of existing PHY and MAC layer technologies used for beaconing or related multiple-access problems is necessary to identify concepts which could be used in a spectrally efficient aeronautical surveillance beaconing system. The first open issue is thus:

- I1** What PHY and MAC layer technologies promise the highest spectral efficiency for aeronautical surveillance beaconing?

As explained in Chapter 3, cell-based self-organizing TDMA (CB-SOTDMA) and Aloha with successive interference cancellation (SIC) in the receiver are selected as

promising candidates. Due to the fact that it is used by the most important existing aeronautical surveillance beaconing systems 1090ES and UAT, the combination of Aloha MAC and simple receiver algorithms which do not use interference cancellation or any other form of multi-user detection is also of interest for comparison to any new scheme. The primary metric for the comparison of the aforementioned three technologies is their spectral efficiency. The second open issue is thus:

- I2** What spectral efficiency can be achieved when Aloha MAC and simple receiver structures are used for aeronautical surveillance beaconing?

The two candidate technologies CB-SOTDMA and Aloha with SIC have not been considered for aeronautical beaconing before. Both candidates require some adaptations to overcome special challenges of aeronautical surveillance beaconing. With these adaptations, their spectral efficiency has to be derived, which involves the optimization of system parameters. This gives rise to the next open issues:

- I3** How can CB-SOTDMA be adapted to aeronautical surveillance beaconing?
- I4** What PHY and MAC layer parameters optimize the spectral efficiency of aeronautical surveillance beaconing with CB-SOTDMA, and what spectral efficiency can be achieved?
- I5** How can Aloha with SIC be adapted to aeronautical surveillance beaconing?
- I6** What PHY and MAC layer parameters optimize the spectral efficiency of aeronautical surveillance beaconing with Aloha and SIC, and what spectral efficiency can be achieved?

The answers to open issues **I2-I6** rely on simplified, semi-analytical system models and a simplified air traffic scenario. On this basis, Aloha with SIC is selected as the most promising scheme for aeronautical surveillance beaconing in Chapter 4. To analyze the spectral efficiency of the most promising scheme in a realistic scenario taking into account important real-world effects, a complete design of the PHY and MAC layer is needed. Thus, the next open issue is:

- I7** How can an aeronautical surveillance beaconing system using Aloha with SIC be designed, including realistic solutions for important system aspects which were treated in a simplified way in the semi-analytical model?

Once the required design of an aeronautical surveillance beaconing system using Aloha with SIC is available, the validity of the semi-analytical model and the effectiveness of the developed system need to be demonstrated. The latter requires the analysis of the system under realistic, future air traffic conditions. Thus, the last two open issues addressed in this work are:

- I8** How does the spectral efficiency predicted by the semi-analytical model compare to the spectral efficiency achieved by the full system design using Aloha with SIC in the simplified air traffic scenario?
- I9** What spectral resources are required by the system design using Aloha with SIC for aeronautical surveillance beaconing in a realistic, future air traffic scenario?

## 1.7 Contents and Contributions

In this work, we solve the open issues listed in Section 1.6. To keep our investigations independent of any legacy radio systems, we focus on the case that dedicated radio spectrum is available for aeronautical surveillance beaconing. Important basics are addressed in Chapter 2, where the requirements of aeronautical surveillance beaconing, the channel model and the simplified air traffic scenario are explained and the key challenges for a spectrally efficient aeronautical surveillance beaconing scheme are summarized. Chapter 3 deals with the first open issue **I1**. Its main contribution is:

- C1** We review existing work on PHY and MAC layer schemes which are already used or could most likely be adapted for beaconing. The usefulness of the schemes for spectrally efficient aeronautical surveillance beaconing is assessed, taking into account the requirements and challenges identified in Chapter 2. We then select the two transmission schemes promising the highest spectral efficiency as candidates for further, quantitative evaluation.

Chapter 4 begins with the analysis of Aloha with simple receivers without interference cancellation. We address the corresponding open issue **I2** by the following contribution:

- C2** We develop a semi-analytical model of beaconing with Aloha and no interference cancellation or any other kind of multi-user detection. This model takes into account that beaconing radios typically operate in half-duplex mode, i.e., cannot



transmit and receive simultaneously. The main free parameters in the model are the coding and modulation rate and the beacon generation rate, which are optimized to achieve maximum spectral efficiency in the aeronautical surveillance beaconing scenario with simplified air traffic as described in Chapter 2. The optimization also reveals the achievable spectral efficiency.

The adaptation of CB-SOTDMA to aeronautical surveillance beaconing (cf. **I3**) is addressed as follows:

**C3** We introduce a novel cell nesting scheme for CB-SOTDMA, which allows to combine two multiple-access schemes in a cellular reuse pattern. By appropriate selection of the two multiple-access schemes, the cell nesting scheme helps to increase the transmitted energy per bit and to reduce guard times, while ensuring that the large power differences between messages from closer and more distant aircraft can be tolerated. This is especially useful in aeronautics, due to the long distances, long propagation delays, and high transmission losses.

Issue **I4** is addressed by the following contribution:

**C4** We develop a semi-analytical model for aeronautical surveillance beaconing with CB-SOTDMA. Using this model, the main system parameters, cell size, reuse pattern size and reuse pattern nesting strategy, are optimized for maximum spectral efficiency. In this process, the maximum spectral efficiency which can be achieved in aeronautical surveillance beaconing with CB-SOTDMA is derived as well.

Aloha with SIC in the receiver is analyzed with respect to issues **I5** and **I6**, which leads to the next two contributions:

**C5** We introduce a time hopping scheme to reduce the probability that a beaconing node misses large parts of an incoming message due to its own transmissions. The problem of received signal outage during own transmissions, which is inherent to half-duplex beaconing radios, has not yet been considered in Aloha with SIC, as such a scheme has not been used for beaconing before.

**C6** We extend a known semi-analytical model of Aloha with SIC to cover (i) half-duplex radios and (ii) the aforementioned time hopping scheme. Using the extended model, the main system parameters, coding and modulation rate, time hopping sparsity and beacon generation rate, are optimized to maximize the spectral efficiency of aeronautical surveillance beaconing with Aloha and SIC. This reveals the achievable spectral efficiency.

The results of Chapter 4 reveal that CB-SOTDMA and Aloha with SIC both achieve a substantially higher spectral efficiency than Aloha with simple receivers. Based on the spectral efficiency predicted by the semi-analytical models and on further criteria discussed in Chapter 2, Aloha with SIC is selected as the most promising scheme for aeronautical surveillance beaconing.

Chapter 5 focuses on the system design which is needed for more detailed simulations of aeronautical surveillance beaconing with Aloha and SIC, cf. open issue **I7**. Its contribution is:

**C7** We design the Interference Canceling Beacon Transceiver (ICBT), a novel aeronautical surveillance beaconing system using Aloha with SIC and time hopping (cf. **C5**). The design of ICBT details all components needed to simulate PHY and MAC layer in a realistic scenario. This includes message detection, channel estimation and interference cancellation. Our design does not assume received messages to be synchronous to, e.g., a common symbol clock. Additionally, we optimize the placement of known synchronization symbols in the messages such that Doppler shifts can be accurately estimated by the receiver. The resulting structure of synchronization symbols also enables a message detection scheme with reduced computational complexity.

The performance of our system design proposal ICBT is investigated by Monte-Carlo simulations in Chapter 6. This enables the last two contributions of this work, addressing open issues **I8** and **I9**:

**C8** We compute the spectral efficiency of ICBT in the simplified air traffic scenario and confirm important design decisions by means of Monte-Carlo simulations. The simulations include the main relevant propagation effects and do not use any knowledge at the receiver which would in reality not be available. The spectral efficiency resulting from the simulations is compared to the one predicted by the semi-analytical model.

**C9** We compute the bandwidth required by ICBT to fulfill the beaconing requirements defined in Chapter 2 in a realistic, future air traffic scenario. To obtain a realistic air traffic model, our scenario is based on a published database of flight schedules. The air traffic is up-scaled to the estimated volume for the year 2035 according to predictions available from the literature. The results show that the complete beaconing traffic can be handled within a bandwidth which is even smaller than that of the existing systems, although we assume that both the range and the packet size are increased in ICBT.

---

## Chapter 2

# Beaconing Scenario and Requirements

### 2.1 Introduction

In this chapter, we formally describe all aspects of aeronautical surveillance beaconing which are required in later chapters to find a spectrally efficient aeronautical surveillance beaconing system. First, we explain the communication task and quantitatively describe the requirements to be fulfilled by an aeronautical surveillance beaconing system in Section 2.2. Next, the multiple-access channel for the transmission of beacon messages is introduced in Section 2.4, including the relevant basics of signal propagation. Section 2.5 then focuses on the distribution and movement of aircraft and explains an air traffic scenario suitable for the analysis of aeronautical beaconing schemes in later chapters. Note that in [Fra11, Fra12], we employed the same air traffic scenario and multiple-access channel model as in this work. The combination of multiple-access channel and air traffic scenario may be seen as the working conditions of an aeronautical surveillance beaconing system. Next to the aforementioned requirements and working conditions, a quantitative definition of the spectral efficiency of aeronautical surveillance beaconing is required for the comparison of beaconing schemes in later chapters. We present such a quantitative definition in Section 2.6. Finally, we discuss select aspects of aeronautical surveillance beaconing, which have to be taken into account in the assessment of an aeronautical beaconing scheme.

### 2.2 The Task of Surveillance Beaconing and Required Beaconing Performance

In the following, the task of surveillance beaconing is at first described qualitatively, before we define quantitative performance requirements for aeronautical surveillance beaconing. As already explained in Section 1.1, aeronautical surveillance beaconing is used to ensure that aircraft are aware both of the presence and current state of other aircraft in their surrounding. This is accomplished by letting each aircraft broadcast its current state, which may include information such as position, speed and heading [RTC02]. As displayed in Figure 1.1, the beacon messages broadcast by each aircraft are needed by all other aircraft at distances not exceeding the required beaconing range  $r_b$ .

Generally, in surveillance beaconing, the transmitted state information can be seen as a time-continuous signal which can be sampled by a transmitter at any time. A node is therefore able to encode the most recent state information into a message at the time of transmission. Thus, neglecting signal processing and signal propagation delays, it can approximately be assumed that the state information received in surveillance beaconing is up-to-date at the time of reception [RG12]. This differs from traditional data communication, where packets may be waiting in a queue for a medium access opportunity. State tracking algorithms are typically used to estimate, e.g, the current position of a neighboring node from state information received in the past [RG12]. The uncertainty in such an estimate, however, grows with increasing time since the last beacon message was received from a neighboring node. Thus, an aeronautical surveillance beaconing system must ensure that for each aircraft, the information most recently received from neighboring aircraft within a radius of  $r_b$  is, with a very high probability, never outdated.

Let us now formally define the requirements to be fulfilled by an aeronautical surveillance beaconing system. The air space within which surveillance beaconing shall be used to support air traffic management is denoted by  $V$ . Typically,  $V \subset \mathbb{R}^3$ , where  $V$  would be limited to points above the earth, between the ground and some maximum altitude. In the following, we consider the timeliness of information received by some aircraft  $B$  at  $\mathbf{x}_B \in V$ . At time  $t$ , let  $T_u(t, A, B)$  denote the time elapsed since  $B$  received the last update from another aircraft  $A$ . We call  $T_u(t, A, B)$  the data age. Note that  $T_u(t, A, B) = \infty$  if  $B$  has not received any information from  $A$  at or before time  $t$ . In this work, the information about aircraft  $A$  is considered to be outdated at  $B$  if and only if  $T_u(t, A, B)$  exceeds the critical data age  $T_{u,\text{crit}}$ . Figure 2.1 shows a distance interval around aircraft  $B$  with inner radius  $r - \Delta r/2$  and outer radius  $r + \Delta r/2$ . Let  $\mathbb{M}_{\text{ac}}(B, t, r, \Delta r)$  denote the set of aircraft in this distance interval at time  $t$ . The set contains  $N_{\text{ac}}(B, t, r, \Delta r) = |\mathbb{M}_{\text{ac}}(B, t, r, \Delta r)|$  aircraft. The number  $N_{\text{ac}}^{\text{out}}(B, t, r, \Delta r)$  of aircraft about which the information available at  $B$  is outdated can be obtained as

$$N_{\text{ac}}^{\text{out}}(B, t, r, \Delta r) = \left| \left\{ A \in \mathbb{M}_{\text{ac}}(B, t, r, \Delta r) : T_u(t, A, B) > T_{u,\text{crit}} \right\} \right|. \quad (2.1)$$

The probability  $p_{\text{out}}(B, t, r)$  that the data from some aircraft at distance  $r$  is outdated is given by

$$p_{\text{out}}(B, t, r) = \lim_{\Delta r \rightarrow 0} \frac{E\{N_{\text{ac}}^{\text{out}}(B, t, r, \Delta r)\}}{E\{N_{\text{ac}}(B, t, r, \Delta r)\}}. \quad (2.2)$$

We assume that a small probability  $\xi$  of outdated information can be tolerated. The performance requirement to be satisfied by the beaconing system may thus be stated as

$$p_{\text{out}}(B, t, r) \leq \xi \quad \forall r \leq r_b, t \in \mathbb{R}, \mathbf{x}_B \in V. \quad (2.3)$$

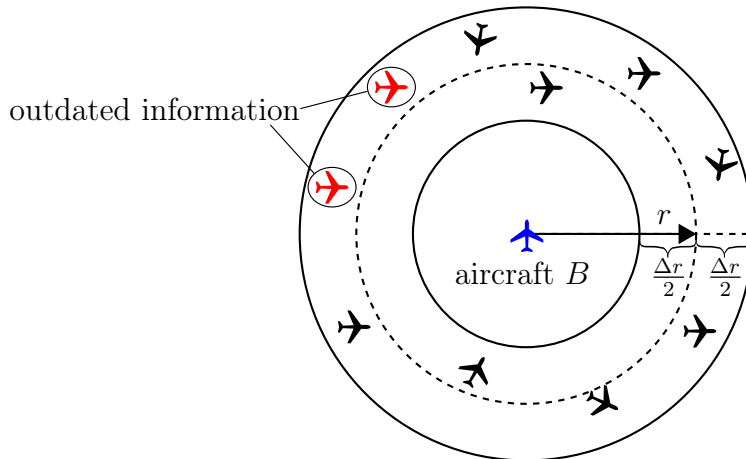


Figure 2.1. Aircraft in distance interval of width  $\Delta r$  around aircraft  $B$ . The total number of aircraft is  $N_{ac}(B, t, r, \Delta r) = 10$ . The information about the  $N_{ac}^{out}(B, t, r, \Delta r) = 2$  red aircraft is outdated at  $B$ .

In reality, several requirements of the form (2.3) may exist at the same time for several different beaconing ranges. One example are the requirements for ADS-B, where the tolerable time between consecutive updates is smaller for aircraft at closer distances [RTC02]. In this work, we restrict attention to only one set of required parameters  $(r_b, T_{u,crit}, \xi)$ . The number  $L$  of information bits each beacon message needs to carry is another requirement. In accordance with [Eur07c], we assume a constant size  $L$  for all aeronautical surveillance beacon messages.

In the following chapters, actual values for the parameters  $r_b$ ,  $T_{u,crit}$ ,  $\xi$  and  $L$  are sometimes required to argue why a certain beaconing scheme is better suited to the aeronautical scenario than another. Challenging requirements are used herein in an attempt to cover future aeronautical beaconing applications. For the required range,  $r_b = 150$  nmi is assumed. This corresponds to the surveillance range envisaged for future autonomous air-to-air operations in [ADS01], and is also identical to the largest fixed-range transmission volume defined for broadcast in [Eur07c]. In the current ADS-B standard [RTC02], a range of 120 nmi is desired, but only 90 nmi are required. Also, in contrast to this work, the longest range requirements in [RTC02] apply only in the forward direction. For the critical data age,  $T_{u,crit} = 1$  s is used in this work. This corresponds to the desired update interval for lower ranges from [RTC02]. The tolerable probability of outdated information is set to  $\xi = 10^{-3}$ . This goes beyond the strictest requirement from [RTC02], which tolerates excessive delay between consecutive updates in one percent of the cases. The message size is assumed to be 40 bytes, i.e.,  $L = 320$  bits. This is slightly more than the 34 bytes assumed for surveillance broadcasts in [Eur07c].

## 2.3 Message Error Rates and Scheduling Decisions

According to the previous description, the information about some aircraft at distance  $r$  from aircraft  $B$  is outdated at time  $t$  if and only if no message was received from this aircraft during the past time interval of duration  $T_{u,\text{crit}}$ . Because of this,  $p_{\text{out}}(B, t, r)$  depends both on how many messages an aircraft transmits within  $T_{u,\text{crit}}$  and on the probability that  $B$  loses a certain number of consecutive messages from the same aircraft. How many messages are transmitted depends on the scheduling decisions. They are the output of the distributed algorithm which runs at each aircraft and, based on locally available information, decides when and how to transmit messages. In the most simple case, each aircraft transmits at a regular rate of  $\lambda' = \tilde{k}/T_{u,\text{crit}}$  messages per time, with integer  $\tilde{k}$ . Then,  $p_{\text{out}}(B, t, r)$  is equivalent to the probability that  $B$  has lost the last  $\tilde{k}$  messages transmitted by an aircraft at distance  $r$ . A beacons scheme may use  $\tilde{k} > 1$  to compensate message loss [RG12], or may transmit with  $\lambda' = 1/T_{u,\text{crit}}$  ( $\tilde{k} = 1$ ). In the latter case,  $p_{\text{out}}(B, t, r)$  is identical to the message error rate (MER) for messages received by aircraft  $B$  from aircraft at distance  $r$ , if one ignores the change of  $r$  during the time  $T_{u,\text{crit}}$ . Requirement (2.3) is then identical to a MER requirement.

## 2.4 Channel Model

### 2.4.1 Introduction

A central element of the problems addressed in this work is the multiple-access channel through which messages are exchanged between aircraft. The input to the channel consists of all beacon messages transmitted over it. For any receiving station, the channel model describes the received signal and its dependence on the channel input. In the following, the channel model and all relevant signals are described in the complex baseband. We compute the received signal, i.e., the channel output, at one particular receiving aircraft. For any other aircraft, the received signal may be obtained in the same way. Looking at a single message transmission, the radio signal propagation between two aircraft is described in Section 2.4.2. In Section 2.4.3, we describe the signal outage caused by own transmissions of the receiving aircraft. Additive thermal noise is addressed in Section 2.4.4. Combining the aforementioned effects, and taking into account that many messages transmitted by a large number of aircraft contribute to the received signal, the entire received signal is computed in Section 2.4.5. Additionally, some beacons schemes considered in this work subdivide the transmission channel into subchannels, which is explained in Section 2.4.6.

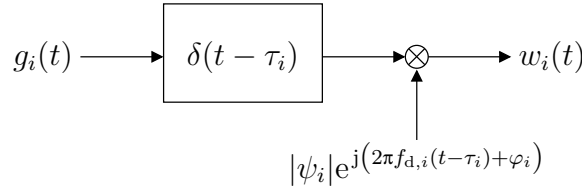


Figure 2.2. Propagation path with delay, path loss, Doppler shift and phase shift.

## 2.4.2 Signal Propagation Effects

The effects of signal propagation are discussed by looking at one particular beacon message of index  $i \in \mathbb{N}$ . We assume a single propagation path as depicted in Figure 2.2. It is characterized by its path loss  $|\psi_i|^{-2}$ , its delay  $\tau_i$ , its phase rotation  $\varphi_i$  and its Doppler shift  $f_{d,i}$ . The complex channel coefficient  $\psi_i = |\psi_i|e^{j\varphi_i}$  summarizes the effects of path loss and phase rotation. Let  $g_i(t - t_{\text{tx},i})$  be the transmit signal for message  $i$ , which is transmitted at time  $t_{\text{tx},i}$ . We assume that all nonzero parts of  $g_i(t)$  are contained in a short interval of time, which nominally begins at  $t = 0$  and ends after the nominal message duration  $T_{\text{msg},i}$ . In the most simple case,  $g_i(t)$  consists of a single transmission burst nominally lasting from  $t = 0$  to  $t = T_{\text{msg},i}$ . In later chapters, we will make use of the possibility to compose a message of multiple such bursts spaced by gaps. In this case, the first burst nominally begins at  $t = 0$  and the last burst nominally ends at  $t = T_{\text{msg},i}$ . Note that while every message contains  $L$  bits of information, the PHY layer of a beaconing scheme could potentially encode and modulate messages in different ways. Thus,  $T_{\text{msg},i}$  is not necessarily the same for all messages. Furthermore, the nominal duration of a transmission burst may be extended marginally by rising and falling signal edges, which are not accounted for in  $T_{\text{msg},i}$ . The channel response to  $g_i(t - t_{\text{tx},i})$  is defined as  $w_i(t - t_{\text{tx},i})$ , where  $w_i(t)$  is given by

$$w_i(t) = \psi_i g_i(t - \tau_i) e^{j2\pi f_{d,i}(t - \tau_i)}. \quad (2.4)$$

We assume that the channel parameters  $\psi_i$ ,  $\tau_i$  and  $f_{d,i}$  stay constant over the duration  $T_{\text{msg},i}$  of one beacon message, but change from one message to the next due to the movement of the aircraft.

For a distance of  $r_i$  between transmitter and receiver, the propagation delay is given by

$$\tau_i = \frac{r_i}{c}. \quad (2.5)$$

The relative speed  $v_{\text{rel},i}$  of transmitter and receiver causes the Doppler shift. It is defined as  $v_{\text{rel},i} = dr_i/dt|_{t=t_{\text{tx},i}}$ . To be exact, nonzero  $v_{\text{rel},i}$  also leads to a time expansion or contraction of  $g_i(t)$ . However, we assume messages to be short enough so that

this can be neglected. The Doppler shift is obtained from the well-known relationship [Rap01]

$$f_{d,i} = f_c \frac{v_{\text{rel},i}}{c}. \quad (2.6)$$

For the system design in Chapter 5, the frequency range which has to be searched by a receiver to find the Doppler shift of an incoming message is of importance. This frequency range is called the Doppler search range and is denoted by  $W_d$ . It is equal to the difference between the highest and lowest possible value of  $f_{d,i}$ , which, according to (2.6), is proportional to the difference between the highest and lowest possible relative speed. Assuming a maximum aircraft speed of  $v_{\text{ac}}$ , the relative speed is bounded by  $-2v_{\text{ac}} \leq v_{\text{rel},i} \leq +2v_{\text{ac}}$ , where the extreme values are assumed when transmitter and receiver are flying directly towards or away from each other. Then,  $W_d$  is given by

$$W_d = 4f_c \frac{v_{\text{ac}}}{c}. \quad (2.7)$$

For example at carrier frequencies in the aeronautical L-band, i.e., around  $f_c = 1$  GHz,  $W_d$  would amount to 4 kHz at an aircraft speed of  $v_{\text{ac}} = 300$  m/s. The complex channel coefficient can be computed as

$$\psi_i = \sqrt{\frac{P_{\text{rx}}(r_i, r_s)}{P_{\text{tx}}}} e^{j\varphi_i}, \quad (2.8)$$

where  $P_{\text{tx}}$  denotes the transmit power,  $P_{\text{rx}}(r_i, r_s)$  denotes the received power, and  $r_s$  is the line of sight range explained later in this section. The phase  $\varphi_i$  of  $\psi_i$  is assumed to be independent and identically distributed (i.i.d.) for different beacon messages, following a uniform distribution in  $[-\pi, \pi)$ .

The path loss  $|\psi_i|^{-2}$  between aircraft at carrier frequencies in the bands available for aeronautical communications is described in detail in [Int12b]. As long as transmitting and receiving aircraft are within line of sight, this path loss is commonly approximated by free space propagation [ADS01, SD99, Int09, RTC09, MHRR12, Hof14]. Free space propagation is a special case of the log-distance path loss model [Rap01]. The received power  $P_{\text{rx,LD}}(r_i)$  according to the log-distance path loss model is

$$P_{\text{rx,LD}}(r_i) = P_{\text{tx}} \left( \frac{r_{\text{ref}}}{r_i} \right)^\alpha, \quad (2.9)$$

where  $\alpha$  is the channel loss exponent and  $r_{\text{ref}}$  denotes the distance at which the transmission loss would hypothetically be 0 dB. In reality, (2.9) is typically only valid when  $r_i \gg r_{\text{ref}}$ . Free space propagation corresponds to  $\alpha = 2$ . For distances beyond the line of sight range, the path loss reported in [Int12b] quickly increases to extremely high values. Therefore, we assume in this work that propagation is limited by the line of



sight range  $r_s$  [Hof14, SD99]. Hence, the received power  $P_{\text{rx}}(r_i, r_s)$  is given by

$$P_{\text{rx}}(r_i, r_s) = \begin{cases} P_{\text{rx,LD}}(r_i), & \text{if } r_i \leq r_s, \\ 0, & \text{if } r_i > r_s. \end{cases} \quad (2.10)$$

It remains to be noted that although (2.9) cannot be valid for  $r_i < r_{\text{ref}}$  and will typically only be valid when  $r_i/r_{\text{ref}}$  is large, we use (2.9) even for small  $r_i$ . This may be done in aeronautical surveillance beaconing for the following reason. In free space ( $\alpha = 2$ ), (2.9) holds when the receiver is in the far field of the transmitter according to the far field conditions given in [Rap01], which depend on the antenna sizes. Typical aeronautical beaconing antennas are omnidirectional in azimuth and have physical dimensions not exceeding one wavelength  $c/f_c$ , where  $c$  is the speed of light and  $f_c$  is the carrier frequency used for beaconing. For such antennas, the far field conditions are fulfilled when  $r_i > 2c/f_c$ . However, for the radio frequencies of interest herein, aircraft are in any practical situation separated by  $r_i \gg 2c/f_c$ .

To evaluate the complex channel coefficient (2.8), the line of sight range between aircraft is required. In the context of radio communications, a line of sight refers to a direct propagation path between transmitter and receiver for radio waves at the carrier frequency  $f_c$  of the beaconing system. Due to refraction in the atmosphere, radio waves bend around the curvature of the earth, which increases the line of sight range compared to the hypothetical case of propagation along a straight line. To approximate this range increase, the line of sight range can be computed assuming a straight propagation path over a spherical earth of increased radius  $k_E R_E$ , where  $R_E = 6370$  km is the earth radius and  $k_E = 4/3$  is the effective earth radius factor [Par00]. Accordingly, in a realistic, three dimensional air traffic scenario, the line of sight range  $r_{\text{s,3D}}(h_1, h_2)$  between two aircraft at altitudes  $h_1$  and  $h_2$  above ground is obtained as [Hof14]

$$r_{\text{s,3D}}(h_1, h_2) = \sqrt{h_1^2 + 2h_1 k_E R_E} + \sqrt{h_2^2 + 2h_2 k_E R_E}. \quad (2.11)$$

Furthermore, the distance  $r_{\text{ref,FS}}$  at which the transmission loss in free space would hypothetically be 0 dB can be derived from the Friis free space equation [Rap01]. According to this well known equation, the received power is

$$P_{\text{rx,FS}}(r_i) = P_{\text{tx}} \mathcal{G}_{\text{tx}} \mathcal{G}_{\text{rx}} \left( \frac{c}{4\pi f_c r_i} \right)^2, \quad (2.12)$$

where  $\mathcal{G}_{\text{tx}}$  and  $\mathcal{G}_{\text{rx}}$  denote the transmit and receive antenna gains, respectively. Comparing (2.12) to (2.9) for the case  $\alpha = 2$ , we can easily determine that

$$r_{\text{ref,FS}} = \sqrt{\mathcal{G}_{\text{tx}} \mathcal{G}_{\text{rx}}} \frac{c}{4\pi f_c r_b}. \quad (2.13)$$

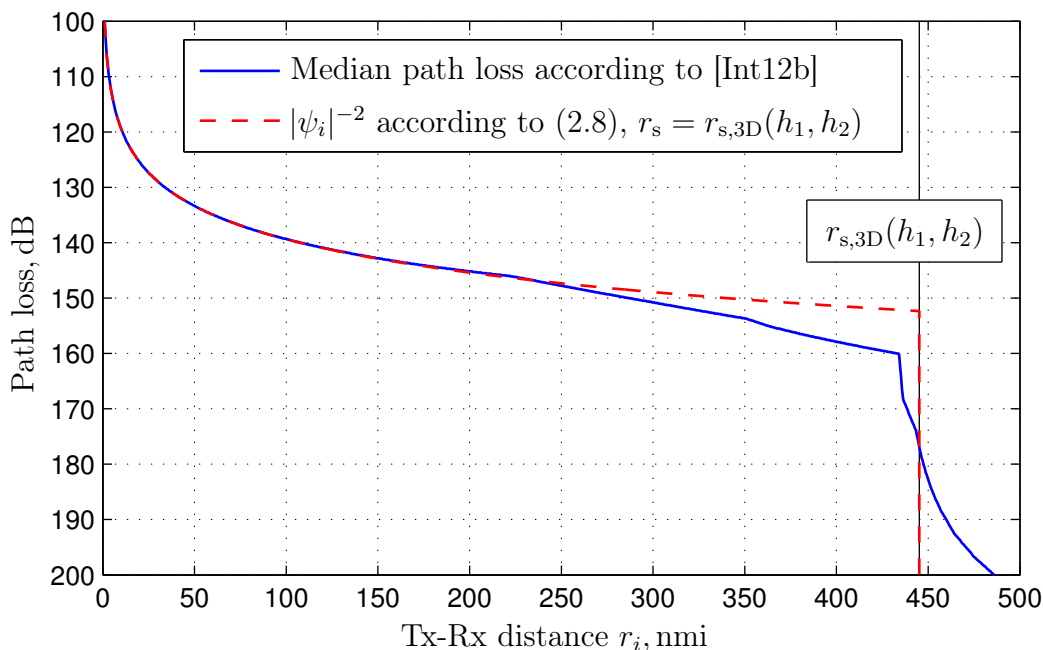


Figure 2.3. Median path loss according to [Int12b] compared to (2.8) with  $r_s = r_{s,3D}(h_1, h_2)$ , for aircraft altitudes  $h_1 = h_2 = 10000$  m,  $f_c = 1200$  MHz,  $\alpha = 2$ ,  $\mathcal{G}_{\text{tx}} = \mathcal{G}_{\text{rx}} = 0$  dBi.

Let us now compare the path loss according to (2.8) and line of sight range (2.11) to the path loss reported in [Int12b] for signal propagation between aircraft. Of the frequencies considered in [Int12b],  $f_c = 1200$  MHz comes closest to the L-band frequency range of interest for aeronautical beaoning according to Section 1.3. For two aircraft at the same altitude of  $h_1 = h_2 = 10000$  m and for a frequency of  $f_c = 1200$  MHz, Figure 2.3 shows the median path loss according to [Int12b] as a function of distance. Note that [Int12b] assumes  $\mathcal{G}_{\text{tx}} = \mathcal{G}_{\text{rx}} = 0$  dBi. Additionally,  $|\psi_i|^{-2}$  according to (2.8) and  $r_s = r_{s,3D}(h_1, h_2)$  is plotted in Figure 2.3. For the plot of  $|\psi_i|^{-2}$ , we assumed the same frequency, aircraft altitudes and antenna gains as before, as well as  $\alpha = 2$  and  $r_{\text{ref}} = r_{\text{ref,FS}}$  according to (2.13). We observe that up to a distance of  $r_i = 250$  nmi, there is almost no difference between the two curves plotted in Figure 2.3. This indicates that the path loss according to (2.8) and  $r_s = r_{s,3D}(h_1, h_2)$  closely matches the median path loss according to [Int12b] up to distances significantly exceeding the required beaoning range of  $r_b = 150$  nmi (cf. Section 2.2). At  $r_i > 250$  nmi, our model (2.8) with  $r_s = r_{s,3D}(h_1, h_2)$  overestimates the received power in the example shown in Figure 2.3. This leads to an overestimation of interference created by beacon messages from transmitters within the range  $250 \text{ nmi} < r_i \leq r_{s,3D}(h_1, h_2)$ . We consider this overestimation of interference from faraway sources as a prudent assumption in the analysis of aeronautical beaoning schemes. Figure 2.3 also shows that the median path loss according to [Int12b] is very high at  $r_i > r_{s,3D}(h_1, h_2)$  and increases rapidly

with  $r_i$ . Neglecting any signal from transmitters beyond the line of sight range thus appears justified.

### 2.4.3 Received Signal Outage During Own Transmissions

In the following, we describe a model for the outage of the received signal while the receiving aircraft is transmitting itself. Radio devices are typically unable to transmit and receive at the same time and on the same frequency [Rap01]. The propagation path loss usually leads to a huge disparity between transmitted and received power. Due to this, it is usually not possible or too costly to install sufficient isolation between the transmitter and receiver parts of the same radio device. This means that an ongoing transmission in the same frequency range as the one covered by the receiver input filter renders the receiver deaf, e.g., by saturating the input amplifier and/or the analog-to-digital converter. Concurrent transmission and reception is only possible by using different frequency ranges which are separated by filters in the analog domain [Rap01]. Should two or more such frequency ranges exist, they are regarded herein as independent physical channels.

The deafness of a receiver during its own transmissions on the same channel can be modeled by the addition of a very strong noise term  $n_{\text{own}}(t)$  to the received signal. To calculate  $n_{\text{own}}(t)$ , let  $\mathbb{M}_{\text{own}}$  be the set of message indices of all messages transmitted by the receiving aircraft. Then, this aircraft's own transmit signal  $g_{\text{own}}(t)$  is given by

$$g_{\text{own}}(t) = \sum_{i \in \mathbb{M}_{\text{own}}} g_i(t - t_{\text{tx},i}). \quad (2.14)$$

Let  $n_{\infty}(t)$  be a white Gaussian noise process of infinite power within any bandwidth. Then,  $n_{\text{own}}(t)$  is obtained as

$$n_{\text{own}}(t) = \begin{cases} n_{\infty}(t), & \text{if } t \in \text{supp}(g_{\text{own}}(t)), \\ 0, & \text{otherwise,} \end{cases} \quad (2.15)$$

where  $\text{supp}(f(t))$  denotes the support of the function  $f(t)$ , which is the closure of the set of all points where  $f(t)$  is nonzero. Obviously, the accumulated duration of received signal loss depends both on the duration of all transmission bursts in a message, as well as on the message generation rate  $\lambda'$ . Note that either an arbitrary portion or the entirety of a received message may be affected by received signal outage. Whether a partial outage leads to loss of a received message or not, depends on the PHY layer of the beaconing scheme. For example, low-rate forward error correction may be able to decode a message even if some part is missing.

### 2.4.4 Thermal Noise

As last characteristic of the channel, the received signal is impaired by the thermal noise process  $n(t)$ , which is assumed to be additive white Gaussian noise (AWGN). The one-sided power spectral density of  $n(t)$  is denoted by  $N_0$ . Here,  $n(t)$  is the entire equivalent noise at the antenna input of the receiver, which is the sum of background noise and receiver noise [Rap01]. With receiver noise figure  $F_{\text{dB}}$ , given in dB, we have

$$N_0 = -174 \text{ dBm/Hz} + F_{\text{dB}}, \quad (2.16)$$

where  $-174 \text{ dBm/Hz}$  is the background noise power spectral density at 290K.

### 2.4.5 Complete Description of the Channel

Figure 2.4 depicts how the transmit signal  $g_i(t - t_{\text{tx},i})$  of message  $i$  undergoes the propagation channel, leading to the channel response  $w_i(t - t_{\text{tx},i})$  at the receiver. For message  $i$ , the channel responses  $w_k(t - t_{\text{tx},k})$  of all other messages  $\{k : k \neq i, k \notin \mathbb{M}_{\text{own}}\}$  transmitted by other aircraft constitute potential multiple-access interference (MAI), since, depending on the MAC layer, they may overlap with message  $i$  at the receiver. Summing up all channel responses, the impairment term  $n_{\text{own}}(t)$  due to own transmissions and the thermal noise  $n(t)$  yields the received signal  $\tilde{w}(t)$ :

$$\tilde{w}(t) = \sum_{i \notin \mathbb{M}_{\text{own}}} w_i(t - t_{\text{tx},i}) + n_{\text{own}}(t) + n(t). \quad (2.17)$$

### 2.4.6 Use of Subchannels

Some beaconing schemes considered in this work require the introduction of subchannels. Subchannels are a way of subdividing the physical channel for multiple-access. Each subchannel corresponds to a special way of creating the transmit signals  $g_i(t)$  and choosing the access times  $t_{\text{tx},i}$ . The idea is to design the signals such that the interference between messages received on different subchannels is minimized. For example, the PHY layer can subdivide the bandwidth of the channel into several sub-bands and a message  $g_i(t)$  can be designed such that its spectrum falls predominantly into only one of them. Each band is then called a frequency-division multiple-access (FDMA) subchannel [Rap01]. Another possibility is to provide a noise-like spreading code for each subchannel. In this case, we are looking at a number of code-division multiple-access (CDMA) subchannels [Rap01]. Note that the use of orthogonal spreading codes does not make sense in beaconing, since they are typically only orthogonal when syn-

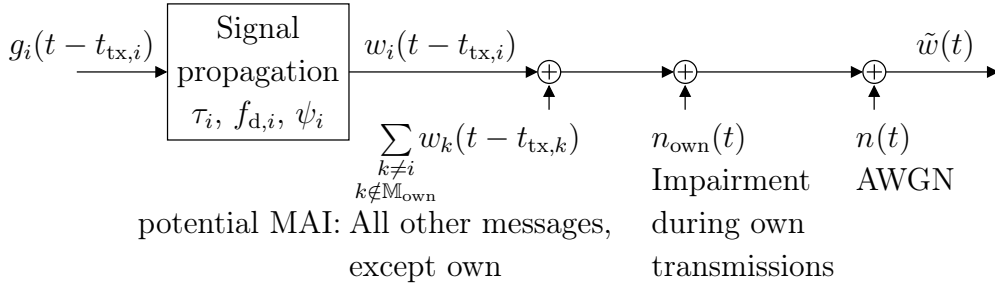


Figure 2.4. Transmission channel with signal propagation, multiple-access interference and additive noise.

chronized in time. In beaconing, however, there are many receivers and it is impossible to synchronize messages such that they arrive synchronously at each of them. CDMA codes should thus provide a low cross-correlation not only when they are perfectly synchronized. Note that FDMA and CDMA do not impose any restriction on the access times  $t_{tx,i}$ . If the subchannels are designed such that the level of cross-talk between them is low enough, messages on different subchannels can be received at the same time even when their received powers differ by a large factor. However, we assume that concurrent transmission and reception is not possible, regardless of what subchannels are used. Due to the extreme power difference between transmitted and received signal, concurrent transmission and reception on different subchannels is typically not possible for CDMA, or requires large guard bands and analogue duplexing filters for FDMA.

Another option is the use of time-division multiple-access (TDMA) subchannels. In TDMA, time is divided into slots, i.e., consecutive intervals of time [Rap01]. In their most simple form, the slot duration is constant and designed for the transmission of a single message. Nodes may only access the channel (start to transmit a message) at the beginning of a time slot. The slot duration accounts not only for the message duration, but also for propagation delays and possible timing errors at the transmitting node. The excess time is called the guard time, as it protects messages from colliding with other messages transmitted in adjacent slots. The slots are grouped into consecutive sections called frames, where each frame holds the same number of slots. To establish TDMA subchannels, a frame is subdivided into multiple sections, where each section belongs to a subchannel. A message on a particular subchannel may be transmitted in any frame, but only in the section of slots belonging to the subchannel. Thus, TDMA subchannels do not impose any restrictions on the waveforms of the messages, but restrict them to separate intervals in the time domain. In consequence, transmitting on a particular TDMA subchannel does not cause signal outage on any other TDMA subchannel. Any other subchannel concept cannot by itself guarantee this, as an ongoing transmission on any subchannel destroys the entire received signal according to (2.15).

## 2.5 2-D Aircraft Distribution and Movement Model for the Analysis of Beacons Schemes

In the following, we describe the simplified air traffic scenario used for the analysis of beacons schemes in Chapters 3 to 6 of this work. A more realistic model of future air traffic is introduced in Section 6.4 and used to demonstrate the effectiveness of the system design we develop in Chapter 5. In the simplified air traffic scenario, aircraft are located on a two-dimensional plane, which is why this scenario is in the following also called the 2-D model. In reality, the line of sight range (2.11) at typical cruise altitudes is much larger than the maximum altitude at which aircraft can fly. Also, the vertical speed of an aircraft is in typical situations much smaller than its horizontal speed. Hence, a two-dimensional air traffic distribution reasonably approximates the distances and relative speeds between aircraft, as needed to determine all signal propagation conditions described in Section 2.4.2. The only exception is the line of sight range, which we assume to be  $r_s = 500$  nmi for all pairs of aircraft in the 2-D model. Such a large  $r_s$  is a worst-case assumption for the following reason. A planar aircraft arrangement with constant line of sight range  $r_s$  corresponds to a three-dimensional case where all aircraft are at the same altitude. The aircraft altitude  $h_{2D}$  corresponding to the 2-D model can be obtained from (2.11) by solving  $r_{s,3D}(h_{2D}, h_{2D}) = 500$  nmi for  $h_{2D}$ , which results in  $h_{2D} = 41373$  ft. For comparison, an air traffic scenario described in [Int09] uses exponentially distributed altitudes, with a mean of 5500 ft, in which case only 1 in 1849 aircraft would exceed  $h_{2D} = 41373$  ft. Furthermore, the altitude range from 35000 ft to 40000 ft is called “high altitude” in [Int09]. This indicates that the vast majority of air traffic does not exceed  $h_{2D} = 41373$  ft, which implies that the line of sight range exceeds  $r_s = 500$  nmi only in rare cases. Hence, the 2-D model with  $r_s = 500$  nmi is a worst-case assumption in terms of multiple-access interference, which is more difficult to handle when more aircraft are within line of sight of a receiving aircraft.

Concerning the spatial node distribution, we assume random aircraft locations determined by a two-dimensional Poisson point process (PPP) with constant density  $\rho$ . Thus, the number of aircraft in an area of size  $A$  is Poisson distributed with mean  $\rho A$  and the aircraft counts in disjoint areas are statistically independent. The assumption of a two-dimensional PPP is widespread in the analysis of MANETs, since it facilitates analytical investigations [SS90, WAJ10, MJ14, BM10]. To model the movement of aircraft, we assume a constant speed of  $v_{ac} = 300$  m/s (583 kts). This is very close to the maximum aircraft speed of 600 kts assumed in [RTC02] for various worst-case scenarios. The directions of movement are i.i.d., following a uniform distribution between  $0^\circ$  and  $360^\circ$ .

Table 2.1. Properties and Parameters of the 2-D Model.

Aircraft locations	two-dimensional PPP, density $\rho$
Direction of movement	random, uniformly distributed in $[0^\circ, 360^\circ)$
Aircraft speed $v_{ac}$	300 m/s
Line of sight range $r_s$	500 nmi

The 2-D model is summarized in Table 2.1. Note that in the 2-D model, no value is specified for the aircraft density  $\rho$ , since in later chapters, we seek the maximum  $\rho$  a certain beaconing scheme can handle in a given bandwidth. While we try to keep the discussion of spectral efficiency in Chapters 3 to 5 as independent of the actual aircraft density as possible, some conclusions require an understanding of at least the magnitude of  $\rho$  to be expected in reality. The reason is that the impact of some effects, such as control data overhead, can depend on the actual number of nodes within range. Due to this, we state already here that a typical aircraft density to be expected in the future over Europe is in the order of  $\rho_{typ} = 0.015$  aircraft per nmi<sup>2</sup> according to the more realistic model of future air traffic to be presented in Section 6.4.

## 2.6 Spectral Efficiency as Performance Metric

As explained in Section 1.3, bandwidth is a critical resource for aeronautical surveillance beaconing. We will therefore employ the spectral efficiency as performance metric for the evaluation and comparison of different beaconing schemes in this work. In this section, we introduce an appropriate formal definition of the spectral efficiency of surveillance beaconing. Assume that all signals  $g_i(t)$  used by the beaconing system (cf. Section 2.4) comply with some spectral mask of bandwidth  $W_{sys}$ . In this case,  $W_{sys}$  may be called the bandwidth occupied by the beaconing system. As explained in Section 1.7, we assume that spectrum of bandwidth  $W_{sys}$  is available exclusively for the beaconing system. According to Section 2.3, a single aircraft transmits  $\lambda'$  messages per time. The normalized message transmission rate  $\lambda$  of a single aircraft is defined as

$$\lambda = \lambda' \frac{L}{W_{sys}}, \quad (2.18)$$

which is identical to the average amount of information transmitted by each aircraft per time and bandwidth. To assess the efficiency of a beaconing scheme, however, we are interested in the maximum aircraft density  $\rho$  for which the beaconing requirements (2.3) can be fulfilled using a bandwidth of  $W_{sys}$ . In this respect, the data rate transmitted

by a single aircraft or the aggregate data rate of messages successfully received from surrounding aircraft matter only indirectly. This is because aircraft may transmit at an increased rate to compensate message loss, as explained in Section 2.3. In the same way, more messages may be received from a certain neighboring aircraft than absolutely necessary to prevent outdated information. Therefore, we define the nominal normalized message transmission rate as

$$\lambda_{\text{nom}} = \frac{L}{T_{\text{u,crit}} W_{\text{sys}}}, \quad (2.19)$$

which is the minimum  $\lambda$  at which a beaconing system could hypothetically avoid outdated information in the absence of message loss. The maximum aircraft density  $\rho_{\text{max}}$  which can be supported by a given beaconing system without violating the requirement (2.3) is

$$\rho_{\text{max}} = \sup\{\rho : \text{Requirement (2.3) fulfilled}\}, \quad (2.20)$$

where  $\sup(\mathbb{M})$  denotes the supremum, or least upper bound, of the set  $\mathbb{M}$ . By means of  $\rho_{\text{max}}$ , we can determine the maximum nominal normalized data rate received by an aircraft from other aircraft at distances  $r \leq r_{\text{b}}$ . We call it the nominal spectral efficiency  $\eta$  and define it as

$$\eta = \rho_{\text{max}} \lambda_{\text{nom}} \pi r_{\text{b}}^2. \quad (2.21)$$

Note that  $\eta$  may be seen as a normalization of  $\rho_{\text{max}}$  and that the search in the following chapters for the beaconing scheme that maximizes  $\eta$  is identical to looking for the scheme that supports an as large as possible user density  $\rho_{\text{max}}$  within an as small as possible bandwidth  $W_{\text{sys}}$ . Defined as above,  $\eta$  may be expressed in received bits per time and bandwidth. Without message loss and with  $\lambda' = 1/T_{\text{u,crit}}$ , the nominal spectral efficiency  $\eta$  would be identical to the aggregate data rate received by an aircraft from all others within  $r_{\text{b}}$ . Another criterion looking at the aggregate rate at a receiver is the local capacity defined in [MJ14] to assess MANET communication. The difference is that the local capacity considers any correctly received data packet, while (2.21) considers only the information of interest, i.e., only messages from distances  $r \leq r_{\text{b}}$  and only the minimum necessary beaconing rate  $\lambda_{\text{nom}}$ .

## 2.7 Special Aspects of Aeronautical Surveillance Beaconing

Some aspects of aeronautical surveillance beaconing are especially relevant for the assessment of beaconing schemes in the following chapters. These aspect, which can be seen as special challenges in aeronautical surveillance beaconing, result from the aeronautical scenario and the surveillance beaconing requirements.



1. Number of nodes: In aeronautical beaconing, both the line of sight range  $r_s$  and the required beaconing range  $r_b$  are much larger than in other typical beaconing applications. It has to be expected that the number of aircraft within a circle of radius  $r_b = 150$  nmi is in the order of  $\rho_{\text{typ}}\pi r_b^2 \approx 1000$ . The fact that the received data traffic consists of transmissions from this many sources may lead to excessive control data overhead in a communication protocol. For a more detailed discussion of the air traffic density, cf. Section 6.4.
2. Interference from nodes outside the desired range: The line of sight range between aircraft at cruise altitude is usually much larger than the required beaconing range  $r_b$ . Even the relatively large value of  $r_b = 150$  nmi considered herein amounts to only 30% of the line of sight range between aircraft at cruise altitude. In a homogeneous aircraft distribution, this means that only 9% of the messages contributing to the received signal are of interest to the receiver. Additionally, the ratio of interference power to signal power for a far away interfering node at distance  $r_{\text{int}}$ , where  $r_b < r_{\text{int}} \leq r_s$ , and a desired node at distance  $r_{\text{des}} \leq r_b$  is  $(r_{\text{des}}/r_{\text{int}})^\alpha$  according to (2.10). In free space, i.e., for  $\alpha = 2$ , this interference to signal ratio is much larger than it would be in ground-based communication, where  $\alpha$  is typically around 4 [SS90, AWH07]. In conclusion, an aeronautical surveillance beaconing system has to fulfill the requirement (2.3) in the presence of a high amount of transmissions from nodes outside its intended range, while at the same time, the interference created by any single such transmission is more severe than in ground-based communication.
3. Propagation delays: The large ranges between aircraft also lead to unusually long delays. Signals communicated over a distance of  $r_b = 150$  nmi will experience a propagation delay of 920  $\mu\text{s}$ . To travel the line of sight range of 500 nmi, signals even take about 3 ms. As will be discussed in Chapter 3, propagation delays are known to impair the performance of various MAC schemes, for example due to required guard times or due to the time delay until a distant node becomes aware of an ongoing transmission.
4. Robustness: Aeronautical surveillance beaconing is a safety critical service for air traffic management. The employed beaconing scheme should therefore be robust against protocol failures, which may occur, e.g., through errors in any part of the control data. Also, in the case of system overloading through an excessive aircraft density  $\rho$ , the performance should degrade gracefully. For example, if the requirement (2.3) cannot be fulfilled anymore at  $\rho > \rho_{\text{max}}$ , then a reduced beaconing range  $r_{b,\text{red}} < r_b$  should exist such that (2.3) is at least fulfilled for distances  $r \leq r_{b,\text{red}}$ . Additionally,  $r_{b,\text{red}}$  should not become significantly smaller than  $r_b$  when  $\rho$  only slightly exceeds  $\rho_{\text{max}}$ .

5. Dependency on other systems: As aeronautical beacons is critical for safety (cf. point 4), it has to stay operational even when other systems fail. In civil aviation, it can be challenging to address concerns about the reliability of global navigation satellite systems (GNSSs) due to the possibility of signal outage or jamming [SEH11, MB11]. However, many transmission schemes for infrastructureless communication, including important beacons schemes, rely on the precise time reference provided by a GNSS to schedule their transmissions. For this reason, any aeronautical beacons scheme requiring a precise time reference has to be able to operate at least in an acceptable degraded mode in the absence of its time reference. As a consequence, a beacons scheme which relies on a GNSS should only be considered for use in aeronautics if it offers advantages over other schemes, such as a significantly higher spectral efficiency. Note that in aviation, backup systems are available to determine the location of an aircraft in the event of a GNSS outage [Inta]. Therefore, position reports can still be broadcast in such a case. Unfortunately, the currently available backup systems for positioning do not provide an accurate time reference in the way a GNSS does.

---

## Chapter 3

# Review and Evaluation of Existing PHY/MAC Layer Techniques

### 3.1 Introduction

This chapter gives an overview of the most important beaconing schemes known from the literature. Additionally, we consider known PHY and MAC layer techniques that could be applicable to beaconing, but were not designed for it. The contribution of this chapter is the qualitative assessment of the suitability of each scheme for spectrally efficient aeronautical surveillance beaconing in light of the special challenges listed in Section 2.7. Based on this assessment, we select the most promising schemes for further, quantitative analysis in Chapter 4. Note that a similar discussion may also be found in [RG12], albeit for the design of a surveillance beaconing system for trains.

By the term “beaconing scheme”, we refer to the combination of a MAC layer scheme and a PHY layer scheme for beaconing. The tasks of MAC for surveillance beaconing go beyond those of traditional MAC. As explained in Section 2.2, an up-to-date version of the surveillance data contained in a beacon message is available at any time. Therefore, surveillance beacon messages are not entering a queue where they await transmission, but may be transmitted by the MAC layer at any time and any rate. In consequence, a surveillance beaconing MAC layer also has to decide how many messages shall be transmitted per time. The PHY layer maps the beacon message data onto a physical transmit signal according to instructions provided by the MAC layer and transmits the resulting signal at the time determined by the MAC. In the receiver, the PHY layer handles signal processing. The receiver algorithm determines the conditions under which a message can be received successfully and can have a large impact on the spectral efficiency of beaconing.

Within this chapter, the different capabilities of single-user and multiple-user receiver algorithms have to be considered. Single-user receivers treat messages independent of each other, considering any overlapping messages as noise. In their most primitive form, correct reception cannot be guaranteed in the presence of an overlapping message even if the desired message is of much higher power than the overlapping one. Other single-user receivers are able to capture any message if the interference caused by overlapping messages is sufficiently weak [Rap01]. This is in the following referred to

as message capture capability. Multiple-user detection based receivers jointly process all messages involved in a group of overlapping messages. The theoretically optimum joint decision strategy is very often replaced by a suboptimal approximation algorithm based on interference cancellation, due to the prohibitive computational complexity of the optimum solution. Multiple-user detection is inherently capable of message capture and often succeeds to decode even the weaker messages involved in a collision.

Note that improving the decoding capabilities of the receiver should not be understood merely as a performance boost which is independent of the rest of the system. The optimum design of physical signals and MAC layer can be very different for systems designed with a simple receiver in mind or optimized, e.g., for a multi-user receiver which uses interference cancellation. In the first case, it may be best to use a high channel coding and modulation rate, which makes messages short and thereby reduces the probability of message collisions. In the second case, the efficiency may be best for a low channel coding and modulation rate, where collisions happen most of the time, but overlapping signals can be decoded in the receiver.

The structure of this chapter follows the different MAC options for beaconing. In many cases, the initial assessment whether a beaconing scheme should be considered for aeronautical surveillance beaconing can be made by looking at its MAC strategy. A fundamental division of MAC strategies can be made by looking at whether they try to coordinate the medium access of individual nodes in order to avoid message loss. This leads to the categorization into coordinated and uncoordinated MAC. The PHY layer will only be considered when necessary to assess the appropriateness of the scheme for the aeronautical scenario. This will especially be the case for uncoordinated schemes, where the receiver algorithm determines whether overlapping messages can be decoded.

## 3.2 Uncoordinated MAC

### 3.2.1 Unslotted Aloha Designed for Single-User Receivers

A very simple surveillance beaconing scheme is to use unslotted Aloha as MAC strategy, together with a fixed average transmission rate  $\lambda$  at each node and single-user receivers [Ebn05]. Unslotted Aloha refers to completely uncoordinated and unsynchronized channel access by each node of a wireless system [Pro01]. Such kind of channel access is in the literature often called Aloha because it was used in the Aloha system,

which was conceived for wireless communications by Abramson in 1970 [Abr70]. We use the term “unslotted Aloha” to distinguish Aloha without time slots from Aloha with time slots, which is introduced later. In unslotted Aloha, messages from different transmitters arrive at a receiver in a completely random way, such that any degree of overlap between two messages is possible.

Currently, unslotted Aloha is used by all aeronautical surveillance beaconing systems which are in widespread use. These are the SSR Mode S Extended Squitter transmitted on 1090 MHz (1090ES) [RTC09], and the Universal Access Transceiver (UAT) [Int09] (cf. Section 1.4). Contradictory to the principle of unslotted Aloha, UAT restricts message transmission times to a discrete grid, which is precisely time synchronized via GNSS. However, the intention behind using discrete transmission times in UAT is not to improve medium access, but to allow time synchronized receivers to deduce the propagation delay from the time of transmission, which is encoded in the message [Int09]. The time grid spacing in UAT is only  $250\ \mu\text{s}$ , which is less than the shortest UAT message duration of  $280\ \mu\text{s}$ , and significantly less than the maximum possible propagation delay. Therefore, UAT messages may partially overlap at a receiver just as in unslotted Aloha [ADS01], which is why we view the UAT MAC as unslotted Aloha. To the best of our knowledge, unslotted Aloha is not commonly used in surveillance beaconing systems for other types of mobile nodes than aircraft. While neither 1090ES nor UAT excludes the use of a multi-user or interference canceling receiver, they were not specifically designed to support interference resolution. For example, [RTC09, appendix I.4.1.8] assumes that a 1090ES receiver cannot decode more than one message at a time.

Unslotted Aloha, regardless of receiver algorithm, has several advantages for aeronautical surveillance beaconing. As aircraft do not coordinate their transmissions, no exchange of control data is necessary. In consequence, the efficiency of unslotted Aloha does not suffer from excessive control data overhead when a large number of aircraft are in range (cf. point 1 in Section 2.7). As transmissions are asynchronous, unslotted Aloha does not rely on any time reference (cf. point 5 in Section 2.7) and its efficiency is also independent of propagation delays (cf. point 3 in Section 2.7). Degradation in the presence of an excessive aircraft density happens gracefully under the propagation model (2.10), as weaker messages from further away are lost first while stronger ones remain intelligible (cf. point 4 in Section 2.7). Note, however, that this requires a receiver capable of message capture. Due to the aforementioned advantages and due to the widespread use of unslotted Aloha with single-user receivers in aeronautical surveillance beaconing, its spectral efficiency is analyzed in more detail in Section 4.3.

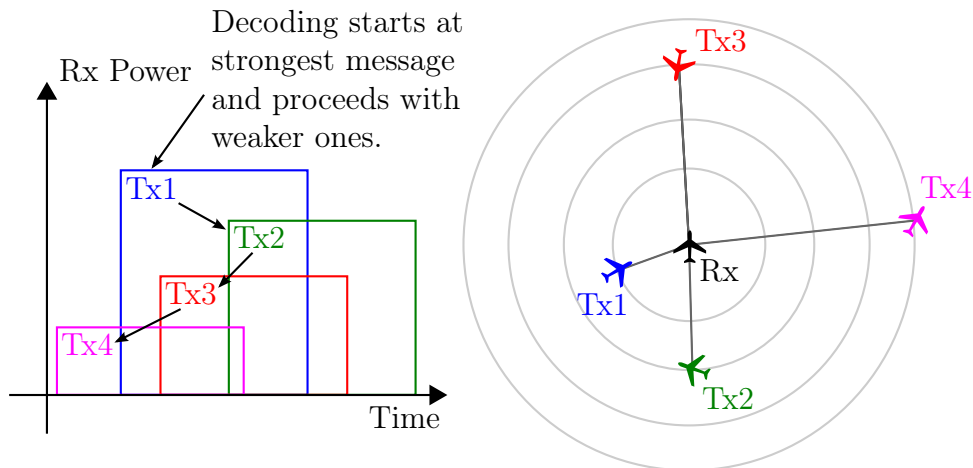


Figure 3.1. Order of processing in Aloha with SIC.

### 3.2.2 Unslotted Aloha Designed for SIC

A major problem in any Aloha system is message loss due to overlapping transmissions. One way to mitigate this effect is to employ successive interference cancellation (SIC) in the receiver. The idea of SIC is to first decode the strongest incoming message, and, in case of success, subtract it from the received signal. The receiver then proceeds with the next strongest message. This way, messages can be decoded which are overlapped by substantially stronger ones. An example for the order of processing is shown in Figure 3.1.

After earlier work by Viterbi [Vit90], recent work on satellite communications has confirmed that the spectral efficiency of unslotted Aloha may be greatly increased when SIC is used by the receiver, together with an appropriate PHY layer transmission scheme. For instance, the Enhanced Spread Spectrum Aloha (E-SSA) system has been proposed for random access in the satellite return link [dRHdG09, dRHdG12]. A concept similar to E-SSA is also described in [FEB09]. In E-SSA, many users try to access a central point, such as a satellite, via the same channel. Two further access schemes combining unslotted Aloha with SIC for the same satellite scenario are Contention Resolution Aloha (CRA) [Kis11] and its extension Enhanced Contention Resolution Aloha (ECRA) [CK13]. While E-SSA employs spreading and channel coding to protect messages against interference, CRA and ECRA repeat each message multiple times with random delays in between. Each message contains the time offsets to all of its replicas. If any of the replicas can be decoded, CRA is capable of subtracting all of them from the received signal. In addition, ECRA combines parts taken from multiple replicas to improve the decoding performance.

To the best of our knowledge, unslotted Aloha with SIC has so far not been applied to beaconing. Due to the advantages of unslotted Aloha for aeronautical surveillance beaconing already explained in Section 3.2.1 and the aforementioned promising results, unslotted Aloha with SIC is analyzed in more detail in Section 4.5

### 3.2.3 Slotted Aloha Designed for Single-User Receivers

A popular improvement of unslotted Aloha is the introduction of time slots as described for TDMA in Section 2.4.6. As transmissions may only start at the beginning of a time slot, messages transmitted in different slots cannot overlap. Under the assumption that any overlap of messages leads to the loss of all messages involved, the well-known textbook result may be derived that slotted Aloha is two times more efficient than unslotted Aloha [Pro01]. However, the advantage of slotted over unslotted Aloha is much smaller when a single-user receiver capable of message capture is used with a node distribution and channel model similar to the 2-D model described in Section 2.5. Assuming  $r_s = \infty$ , the efficiency of slotted Aloha can be shown to approach that of unslotted Aloha as the channel loss exponent  $\alpha$  approaches 2 [BM10].

To the best of our knowledge, slotted Aloha is currently not used by any infrastructureless system for beacon exchange between vehicles, aircraft or ships. For aeronautical surveillance beaconing, the advantages and disadvantages of slotted Aloha are equivalent to those stated for unslotted Aloha in Section 3.2.1, with the following two disadvantageous exceptions. First, the use of time slots in Aloha requires guard times, which must comprise the propagation delays. In aeronautics, those are in the order of 1 ms (cf. point 3 in Section 2.7), which is substantially more than in most ground-based wireless communication systems. Second, slotted Aloha requires nodes to be synchronized to a common time reference. This has undesirable implications in aeronautical surveillance beaconing, cf. point 5 in Section 2.7. Due to these disadvantages and the results from [BM10], slotted Aloha with single-user receivers is not considered further in this work.

### 3.2.4 Slotted Aloha Designed for SIC

Even with SIC in the receiver, the disadvantages of time slots in Aloha as detailed in Section 3.2.3 still hold. For this reason, slotted Aloha with SIC is also not considered further in this work. For completeness, we briefly discuss related work which combines SIC with slotted Aloha.

The efficiency of slotted Aloha with SIC is analyzed for a MANET in [WAYdV07]. In contrast to this work, [WAYdV07] considers unicast communication, i.e., one receiving node for each transmitting node. As in [WAYdV07], the receivers are all at the same distance to their transmitter, the results can in principle be used to analyze the MER for a node at distance  $r_b$  from a transmitter in beaconing. However, [WAYdV07] only looks at the case of  $r_s = \infty$  and  $\alpha > 2$ . While these two assumptions are common for ground-based communications, they are not applicable to aeronautical beaconing. Two notable access schemes using slotted Aloha with SIC are Contention Resolution Diversity Slotted Aloha (CRDSA) and its improved version Irregular Repetition Slotted Aloha (IRSA) [Liv11]. Both are designed for random access in the satellite return link. CRDSA may be seen as the slotted version of the unslotted CRA, cf. Section 3.2.2. Messages are repeated two or more times in random slots over the duration of one larger section of slots called a frame. Like in CRA, the correct decoding of any replica allows the receiver to subtract all replicas of the respective message from the received signal. In CRDSA, the number of packet repetitions is fixed. As shown in [Liv11], the efficiency of CRDSA can be increased by using a random number of repetitions according to some probability distribution. Doing so leads to the improved access scheme IRSA.

### 3.3 Coordinated MAC

#### 3.3.1 Carrier Sense Multiple-Access

A straightforward method for coordinating transmissions is to listen to the channel and only start to transmit if the channel is perceived to be free. This MAC strategy is commonly known as carrier sense multiple-access (CSMA). A common carrier sensing method is to consider the channel busy when the received power exceeds some sensing threshold [KJO11]. Under the channel model (2.10), this leads to a sensing range  $r_{\text{sense}}$ . Each node is able to sense, but not necessarily to decode, transmissions made within a circle of  $r_{\text{sense}}$  around its position. CSMA is widespread in both wired and wireless communications. As long as all nodes in a system are within sensing range of each other and propagation delays are negligible, CSMA can utilize the channel very efficiently. This means that the channel is almost always occupied by a transmission and almost all transmissions are successful.

In surveillance beaconing, the most prominent system using CSMA is the IEEE 802.11 standard [IEE12], which in its latest version includes the IEEE 802.11p amendment for



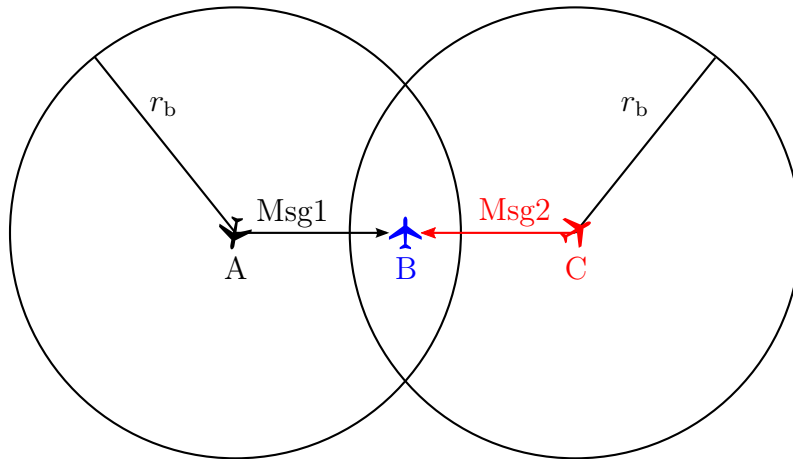


Figure 3.2. Hidden node problem. For simplicity,  $r_{\text{sense}} = r_b$  is assumed. Msg1 and Msg2 collide at aircraft B because A and C cannot sense each other's transmissions.

vehicular communications [IEE10]. IEEE 802.11p is not limited to beaconing, but the surveillance beacons broadcast by each vehicle are an important part of it.

The performance of CSMA in aeronautical surveillance beaconing is mainly impaired by two effects: (i) the hidden node problem, and (ii) the vulnerable time. The hidden node problem can occur when not all aircraft are within sensing range of each other, which is the typical situation. In the example shown in Figure 3.2, the aircraft labeled A cannot sense the transmissions from aircraft C, although A and C should not transmit at the same time to avoid collision at aircraft B. Thus, C is a hidden node for A. Due to the large number of aircraft within line of sight of a receiver (cf. point 2 in Section 2.7), the hidden node problem can be especially severe in aeronautical surveillance beaconing. Its impact depends crucially on the sensing range, as well as on the ability of the receiver algorithm to decode overlapping messages.

The vulnerable time is the duration from the start of a transmission until the time at which the last node within sensing range of the transmitting node has detected that the channel is busy [BB99]. Within the vulnerable time, other nodes may start to transmit and cause interference because they have not yet realized that the channel is busy. Ignoring any processing delay in the receiver, the vulnerable time is equal to the propagation delay. If the sensing range  $r_{\text{sense}}$  is similar to the required beaconing range, the propagation delay is around 1 ms in the aeronautical scenario. For  $r_{\text{sense}}$  close to the line of sight range, it can amount to 3 ms (cf. point 3 in Section 2.7). If receivers are not capable of decoding overlapping messages, CSMA can only work efficiently if the duration of messages is much longer than the vulnerable time [Pro01]. In aeronautics, the number of messages received per second would have to be in the order of 1000, due to the number of aircraft within the required beaconing range (cf. point 1 in Section

2.7). If all those messages need to arrive at a receiver without overlaps, they would have to be shorter than the vulnerable time. Due to the hidden node problem and the vulnerable time, CSMA is not considered further in this work.

### 3.3.2 Basic Version of Self-Organizing TDMA

Self-organizing time-division multiple-access (SOTDMA) is a MAC strategy that enables the use of TDMA for communication in a MANET, of which beaconing is a special case. This section describes the basic version of SOTDMA [Lan96]. We consider a receiver architecture which can decode the strongest message involved in a collision if the SINR is sufficient. As described in Section 2.4.6, TDMA divides the time into slots which are grouped into frames and accessed according to some transmission schedule. Figure 3.3 shows an example frame structure. Normally, TDMA requires some central node such as a base station to determine the transmission schedule. In SOTDMA, a distributed algorithm is used to negotiate the schedule without any infrastructure. The main idea is that each node announces which slots it wishes to use in future frames. These announcements are called reservations and are normally transmitted as additional control data within a regular message.

For surveillance beaconing, the length of a frame can for example be set to the required update time  $T_{u,crit}$  and each node can then reserve one slot per frame [RG12]. When a node enters the network, it first has to listen to the channel for at least one frame to learn the transmission schedule from the reservations of all nodes within range. Once the schedule is known, the node selects an unoccupied slot in the next frame and transmits its first packet in this slot. An example is depicted in Figure 3.3, where the red aircraft has to listen to frame 2 before being able to pick an unreserved slot in frame 3. From the first transmission of the new node, its neighbors will learn about its presence and about its reservations in the transmission schedule. Note that a node does not necessarily have to reserve the same slot in each frame. In Figure 3.3, the blue aircraft switches its slot in frame 3. At least when all nodes are within range of each other, SOTDMA is able to use almost every slot for a collision-free and hence successful transmission.

SOTDMA in its basic version is used by two existing surveillance beaconing systems, the airborne VHF Digital Link Mode 4 (VDL4) [Int04], and the shipborne Automatic Identification System (AIS) [Int10]. Both VDL4 and AIS were not exclusively designed for beaconing, but can also be used for other types of data traffic.

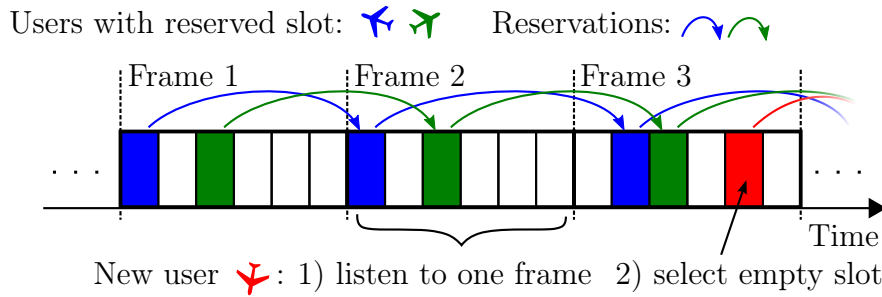


Figure 3.3. Slot reservation and network entry in SOTDMA.

For aeronautical surveillance beaconing, the basic version of SOTDMA has the advantage that each node only transmits its own reservations as control information. Why this is an advantage will become clear in comparison to schemes using more control data, which will be described in later sections. To let each node transmit once per frame, the number of slots in a frame must be at least in the order of the number of nodes within the required beaconing range. The bits necessary to transmit a reservation can therefore be roughly estimated to grow only with the logarithm of the number of nodes in range. It may therefore be assumed that even the large expected number of nodes in range in an aeronautical scenario does not cause excessive overhead in the basic version of SOTDMA (cf. point 1 in Section 2.7). However, as a node cannot receive reservations transmitted outside of its range, the basic version of SOTDMA suffers from the hidden node problem explained in Section 3.3.1 [Ebn05]. According to point 2 in Section 2.7, the number of nodes outside of the required beaconing range  $r_b$  of a node, but still close enough to cause interference, is large in aeronautics. Even for surveillance beaconing between vehicles on the ground, where the interference from nodes out of beaconing range should be less severe due the higher path loss exponent, it was found in [RG12] that the basic version of SOTDMA does not perform much better than slotted Aloha. Another problem for SOTDMA are the guard times which are required just like in slotted Aloha, cf. Section 3.2.3. Furthermore, SOTDMA depends on the global availability of an accurate timing source to schedule messages, which is usually provided by a GNSS. Dependency on a GNSS is undesired in aeronautics, as discussed under point 5 in Section 2.7. While the existing VDL4 includes fallback procedures for the case of a GNSS outage [Int04], such procedures typically degrade the spectral efficiency.

Mainly due to the impact of the hidden node problem, the basic version of SOTDMA is not considered further in this work. Instead, several extensions of SOTDMA are discussed in the following sections which try to mitigate the hidden node problem.

### 3.3.3 Cell-Based Self-Organizing TDMA

One method to solve the hidden node problem in SOTDMA is to introduce a map of hexagonal network cells, which we call cell-based self-organizing TDMA (CB-SOTDMA). This method was first used by the MAC protocol Cell-Based Orientation Aware MAC Broadcast (COMB), designed for surveillance beaconing between trains [RGLS08, RG12]. The map of cells may span the whole globe, or only the area where the surveillance beaconing system is needed. The physical propagation channel is divided into several subchannels (cf. Section 2.4.6) and each cell is assigned a subchannel by means of a cellular reuse pattern [Rap01]. An example for such a cellular reuse pattern is shown in Figure 3.4, where each cell is assigned one of four TDMA subchannels. Note that cellular reuse patterns are addressed in more detail in Section 4.4.1.

Within each cell of CB-SOTDMA, the nodes use SOTDMA to coordinate access to the subchannel of their cell. Coordination with nodes in other cells is not necessary, since they use a different subchannel. If the cell diameter does not exceed  $r_b$ , all nodes in a cell are in range of each other, which eliminates the hidden node problem. Note that to fulfill the surveillance beaconing requirement (2.3), nodes must listen to the subchannels of all cells within a radius of  $r_b$ . Furthermore, the reuse distance, which is the minimum distance between two cells using the same subchannel, must be large enough to avoid excessive interference.

In [RG12], the use of CDMA, FDMA or TDMA subchannels is considered. It is mentioned that the use of CDMA or FDMA subchannels creates the risk of losing messages from a neighboring cell, due to the inability to receive while transmitting. This is in accordance with the assumptions made in this work and means that TDMA subchannels have to be used to make sure a node can overhear transmissions from neighboring cells.

For aeronautical surveillance beaconing, CB-SOTDMA is an interesting MAC option, as it can solve the hidden node problem of SOTDMA without any increase in control data overhead. Additionally, the guard times in TDMA can be reduced by roughly 90% if the order of transmitters is chosen according to a method introduced in [NA02]. As we discussed in [WFS10], this method can be applied to CB-SOTDMA. Apart from this, the advantages and disadvantages of SOTDMA described in Section 3.3.2 are also valid for CB-SOTDMA. In Chapter 4, it will be analyzed how CB-SOTDMA can be adapted to aeronautical surveillance beaconing and what spectral efficiency can be achieved with it.

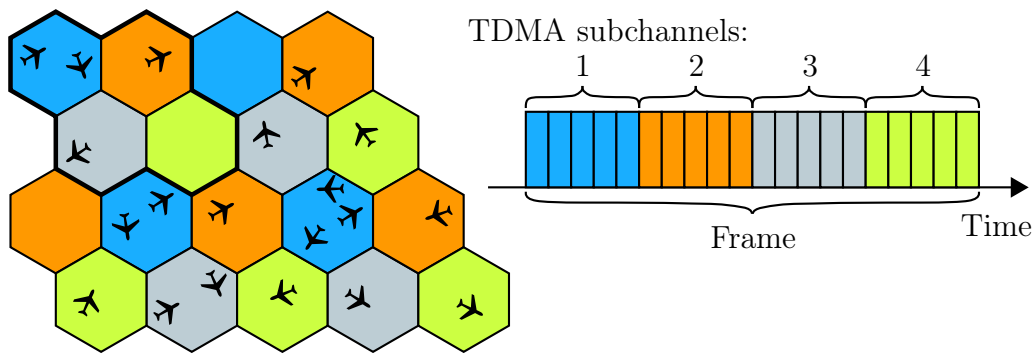


Figure 3.4. Cellular reuse pattern with four TDMA subchannels.

### 3.3.4 Further MAC Strategies Based on Cells

In the literature, some other cell-based MAC strategies for MANETs have been described. One notable idea is to make the cells so small that there is never more than one node in a cell. In this case, nodes can access the subchannel of their cell without having to coordinate their transmissions with other nodes. Examples are a special version of space-division multiple-access (SDMA) described in [BV01], and the Location-Based Channel Access (LCA) protocol [KMR<sup>+</sup>03]. How efficient such a MAC strategy can be depends on the percentage of cells that are actually occupied by exactly one node. For very regular node distributions, this percentage could be high, in which case almost every subchannel would be in use. However, when node locations are random and the distance from a node to its nearest neighbor varies significantly, using small cells with capacity for only one node per cell is very inefficient. The reason is that in this case, cells would have to be made so small that the vast majority of them would remain empty. One has to design the cell size as the largest area (or 3-D volume) within which the existence of more than one node can be excluded, or is less probable than some acceptable probability. Obviously, this probability would have to be very low in a reliable system, in which case the percentage of used subchannels is approximately equal to the expected number of nodes per cell. For aeronautics, a cell could certainly not be larger than the minimum safe separation distances between aircraft, which are in the order of a few nautical miles laterally and 1000 feet vertically [Eur07c]. Even in high-density airspace, the average number of aircraft within such a space would be very low. Therefore, the use of very small cells cannot lead to an efficient surveillance beaconing scheme in aeronautics and is not considered further.

Another scheme which uses cells is Two-Phase Coding with Power Control (TPCPC) [ZSX03]. Like CB-SOTDMA, it uses cells to avoid the hidden terminal problem. Since the coordination in TPCPC relies on master nodes, we discuss the details of TPCPC in Section 3.3.8, where master nodes are looked at in more detail.

### 3.3.5 MAC Strategies Using Implicit Reservations

In SOTDMA and its variants, each node explicitly announces which slots it plans to use in the future. Such explicit reservations create a certain overhead. Another possibility is to not transmit reservations at all, but to derive future usage of the TDMA slots from what was observed in the past. This requires nodes to access the channel in a predictable way, usually by using the same slot in every frame. Hence, the mere presence of a message in a certain slot can be seen as an implicit reservation for this slot in future frames. Note that implicit reservations are also used in some implementations of SOTDMA, but only as a backup solution in case explicit reservations were lost (cf. Section 3.3.2) [Int04, Ebn05]. Implicit reservations are for example used in the Reservation Aloha (R-Aloha) MAC protocol, cf. [Lam80] and references therein. Another variant of R-Aloha is Sliding Frame R-Aloha, which demonstrates that frame synchronization is unnecessary in R-Aloha [Ma07].

For aeronautical surveillance beconing, implicit reservations are problematic. In reservation-based MANET MAC protocols, nodes are typically required to change their slot every few frames. The reason is that two nodes who are initially at a sufficient distance from each other to use the same slot can move towards each other. Without slot changes, this can lead to conflicting reservations which persist over longer periods of time. With implicit reservations, the slot changes lead to more message collisions than when explicit reservations are used. As described in Section 3.3.2, the overhead for explicit reservations is acceptable. Therefore, beconing schemes relying exclusively on implicit reservations are not considered further.

### 3.3.6 Slotmap Propagation to Improve SOTDMA

Another solution to the hidden node problem in SOTDMA is slotmap propagation. In [BCCF02, SC09, LHSR01], several MAC protocols using slotmap propagation are proposed for vehicular beconing in the FleetNet project [HBE<sup>+</sup>01]. Further examples of slotmap propagation are described in [Ebn05, LIT<sup>+</sup>09]. In a reservation-based scheme, each node keeps track of the status of each slot as seen from its own position. A slot can be free, occupied by a single message (correct reservation), or occupied by more than one message (collision). This information about the status of each slot is called a slotmap. In slotmap propagation, each node broadcasts its slotmap as additional control data in its messages. Through the received slotmaps, nodes know in which slots their neighbors are receiving messages. A node can thus try to transmit in a slot perceived as free both by itself and by all of its neighbors. Hence, the hidden node

problem is alleviated. Note that reporting which slots are in use by all direct neighbors, i.e. other nodes within the beaconing range  $r_b$ , might not be sufficient. Based on the signal propagation conditions and the value of  $r_b$ , nodes from more than one hop away may cause interference. In this case, the usage of slots can be propagated over multiple hops, i.e., it can be reported that a slot is in use by a neighbor who is  $k$  hops away, up to some maximum hop distance.

For aeronautical surveillance beaconing, slotmap propagation has one major drawback. As explained in Section 3.3.2, the number of slots per frame in SOTDMA must be at least in the order of the number of nodes within the beaconing range  $r_b$ , which is roughly estimated as 1000 under point 1 in Section 2.7. This also holds for any other coordinated beaconing scheme which uses slotted MAC and a receiver algorithm capable of decoding at most one message per slot. If a slotmap contains the status of 1000 or more slots, the number of bits needed to transmit it exceeds the size of the actual payload data in aeronautical surveillance beaconing, which is  $L = 320$  bits according to Section 2.2. Therefore, the protocols based on slotmap propagation mentioned in this section would be inefficient when used for aeronautical surveillance beaconing. A further disadvantage of slotmap propagation is that the hidden node problem is only solved as long as all nodes are transmitting. In aeronautical surveillance beaconing, one may want to install monitoring ground stations in areas of dense air traffic to monitor the beacon messages for air traffic control. If the monitoring station comprises only a receiver, it could theoretically still suffer from interference by hidden nodes, because it does not communicate its view of the slotmap. Note that this issue does not exist with the cell-based solution of the hidden node problem. Due to the aforementioned disadvantages, the propagation of slotmaps is not considered further.

### 3.3.7 Handshake-Based Methods

An important class of MAC strategies known from the literature are those employing handshakes to negotiate which nodes are allowed to access the channel. In a handshake-based protocol, a node has to request access to the channel, giving other nodes the opportunity to approve or reject the request before it transmits the actual user data. Special control messages are used both for the request and for the responses.

In an approval-based handshake, the addressees of a message for which channel access is requested have to respond with an approval, and the absence of any approving control message is considered as an objection. A very prominent example is the request to send, clear to send (RTS/CTS) message exchange described in the IEEE 802.11 standard for

wireless local area networks [IEE12]. In IEEE 802.11, RTS/CTS handshakes are only used for unicast messages, i.e., messages with a single addressee. An approval-based handshake for broadcast can be found in the Broadcast Protocol with Busy Tone (BPBT) [CWC07]. However, for broadcasts like surveillance beacon messages, the problem is that a request must be approved by each receiver. This is inefficient when there are usually a lot of nodes within range of any transmitting node (cf. point 1 in Section 2.7). Additionally, waiting for all receivers to approve of a request is not a robust algorithm in a mobile environment, because it critically depends on an up-to-date list of all nodes within range (cf. point 4 in Section 2.7). Therefore, approval-based handshakes are not suitable for surveillance beacons [RG12].

An objection-based handshake allows the requesting node to transmit its payload data unless another node raises an objection. Unlike approvals, which must be transmitted such that the requesting node learns who exactly sent them, objections can be transmitted in a colliding way. Their presence can be detected, e.g., by looking at the received power. Protocols with objection-based handshake that could potentially be used for broadcast may be found in [MKK01, ZC01, TGLA99, KVM<sup>+</sup>09]. All of them use time slots and a frame structure. Special time slots exist for the handshake messages, to make sure they do not collide with the data messages. Notably, the Multi-User Detection MAC (MUD-MAC) protocol is designed for receivers capable of processing multiple overlapping messages [KVM<sup>+</sup>09].

For aeronautical surveillance beacons, the only advantage of objection-based handshakes compared to reservations without slotmap propagation is the alleviation of the hidden node problem. A node receiving conflicting requests from its neighbors can raise an objection. Other advantages of handshakes, like the fast initial channel access or the ability to handle sporadic traffic, are not important for aeronautical surveillance beacons. The initial channel access times of reservation protocols are acceptable, and surveillance beacon messages are not transmitted sporadically, but at regular intervals. At the same time, using handshakes in a spectrally efficient aeronautical surveillance beaconing protocol may be difficult due to the large propagation delays, cf. point 3 in Section 2.7. The round trip delay from a requesting aircraft to a neighbor at distance  $r_b$  and back amounts to roughly 1.8 ms. The time needed for a handshake can obviously not be shorter than this. As the hidden node problem can also be solved with other MAC approaches, such as CB-SOTDMA (cf. Section 3.3.3), handshake-based protocols are not considered further. Lastly, note that handshake methods create the same drawback for monitoring ground stations that only listen to the channel as already described for slotmap propagation in Section 3.3.6. They would not be able to participate in the handshake and could therefore suffer from increased message loss, e.g., through hidden terminals.



### 3.3.8 Methods Based on Master Node Election

Another MAC approach is the use of master nodes. As it is generally considered to be easier to establish a transmission schedule at a central location than in a distributed way, the idea is to let the nodes elect masters amongst themselves. Each master is then responsible for coordinating the medium access of all other nodes within its range, similar to a base station in a network with infrastructure.

One example for a MAC strategy using master nodes in a MANET is TPCPC [ZSX03], as already mentioned in Section 3.3.4. It uses cells with subchannels as in CB-SOTDMA (cf. Section 3.3.3) and lets the nodes in each cell elect a master. Nodes entering a cell have to register with the master and request channel access rights. TPCPC tries to select a master node close to the center of each cell. Once the master node moves away from the center, it indicates that it wishes to hand over its master role. Other nodes close to the center will offer to be the new master and the old master will hand over control of the cell to one of them.

The main concern against using master nodes for aeronautical surveillance beaconing is the robustness of such a scheme (cf. point 4 in Section 2.7). If the master election process fails, there may be either no master in a certain area, or there may be more than one. This problem is more severe if the nodes are moving, as the set of masters constantly has to be adapted to the changing topology. For example, if the master fails to hand over its responsibilities prior to leaving a cell or turning off its radio device in TPCPC, the nodes remaining in the cell must contend for the master role. During the contention phase, other nodes entering the cell will be unable to obtain channel access rights, or conflicting assignments may be made by multiple nodes who each consider themselves as master. For these reasons, MAC schemes using master nodes are not considered further.

### 3.3.9 MAC Scheduling Based on SINR

Almost all of the previously discussed coordinated MAC schemes try to make sure that within a certain distance around a transmitter, no other node transmits at the same time and on the same subchannel, if subchannels are used. This criterion is in general only a coarse approximation of the real conditions under which all messages can be received by their respective addressees without errors. A more accurate criterion is that the SINR at any receiving node must remain above a certain threshold depending on the PHY layer design [Grö03].

An SINR based criterion has for example been proposed for transmission scheduling in spatial reuse TDMA (STDMA) [Grö03]. In order to determine whether a certain message can be transmitted at a certain time in addition to others which have already been scheduled, the distributed scheduling algorithm of [Grö03] looks at two things: First, the SINR for that message at each addressee and second, the increase of interference power at each node within a certain range around the transmitter. Ideally, this range should be identical to the line of sight range, i.e., it should include the whole area affected by the additional message.

Unfortunately, to schedule messages based on SINR, a transmitting node needs to know the current SINR at all receiving nodes within its line of sight range. We assume that distributing this SINR information would lead to excessive control data exchange in aeronautical surveillance beaconing, given the large number of aircraft within line of sight range of a transmitter (cf. point 2 in Section 2.7). Therefore, SINR based scheduling is not considered further.

### 3.4 Selection of Beaconing Schemes for Further Investigation

An important finding of this chapter is that unslotted Aloha is advantageous with respect to most of the challenging aspects of aeronautical surveillance beaconing listed in Section 2.7. Additionally, results from the literature indicate that the poor spectral efficiency of unslotted Aloha with single-user receivers may be substantially improved through the use of SIC in the receiver and an appropriate PHY layer. The combination of unslotted Aloha with SIC is thus a promising candidate scheme for aeronautical surveillance beaconing. How often beacon messages should be transmitted by such a scheme, how to design its PHY layer and what spectral efficiency can be expected is analyzed in Section 4.5. Answers to these questions cannot be found in the literature about Aloha with SIC, because the existing results do not consider beaconing.

Additionally, CB-SOTDMA is a promising candidate scheme for aeronautical surveillance beaconing. It retains the advantages of SOTDMA and solves the hidden node problem without increasing the control overhead. While CB-SOTDMA has been described in the literature for surveillance beaconing before, special care needs to be taken to adapt it to the situation in aeronautics. How this can be done and what spectral efficiency is possible is analyzed in Section 4.4.

---

## Chapter 4

# Semi-Analytical Investigation of the Spectral Efficiency of Selected Beaconsing Schemes

### 4.1 Introduction

In this chapter, we quantitatively analyze, optimize and compare the spectral efficiency of three schemes of interest for aeronautical surveillance beaconsing: unslotted Aloha with single-user receivers, CB-SOTDMA and unslotted Aloha with SIC. For CB-SOTDMA and unslotted Aloha with SIC, we additionally introduce measures needed to overcome challenges specific to aeronautical surveillance beaconsing. CB-SOTDMA and unslotted Aloha with SIC were selected in Section 3.4 as promising candidates with respect to their spectral efficiency. Unslotted Aloha with single-user receivers is considered due to its widespread use in aeronautical surveillance beaconsing. For each scheme, we optimize the PHY and MAC layer parameters to maximize the spectral efficiency. This leads to two results: First, the spectral efficiency gain of the more advanced schemes as compared to the traditional method unslotted Aloha with single-user receivers can be quantified. Second, based on the spectral efficiency and further criteria, the most promising aeronautical surveillance beaconsing scheme can be selected for the detailed system design to be considered in Chapter 5. For the optimization of each beaconsing scheme, we establish mathematical models to compute the spectral efficiency from PHY and MAC layer parameters. To facilitate parameter optimization, we make suitable simplifications which permit the use of analytical expressions as far as possible. Yet, some integrals and expected values are evaluated using numerical methods. Therefore, we call our models semi-analytical [dRHdG12].

Section 4.2 addresses important assumptions under which beaconsing schemes are compared in this chapter. This includes a summary of the beaconsing scenario and requirements already discussed in Chapter 2, as well as further system properties such as the available bandwidth and transmit power. Section 4.3 focuses on the semi-analytical model of unslotted Aloha with single-user receivers, the optimization of parameters in this model, and the resulting spectral efficiency. Section 4.4 deals with CB-SOTDMA. Initially, a novel solution to the problem of large power imbalances between received signals from adjacent cells is described. The existing solution to this problem does not work efficiently in aeronautics due to the long signal propagation ranges. Subsequently, the semi-analytical model of CB-SOTDMA is established and the system

parameters maximizing the spectral efficiency are determined. Section 4.5 considers unslotted Aloha with SIC. We show how to mitigate the negative impact of signal outage during the own transmissions of a half-duplex beaconing radio. Then, we establish the semi-analytical model of unslotted Aloha with SIC and optimize the system parameters to maximize the spectral efficiency. Finally, Section 4.6 compares the spectral efficiency of all schemes previously analyzed and selects the most promising scheme for the detailed design of an aeronautical beaconing system to be considered in Chapter 5. Note that we have published earlier stages of some of the work presented in this chapter in [WFS10, Fra11, Fra12, Fra14].

## 4.2 Assumptions for the Comparison of Beaconing Schemes

In this section, we discuss the assumptions to be applied to all beaconing schemes in this chapter in order to enable a fair comparison. These assumptions can be described by the parameters listed in Table 4.1. With respect to node distribution and movement, line of sight range  $r_s$ , channel loss exponent  $\alpha$ , beaconing range  $r_b$ , critical data age  $T_{u,crit}$ , tolerable outage probability  $\xi$  and message size  $L$ , Table 4.1 merely summarizes the beaconing scenario and requirements already introduced in Chapter 2.

Additionally, some parameters constraining the PHY layer capabilities are required. At first, we assume a bandwidth of  $W_{sys} = 1$  MHz (cf. Table 4.1). This bandwidth is comparable to the state of the art aeronautical beaconing system UAT, where 99% of the emitted power is contained within a bandwidth of 1.3 MHz [Int09, Intb]. Next, we consider the signal to noise ratio (SNR) for a message from a sender at distance  $r_b$  using the whole bandwidth  $W_{sys}$ . This SNR is denoted by  $SNR_b$  and summarizes the effects of (i) the transmitted power  $P_{tx}$ , (ii) the distance  $r_{ref}$  at which the transmission loss would hypothetically be 0 dB, and (iii) the receiver noise figure  $F_{dB}$ . With the received power (2.10), we have

$$SNR_b = \frac{P_{rx}(r_b, r_s)}{W_{sys}N_0}. \quad (4.1)$$

For the semi-analytical models, the SINR needs to be computed for each considered beaconing scheme in order to derive the MER. Generally, the received signal powers are proportional to  $P_{tx}(r_{ref})^\alpha$  as per (2.9). The noise power can be represented as  $SNR_b^{-1}P_{rx}(r_b, r_s)$ , which makes it proportional to  $P_{tx}(r_{ref})^\alpha$  as well. Thus, when  $SNR_b$  is given, the factor  $P_{tx}(r_{ref})^\alpha$  cancels out of the SINR and is not explicitly required

Table 4.1. Assumptions for the Comparison of Beaconing Schemes.

Parameter	Symbol	Value
Node Distribution and Movement		2-D Model, cf. Section 2.5
Line of sight range	$r_s$	500 nmi (as per the 2-D Model)
Channel loss exponent	$\alpha$	2 (cf. Section 2.4.2)
Beaconing range	$r_b$	$0.3r_s = 150$ nmi (cf. Section 2.2)
Critical data age	$T_{u,crit}$	1 s (cf. Section 2.2)
Tolerable outage probability	$\xi$	$10^{-3}$ (cf. Section 2.2)
Data bits per message	$L$	320 (cf. Section 2.2)
System bandwidth	$W_{sys}$	1 MHz
SNR at distance $r_b$	$SNR_b$	10 dB

anymore for the semi-analytical models in this chapter. The noise figure  $F_{dB}$  is contained in  $SNR_b$  since  $N_0$  includes  $F_{dB}$  as per (2.16). The assumption  $SNR_b = 10$  dB made in Table 4.1 is conservative, but realistic for an aeronautical surveillance beaconing system, as can be seen from the following link budget. In free space, we have  $P_{rx}(r_b, r_s) = P_{rx,FS}(r_b)$  according to (2.12), which can be inserted into (4.1). Then, solving for  $P_{tx}$  yields the transmit power required for a certain  $SNR_b$ . Assuming that  $\mathcal{G}_{tx}|_{dB_i} + \mathcal{G}_{rx}|_{dB_i} = F_{dB}$ , a transmit power of  $P_{tx} = 37.3$  dBm would be required for  $SNR_b = 10$  dB at  $r_b = 0.3r_s = 150$  nmi,  $f_c = 1$  GHz and  $W_{sys} = 1$  MHz. Such a transmit power assumption is conservative, since it is lower than the transmit power of existing systems. For example, on-board UAT devices use transmit powers between 42.5 dBm and 54 dBm, depending on equipment class [Int09].

Note that while a line of sight range  $r_s = 500$  nmi is assumed in the 2-D model as per Section 2.4.2, the spectral efficiencies computed in this chapter are independent of the actual value of  $r_s$ , as long as the ratio  $r_b/r_s$  and the value of  $SNR_b$  are not changed.

### 4.3 Unslotted Aloha Designed for Single-User Receivers

This section focuses on the derivation of the semi-analytical model for unslotted Aloha with single-user receivers. This semi-analytical model computes the spectral efficiency from PHY and MAC layer parameters. As outlined in Section 2.3, compliance with the requirement (2.3) depends on the probability to lose too many consecutive messages

from the same neighboring aircraft. Therefore, we require a mathematical model for the MER based on noise and interference power. To this end, we assume that each message consists of complex modulation symbols and contains a single codeword from an error correcting code. Coding and modulation map the  $L$  message bits onto  $L/a$  complex symbols, where  $a$  denotes the number of information bits per complex symbol. For a finite number of channel uses, i.e., modulation symbols, per codeword and a given codeword error rate on an AWGN channel, an approximation of the maximum number of information bits per channel use is given by Polyanskiy et al. in [PPV10, eq. (296)]. Solving this approximation for the codeword error rate yields an approximation  $\Psi(\text{SINR}, a)$  of the minimum possible MER:

$$\Psi(\text{SINR}, a) = \frac{1}{2} \operatorname{erfc} \left( B \left( \log_2(1 + \text{SINR}) - a + \frac{a}{2L} \log_2 \left( \frac{2L}{a} \right) \right) \right), \quad (4.2)$$

where  $\operatorname{erfc}(\cdot)$  denotes the complementary error function [AS64], and  $B$  is given by

$$B = \frac{(1 + \text{SINR}) \ln(2)}{\sqrt{2 \frac{a}{L} \text{SINR} \cdot (2 + \text{SINR})}}. \quad (4.3)$$

The derivation of (4.2) is discussed in more detail in Appendix A.1.1. By using (4.2), we assume Gaussian interference, which is supported by simulations in [dRHdG12]. Figure 4.1 shows (4.2) for the example  $a = 1/3$ . As we shall see later, such a low setting of  $a$  is beneficial for unslotted Aloha with single-user receivers. The two curves for  $L = 320$  and  $L = 32000$  illustrate that (4.2) converges to a step function as  $L \rightarrow \infty$ , where the step is at  $\text{SINR}_{\text{lim}} = 2^a - 1$ . Here,  $\text{SINR}_{\text{lim}}$  is the required SINR to achieve a channel capacity of  $a$  bits per complex channel use under AWGN [Pro01].

Due to the homogeneous node distribution in the 2-D model (cf. Section 2.5), the interference statistics is independent of the receiver location. It is therefore sufficient to check the requirement (2.3) at a single receiver [WAYdV07]. To mathematically describe the interference at this receiver, we assume that each node transmits  $\tilde{k} \in \mathbb{N}$  messages per  $T_{\text{u,crit}}$  (cf. Section 2.3). As an approximation, we assume the locations and times at which messages are created to be the random outcome of a 3-D PPP (cf. Section 2.5) in space and time with density  $\rho \tilde{k} / T_{\text{u,crit}}$ . This approximation is called the Poisson Rain model in [BM10]. As the nodes generate messages at a constant rate, it is sufficient to derive the error probability for a single desired message with arbitrary time of arrival  $t_a$ . The set of interfering messages is denoted by  $\mathbb{M}$  and contains the tuples  $(t_{a,i}, r_i)$  indicating the time of arrival and distance to the transmitter of message  $i$ . Note that  $\mathbb{M}$  contains infinitely many messages generated by the aforementioned PPP.

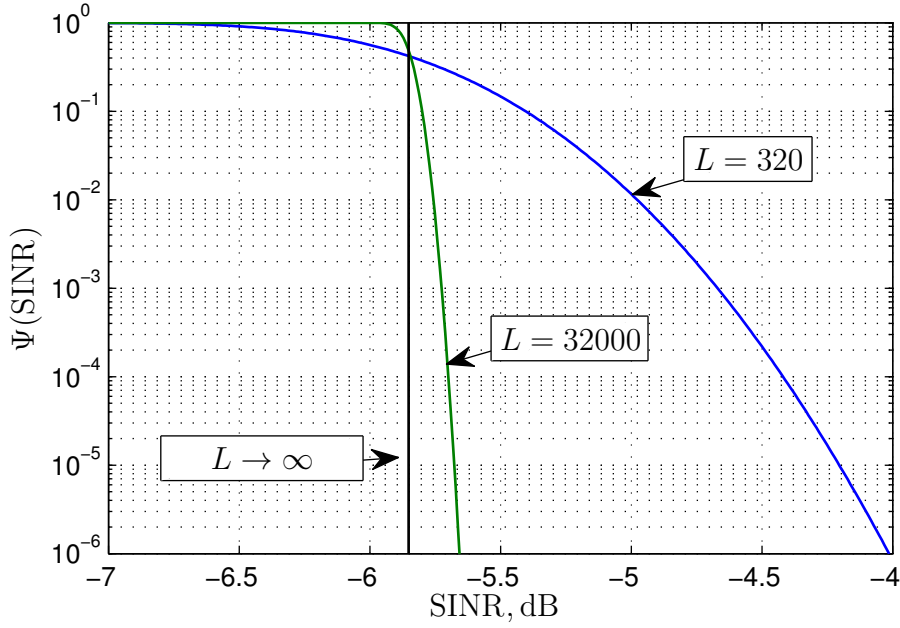


Figure 4.1. MER under AWGN according to (4.2), for  $a = 1/3$ .

We assume the symbol rate to be equivalent to the system bandwidth  $W_{\text{sys}}$ . Hence, the message duration is

$$T_{\text{msg}} = \frac{L}{aW_{\text{sys}}}. \quad (4.4)$$

To calculate the interference power, the power of each interfering message is weighted with the interfering message's relative overlap with the desired message [BM10]. At the receiver, the desired message can be partially destroyed when it is overlapped by an own transmission (cf. Section 2.4.3). If the degree of overlap with an own transmission is  $x_{\text{ov}} \in [0, 1]$ , the usable duration of the desired message is reduced to  $T_{\text{msg}}(1 - x_{\text{ov}})$ . With all times normalized to  $T_{\text{msg}}$ , consider a desired message of duration  $(1 - x_{\text{ov}})$  starting at  $t_a = x_{\text{ov}}/2$  and an interfering message of duration 1 arriving at  $t_a = t$ . Then, the degree of overlap  $\Lambda(t, x_{\text{ov}})$  between desired and interfering message is

$$\Lambda(t, x_{\text{ov}}) = \text{rect}(t) * \text{rect}\left(\frac{t}{1 - x_{\text{ov}}}\right) \frac{1}{1 - x_{\text{ov}}}. \quad (4.5)$$

As usual, the rectangular function is

$$\text{rect}(t) = \begin{cases} 1, & \text{if } |t| \leq \frac{1}{2}, \\ 0, & \text{otherwise.} \end{cases} \quad (4.6)$$

Note that  $\Lambda(t, x_{\text{ov}})$  is a piecewise linear function and assumes values between 0 and 1. When  $x_{\text{ov}} > 0$ , the receiver blanks the parts of the desired message which are overlapped by an own transmission. The probability  $p_{\text{bl,msg}}$  that a message is affected

by blanking can be computed as

$$p_{\text{bl,msg}} = \frac{2\lambda_{\text{nom}}\tilde{k}}{a}. \quad (4.7)$$

The cumulative distribution function (CDF) of  $x_{\text{ov}}$  is

$$\Pr(x_{\text{ov}} \leq x) = (1 - p_{\text{bl,msg}}) + p_{\text{bl,msg}}x \text{ for } x \in [0, 1]. \quad (4.8)$$

The interference power  $P_{\text{int,asu}}$  on the symbols of the desired message is computed as

$$P_{\text{int,asu}} = \sum_{(t_{a,i}, r_i) \in \mathbb{M}} \Lambda\left(\frac{t_{a,i}}{T_{\text{msg}}}, x_{\text{ov}}\right) P_{\text{rx}}(r_i, r_s). \quad (4.9)$$

Although  $\mathbb{M}$  contains an infinite number of messages, only the finite number of messages overlapping with the desired message and transmitted within the line of sight range  $r_s$  of the receiver contribute to (4.9), due to (4.5) and (2.10), respectively.

Using (4.2) and (4.9), the MER for messages received from aircraft at distance  $r$  in unslotted Aloha with single-user receivers, denoted by  $\text{MER}_{\text{asu}}(r)$ , is approximated as

$$\text{MER}_{\text{asu}}(r) \approx E \left\{ \Psi \left( \frac{P_{\text{rx}}(r, r_s)}{\text{SNR}_b^{-1} P_{\text{rx}}(r_b, r_s) + P_{\text{int,asu}}}, \frac{a}{1 - x_{\text{ov}}} \right) \right\}, \quad (4.10)$$

where we optimistically assume that the outage of  $x_{\text{ov}}L/a$  transmitted symbols is equivalent to an increased rate  $a/(1-x_{\text{ov}})$  of bits per symbol. Therefore, (4.10) upper bounds the true MER. With the known distributions of  $x_{\text{ov}}$  and  $\mathbb{M}$ , we can use Monte-Carlo methods to evaluate (4.10). Under the optimistic assumption that consecutive message transmissions are independent, we can compute the probability to lose  $\tilde{k}$  consecutive messages from the same aircraft at distance  $r$  as  $[\text{MER}_{\text{asu}}(r)]^{\tilde{k}}$ . The requirement (2.3) is then equivalent to  $[\text{MER}_{\text{asu}}(r)]^{\tilde{k}} \leq \xi \quad \forall r \leq r_b$  (cf. Section 2.3). As can be shown,  $\text{MER}_{\text{asu}}(r)$  is a nondecreasing function of  $r$ . Therefore, the maximum possible user density  $\rho_{\text{max,asu}}(a, \tilde{k})$  according to (2.20) is

$$\rho_{\text{max,asu}}(a, \tilde{k}) = \sup \left\{ \rho : [\text{MER}_{\text{asu}}(r_b)]^{\tilde{k}} \leq \xi \right\}. \quad (4.11)$$

Equation (4.11) can be solved numerically. From this solution, the optimum parameters  $(a_{\text{opt,asu}}, \tilde{k}_{\text{opt,asu}})$  are obtained as

$$(a_{\text{opt,asu}}, \tilde{k}_{\text{opt,asu}}) = \arg \max_{a, \tilde{k}} \rho_{\text{max,asu}}(a, \tilde{k}). \quad (4.12)$$

The spectral efficiency  $\eta_{\text{asu}}(a, \tilde{k}) = \lambda_{\text{nom}}\rho_{\text{max,asu}}(a, \tilde{k})\pi r_b^2$  is plotted in Figure 4.2 for the parameters given in Table 4.1. The curves show that  $a_{\text{opt,asu}} = 0.337$  and  $\tilde{k}_{\text{opt,asu}} = 5$  maximize the spectral efficiency, with  $\eta_{\text{asu}}(a_{\text{opt,asu}}, \tilde{k}_{\text{opt,asu}}) = 0.0353$  bits/s/Hz.



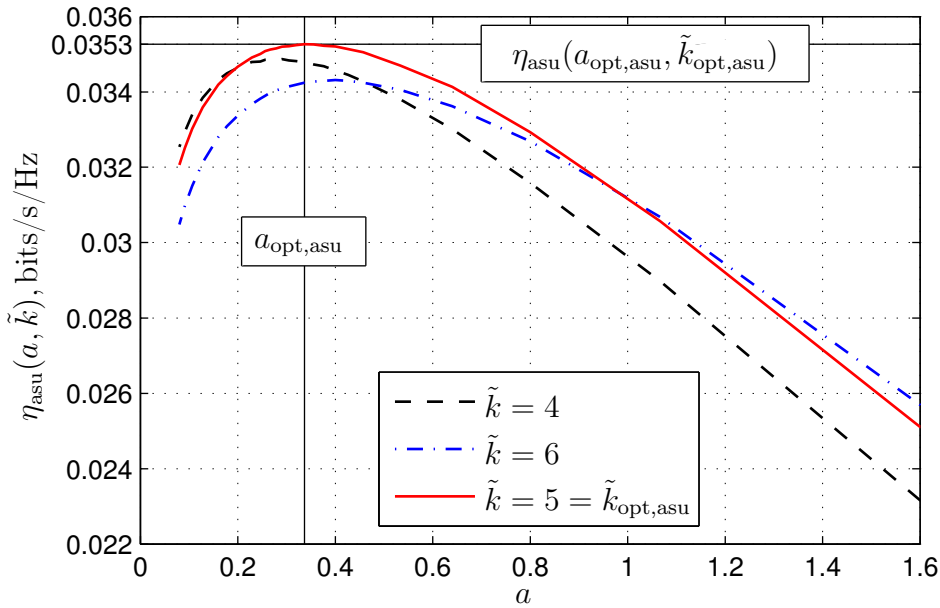


Figure 4.2. Nominal spectral efficiency of unslotted Aloha with single-user receivers.

## 4.4 Cell-Based SOTDMA

### 4.4.1 Hexagonal Reuse Patterns

We briefly review the mathematical description of a reuse pattern of hexagonal cells [Rap01]. A reuse pattern is a map of network cells which assigns a radio channel to each cell using a repetitive pattern. In the context of this work, subchannels of the entire beaconing channel (cf. Section 2.4.6) are assigned to the cells. Generally, a cellular reuse pattern is defined by the radius  $R_{\text{cl}}$  of the circumscribed circle of a cell, which is simply called the cell radius, together with the pattern parameters  $i \in \mathbb{N}$  and  $q \in \mathbb{N}_0$ . Note that in the literature, the pattern parameters are usually denoted by  $(i, j)$ . Instead, the notation  $(i, q)$  is used here to avoid confusion with  $j = \sqrt{-1}$ . As exemplified in Figure 4.3,  $i$  and  $q$  define how co-channel cells are located relative to each other. Starting at any cell, the nearest co-channel cells can be found by moving  $i$  cells into one direction, turning counter-clockwise by  $60^\circ$ , and moving  $q$  cells into the new direction. The number of subchannels necessary to assign exactly one subchannel to each cell is called the reuse pattern size  $N[i, q]$  and can be computed as [Rap01]

$$N[i, q] = i^2 + iq + q^2. \quad (4.13)$$

The reuse distance  $D[N[i, q]]$  indicates the distance between the centers of neighboring co-channel cells and is given by [Rap01]

$$D[N[i, q]] = R_{\text{cl}} \sqrt{3N[i, q]}. \quad (4.14)$$

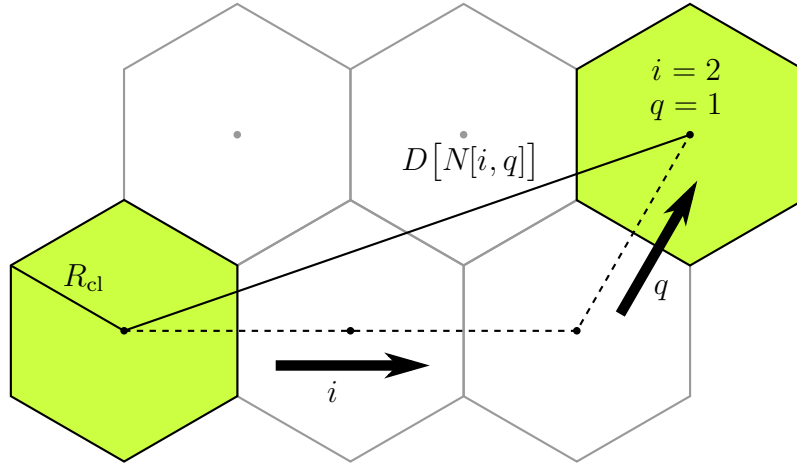


Figure 4.3. Hexagonal cells in a reuse pattern with  $i = 2$  and  $q = 1$ .

Due to (4.13),  $N[i, q]$  can only assume integers from the set  $\mathcal{N}_{\text{reuse}}$ , given by

$$\mathcal{N}_{\text{reuse}} = \{N[i, q] : i \in \mathbb{N}, q \in \mathbb{N}_0\}. \quad (4.15)$$

For a cell centered at  $\mathbf{x}_{\text{cl}} \in \mathbb{R}^2$ , the centers of all co-channel cells can be found at  $\mathbf{x}_{\text{cl}} + k\mathbf{v}_1[i, q] + l\mathbf{v}_2[i, q]$ , with  $k, l \in \mathbb{Z}$  and  $\mathbf{v}_1[i, q], \mathbf{v}_2[i, q] \in \mathbb{R}^2$ , where

$$[\mathbf{v}_1[i, q], \mathbf{v}_2[i, q]] = R_{\text{cl}} \begin{pmatrix} \sqrt{3} & \frac{\sqrt{3}}{2} \\ 0 & \frac{3}{2} \end{pmatrix} \begin{pmatrix} i & -q \\ q & i + q \end{pmatrix}. \quad (4.16)$$

#### 4.4.2 Reuse Pattern Nesting

According to Section 3.3.3, cells closer to each other than some minimum distance must use different TDMA subchannels to avoid message loss during own transmissions. Here, we present a novel reuse concept, which minimizes the number  $N_{\text{T}}$  of TDMA subchannels required for a given total number  $N_{\text{tot}}$  of subchannels. The trivial solution would be to separate all subchannels in the time domain, i.e.,  $N_{\text{T}} = N_{\text{tot}}$ . However, in aeronautical beaconing,  $N_{\text{T}} = N_{\text{tot}}$  is undesirable, as it requires a short message duration  $T_{\text{msg}}$ . To maximize the transmitted energy per bit when the transmit power is limited,  $T_{\text{msg}}$  should be as long as possible. Additionally, the guard time overhead, i.e., the ratio of guard times to useful message transmission times, is less when  $T_{\text{msg}}$  is longer. Both the transmitted energy per bit and the guard time overhead are especially critical in aeronautics due to the large beaconing ranges and the long propagation delays. Therefore, a combination of subchannel concept and reuse concept is required which allows longer  $T_{\text{msg}}$  than the trivial solution  $N_{\text{T}} = N_{\text{tot}}$ , but still ensures that

aircraft in different cells do not transmit at the same time when the cells are too close to each other. In the following, we explain how such a subchannel and reuse concept can be implemented by nesting two reuse patterns [WFS10, Fra14].

The subchannel concept employs  $N_T \in \mathcal{N}_{\text{reuse}}$  TDMA subchannels and further subdivides each of them using a concurrent multiple-access scheme. For this subdivision, we use  $N_F \in \mathcal{N}_{\text{reuse}}$  FDMA subchannels to obtain a total of  $N_{\text{tot}} = N_T N_F$  combined TDMA-FDMA subchannels. Each of them corresponds to a certain time and frequency region in a repetitive frame structure as shown in Figure 4.4 a). Our novel reuse concept assigns the  $N_{\text{tot}}$  subchannels to the cells of a cellular reuse pattern as exemplified in Figure 4.4 b) to d). In a conventional reuse pattern of  $N_T$  TDMA subchannels (Figure 4.4 b), restrict attention to the cells of one particular TDMA subchannel. Into this set of cells, a second reuse pattern of  $N_F$  FDMA channels can be nested as demonstrated in Figure 4.4 c). Accordingly, the TDMA reuse pattern is the outer and the FDMA reuse pattern is the inner reuse pattern. Nesting the FDMA reuse pattern into all TDMA subchannels yields the nested TDMA-FDMA reuse pattern as shown in Figure 4.4 d). It can be shown that  $N_{\text{tot}} \in \mathcal{N}_{\text{reuse}}$  and that the reuse distance of the nested reuse pattern is  $D_{\text{tot}} = D[N_{\text{tot}}]$ .

To ensure that message reception is not impaired by own transmissions, no two aircraft at a distance of  $r_b$  or less may transmit at the same time. This requires a sufficient distance between cells of the same TDMA subchannel. Approximating the cells by circles of radius  $R_{\text{cl}}$ , the separation between neighboring cells of the same TDMA subchannel can be approximated as  $D[N_T] - 2R_{\text{cl}}$ . Then, both  $N_T$  and  $N_{\text{tot}}$  must be restricted to the subset  $\mathcal{N}'_{\text{reuse}}$  of  $\mathcal{N}_{\text{reuse}}$ , given by

$$\mathcal{N}'_{\text{reuse}} = \{n \in \mathcal{N}_{\text{reuse}} : D[n] > 2R_{\text{cl}} + r_b\}. \quad (4.17)$$

For given  $N_{\text{tot}} \in \mathcal{N}'_{\text{reuse}}$ , the longest  $T_{\text{msg}}$  is achieved and the received energy per bit is maximized for the lowest possible choice of  $N_T$ . We therefore set

$$N_T = \min \left\{ n \in \mathcal{N}'_{\text{reuse}} : \frac{N_{\text{tot}}}{n} \in \mathcal{N}_{\text{reuse}} \right\}, \text{ and} \quad (4.18)$$

$$N_F = N_{\text{tot}}/N_T. \quad (4.19)$$

Note that if there is no suitable  $N_T < N_{\text{tot}}$ , then  $N_T = N_{\text{tot}}$  and  $N_F = 1$  is selected in (4.18) and (4.19), respectively.

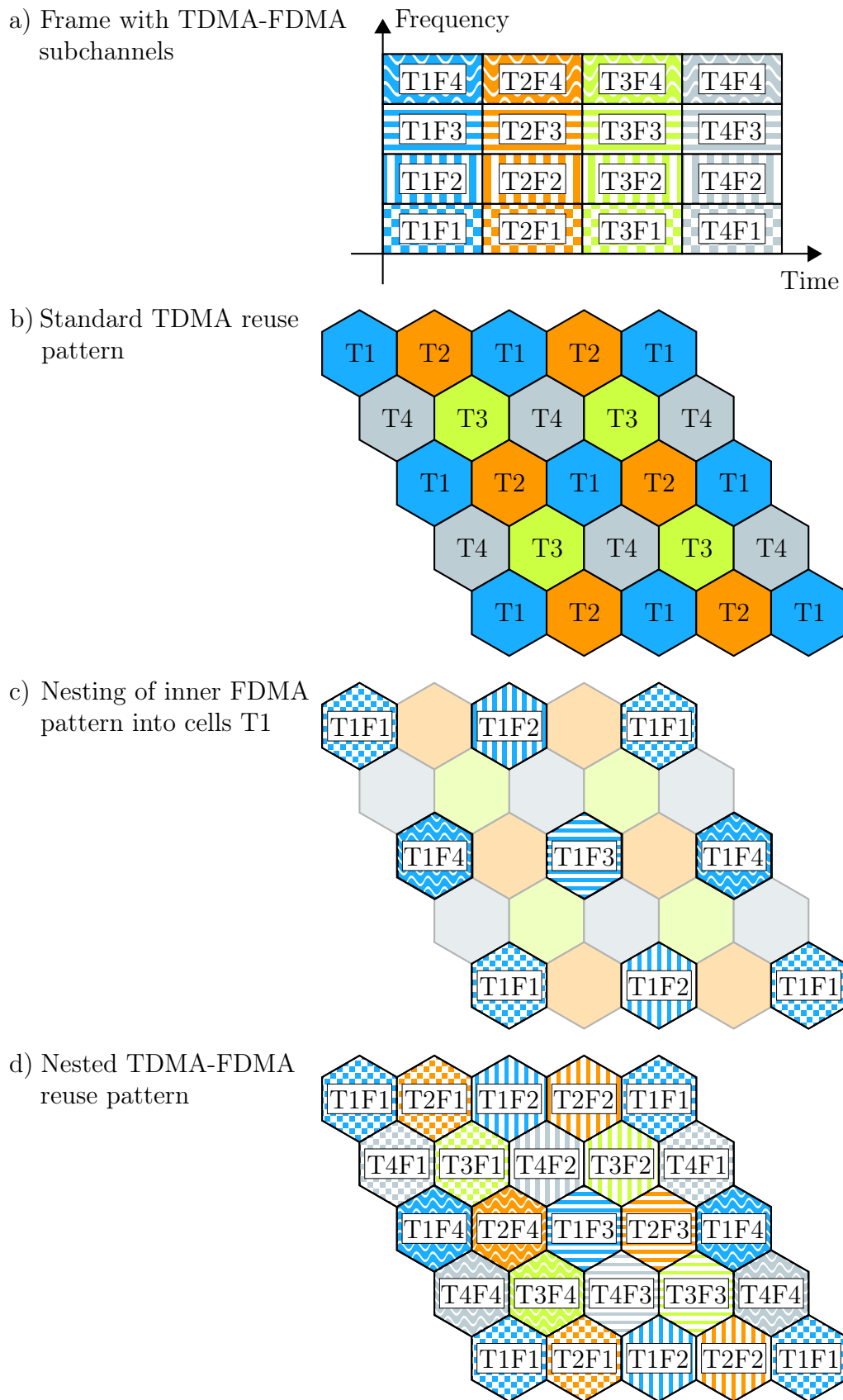


Figure 4.4. Reuse pattern nesting and channel assignment for  $N_T = N_F = 4$  [WFS10, Fra14].

### 4.4.3 Message Scheduling

We assume that the frame duration is  $T_{u,\text{crit}}$  and that each node transmits once per frame. To derive the spectral efficiency of CB-SOTDMA, the following simplifying assumptions about message scheduling are made:

- Propagation delays and guard times are ignored. As discussed in Section 3.3.3, appropriate scheduling can reduce the guard times required in CB-SOTDMA by roughly 90%. Due to the complexity of such appropriate scheduling [WFS10], its implementation is non-trivial and would be difficult to include in the semi-analytical model. Therefore, we omit guard times, which is an optimistic assumption with respect to the spectral efficiency.
- Control data overhead is ignored. This means that each message contains only the  $L$  payload data bits.
- The coordination of transmissions works perfectly. This means that the nodes within a cell transmit one after the other during the time interval belonging to the TDMA subchannel of their cell.
- The available resources are shared equally and entirely. This means that the entire time interval belonging to the TDMA subchannel of a cell is equally divided between the nodes in the cell.

### 4.4.4 Selection of the Coding and Modulation Rate

We assume that each message consists of complex modulation symbols transmitted at a rate of  $W_{\text{sys}}/N_{\text{F}}$ . Since each node transmits once per frame, each cell can be assigned a transmission time of  $T_{u,\text{crit}}/N_{\text{T}}$ . Neglecting guard times, the combined number of symbols which can be transmitted per frame by all nodes in a cell is thus  $(T_{u,\text{crit}}W_{\text{sys}})/(N_{\text{F}}N_{\text{T}})$ , which can be expressed as  $L/(\lambda_{\text{nom}}N_{\text{tot}})$  by means of (2.19). As the number  $M_{\text{cl}}$  of nodes in a single cell changes over time, the time, or number of symbols, available to each node for message transmission varies as well (cf. Section 4.4.3). In order to adapt the message duration  $T_{\text{msg}}$  while maintaining a constant number of payload bits  $L$ , the number of bits  $a_{\text{cl}}[M_{\text{cl}}]$  transmitted per complex symbol is set to

$$a_{\text{cl}}[M_{\text{cl}}] = \lambda_{\text{nom}}N_{\text{tot}}M_{\text{cl}}. \quad (4.20)$$

Under the 2-D model (cf. Section 2.5), The number of nodes in a single cell is Poisson-distributed with  $E\{M_{\text{cl}}\} = \rho A_{\text{cl}}$ , where the cell area  $A_{\text{cl}}$  is given by

$$A_{\text{cl}} = \frac{3\sqrt{3}}{2}R_{\text{cl}}^2. \quad (4.21)$$

### 4.4.5 Calculation of the Message Error Rate

Here, we calculate the MER for CB-SOTDMA with a nested TDMA-FDMA reuse pattern according to Section 4.4.2 using the assumptions about message scheduling and coding and modulation rate discussed in Section 4.4.3 and Section 4.4.4, respectively. Due to the homogeneous aircraft distribution of the 2-D model, the constant message generation rate of each aircraft and the perfect message scheduling, the MER is time-invariant. Thus, the arrival time of the desired message is not explicitly considered. Initially, we compute the MER for a given receiver location  $\mathbf{x}_{\text{rx}} \in \mathbb{R}^2$ , transmitter location  $\mathbf{x}_{\text{tx}} \in \mathbb{R}^2$ , node density  $\rho$ , cell radius  $R_{\text{cl}}$  and parameters  $(i_{\text{tot}}, q_{\text{tot}})$  of the combined TDMA-FDMA reuse pattern. The geometry is exemplified in Figure 4.5, where the largest relevant transmitter-receiver distance  $\|\mathbf{x}_{\text{tx}} - \mathbf{x}_{\text{rx}}\| = r_{\text{b}}$  is assumed. In the example shown, the cell radius is  $R_{\text{cl}} = 58$  nmi, while the ranges  $r_{\text{s}}$  and  $r_{\text{b}}$  correspond to the values given in Table 4.1. The transmitter is located in a cell centered at  $\mathbf{x}_{\text{cl}} \in \mathbb{R}^2$ . This cell center location can be written as

$$\mathbf{x}_{\text{cl}} = k_{\text{cl}}\mathbf{v}_1[1, 0] + l_{\text{cl}}\mathbf{v}_2[1, 0], \quad (4.22)$$

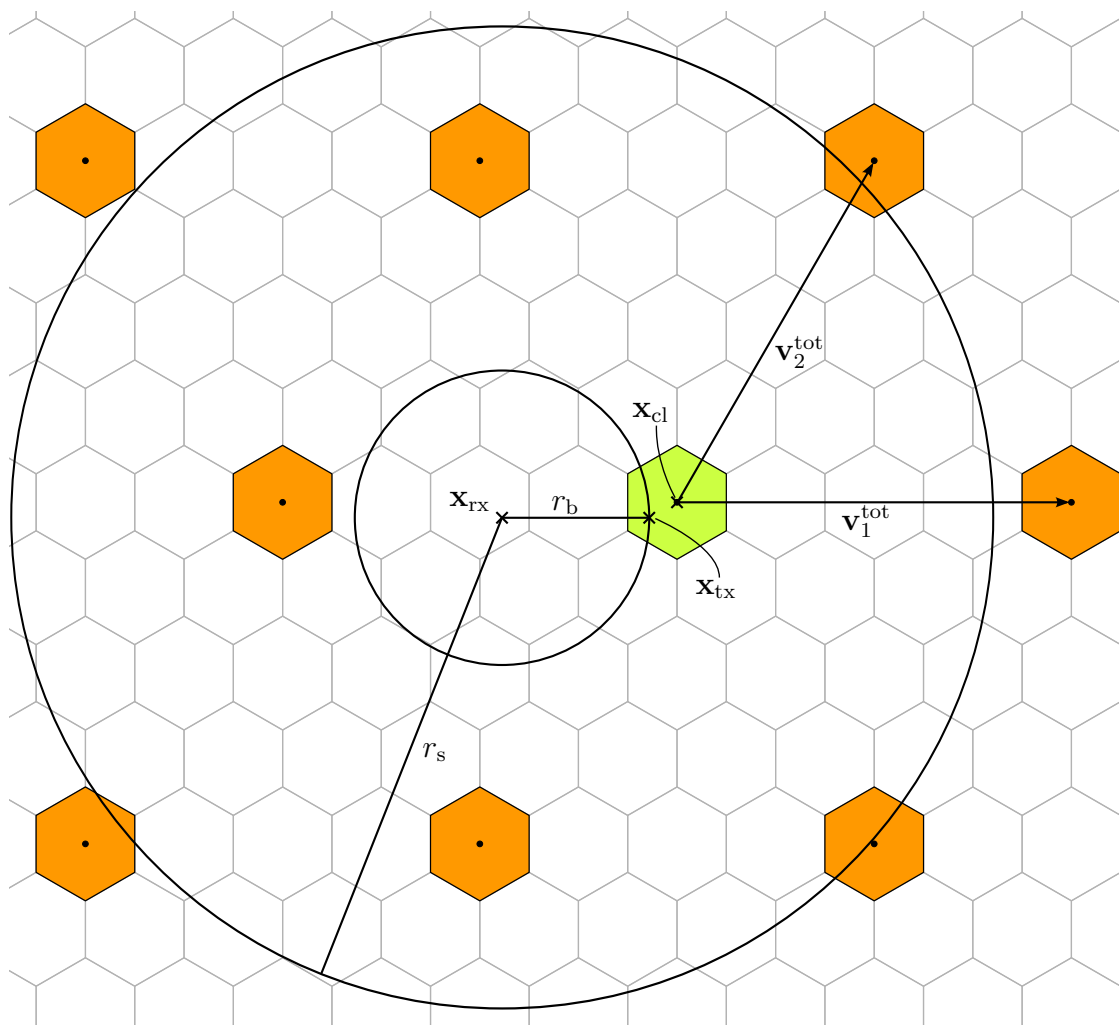
where the cell coordinates  $(k_{\text{cl}}, l_{\text{cl}}) \in \mathbb{Z}^2$  are found to be

$$(k_{\text{cl}}, l_{\text{cl}}) = \arg \min_{k,l} \|k\mathbf{v}_1[1, 0] + l\mathbf{v}_2[1, 0] - \mathbf{x}_{\text{tx}}\|. \quad (4.23)$$

Relative to  $\mathbf{x}_{\text{cl}}$ , all co-channel cells are located at integer multiples of the co-channel cell offset vectors  $\mathbf{v}_1^{\text{tot}} = \mathbf{v}_1[i_{\text{tot}}, q_{\text{tot}}]$  and  $\mathbf{v}_2^{\text{tot}} = \mathbf{v}_2[i_{\text{tot}}, q_{\text{tot}}]$ . Due to the coordinated channel access, there is exactly one interfering transmitter in each nonempty co-channel cell. For the co-channel cell at  $\mathbf{x}_{\text{cl}} + k\mathbf{v}_1^{\text{tot}} + l\mathbf{v}_2^{\text{tot}}$  with  $k, l \in \mathbb{Z}$ , this interfering transmitter is placed at the random offset  $R_{\text{cl}}\mathbf{z}_{k,l} \in \mathbb{R}^2$  from the cell center. The normalized offsets  $\mathbf{z}_{k,l}$  are i.i.d. with uniform distribution in a cell of radius  $R_{\text{cl}} = 1$  centered at the origin. Let  $d_{k,l} \in [0, 1]$  for  $k, l \in \mathbb{Z}$  denote random variables, where  $d_{k,l} = 1$  if the co-channel cell at  $\mathbf{x}_{\text{cl}} + k\mathbf{v}_1^{\text{tot}} + l\mathbf{v}_2^{\text{tot}}$  contains at least one aircraft, and  $d_{k,l} = 0$  otherwise. As the node locations form a PPP, the random variables  $d_{k,l}$  are i.i.d., with  $\Pr(d_{k,l} = 0) = \Pr(M_{\text{cl}} = 0) = e^{-\rho A_{\text{cl}}}$ . The interference can be computed as

$$P_{\text{int,cl}} = \sum_{(k,l) \in \mathbb{Z}^2 \setminus (0,0)} d_{k,l} P_{\text{rx}} \left( \|\mathbf{x}_{\text{cl}} + k\mathbf{v}_1^{\text{tot}} + l\mathbf{v}_2^{\text{tot}} + R_{\text{cl}}\mathbf{z}_{k,l} - \mathbf{x}_{\text{rx}}\|, r_{\text{s}} \right). \quad (4.24)$$

Note that due to (2.10), interfering transmitters outside of the line of sight range  $r_{\text{s}}$  of the receiver do not contribute to (4.24). This permits us to numerically generate random realizations of (4.24) by only considering co-channel cells which intersect with



Legend:



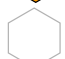
-  Cell containing the desired transmitter at  $\mathbf{x}_{tx}$
-  Co-channel cell at  $\mathbf{x}_{cl} + k\mathbf{v}_1^{\text{tot}} + l\mathbf{v}_2^{\text{tot}}$ ; contains  $d_{k,l} \in [0, 1]$  interfering transmitters
-  Cell using a different subchannel than the desired transmitter

Figure 4.5. Example geometry for calculation of the SINR.  $i_{\text{tot}} = q_{\text{tot}} = 4$  ( $N_{\text{tot}} = 16$ ),  $R_{\text{cl}} = 58$  nmi. Transmitter at  $\mathbf{x}_{tx}$  and receiver at  $\mathbf{x}_{rx}$  are located at a distance of  $r = r_b$ .

a disc of radius  $r_s$  around  $\mathbf{x}_{\text{rx}}$ . Employing (4.2), the MER, denoted by  $\text{MER}_{\text{cl}}(\mathbf{x}_{\text{rx}}, \mathbf{x}_{\text{tx}})$ , is approximated as

$$\text{MER}_{\text{cl}}(\mathbf{x}_{\text{rx}}, \mathbf{x}_{\text{tx}}) \approx E \left\{ \Psi \left( \frac{P_{\text{rx}}(\|\mathbf{x}_{\text{tx}} - \mathbf{x}_{\text{rx}}\|, r_s)}{(N_{\text{F}} \text{SNR}_{\text{b}})^{-1} P_{\text{rx}}(r_{\text{b}}, r_s) + P_{\text{int,cl}}}, a_{\text{cl}}[M_{\text{cl}} + 1] \right) \right\}, \quad (4.25)$$

where we assume that  $\mathbf{x}_{\text{rx}}$  and  $\mathbf{x}_{\text{tx}}$  are in different cells. Due to the Poisson assumption of the 2-D model, the number of other aircraft in the cell of the transmitter follows the same statistical distribution as  $M_{\text{cl}}$ , and hence,  $a_{\text{cl}}[M_{\text{cl}} + 1]$  bits are transmitted per complex symbol. The expectation (4.25) can be evaluated through Monte-Carlo simulations.

The mean MER at  $\mathbf{x}_{\text{rx}}$  for distance  $r = \|\mathbf{x}_{\text{tx}} - \mathbf{x}_{\text{rx}}\|$  is denoted by  $\overline{\text{MER}}_{\text{cl}}(\mathbf{x}_{\text{rx}}, r)$  and computed by averaging over a circle:

$$\overline{\text{MER}}_{\text{cl}}(\mathbf{x}_{\text{rx}}, r) = \frac{1}{2\pi} \int_0^{2\pi} \text{MER}_{\text{cl}} \left( \mathbf{x}_{\text{rx}}, \mathbf{x}_{\text{rx}} + r \begin{pmatrix} \cos(\vartheta) \\ \sin(\vartheta) \end{pmatrix} \right) d\vartheta. \quad (4.26)$$

Note that  $\text{MER}_{\text{cl}}(\mathbf{x}_{\text{rx}}, \mathbf{x}_{\text{tx}})$  is constant for all  $\mathbf{x}_{\text{tx}}$  within the intersection of any cell with the circle  $\{\mathbf{x}_{\text{tx}} : \|\mathbf{x}_{\text{tx}} - \mathbf{x}_{\text{rx}}\| = r\}$ . The reason is that the interference (4.24) has the same statistical distribution for all  $\mathbf{x}_{\text{tx}}$  in the same cell. Hence, the integrand in (4.26) is piecewise constant, which simplifies the numerical evaluation of the integral.

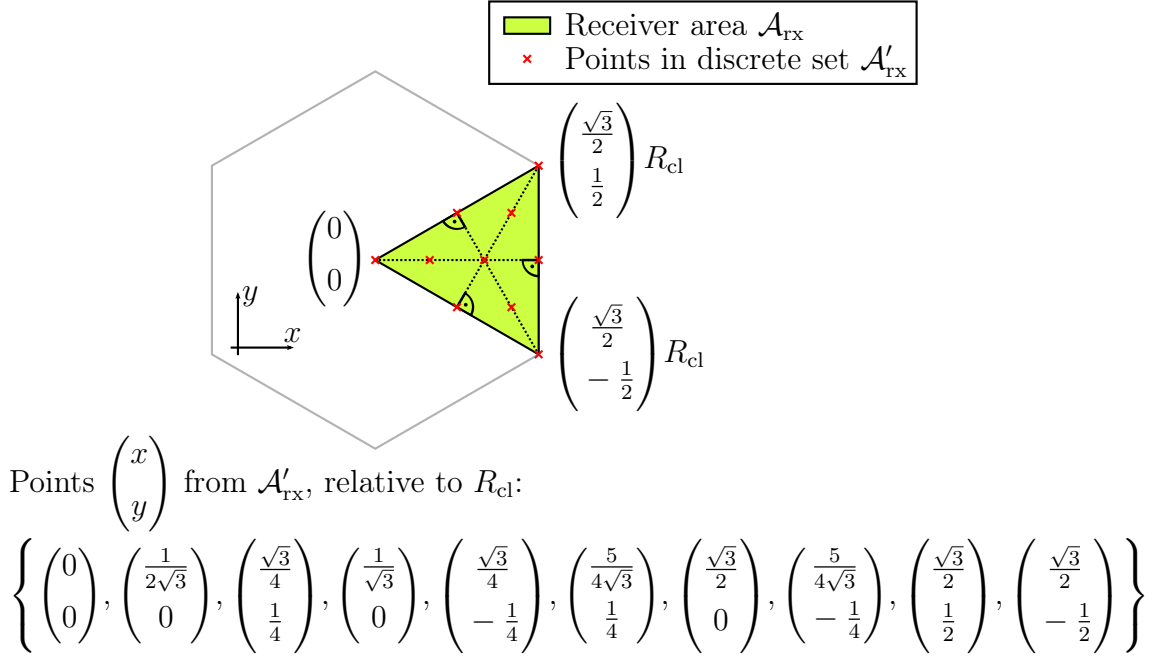
#### 4.4.6 Parameter Optimization for Maximum Spectral Efficiency

In this section, we seek the reuse pattern parameters  $i_{\text{tot}}$ ,  $q_{\text{tot}}$  and  $R_{\text{cl}}$  maximizing the spectral efficiency. Since each aircraft transmits only once per  $T_{\text{u,crit}}$ , the requirement (2.3) is equivalent to a MER requirement (cf. Section 2.3). Since the MER is time-invariant (cf. Section 4.4.5), it is sufficient to check (2.3) at a single point in time. As the MER depends on the reuse pattern parameters  $i_{\text{tot}}$ ,  $q_{\text{tot}}$  and  $R_{\text{cl}}$ , this is also the case for the maximum possible node density  $\rho_{\text{max,cl}}(i_{\text{tot}}, q_{\text{tot}}, R_{\text{cl}})$ . According to (2.20),  $\rho_{\text{max,cl}}(i_{\text{tot}}, q_{\text{tot}}, R_{\text{cl}})$  is given by

$$\rho_{\text{max,cl}}(i_{\text{tot}}, q_{\text{tot}}, R_{\text{cl}}) = \min_{\mathbf{x}_{\text{rx}} \in \mathcal{A}_{\text{rx}}} \max \left\{ \rho : \overline{\text{MER}}_{\text{cl}}(\mathbf{x}_{\text{rx}}, r) \leq \xi \quad \forall r \leq r_{\text{b}} \right\}, \quad (4.27)$$

where we have to minimize over  $\mathbf{x}_{\text{rx}}$ , as the MER depends on the receiver location. Due to symmetry, it is sufficient to consider  $\mathbf{x}_{\text{rx}} \in \mathcal{A}_{\text{rx}}$ , where the receiver area  $\mathcal{A}_{\text{rx}}$  corresponds to the triangle depicted in Figure 4.6. The nominal spectral efficiency



Figure 4.6. Cell section  $\mathcal{A}_{\text{rx}}$  and set of points  $\mathcal{A}'_{\text{rx}}$ .

$\eta_{\text{cl}}(i_{\text{tot}}, q_{\text{tot}}, R_{\text{cl}})$  is obtained by inserting (4.27) into (2.21). For numerical evaluations of (4.27), we use two approximations. First, we replace  $\mathcal{A}_{\text{rx}}$  by a discrete set of receiver locations  $\mathcal{A}'_{\text{rx}} \subset \mathcal{A}_{\text{rx}}$ . Since the minimum in (4.27) cannot be solved analytically, it can only be evaluated numerically over a finite set of points  $\mathcal{A}'_{\text{rx}}$ . In our numerical evaluation of (4.27), the computational effort for  $|\mathcal{A}'_{\text{rx}}| = 10$  proved feasible. For this reason the set  $\mathcal{A}'_{\text{rx}}$  shown in Figure 4.6 was selected. Note that when only a subset of  $\mathcal{A}_{\text{rx}}$  is checked in (4.27), the resulting minimum is an upper bound for the exact minimum. As second approximation, we only check  $\overline{\text{MER}}_{\text{cl}}(\mathbf{x}_{\text{rx}}, r_{\text{b}}) \leq \xi$ , i.e., only consider  $r = r_{\text{b}}$ . Again, this serves the purpose of keeping the computational effort for evaluating (4.27) within feasible limits. When transmitting a beacon message over a distance of  $r < r_{\text{b}}$ , the SINR will typically not be substantially smaller than for  $r = r_{\text{b}}$ . Due to this, it may be assumed that the effect of the second approximation is limited. As was the case for the first approximation, an approximative solution of (4.27) which only considers  $r = r_{\text{b}}$  cannot be smaller than the true  $\rho_{\text{max,cl}}(i_{\text{tot}}, q_{\text{tot}}, R_{\text{cl}})$ . Hence, the results presented in the following upper bound the exact  $\eta_{\text{cl}}(i_{\text{tot}}, q_{\text{tot}}, R_{\text{cl}})$ .

The optimum reuse scheme parameters  $i_{\text{tot}}^{\text{opt}}$  and  $q_{\text{tot}}^{\text{opt}}$  for given  $R_{\text{cl}}$  are computed as

$$\begin{pmatrix} i_{\text{tot}}^{\text{opt}} \\ q_{\text{tot}}^{\text{opt}} \end{pmatrix} = \arg \max_{(i_{\text{tot}}, q_{\text{tot}})} \eta_{\text{cl}}(i_{\text{tot}}, q_{\text{tot}}, R_{\text{cl}}). \quad (4.28)$$

For the parameters listed in Table 4.1, Figure 4.7 plots  $\eta_{\text{cl}}(i_{\text{tot}}^{\text{opt}}, q_{\text{tot}}^{\text{opt}}, R_{\text{cl}})$  versus  $R_{\text{cl}}$ , where  $R_{\text{cl}}$  is sampled in steps of 0.1 nmi between 15 nmi and 75 nmi, and at 4 additional values between 10 nmi and 15 nmi. While both high and low  $R_{\text{cl}}$  turn out to be

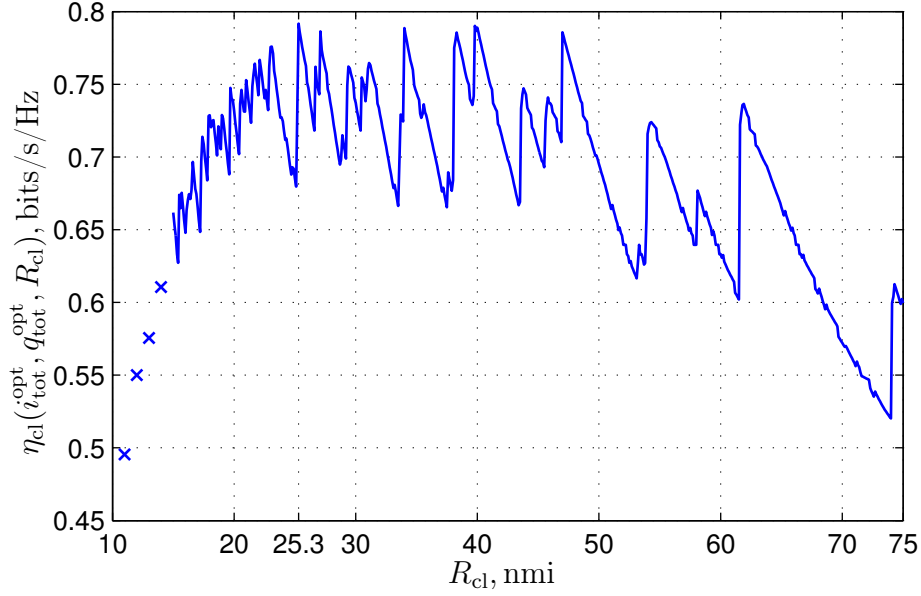


Figure 4.7. Nominal spectral efficiency of CB-SOTDMA.

suboptimal, several similar local maxima of  $\eta_{\text{cl}}(i_{\text{tot}}^{\text{opt}}, q_{\text{tot}}^{\text{opt}}, R_{\text{cl}})$  can be found in the range  $20 \text{ nmi} < R_{\text{cl}} < 50 \text{ nmi}$ . The largest spectral efficiency is found at  $R_{\text{cl}} = 25.3 \text{ nmi}$ , with  $\eta_{\text{cl}}(i_{\text{tot}}^{\text{opt}}, q_{\text{tot}}^{\text{opt}}, R_{\text{cl}}) = 0.79 \text{ bits/s/Hz}$ . At  $R_{\text{cl}} = 25.3 \text{ nmi}$ , the optimal reuse pattern parameters maximizing the spectral efficiency are  $(i_{\text{tot}}^{\text{opt}}, q_{\text{tot}}^{\text{opt}}) = (12, 6)$ , leading to  $N_{\text{tot}}^{\text{opt}} = N[i_{\text{tot}}^{\text{opt}}, q_{\text{tot}}^{\text{opt}}] = 252$ . From (4.18) and (4.19), we obtain  $N_{\text{T}} = 21$  and  $N_{\text{F}} = 12$  at  $N_{\text{tot}} = N_{\text{tot}}^{\text{opt}}$ .

The other local maxima of  $\eta_{\text{cl}}(i_{\text{tot}}^{\text{opt}}, q_{\text{tot}}^{\text{opt}}, R_{\text{cl}})$  coming close to the maximum at  $R_{\text{cl}} = 25.3$  are found for larger  $R_{\text{cl}}$ . However, when the spectral efficiency is similar, smaller cells are preferable to larger cells, as the line of sight range required for communication between all aircraft within a smaller cell is lower.

In Figure 4.8, the reuse distance  $D[i_{\text{tot}}^{\text{opt}}, q_{\text{tot}}^{\text{opt}}]$  of the optimal reuse pattern is displayed as a function of  $R_{\text{cl}}$ . The smallest reuse distance at which interference becomes possible can be upper bounded by  $2R_{\text{cl}} + r_{\text{b}} + r_{\text{s}}$ . This upper bound is shown in Figure 4.8 as well. Comparing it to the optimal reuse distance shows that the largest spectral efficiency is always achieved when only little or no interference exists within line of sight range of any receiver.

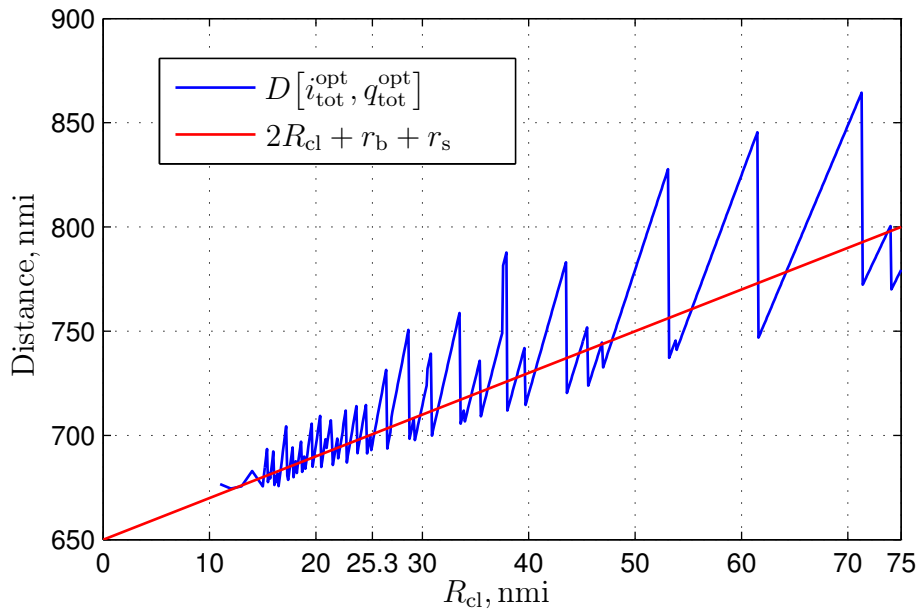


Figure 4.8. Optimal reuse distance in CB-SOTDMA.

## 4.5 Unslotted Aloha Designed for SIC

### 4.5.1 Message Error Rate as a Function of SINR under Blanking Impairment

In this section, we explain how the MER is computed as a function of SINR in the semi-analytical model of Aloha with SIC to be derived in Section 4.5.3. As explained in Section 4.3, a beaconing scheme with Aloha MAC suffers from the half-duplex operation of beaconing radios. In the following, we assume that during its own transmissions, i.e., during the support of (2.14), a beaconing radio sets the received signal to zero, e.g., to protect itself against the substantial  $n_{\text{own}}(t)$  created by own transmissions according to Section 2.4.3. Setting the received signal to zero is also called blanking [Zhi08]. Just as in Section 4.3, we assume that the messages transmitted in unslotted Aloha designed for SIC consist of complex modulation symbols transmitted at a rate of  $W_{\text{sys}}$ . In (4.10), we made the optimistic assumption that lost sections in the received signal merely increase the coding and modulation rate  $a$ . Here, we remove this assumption, and instead, represent the transmission channel as a fading channel with a given SINR on non-blanked symbols and  $\text{SINR} = 0$  on blanked symbols. Each symbol is blanked with probability  $p_{\text{bl}}$  and the blanking of different symbols is for simplicity assumed to be independent. An approximation of the maximum number of information bits per complex symbol on an AWGN fading channel for a finite number of complex symbols per codeword and a given codeword error rate is available from [PV11, eq. (34)].

Solving for the codeword error rate, the blanking AWGN MER model  $\Psi_{\text{bl}}(\text{SINR}, a, p_{\text{bl}})$  is obtained as

$$\Psi_{\text{bl}}(\text{SINR}, a, p_{\text{bl}}) = \frac{1}{2} \operatorname{erfc}\left(B_{\text{bl}}\left((1 - p_{\text{bl}}) \log_2(1 + \text{SINR}) - a\right)\right), \quad (4.29)$$

where

$$B_{\text{bl}} = \frac{\ln(2)}{\sqrt{2 \frac{a}{L} \left( p_{\text{bl}}(1 - p_{\text{bl}}) (\ln(1 + \text{SINR}))^2 + 1 - \left( \frac{1 + p_{\text{bl}} \text{SINR}}{1 + \text{SINR}} \right)^2 \right)}}. \quad (4.30)$$

The derivation of (4.29) is explained in more detail in Appendix A.1.2. Note that for  $p_{\text{bl}} = 0$ , equation (4.30) simplifies to (4.3), but (4.29) still differs from (4.2). More precisely,  $\Psi_{\text{bl}}(\text{SINR}, a, 0) > \Psi(\text{SINR}, a)$  as long as  $2L > a$ . This is due to the fact that [PPV10, eq. (296)], based on which we computed the AWGN MER model (4.2), uses a more accurate approximation of the maximum number of information bits per channel use than [PV11, eq. (34)], which we used for the blanking AWGN MER model (4.29).

## 4.5.2 Time Hopping

To mitigate the negative effects of blanking during own transmissions, we propose the use of time hopping. Time hopping splits up each message into multiple smaller transmission bursts, which are transmitted with gaps of random length in between, as illustrated in Figure 4.9. As a node is able to listen to the channel during the gaps in an outgoing message, the chance of losing large parts of any incoming message is reduced. With time hopping, the transmit signal can be described as sparse. The sparsity  $S$  indicates the factor by which the duration  $T_{\text{msg}}$  of each message is increased with respect to a contiguous transmission. As a generalization of (4.4), the message duration with time hopping can be expressed as

$$T_{\text{msg}} = S \frac{L}{aW_{\text{sys}}}. \quad (4.31)$$

The probability that the received signal is lost at any point in time during an own transmission is only  $1/S$  when time hopping is applied.

In general, the receivers need to learn the time hopping parameters of each incoming message, which may be accomplished by detecting special synchronization sequences contained in each message. This issue is addressed in Chapter 5. Here, we assume message detection and parameter estimation to work perfectly.

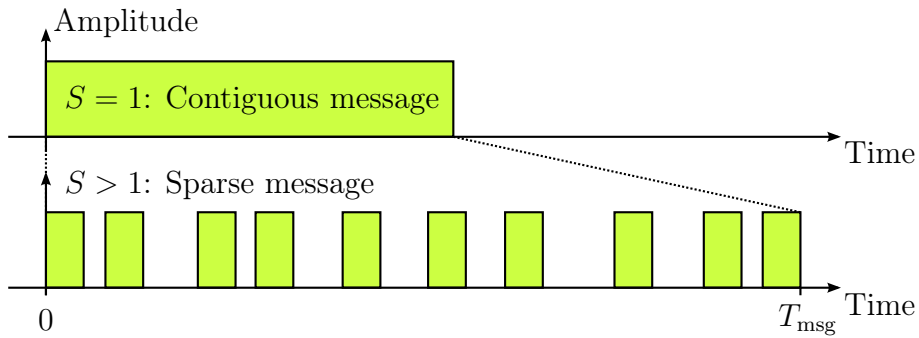


Figure 4.9. Example for time hopping with sparse message structure.

### 4.5.3 Calculation of the Message Error Rate after SIC

In the following, we derive a semi-analytical model of the MER in beaconing with unslotted Aloha and SIC. As in the case of Aloha without SIC explained in Section 4.3, in the 2-D model (cf. Section 2.5), it is sufficient to consider message reception at a single aircraft. Our derivations are based on the MER model presented in [dRHdG12]. Since [dRHdG12] considers neither blanking nor time hopping, we contribute an extension of this model which enables us to calculate the MER for a half-duplex beaconing node affected by blanking during its own, sparse transmissions.

The basic idea of [dRHdG12] is to represent the interference power as a function of the MER and vice versa. Initially, prior to the application of interference cancellation (IC), the receiver is able to decode a certain percentage of the incoming messages. Assuming that the decoded messages are perfectly canceled, the interference power is reduced, which can be exploited in an iterative receiver structure. In each processing step, the remaining interference power is updated based on the current MER and the MER is updated based on the updated interference power.

Additionally, the MER achieved by the receiver after a given number of iterations is a function of received power. To facilitate the mathematical analysis, a discrete set of  $N_{\text{pwr}}$  different received power levels is assumed, which are denoted by  $P_{\text{rx},m}$ ,  $0 \leq m < N_{\text{pwr}}$  [dRHdG12]. The power levels are ordered such that  $P_{\text{rx},m+1} > P_{\text{rx},m}$ . The fraction of received messages having a power of  $P_{\text{rx},m}$  is denoted by  $g_{\text{pwr}}[m]$ . Going beyond [dRHdG12], we take into account that in beaconing, the MER additionally depends on the message arrival time, due to a possible overlap with an own transmission. We assume that each node periodically transmits one message per  $1/\lambda'$  (cf. Section 2.3). Under this condition, the MER is periodic in time of arrival with periodicity  $1/\lambda'$ . Without loss of generality, we assume that the receiving node transmits its messages at  $t = n/\lambda'$ ,  $n \in \mathbb{Z}$ . We compute the MER for  $N_{\text{toa}}$  different times of arrival  $t_l$ , given

by

$$t_l = T_{\text{toa}} \left( l - \left\lfloor \frac{N_{\text{toa}}}{2} \right\rfloor \right), 0 \leq l < N_{\text{toa}}, \quad (4.32)$$

with spacing  $T_{\text{toa}}$  defined by

$$T_{\text{toa}} = (N_{\text{toa}} \lambda')^{-1}. \quad (4.33)$$

Consider a desired message received at  $t = t_l$  and one interfering message arriving in the interval  $(t - t_l)/T_{\text{toa}} \in [\Delta l - 1/2, \Delta l + 1/2]$ , with integer time offset  $\Delta l$ . The average overlap  $\Lambda[\Delta l]$  between desired and interfering message is now

$$\Lambda[\Delta l] = \begin{cases} S^{-1} \left( 1 - \frac{T_{\text{toa}}}{4T_{\text{msg}}} \right), & \Delta l = 0, \\ S^{-1} \left( 1 - |\Delta l| \frac{T_{\text{toa}}}{T_{\text{msg}}} \right), & 0 < |\Delta l| < \Delta l_{\text{max}}, \\ \frac{T_{\text{msg}} - (\Delta l_{\text{max}} - 1/2)T_{\text{toa}}}{2T_{\text{msg}}S}, & |\Delta l| = \Delta l_{\text{max}}, \\ 0, & \text{otherwise,} \end{cases} \quad (4.34)$$

with the maximum integer time offset  $\Delta l_{\text{max}}$  computed as

$$\Delta l_{\text{max}} = \left\lceil \frac{T_{\text{msg}}}{T_{\text{toa}}} - \frac{1}{2} \right\rceil. \quad (4.35)$$

Out of all overlapping messages, the fraction arriving in the interval  $(t - t_l)/T_{\text{toa}} \in [\Delta l - 1/2, \Delta l + 1/2]$  is denoted by  $g_{\text{toa}}[\Delta l]$  and given by

$$g_{\text{toa}}[\Delta l] = \begin{cases} \frac{T_{\text{toa}}}{2T_{\text{msg}}}, & |\Delta l| < \Delta l_{\text{max}}, \\ \frac{T_{\text{msg}} - (\Delta l_{\text{max}} - 1/2)T_{\text{toa}}}{2T_{\text{msg}}}, & |\Delta l| = \Delta l_{\text{max}}, \\ 0, & \text{otherwise.} \end{cases} \quad (4.36)$$

For a message arriving at  $t_l$ , the probability  $p_{\text{bl}}[l]$  that a certain symbol of the message is blanked can be obtained as

$$p_{\text{bl}}[l] = S^{-1} \max \left\{ 1 - \frac{|t_l|}{T_{\text{msg}}}, 0 \right\}, \quad (4.37)$$

where  $S^{-1}$  is the probability that a symbol received during an own transmission is blanked, and  $\max\{1 - |t_l|/T_{\text{msg}}, 0\}$  is the degree of overlap between the message arriving at  $t_l$  and the own transmission starting at  $t = 0$ . Note that (4.37) is only valid for  $T_{\text{msg}} < (2\lambda')^{-1}$ , which is assumed to be the case in the following.

Let us now describe the order of message processing assumed in the semi-analytical model of Aloha with SIC. As illustrated in Figure 3.1, messages of higher received power are processed first [dRHdG12]. However, in our case, the combinations  $(t_l, P_{\text{rx},m})$  of time of arrival and received power need to be processed consecutively. Hence, for

Table 4.2. Example Processing Order  $\nu[l, m]$ .  $N_{\text{pwr}} = 2$ ,  $N_{\text{toa}} = 4$ .

$l$	0	1	2	3
$t_l/T_{\text{toa}}$	-2	-1	0	1
$\nu[l, 1]$	0	2	3	1
$\nu[l, 0]$	4	6	7	5

messages of the same  $P_{\text{rx},m}$  but different  $t_l$ , we additionally require a suitable order of processing in time direction. Since SIC can only reduce the interference in case of successful decoding, it is reasonable to process messages which are easy to decode prior to messages received under more difficult circumstances. Due to signal outage, messages having a larger degree of overlap with an own transmission are more difficult to decode. Therefore, we assume that messages are processed in descending order of their time offset  $|t_l|$  to the own transmission at  $t = 0$ . Let the order of processing be given by the function  $\nu[l, m] \in \{0, \dots, N_{\text{pwr}}N_{\text{toa}} - 1\}$ , which indicates the number of combinations  $(t_{\tilde{l}}, P_{\text{rx},\tilde{m}})$  processed prior to the combination  $(t_l, P_{\text{rx},m})$ . According to the previous discussion, we compute  $\nu[l, m]$  as

$$\nu[l, m] = N_{\text{toa}}(N_{\text{pwr}} - 1 - m) - 1 - \mathbf{1}\{t_l > 0\} + \sum_{\tilde{l}=0}^{N_{\text{toa}}-1} \mathbf{1}\{|t_{\tilde{l}}| \geq |t_l|\}, \quad (4.38)$$

where the indicator function  $\mathbf{1}\{C\}$  yields 1 if the boolean expression  $C$  is true and zero otherwise. An example with  $N_{\text{pwr}} = 2$  and  $N_{\text{toa}} = 4$  is shown in Table 4.2.

The receiver processes the received signal in multiple iterations, which we term processing passes. Within each processing pass, the combinations  $(t_l, P_{\text{rx},m})$  are processed consecutively, in the order (4.38). Each  $(t_l, P_{\text{rx},m})$  is processed exactly once per processing pass. In total, the receiver performs  $p_{\text{max}}$  processing passes. Let  $\text{MER}_{\text{SIC}}^{(p)}[l, m]$ ,  $0 \leq l < N_{\text{toa}}$ ,  $0 \leq m < N_{\text{pwr}}$ , denote the message error rate for time of arrival  $t_l$  and received power  $P_{\text{rx},m}$  after processing pass  $p \in \{1, \dots, p_{\text{max}}\}$ . Initially, we set  $\text{MER}_{\text{SIC}}^{(0)}[l, m] = 1$  for all  $0 \leq l < N_{\text{toa}}$  and  $0 \leq m < N_{\text{pwr}}$ , since no messages have yet been decoded. During processing pass  $p$ ,  $\text{MER}_{\text{im}}^{(p)}[l, m, \tilde{l}, \tilde{m}]$  denotes the intermediate MER which is valid for time of arrival  $t_{\tilde{l}}$  and received power  $P_{\text{rx},\tilde{m}}$  during the processing of time of arrival  $t_l$  and received power  $P_{\text{rx},m}$ .  $\text{MER}_{\text{im}}^{(p)}[l, m, \tilde{l}, \tilde{m}]$  is obtained as

$$\text{MER}_{\text{im}}^{(p)}[l, m, \tilde{l}, \tilde{m}] = \begin{cases} \text{MER}_{\text{SIC}}^{(p)}[\tilde{l}, \tilde{m}], & \text{if } \nu[\tilde{l}, \tilde{m}] < \nu[l, m], \\ \text{MER}_{\text{SIC}}^{(p-1)}[\tilde{l}, \tilde{m}], & \text{if } \nu[\tilde{l}, \tilde{m}] \geq \nu[l, m]. \end{cases} \quad (4.39)$$

In processing pass  $p$ , during the decoding of a desired message with time of arrival  $t_l$  and received power  $P_{\text{rx},m}$ , the average interference caused by a single overlapping message can be expressed as

$$P_{\text{int,s}}^{(p)}[l, m] = \sum_{\tilde{m}=0}^{N_{\text{pwr}}-1} P_{\text{rx},\tilde{m}} g_{\text{pwr}}[\tilde{m}] \sum_{\Delta l=-\Delta l_{\text{max}}}^{\Delta l_{\text{max}}} g_{\text{toa}}[\Delta l] \Lambda[\Delta l] \text{MER}_{\text{im}}^{(p)}[l, m, (l + \Delta l) \bmod N_{\text{toa}}, \tilde{m}]. \quad (4.40)$$

Here, we average over all overlapping messages which were initially present. The probability that any of the initially present messages with time of arrival  $t_{\tilde{l}}$  and received power  $P_{\text{rx},\tilde{m}}$  has not yet been decoded and canceled is equivalent to  $\text{MER}_{\text{im}}^{(p)}[l, m, \tilde{l}, \tilde{m}]$ . Conditioned on the initial number  $k$  of overlapping messages, which were present prior to any interference cancellation, the message error rate  $\text{MER}_{\text{cnd}}^{(p)}[l, m|k]$  can be approximated as

$$\text{MER}_{\text{cnd}}^{(p)}[l, m|k] \approx \Psi_{\text{bl}} \left( \frac{P_{\text{rx},m}}{\text{SNR}_{\text{b}}^{-1} P_{\text{rx}}(r_{\text{b}}, r_{\text{s}}) + k P_{\text{int,s}}^{(p)}[l, m]}, a, p_{\text{bl}}[l] \right). \quad (4.41)$$

The number of messages initially overlapping with a certain desired message is Poisson distributed with mean  $G_{\text{msg}}$  given by

$$G_{\text{msg}} = \rho \pi r_{\text{s}}^2 \lambda' 2T_{\text{msg}}. \quad (4.42)$$

Averaging  $\text{MER}_{\text{cnd}}^{(p)}[l, m|k]$  with respect to  $k$  yields the MER for messages with time of arrival  $t_l$  and received power  $P_{\text{rx},m}$  after processing pass  $p$ :

$$\text{MER}_{\text{SIC}}^{(p)}[l, m] = \sum_{k=0}^{\infty} \text{MER}_{\text{cnd}}^{(p)}[l, m|k] \frac{G_{\text{msg}}^k}{k!} e^{-G_{\text{msg}}}. \quad (4.43)$$

The semi-analytical model for beaconing with Aloha and SIC is based on repetitive computations of (4.40) and (4.43). Note that (4.39) ensures that the computation of  $\text{MER}_{\text{SIC}}^{(p)}[l, m]$  depends only on MER values which have already been computed according to the order of processing (4.38). The receiver algorithm and the order of processing are also described by the pseudocode in Figure 4.10. For simplicity, this pseudocode assumes even  $N_{\text{toa}}$ . After  $p$  processing passes, the average MER for each received power level, denoted by  $\overline{\text{MER}}_{\text{SIC}}^{(p)}[m]$ , is computed as

$$\overline{\text{MER}}_{\text{SIC}}^{(p)}[m] = \frac{1}{N_{\text{toa}}} \sum_{l=0}^{N_{\text{toa}}-1} \text{MER}_{\text{SIC}}^{(p)}[l, m]. \quad (4.44)$$

To better understand the differences between our semi-analytical model and [dRHdG12], note that our model simplifies to the one from [dRHdG12] for  $S = 1$ ,



```

1: Initialization:  $\text{MER}_{\text{SIC}}^{(0)}[l, m] := 1$  for  $0 \leq l < N_{\text{toa}}$  and  $0 \leq m < N_{\text{pwr}}$ 
2: for processing pass  $p = 1$  to  $p_{\text{max}}$  do
3:   for power level  $m = N_{\text{pwr}} - 1$  down to  $0$  do
4:     for  $l = 0$  to  $N_{\text{toa}}/2 - 1$  do
5:       Compute interference power  $P_{\text{int,s}}^{(p)}[l, m]$  as per (4.40)
6:       Compute  $\text{MER}_{\text{SIC}}^{(p)}[l, m]$  as per (4.43)
7:       Compute interference power  $P_{\text{int,s}}^{(p)}[N_{\text{toa}} - 1 - l, m]$  as per (4.40)
8:       Compute  $\text{MER}_{\text{SIC}}^{(p)}[N_{\text{toa}} - 1 - l, m]$  as per (4.43)
9:     end for
10:   end for
11: end for

```

Figure 4.10. Pseudocode describing semi-analytical model for iterative SIC beacon message receiver.

$p_{\text{bl}}[l] = 0$ ,  $N_{\text{toa}} = 1$ ,  $\Delta l_{\text{max}} = 0$ ,  $\Lambda[0] = 1/2$  and  $g_{\text{toa}}[0] = 1$ . Furthermore, instead of (4.29), [dRHdG12] uses the MER(SINR) characteristic of a specific channel code with a fixed coding and modulation rate  $a$ . This precludes the optimization of  $a$  for maximum spectral efficiency.

#### 4.5.4 Discretization of Received Power and Message Arrival Time

To numerically evaluate  $\text{MER}_{\text{SIC}}^{(p)}[l, m]$ , the power levels  $P_{\text{rx},m}$  need to be selected appropriately. To this end, we choose  $N_{\text{pwr}} + 1$  transmitter-receiver distances  $r_m$ ,  $0 \leq m \leq N_{\text{pwr}}$ , and by means of (2.10), compute the power levels as

$$P_{\text{rx},m} = \frac{P_{\text{rx}}(r_m, r_s) + P_{\text{rx}}(r_{m+1}, r_s)}{2}. \quad (4.45)$$

The distances  $r_m$  are selected such that  $P_{\text{rx}}(r_{m+1}, r_s)/P_{\text{rx}}(r_m, r_s) = 0.1$  dB, starting at  $r_0 = r_s$  and going down to  $r_{N_{\text{pwr}}} = r_b/500$ . With the parameters given in Table 4.1, this requires  $N_{\text{pwr}} = 644$  power levels. Note that the selection of  $r_{N_{\text{pwr}}} = r_b/500$  as closest distance implies that messages from closer transmitters are always correctly decoded and canceled. In Section 4.5.5, we verify that the impact of this optimistic assumption on the presented results can be neglected. For the homogeneous node distribution of the 2-D model (cf. Section 2.5), the probability  $g_{\text{pwr}}[m]$  is obtained as

$$g_{\text{pwr}}[m] = \frac{r_m^2 - r_{m+1}^2}{r_s^2}. \quad (4.46)$$

We select the spacing  $T_{\text{toa}}$  such that (i)  $T_{\text{toa}} \leq T_{\text{msg}}/2$ , and (ii)  $N_{\text{toa}}\xi \geq 2$ . These two conditions are heuristic approaches to ensure (i) that the temporal correlation of  $\text{MER}_{\text{SIC}}^{(p)}[l, m]$  is not underestimated, and (ii) that very short periods of time with high MER do not lead to significant errors in the temporal average (4.44).

#### 4.5.5 Parameter Optimization for Maximum Spectral Efficiency

In this section, we employ the semi-analytical MER model of Section 4.5.3 and the discretization of power and time explained in Section 4.5.4 to compute the spectral efficiency of unslotted Aloha with SIC for the parameters given in Table 4.1. As a function of message duration, we determine the optimum sparsity which maximizes the spectral efficiency. Note that this is equivalent to determining the optimum coding and modulation rate  $a$ , since  $a$  depends on message duration and sparsity according to  $a = LS/(T_{\text{msg}}W_{\text{sys}})$ , cf. (4.31). Additionally, we investigate the per-aircraft message generation rate to be used for maximum spectral efficiency. Coinciding with the assumptions for Aloha with single-user receivers in Section 4.3, the message generation rate is assumed to be  $\lambda' = \tilde{k}/T_{\text{u,crit}}$ ,  $\tilde{k} \in \mathbb{N}$ . Similar to (4.11), the maximum possible node density can then be computed as

$$\rho_{\text{max,SIC}}(T_{\text{msg}}, S, \tilde{k}) = \sup \left\{ \rho : \left[ \overline{\text{MER}}_{\text{SIC}}^{(p_{\text{max}})}[m] \right]^{\tilde{k}} \leq \xi \quad \forall m : P_{\text{rx},m} \geq P_{\text{rx}}(r_{\text{b}}, r_{\text{s}}) \right\}, \quad (4.47)$$

where it is sufficient to check all power levels  $P_{\text{rx},m} \geq P_{\text{rx}}(r_{\text{b}}, r_{\text{s}})$  due to the fact that (2.10) is a nonincreasing function of distance. The maximum possible node density  $\rho_{\text{max,SIC}}(T_{\text{msg}}, S, \tilde{k})$  can be seen as a function of  $T_{\text{msg}}$ ,  $S$  and  $\tilde{k}$  as the calculation of  $\overline{\text{MER}}_{\text{SIC}}^{(p_{\text{max}})}[m]$  depends on these parameters. The spectral efficiency  $\eta_{\text{SIC}}(T_{\text{msg}}, S, \tilde{k})$  follows from the insertion of (4.47) into (2.21). The optimum sparsity  $S_{\text{opt}}(T_{\text{msg}})$ , which maximizes the spectral efficiency for given  $T_{\text{msg}}$ , can be computed as

$$S_{\text{opt}}(T_{\text{msg}}) = \arg \max_S \eta_{\text{SIC}}(T_{\text{msg}}, S, \tilde{k}). \quad (4.48)$$

Using the settings discussed in Section 4.5.4, the average MER according to (4.44) can be computed. Repeating this computation for different aircraft densities  $\rho$ , equations (4.47) and (4.48) can be solved numerically for a given value of  $p_{\text{max}}$  without particular difficulties. For the following results, the number of SIC processing passes is set to  $p_{\text{max}} = 6$ . We observed empirically that the MER reduction between  $p = 5$  and  $p = 6$  is negligible in all cases considered herein. This suggests that for the system parameters

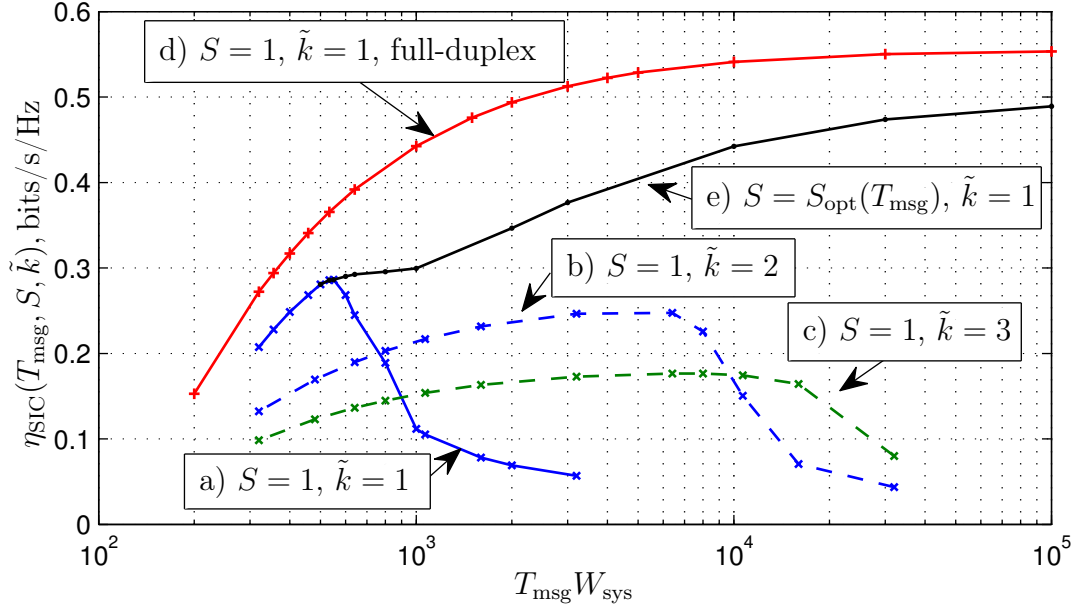


Figure 4.11. Nominal spectral efficiency of unslotted Aloha with SIC as a function of  $T_{\text{msg}}$ .

considered herein, the MER achieved with  $p_{\text{max}} = 6$  cannot be improved significantly by using  $p_{\text{max}} > 6$ . Unfortunately, the MER for  $p \rightarrow \infty$  is not known, which is why we have to rely on this empirical evidence.

For the parameters given in Table 4.1, the spectral efficiency obtained by inserting (4.47) into (2.21) is plotted in Figure 4.11. Without time hopping ( $S = 1$ ), the curves a), b) and c) for  $\tilde{k} \in \{1; 2; 3\}$  demonstrate that an increased beaconing rate ( $\tilde{k} > 1$ ) is not beneficial in the case of Aloha with SIC. When the message duration  $T_{\text{msg}}$  is selected to maximize the spectral efficiency, the maximum of curve a) ( $\tilde{k} = 1$ ) exceeds the maximum spectral efficiency obtained for  $\tilde{k} > 1$ . We therefore restrict attention to  $\tilde{k} = 1$  in the following.

To assess the impact of blanking and to obtain an upper bound of the spectral efficiency, results can be computed for the full-duplex case, i.e., under the assumption that nodes can transmit and receive simultaneously. To this end, we set  $p_{\text{bl}}[l] = 0$ ,  $0 \leq l < N_{\text{toa}}$ , instead of (4.37). The spectral efficiency for full-duplex radios and without time hopping is shown by curve d) in Figure 4.11. The effect of time hopping in the full-duplex case would be small, as it mainly mitigates the negative impact of blanking. Comparing curves a) and d), we observe that the efficiency loss incurred by blanking is only moderate at short  $T_{\text{msg}}$ , but grows with  $T_{\text{msg}}$ . While curve d) appears to grow monotonically with  $T_{\text{msg}}$  and to converge to some positive limit as  $T_{\text{msg}} \rightarrow \infty$ , curve a) exhibits a maximum at  $T_{\text{msg}} W_{\text{sys}} = 550$ , with an efficiency of  $\eta_{\text{SIC}}(T_{\text{msg}}, 1, 1) =$

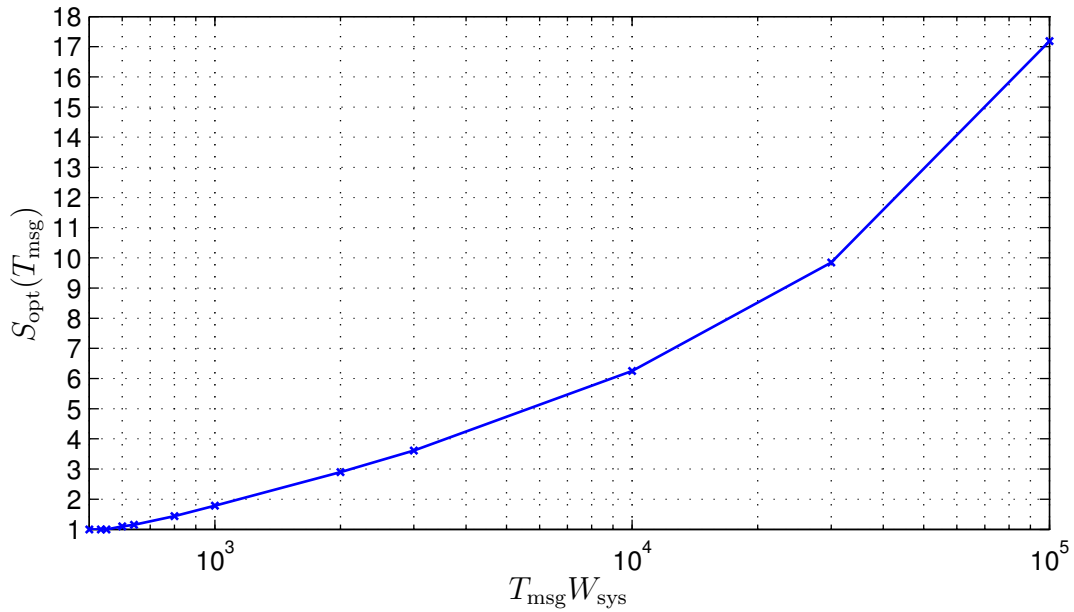


Figure 4.12. Optimal sparsity  $S_{\text{opt}}(T_{\text{msg}})$ ;  $\tilde{k} = 1$ .

0.29 bits/s/Hz. For  $T_{\text{msg}} W_{\text{sys}} > 550$ , curve a) decreases due to the growing impact of blanking at large  $T_{\text{msg}}$  and  $S = 1$ .

The spectral efficiency with optimal sparsity  $S_{\text{opt}}(T_{\text{msg}})$  according to (4.48) is shown by curve e) in Figure 4.11. While time hopping ( $S > 1$ ) is not able to improve the spectral efficiency for  $T_{\text{msg}} W_{\text{sys}} \leq 550$ , it drastically increases the spectral efficiency at longer message durations. Using  $S = S_{\text{opt}}(T_{\text{msg}})$ , the spectral efficiency shown by curve e) approaches curve d) and grows significantly larger than the maximum of curve a). For example, at  $T_{\text{msg}} W_{\text{sys}} = 30 \cdot 10^3$ , we obtained  $\eta_{\text{SIC}}(T_{\text{msg}}, S_{\text{opt}}(T_{\text{msg}}), 1) = 0.47$  bits/s/Hz. This result demonstrates that the adverse impact of blanking can be mitigated by time hopping. The optimal sparsity  $S_{\text{opt}}(T_{\text{msg}})$  is plotted in Figure 4.12, revealing that  $S_{\text{opt}}(T_{\text{msg}})$  grows with  $T_{\text{msg}}$  in the analyzed range  $500 \leq T_{\text{msg}} W_{\text{sys}} \leq 10^5$ .

In Figure 4.13, the spectral efficiency is plotted as a function of  $S$  for three message durations. As already indicated, the setting  $S = 1$  maximizes the spectral efficiency for  $T_{\text{msg}} W_{\text{sys}} = 500$ . At the longer message duration of  $T_{\text{msg}} W_{\text{sys}} = 2000$ , the spectral efficiency is maximized for  $S_{\text{opt}}(2000/W_{\text{sys}}) = 2.9$ , and the spectral efficiency with this optimal sparsity is about 5 times larger than the spectral efficiency without time hopping ( $S = 1$ ). When the message duration is increased further to  $T_{\text{msg}} W_{\text{sys}} = 30 \cdot 10^3$ , both the optimum sparsity  $S_{\text{opt}}(T_{\text{msg}})$  and the maximum spectral efficiency  $\eta_{\text{SIC}}(T_{\text{msg}}, S_{\text{opt}}, 1)$  are larger than at  $T_{\text{msg}} W_{\text{sys}} = 2000$ .

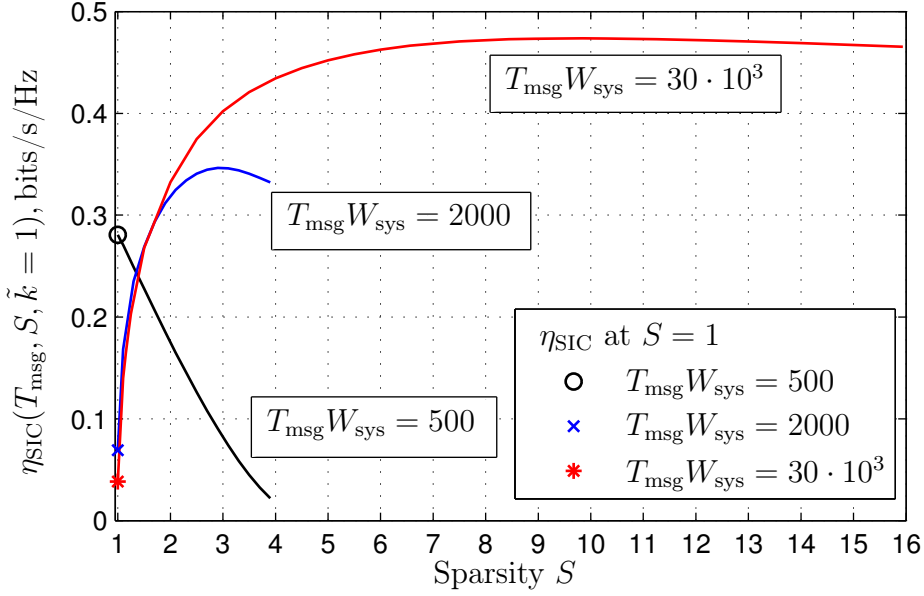


Figure 4.13. Nominal spectral efficiency of unslotted Aloha with SIC as a function of  $S$ , for different message lengths and  $\tilde{k} = 1$ .

Finally, Figure 4.14 shows  $\text{MER}_{\text{SIC}}^{(p)}[l, m]$  after different processing passes  $p$ . The error rate  $\text{MER}_{\text{SIC}}^{(p)}[l, m]$  is plotted as a function of  $t_l$  and distance  $r$  corresponding to each received power level  $P_{\text{rx},m}$  according to (2.10). The thick dashed contour lines indicate the distances at which  $\text{MER}_{\text{SIC}}^{(p)}[l, m] = 10^{-k}$ ,  $k \in \{0, 1, \dots, 6\}$ . The thick red line indicates the MER at  $r = r_b$ . In the example shown, the MER does not change noticeably anymore between  $p = 3$  and  $p = p_{\text{max}} = 6$ .

Due to the selection of received powers in Section 4.5.4, messages from transmitters closer than  $r_{N_{\text{pwr}}} = r_b/500$  have not been considered for the results just presented. The impact of this simplification on the results cannot be significant for the following reasons. The probability that more than one transmitter is closer than  $r_{N_{\text{pwr}}}$  to the receiver is negligible compared to the tolerable outage probability  $\xi$  in all cases considered above. This can be concluded from the Poisson distribution of nodes and the maximum tolerable node density  $\rho_{\text{max,SIC}}(T_{\text{msg}}, S, \tilde{k})$ . Hence, attention may be restricted to possible deterioration of the MER due to a single transmitter at a distance lower than  $r_{N_{\text{pwr}}}$ . Even without any interference cancellation, the messages of this transmitter experience a SINR which is always sufficient for decoding if no blanking has occurred, due to the high received power. Therefore, the only case which could make the MER worse than the presented results is the loss of messages from a single transmitter closer than  $r_{N_{\text{pwr}}}$  due to collisions with own transmissions. It can be shown that the probability for this case is negligible compared to  $\xi$ .

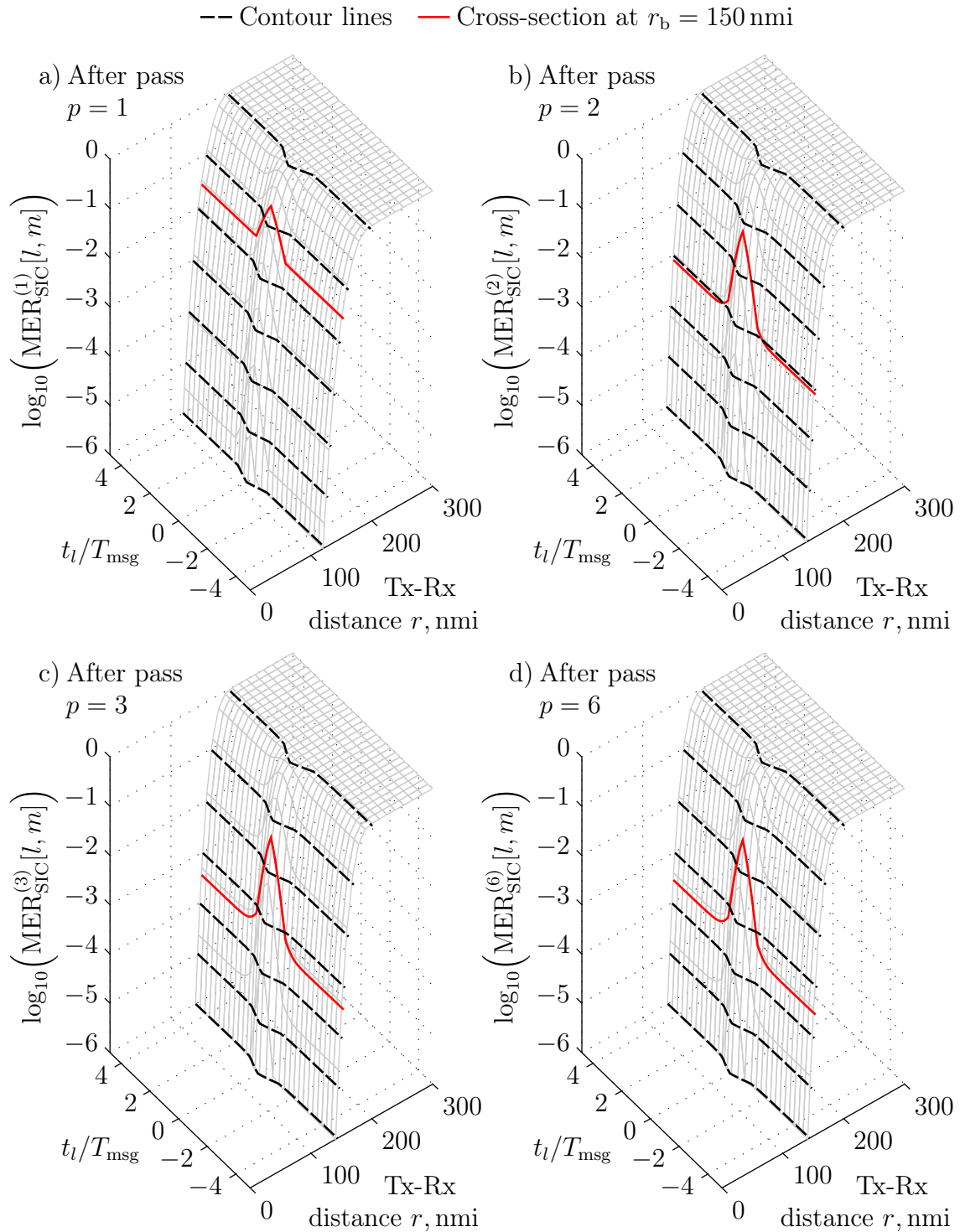


Figure 4.14. Message error rate after  $p$  processing passes.  $T_{\text{msg}}W_{\text{sys}} = 30 \cdot 10^3$ ,  $\tilde{k} = 1$ ,  $S = S_{\text{opt}}(T_{\text{msg}})$  and  $\rho = \rho_{\text{max,SIC}}(T_{\text{msg}}, S, \tilde{k})$ .

Table 4.3. Summary of the Results.

Beaconing Scheme	Spectral Efficiency, bits/s/Hz	Spectral Efficiency, relative to scheme 1
1) Unslotted Aloha, Single-User Rx	0.0353	1
2) CB-SOTDMA	0.79	22.4
3) Unslotted Aloha with SIC, $T_{\text{msg}}W_{\text{sys}} = 30 \cdot 10^3$	0.47	13.3

## 4.6 Selection of the Most Promising Beaconing Scheme

In Table 4.3, the spectral efficiencies derived in this chapter are summarized. For unslotted Aloha with SIC, a message duration of  $T_{\text{msg}} = 30$  ms is assumed, i.e.,  $T_{\text{msg}}W_{\text{sys}} = 30 \cdot 10^3$  (cf. Table 4.1). While a slight increase of the spectral efficiency has been observed for larger  $T_{\text{msg}}W_{\text{sys}}$ , it appears questionable whether longer messages would be acceptable at a critical data age of  $T_{\text{u,crit}} = 1$  s, given that the transmission delay cannot be lower than  $T_{\text{msg}}$ .

As the results reveal, both CB-SOTDMA and unslotted Aloha with SIC significantly outperform unslotted Aloha with single-user receivers. CB-SOTDMA provides a 68% higher spectral efficiency than unslotted Aloha with SIC. However, this gain is achieved at the expense of time synchronization between all aircraft. Methods which achieve this time synchronization in a reliable way as required in aeronautical communication (cf. point 5 in Section 2.7) would most likely degrade the spectral efficiency of CB-SOTDMA. Additionally, guard times were not considered in the semi-analytical model of CB-SOTDMA, and perfect message scheduling was assumed (cf. Section 4.4). We argue that it would be questionable whether a significant part of the spectral efficiency gain of 68% would remain once the issue of time synchronization is solved, guard times are accounted for and realistic message scheduling is considered. Therefore, we conclude that unslotted Aloha with SIC is the most promising beaconing scheme for future aeronautical applications, and focus on this beaconing scheme in the remainder of this work. In Chapter 6, the bandwidth required for the high volume of future aeronautical beaconing traffic is calculated for the beaconing system ICBT designed in Chapter 5 based on Aloha with SIC. As will be shown, this required bandwidth is quite moderate, which further supports the decision to use Aloha with SIC.





## Chapter 5

# Design of the Interference Canceling Beacon Transceiver

### 5.1 Introduction

In this chapter, we propose a novel aeronautical beaoning system, which we call the Interference Canceling Beacon Transceiver (ICBT). The design of ICBT is based on unslotted Aloha with SIC and is explained in the following. Going beyond the simplifying assumptions of Chapter 4, realistic mathematical models are used for the following effects and system components:

- message detection,
- estimation of message parameters such as Doppler shift  $f_{d,i}$ , arrival time  $t_{a,i}$  and complex channel coefficient  $\psi_i$  (cf. Section 2.4.2),
- interference cancellation,
- channel coding,
- receiver algorithm,
- received signal blanking due to own transmissions (cf. Section 2.4.3).

Section 5.2 gives an overview of the system concept and explains the receiver algorithm. In Section 5.3, we describe our main contributions with respect to time hopping, synchronization and IC. Section 5.4 discusses how the system parameters can be selected in practice, which completes the design of ICBT. Note that the design of ICBT is also described in a paper we recently submitted for publication [FS15].

### 5.2 Basic System Description

#### 5.2.1 Beaoning Link

To illustrate the system concept, we consider the transmission of message  $i$  from its transmitter to some other aircraft. Figure 5.1 shows a baseband model of this process.

The transmitter maps the  $L$  message bits onto  $L/a$  modulation symbols. The resulting symbol vector  $\mathbf{d}_0 \in \mathbb{C}^{L/a}$  is then pseudo-randomized through interleaving, scrambling and time hopping. Interleaving and scrambling are needed to enable the separation of several messages arriving at a receiver at similar time instances and with similar power levels [dRHdG09, dRHdG12]. As shown by the semi-analytical model of Aloha and SIC in Section 4.5, time hopping increases the spectral efficiency by reducing message loss during the receiving node's own transmissions. Due to time hopping, the message has a total length of  $N_{\text{all}} > L/a$  symbols. The transmitter has a pool of  $M$  different pseudo-randomization options, from which it randomly selects one for each message. Each pseudo-randomization option  $m$ ,  $1 \leq m \leq M$ , corresponds to a specific realization of interleaving, scrambling and time hopping. The interleaving pattern is defined by the permutation matrix  $\mathbf{\Pi}_m \in \mathbb{R}^{(L/a) \times (L/a)}$ , which shuffles the symbols in  $\mathbf{d}_0$ . The vector  $\mathbf{c}_m \in \mathbb{C}^{L/a}$  contains the scrambling sequence of unit-magnitude elements, and the time-hopping matrix  $\mathbf{T}_m \in \mathbb{R}^{N_{\text{all}} \times (L/a)}$  partitions the symbol vector into smaller zero-padded symbol bursts. The matrix  $\mathbf{T}_m$  is constructed by inserting  $N_{\text{all}} - L/a$  all-zero rows into an identity matrix of dimension  $(L/a) \times (L/a)$ , thus increasing its row count to  $N_{\text{all}}$ . For pseudo-randomization option  $m$ , the pseudo-randomized symbol vector  $\mathbf{d}_{\text{pr}} \in \mathbb{C}^{N_{\text{all}}}$  is constructed as

$$\mathbf{d}_{\text{pr}} = \mathbf{T}_m \text{diag}(\mathbf{c}_m) \mathbf{\Pi}_m \mathbf{d}_0, \quad (5.1)$$

where  $\text{diag}(\mathbf{c}_m)$  denotes a diagonal matrix with the elements of vector  $\mathbf{c}_m$  on its main diagonal.

To enable message detection at the receiver, it is necessary to include synchronization symbols into each ICBT message. To this end, for each randomization option  $m$ , a sparse vector  $\mathbf{s}_m \in \mathbb{C}^{N_{\text{all}}}$  containing  $N_{\text{sync}}$  synchronization symbols is created such that  $\mathbf{T}_m^T \mathbf{s}_m = \mathbf{0}$ . This implies that  $[\mathbf{s}_m]_{k'} = 0$  when  $[\mathbf{d}_{\text{pr}}]_{k'} \neq 0$ , where  $k' \in [0, \dots, N_{\text{all}} - 1]$  denotes the symbol index. The transmitted symbol vector  $\mathbf{q} \in \mathbb{C}^{N_{\text{all}}}$  is then obtained as

$$\mathbf{q} = \mathbf{d}_{\text{pr}} + \mathbf{s}_m. \quad (5.2)$$

The structure of the message  $\mathbf{q}$  is exemplified in Figure 5.2.

Once  $\mathbf{q}$  has been generated, the symbols are serialized and transmitted at a Nyquist symbol rate of  $1/T_s$ , using a continuous-time elementary baseband waveform  $u_{\text{tx}}(t)$ . Thus, the nominal message duration (cf. Section 2.4.2) is

$$T_{\text{msg}} = N_{\text{all}} T_s. \quad (5.3)$$

The baseband transmit signal  $g_i(t - t_{\text{tx},i})$  (cf. Section 2.4) can be represented as

$$g_i(t - t_{\text{tx},i}) = \sqrt{P_{\text{tx}}} \sum_{k'=0}^{N_{\text{all}}-1} q[k'] u_{\text{tx}}(t - t_{\text{tx},i} - k' T_s), \quad (5.4)$$

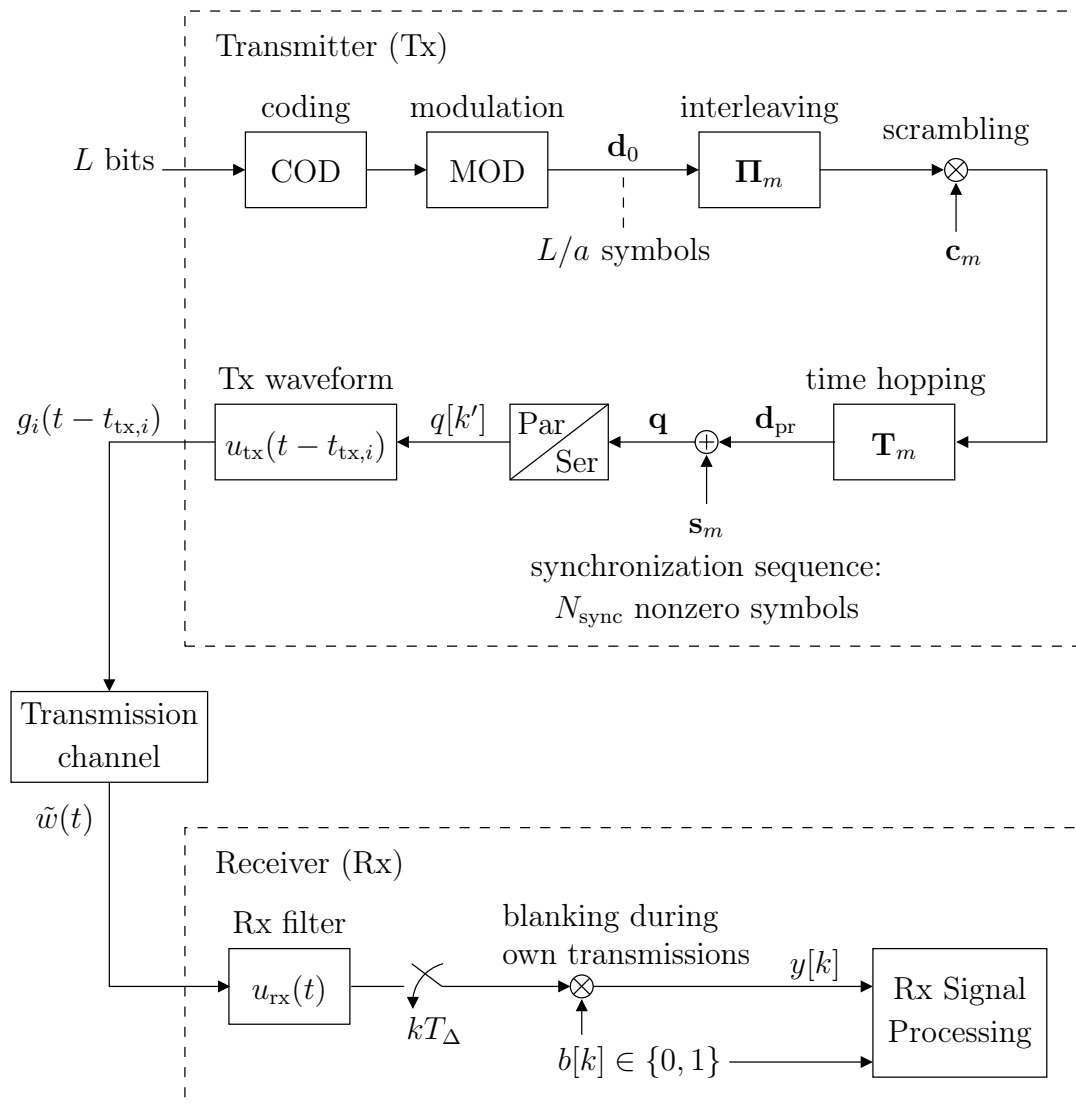


Figure 5.1. ICBT beacon message generation, transmission and reception in complex baseband.

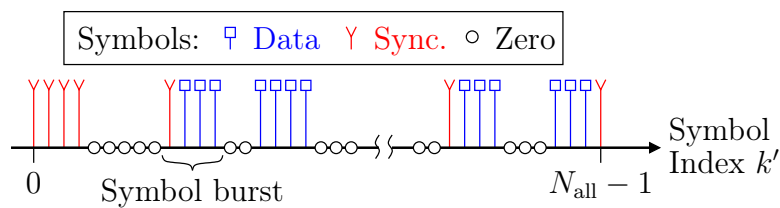


Figure 5.2. Composition of ICBT symbol vector  $\mathbf{q}$  of length  $N_{\text{all}}$ .

where  $q[k']$  denotes element  $k'$  of  $\mathbf{q}$ . We assume all data and synchronization symbols to be normalized such that  $E\{|q[k']|^2\} \in \{0, 1\}$ . Furthermore, we assume that  $u_{\text{tx}}(t)$  is dimensionless and normalized such that

$$\int_{-\infty}^{+\infty} |u_{\text{tx}}(t)|^2 dt = T_s. \quad (5.5)$$

The aforementioned two assumptions ensure appropriate scaling of the transmit signal such that the average transmitted energy per nonzero symbol is  $P_{\text{tx}}T_s$ . On its way to the receiver,  $g_i(t - t_{\text{tx},i})$  undergoes the propagation channel described in Section 2.4. The received signal  $\tilde{w}(t)$  is given by (2.17).

The receiver applies a filter with impulse response  $u_{\text{rx}}(t)$  to the received signal, and samples the resulting signal at a rate of  $1/T_\Delta = \kappa/T_s$ , where  $\kappa$  is the oversampling factor. Since typically, multiple messages with asynchronous and initially unknown symbol timing overlap at the receiver, it is not possible to synchronize the sampling instants to the symbol timing of a particular incoming message. For this reason,  $u_{\text{rx}}(t)$  is not selected as a filter matched to  $u_{\text{tx}}(t)$ . Instead, we design  $u_{\text{rx}}(t)$  as an anti-aliasing low-pass filter and oversample its output. The filtering necessary for decoding a particular message may then be performed on the sampled received signal after estimating required parameters such as the message arrival time. We address this additional filtering in more detail in Section 5.4.4.

According to (2.15), the receiver is impaired by very strong additive noise  $n_{\text{own}}(t)$  whenever its own transmit signal  $g_{\text{own}}(t)$  is nonzero. Obviously, this causes the loss of all samples received during the support of  $g_{\text{own}}(t) * u_{\text{rx}}(t)$ . The sequence  $y[k]$  of received samples available for further processing is thus obtained from the sampled receiver filter output by blanking the samples collected during own transmissions. This is modeled as a multiplication with a blanking sequence  $b[k]$ :

$$b[k] = \begin{cases} 0, & \text{if } kT_\Delta \in \text{supp}(g_{\text{own}}(t) * u_{\text{rx}}(t)), \\ 1, & \text{otherwise.} \end{cases} \quad (5.6)$$

Both  $y[k]$  and  $b[k]$  are used for further signal processing.

## 5.2.2 Receiver Signal Processing

In this section, we describe the receiver signal processing algorithm, i.e., the last block in the chain of blocks shown in Figure 5.1. In ICBT, signal processing at the receiver is largely based on the ideas described in [dRHdG09] and [dRHdG12], where Aloha with

SIC is applied to random access in the return link of a satellite communication system. In contrast to a receiver in a coordinated communication system, which processes a consecutive stream of incoming messages, ICBT applies SIC to process overlapping messages. To allow the receiver to decode and cancel stronger messages first, the received signal is processed in segments, called processing windows, within which the receiver can process messages in arbitrary order. Each processing window is processed in multiple processing passes, similar to the signal processing in the semi-analytical model described in Section 4.5. Within each processing pass, the receiver processes messages until it cannot detect any unprocessed message anymore. Message processing consists of three steps: (i) detection of the message with the highest SINR, (ii) decoding of the detected message, and (iii) cancellation of the channel response to the message from the received signal. In the same processing pass, each detected message is processed only once. If decoding fails, the respective message is excluded from further message detection attempts within this processing pass. Sometimes, a message which was already processed and could not be decoded becomes intelligible after other messages overlapping with this message are decoded and canceled. The reason for this is that the order of message processing relies on a realistic estimate of SINR and is therefore not always perfect. To mitigate this problem, the receiver performs multiple processing passes for each processing window, whereby a message which could not be decoded in one pass is processed again in the next pass.

Message detection relies on the function  $\beta_{\text{cs}}(k, f, m) \in \mathbb{R}_0^+$ , which is termed the coarse synchronization metric and indicates the likelihood that a message of randomization option  $m$  has been received with arrival time  $kT_\Delta$  (i.e., at sample index  $k$ ) and with a Doppler shift  $f$ . The computation of  $\beta_{\text{cs}}(k, f, m)$  will be considered later in Section 5.3.4. To understand the receiver algorithm, it is sufficient to know that messages with better SINR on average generate a larger peak in  $\beta_{\text{cs}}(k, f, m)$ . In processing window  $n$ , the coarse synchronization metric  $\beta_{\text{cs}}(k, f, m)$  is computed for the time interval  $k_{\text{offs}}[n] \leq k < k_{\text{offs}}[n] + L_{\text{win}}$ , where  $k_{\text{offs}}[n]$  is the first sample index in processing window  $n$  and  $L_{\text{win}}$  is the processing window length. With respect to Doppler, the metric  $\beta_{\text{cs}}(k, f, m)$  is only evaluated at discrete frequencies  $f = l\Delta f_{\text{cs}}$ ,  $l \in \mathbb{Z}$ , where  $\Delta f_{\text{cs}}$  denotes the coarse synchronization frequency step size. Considering only values of  $\beta_{\text{cs}}(k, l\Delta f_{\text{cs}}, m)$  larger than some detection threshold  $\Theta[k, m]$ , message detection within the current processing window is implemented by solving

$$\begin{aligned} (\hat{k}, \hat{l}, \hat{m}) &= \arg \max \beta_{\text{cs}}(k, l\Delta f_{\text{cs}}, m), \\ \text{s.t. } \beta_{\text{cs}}(\hat{k}, \hat{l}\Delta f_{\text{cs}}, \hat{m}) &> \Theta[\hat{k}, \hat{m}] \text{ and } k_{\text{offs}}[n] \leq \hat{k} < k_{\text{offs}}[n] + L_{\text{win}}. \end{aligned} \quad (5.7)$$

The threshold  $\Theta[k, m]$  depends on sample time and randomization option, and will be modified at runtime: After an unsuccessful decoding attempt, we set  $\Theta[k, \hat{m}] = \infty$

for  $|k - \hat{k}| \leq \Delta k_h$ , where  $\Delta k_h$  is the detection hold-off time in samples. This ensures that a peak in  $\beta_{cs}(k, f, m)$  at which an error is detected (e.g., through a checksum in the message) is ignored in subsequent evaluations of (5.7). The number of peaks exceeding the threshold is reduced in each message processing step, either through IC or by an additional detection holdoff period. At the beginning of each processing pass, the threshold is reset to  $\Theta[k, m] = \Theta_{ini}[k - k_{offs}[n]]$ , for  $0 \leq k - k_{offs}[n] < L_{win}$  and  $1 \leq m \leq M$ , with some initial threshold function  $\Theta_{ini}[k]$ . By resetting the threshold, we ensure that messages which could not yet be decoded are processed again in the next processing pass.

In total,  $p_{max}$  processing passes are performed for each processing window. Once all  $p_{max}$  processing passes are finished, the receiver moves on to the next processing window. Consecutive processing windows have to overlap to prevent increased message error rates at their borders. Denoting the length of this overlap by  $K_{win}$ , the window offset advances as

$$k_{offs}[n + 1] = k_{offs}[n] + L_{win} - K_{win}. \quad (5.8)$$

The receiver algorithm just described is depicted in Figure 5.3 as pseudo-code and as a flowchart, in which  $p \in \{1, \dots, p_{max}\}$  denotes the current processing pass. At the beginning of each processing window, the receiver needs to compute the coarse synchronization metric  $\beta_{cs}(k, f, m)$  for the whole processing window. Note that interference cancellation, i.e., the removal of the channel response to a decoded message from the received signal, modifies the memory of received samples  $y[k]$ . Therefore,  $\beta_{cs}(k, f, m)$  needs to be updated wherever it depends on the changed samples in  $y[k]$  after each interference cancellation step. Message processing, i.e., detection, decoding and interference cancellation, is handled by the inner loop of the algorithm, which is marked in the flowchart in Figure 5.3.

## 5.3 Special Challenges in Beaconing with Unslotted Aloha and SIC

### 5.3.1 Suitable Structure for Long and Sparse Messages

As indicated by the results in Section 4.5, the spectral efficiency of unslotted Aloha with SIC can be increased by using long and sparse messages to mitigate partial signal outage due to own transmissions. In practice, however, this approach creates a new

```

1: for processing window  $n = 1, \dots, \infty$  do
2:   Compute coarse sync. metric  $\beta_{cs}(k, l\Delta f_{cs}, m)$  for entire processing window  $n$ 
3:   for processing pass  $p = 1, \dots, p_{\max}$  do
4:     Reset threshold:  $\Theta[k, m] = \Theta_{\text{ini}}[k - k_{\text{offs}}[n]]$ 
5:     while solution  $(\hat{k}, \hat{l}, \hat{m})$  to (5.7) can be found do
6:       Try to decode the message at  $(\hat{k}, \hat{l}, \hat{m})$ 
7:       if new message decoded then
8:         Perform IC. This alters the memory of received samples  $y[k]$ .
9:         Update  $\beta_{cs}(k, l\Delta f_{cs}, m)$  where it depends on changed samples in  $y[k]$ .
10:      else
11:        Set hold-off:  $\Theta[k, \hat{m}] = \infty$  for  $|k - \hat{k}| \leq \Delta k_h$ 
12:      end if
13:    end while
14:  end for
15: end for

```

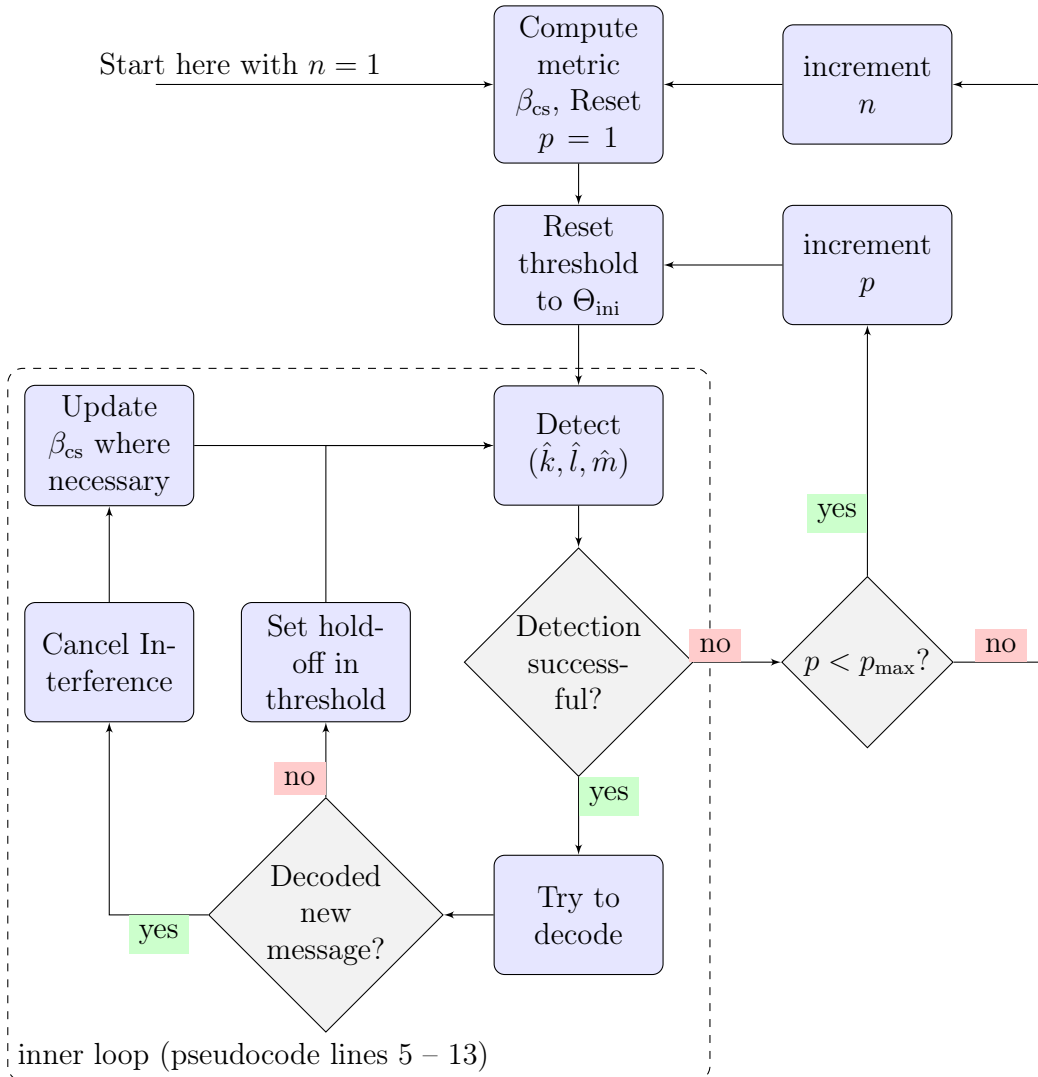


Figure 5.3. ICBT receiver algorithm pseudocode and flowchart.

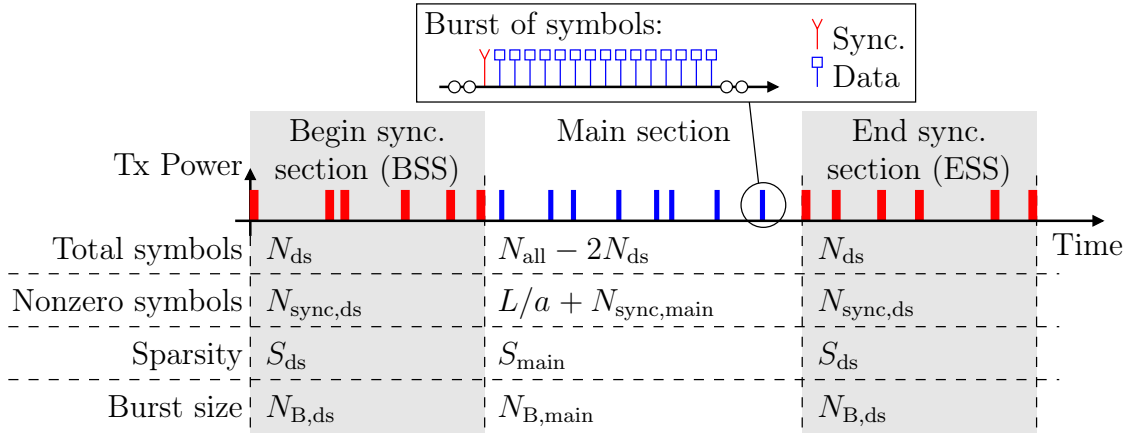


Figure 5.4. Sparse ICBT message structure with bursts of nonzero symbols. The magnified main section burst has one synchronization symbol in this example.

challenge: Longer message durations require a higher Doppler estimation accuracy for the coherent demodulation of data. In the following sections, we will explain how an appropriate time hopping scheme and high accuracy Doppler estimation can be realized for the ICBT message structure shown in Figure 5.4. Each message is composed of a main section enclosed by two dedicated synchronization sections, referred to as begin synchronization section (BSS) and end synchronization section (ESS). Both BSS and ESS contain  $N_{sync,ds}$  synchronization symbols and are filled with zeros to a total length of  $N_{ds}$  symbols. We employ BSS and ESS for two main reasons. First, as will be explained in Section 5.3.4, message detection benefits both from the short length  $N_{ds} \ll N_{all}$  and from the large temporal separation of BSS and ESS. Second, following the results of [WLJ93], concentrating signal energy at the beginning and end of the synchronization sequence  $\mathbf{s}_m$  improves the Doppler estimation accuracy. The main section of length  $N_{all} - 2N_{ds}$  contains the  $L/a$  data symbols and the remaining  $N_{sync,main} = N_{sync} - 2N_{sync,ds}$  synchronization symbols. As will be discussed in Section 5.4.5,  $N_{sync,main} > 0$  is necessary to avoid ambiguities in Doppler estimation. Note that the sparsities and burst sizes given in Figure 5.4 will be explained in Section 5.3.2.

### 5.3.2 Time Hopping

To implement time hopping,  $N_{all} - (L/a + N_{sync})$  zero symbols are inserted into each message. The nonzero symbols are transmitted in bursts as illustrated in Figure 5.4. Typically, the blanked time for a single transmitted symbol, i.e., the support of  $u_{tx}(t) * u_{rx}(t)$ , exceeds  $T_s$ . Hence, burst transmissions reduce the number of blanked samples in the received signal. For each randomization option  $m$ , a different, pseudo-random



distribution of the zero symbols is used. This increases the chance that during an own transmission, the blanked samples will fall into the zero-symbol segments of any incoming message, thus allowing message reception.

The sparsity  $S$  is given by the ratio of total symbols to nonzero symbols and can be computed as

$$S = \frac{N_{\text{all}}}{L/a + N_{\text{sync}}}. \quad (5.9)$$

Note that  $S$  denotes the overall sparsity of the whole message. Inside of the message, BSS and ESS have a sparsity of  $S_{\text{ds}}$ , while the main section has a sparsity of  $S_{\text{main}}$ . As will be discussed in Section 5.3.4, the computational effort of message detection can be reduced by decreasing  $S_{\text{ds}}$ .

The burst size in BSS and ESS is  $N_{\text{B,ds}}$  symbols, while a burst size of  $N_{\text{B,main}}$  symbols is used in the main section. If the number of nonzero symbols in a section is not an integer multiple of the burst size, then the symbols which remain after integer division are equally distributed over all bursts. We use  $N_{\text{B,ds}} > N_{\text{B,main}}$  in order to protect the BSS and ESS bursts against collision with the main section bursts of an own transmission. In the event of such a collision, only a part of the synchronization symbols in the affected BSS or ESS burst are lost due to blanking.

### 5.3.3 Hierarchical Synchronization Concept

In this section, we motivate the use of a hierarchical synchronization concept in ICBT. The insertion of synchronization symbols  $\mathbf{s}_m$  into each message serves two purposes: (i) message detection, and (ii) estimation of message and channel parameters, such as randomization option  $m$ , arrival time  $t_a$ , Doppler shift  $f_d$ , and complex channel amplitude  $\psi$ . In general, auto-correlation methods such as the Schmidl-Cox algorithm [SC97] can solve both problems. Yet, the performance of such auto-correlation methods degrades for  $\text{SINR} \ll 0$  dB [FWD<sup>+</sup>03]. For unslotted Aloha with SIC, the results of Section 4.5 predict the optimal  $a$  which maximizes the spectral efficiency. This optimal  $a$  is typically low enough to permit message decoding at  $\text{SINR} \ll 0$  dB (e.g.,  $a \approx 0.1$  at  $T_{\text{msg}}W_{\text{sys}} = 30 \cdot 10^3$ ), which only makes sense if message detection works for  $\text{SINR} \ll 0$  dB as well. Thus, the Schmidl-Cox algorithm would not deliver the required performance. Instead, we detect messages and estimate their parameters with a bank of filters matched to frequency-shifted replicas of the known synchronization sequences  $\mathbf{s}_m$  for each considered  $t_a$ . This corresponds to a two-dimensional grid search for  $t_a$  and  $f_d$ .

In a grid search, the accuracy of the obtained estimates directly depends on the size of the grid cells. The accuracy needed for the coherent demodulation of data requires a search cell size in frequency domain well below  $(N_{\text{all}}T_s)^{-1}$ . The bandwidth  $W_d$  between the highest and lowest  $f_d$  is given by (2.7). For large  $W_d N_{\text{all}}T_s$ , the number of filters required for a full search of  $W_d$ , i.e., the required number of search cells in frequency domain, becomes numerically prohibitive. Therefore, we propose a hierarchical approach with two stages. At the first stage, termed coarse synchronization, the metric  $\beta_{\text{cs}}(k, f, m)$  in (5.7) is designed to have a low frequency resolution. This allows us to use a frequency spacing (cell size)  $\Delta f_{\text{cs}} \gg (N_{\text{all}}T_s)^{-1}$  for message detection. The obtained coarse estimates  $(\hat{k}, \hat{l}, \hat{m})$  are then refined in the second stage, termed fine synchronization, where we increase the frequency resolution as needed for the coherent demodulation of data. In fine synchronization, attention may be restricted to a smaller search window centered on the coarse estimates. Note that similar hierarchical approaches have been successfully applied in other areas of signal processing, e.g., in multilevel image processing [TL94]. In the following two sections, we formulate both stages more formally.

### 5.3.4 Coarse Synchronization

Message detection with low frequency resolution can be accomplished through the incoherent combination of several short correlation filters [dRHdG12, JM13]. To this end, we use the two short synchronization sections BSS and ESS in each ICBT message (cf. Figure 5.4). Note that the large temporal separation of BSS and ESS lowers the chance of both being affected by, e.g., blanking.

Let  $x(t)$  stand for the transmitted waveform after the receiver filter, which can be obtained as

$$x(t) = \sqrt{P_{\text{tx}}} u_{\text{tx}}(t) * u_{\text{rx}}(t). \quad (5.10)$$

Furthermore, let  $s_m[k']$  denote element  $k'$  of  $\mathbf{s}_m$ . For a frequency shift  $f$  of the incoming message, the sequence  $\tilde{s}_{\text{BSS}}(k, f, m)$  of received samples for the BSS of randomization option  $m$  is given by

$$\tilde{s}_{\text{BSS}}(k, f, m) = \sum_{k'=0}^{N_{\text{ds}}-1} s_m[k'] x((k - \kappa k')T_{\Delta}) \exp(j2\pi f k T_{\Delta}). \quad (5.11)$$

The sequence  $\tilde{s}_{\text{ESS}}(k, f, m)$  of received samples for the ESS is similarly computed as

$$\tilde{s}_{\text{ESS}}(k, f, m) = \sum_{k'=N_{\text{all}}-N_{\text{ds}}}^{N_{\text{all}}-1} s_m[k'] x((k - \kappa k')T_{\Delta}) \exp(j2\pi f k T_{\Delta}). \quad (5.12)$$

Using these definitions, the correlation filter outputs  $\mu_{\text{BSS}}(k, f, m)$  for the BSS and  $\mu_{\text{ESS}}(k, f, m)$  for the ESS are given by

$$\begin{aligned}\mu_{\text{BSS}}(k, f, m) &= y[k] * \tilde{s}_{\text{BSS}}^*(-k, f, m) \text{ and} \\ \mu_{\text{ESS}}(k, f, m) &= y[k] * \tilde{s}_{\text{ESS}}^*(-k, f, m),\end{aligned}\tag{5.13}$$

respectively. The coarse synchronization metric is now computed as

$$\beta_{\text{cs}}(k, f, m) = \frac{|\mu_{\text{BSS}}(k, f, m)| + |\mu_{\text{ESS}}(k, f, m)|}{\sqrt{\hat{P}_{\text{BSS}}[k, m] + \hat{P}_{\text{ESS}}[k, m]}},\tag{5.14}$$

where the enumerator combines the filter outputs (5.13) according to the nonquadratic, noncoherent postintegration described in [JM13]. This incoherent combination needs to be normalized to account for the time-varying interference power. To this end, we employ the estimates  $\hat{P}_{\text{BSS}}[k, m]$  and  $\hat{P}_{\text{ESS}}[k, m]$  of the variance of  $\mu_{\text{BSS}}(k, f, m)$  and  $\mu_{\text{ESS}}(k, f, m)$ , respectively. We assume that these quantities do not depend on  $f$ , which holds as long as  $W_d T_s \ll 1$ . Under the assumption that  $N_0$  is known, we derive  $\hat{P}_{\text{BSS}}[k, m]$  and  $\hat{P}_{\text{ESS}}[k, m]$  from a running average of the received power  $|y[k]|^2$  over one message duration.

Due to the length of the correlation filters (5.11) and (5.12), the frequency resolution of (5.14) is proportional to  $(N_{\text{ds}} T_s)^{-1}$ . Using a frequency oversampling factor of  $\kappa_{\text{cs}}$ , the frequency spacing used in (5.7) is set to

$$\Delta f_{\text{cs}} = (N_{\text{ds}} T_s \kappa_{\text{cs}})^{-1}.\tag{5.15}$$

Note that  $\lceil W_d / \Delta f_{\text{cs}} \rceil$  different frequencies have to be considered in (5.7). Thus, for a constant number  $N_{\text{sync, ds}}$  of nonzero symbols in BSS and ESS, the computational effort of coarse synchronization grows linearly with  $N_{\text{ds}}$ . In practice,  $N_{\text{ds}}$  can be reduced by lowering the sparsity  $S_{\text{ds}}$ .

### 5.3.5 Fine Synchronization

To obtain refined estimates for  $t_a$  and  $f_d$ , we perform a grid search with increased frequency resolution, followed by interpolation in time and frequency to obtain sub-sample parameter estimates. The grid is restricted to a time and frequency window around the coarse estimates  $(\hat{k}, \hat{l}, \hat{m})$ . We coherently correlate a vector of received samples  $\mathbf{y} \in \mathbb{C}^{N_y}$  with frequency shifted replicas of the *entire* synchronization sequence  $\mathbf{s}_{\hat{m}}$ . As shown in Figure 5.5,  $\mathbf{y}$  contains samples  $y(k)$  in a window around sample index  $\hat{k}$ . To compensate errors in the coarse estimate  $\hat{k} T_s$  of  $t_a$ , and to account for the length

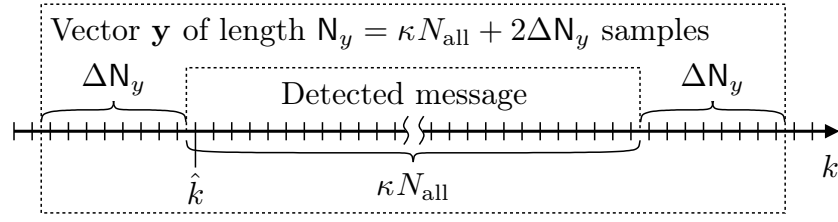


Figure 5.5. Interval of sampling times  $k$  which are cut out from  $y[k]$  to obtain  $\mathbf{y}$ .

of (5.10), the length  $N_y$  of  $\mathbf{y}$  is selected  $2\Delta N_y$  samples longer than a single message:

$$\mathbf{y} = \left[ y[\hat{k} - \Delta N_y], \dots, y[\hat{k} + \kappa N_{\text{all}} + \Delta N_y - 1] \right]^T. \quad (5.16)$$

To express the linear relationship between  $\mathbf{y}$  and the message symbol vector  $\mathbf{q}$ , we further introduce the matrix  $\mathbf{X}(t, f)$ , with element  $k, k'$  defined as:

$$\begin{aligned} [\mathbf{X}(t, f)]_{k, k'} &= x\left(\tilde{t}[k] - k'T_s - t\right) \exp\left(j2\pi f(\tilde{t}[k] - t)\right), \\ &\text{with } k \in [0, \dots, N_y - 1]; k' \in [0, \dots, N_{\text{all}} - 1], \end{aligned} \quad (5.17)$$

where  $\tilde{t}[k] = (\hat{k} - \Delta N_y + k)T_\Delta$  is the sampling time of element  $k$  in  $\mathbf{y}$ . Then, taking into account the channel model (2.4) and the blanking sequence (5.6),  $\mathbf{y}$  can be expressed as

$$\begin{aligned} \mathbf{y} &= \mathbf{B}(\psi \mathbf{X}(t_a, f_d) \mathbf{q} + \mathbf{n} + \mathbf{i}) \\ &= \psi \tilde{\mathbf{X}}(t_a, f_d) \mathbf{q} + \tilde{\mathbf{n}}, \end{aligned} \quad (5.18)$$

where  $\mathbf{B} = \text{diag}\left(b[\hat{k} - \Delta N_y + k]\right)$ ,  $k \in [0, \dots, N_y - 1]$ , describes the blanking operator, and  $\tilde{\mathbf{X}}(t_a, f_d) = \mathbf{B}\mathbf{X}(t_a, f_d)$  denotes the blanked version of  $\mathbf{X}(t_a, f_d)$ . Vector  $\tilde{\mathbf{n}} = \mathbf{B}(\mathbf{n} + \mathbf{i})$  is the effective noise at the output of the receiver filter. It includes the AWGN part  $\mathbf{n}$  and the interference part  $\mathbf{i}$ . Due to the oversampling,  $\mathbf{i}$  is generally not white. Thus, the effective noise needs to be whitened, which requires an estimate  $\hat{\Phi}_{\tilde{\mathbf{n}}\tilde{\mathbf{n}}}$  of the autocorrelation matrix  $\Phi_{\tilde{\mathbf{n}}\tilde{\mathbf{n}}} = E\{\tilde{\mathbf{n}}\tilde{\mathbf{n}}^H\}$ . The fine synchronization metric  $\beta_{\text{fs}}(t, f, \hat{m})$  is then computed as the magnitude of the correlation after noise whitening using the Moore-Penrose pseudoinverse  $\hat{\Phi}_{\tilde{\mathbf{n}}\tilde{\mathbf{n}}}^\dagger$ :

$$\beta_{\text{fs}}(t, f, \hat{m}) = \left| \mathbf{s}_{\hat{m}}^H \tilde{\mathbf{X}}(t, f)^H \hat{\Phi}_{\tilde{\mathbf{n}}\tilde{\mathbf{n}}}^\dagger \mathbf{y} \right|. \quad (5.19)$$

The grid search evaluates  $\beta_{\text{fs}}\left((\hat{k} + k)T_\Delta, \hat{l}\Delta f_{\text{cs}} + l\Delta f_{\text{fs}}, \hat{m}\right)$  for a finite range of integers  $k$  and  $l$  within an appropriate search interval. The frequency resolution of (5.19) is proportional to  $(N_{\text{all}}T_s)^{-1}$ . In contrast to (5.15), the fine synchronization frequency step size  $\Delta f_{\text{fs}}$  is thus set to

$$\Delta f_{\text{fs}} = (N_{\text{all}}T_s\kappa_{\text{fs}})^{-1}, \quad (5.20)$$

where  $\kappa_{\text{fs}}$  denotes the oversampling factor in frequency direction. Using 2-D quadratic interpolation around the maximum value on the search grid, the estimates  $\hat{t}_a$  for  $t_a$  and  $\hat{f}_d$  for  $f_d$  are then computed as

$$\left(\hat{t}_a, \hat{f}_d\right) = \arg \max_{t, f} \beta_{\text{fs}}(t, f, \hat{m}). \quad (5.21)$$

Neglecting the data symbols, i.e., assuming  $\mathbf{q} = \mathbf{s}_{\hat{m}}$ , and assuming Gaussian  $\tilde{\mathbf{n}}$  with  $\Phi_{\tilde{\mathbf{n}}\tilde{\mathbf{n}}} = \hat{\Phi}_{\tilde{\mathbf{n}}\tilde{\mathbf{n}}}$ , maximizing the correlation magnitude (5.19) as in (5.21) yields maximum-likelihood estimates for  $t_a$  and  $f_d$  [VT01].

With the result from (5.21), we can now define  $\hat{\mathbf{X}} = \tilde{\mathbf{X}}(\hat{t}_a, \hat{f}_d)$ , and compute the estimate  $\hat{\psi}$  of  $\psi$  as

$$\hat{\psi} = \left(\mathbf{s}_{\hat{m}}^{\text{H}} \hat{\mathbf{X}}^{\text{H}} \hat{\Phi}_{\tilde{\mathbf{n}}\tilde{\mathbf{n}}}^{\dagger} \hat{\mathbf{X}} \mathbf{s}_{\hat{m}}\right)^{-1} \mathbf{s}_{\hat{m}}^{\text{H}} \hat{\mathbf{X}}^{\text{H}} \hat{\Phi}_{\tilde{\mathbf{n}}\tilde{\mathbf{n}}}^{\dagger} \mathbf{y}. \quad (5.22)$$

To estimate  $\Phi_{\tilde{\mathbf{n}}\tilde{\mathbf{n}}}$ , we note that  $\Phi_{\tilde{\mathbf{n}}\tilde{\mathbf{n}}} = \mathbf{B}(\Phi_{ii} + \Phi_{nn})\mathbf{B}$ , with  $\Phi_{nn} = E\{\mathbf{nn}^{\text{H}}\}$  and  $\Phi_{ii} = E\{\mathbf{ii}^{\text{H}}\}$ . We assume  $\Phi_{nn}$  to be known, which requires knowledge of the noise power spectral density  $N_0$ . To estimate  $\Phi_{ii}$ , we assume that the interference power  $P_{\text{int}}[\hat{k}]$  is constant over the received signal window  $\mathbf{y}$ , but changes for different window positions  $\hat{k}$ . Then, we can write  $\Phi_{ii} = P_{\text{int}}[\hat{k}]\Phi_{ii,0}$ , with the Toeplitz matrix  $\Phi_{ii,0}$  given by

$$[\Phi_{ii,0}]_{k+\Delta k, k} = \frac{\int_{-\infty}^{\infty} x^*(t)x(t + \Delta k T_{\Delta})dt}{\int_{-\infty}^{\infty} |x(t)|^2 dt}. \quad (5.23)$$

An estimate  $\hat{P}_{\text{int}}[\hat{k}]$  for  $P_{\text{int}}[\hat{k}]$  can be derived by averaging over one message duration:

$$\hat{P}_{\text{int}}[\hat{k}] = \max \left( 0, \frac{\sum_{k=\hat{k}}^{\hat{k}+\kappa N_{\text{all}}-1} |y[k]|^2}{\sum_{k=\hat{k}}^{\hat{k}+\kappa N_{\text{all}}-1} b[k]} - N_0 \int_{-\infty}^{\infty} |u_{\text{rx}}(t)|^2 dt \right). \quad (5.24)$$

Note that the power of the message of interest is neglected in (5.24), which is not significant in our targeted setting with SINR  $\ll 0$ . Finally,  $\hat{\Phi}_{\tilde{\mathbf{n}}\tilde{\mathbf{n}}}$  can be computed as

$$\hat{\Phi}_{\tilde{\mathbf{n}}\tilde{\mathbf{n}}} = \mathbf{B} \left( \hat{P}_{\text{int}}[\hat{k}] \Phi_{ii,0} + \Phi_{nn} \right) \mathbf{B}. \quad (5.25)$$

### 5.3.6 Interference Cancellation

Once a message has been decoded, the interference it causes to other messages can be canceled. To this end, we extend a method described by Gallager in [Gal97]. The basic idea is to use a linear channel estimate based on knowledge of the received message, and to subtract the channel response to this message from the received signal  $\mathbf{y}$ . Due to the channel model (2.4), one could attempt to perform the method from [Gal97]

for a channel with one path of delay  $\hat{t}_a$  and Doppler shift  $\hat{f}_d$ . However, this can lead to insufficient IC, due to estimation errors in  $\hat{t}_a$  and  $\hat{f}_d$ . Therefore, we approximate the propagation channel (2.4) with discrete taps on a regular delay and Doppler grid [Bel63]. This allows us to regard the channel response to the message as an element of a linear subspace which we term the cancellation subspace. Vectors spanning this subspace are obtained from the responses of the channel taps to the message. The response  $\mathbf{x}_{ic}[k, l]$  from the tap at time  $\hat{t}_a + kT_\Delta$  and Doppler shift  $\hat{f}_d + l\Delta f_{ic}$  is given by

$$\mathbf{x}_{ic}[k, l] = \tilde{\mathbf{X}}\left(\hat{t}_a + kT_\Delta, \hat{f}_d + l\Delta f_{ic}\right)\hat{\mathbf{q}}, \quad (5.26)$$

where  $\hat{\mathbf{q}}$  is an estimate of the transmitted symbols and  $\Delta f_{ic} < (\mathbf{N}_y T_\Delta)^{-1}$  is the frequency step size of the cancellation subspace. Assuming that decoding failures are always detected, we have  $\hat{\mathbf{q}} = \mathbf{q}$ , since IC is only performed in case of decoding success. We now limit the cancellation subspace to the column span of the matrix  $\mathbf{X}_{ic}$  formed by all  $(2\Delta k_{ic} + 1)(2\Delta l_{ic} + 1)$  vectors from the set  $\{\mathbf{x}_{ic}[k, l] : (k, l) \in [-\Delta k_{ic}, \dots, +\Delta k_{ic}] \times [-\Delta l_{ic}, \dots, +\Delta l_{ic}]\}$ . Here,  $\Delta k_{ic}$  and  $\Delta l_{ic}$  are the maximum cancellation tap time and frequency offset, respectively. The channel response to the message can then be written as  $\mathbf{X}_{ic}\mathbf{h}$ , where  $\mathbf{h}$  is a channel coefficient vector. With the true parameters  $t_a$ ,  $f_d$  and  $\psi$ , the IC error  $\mathbf{y}_e$  can be expressed as

$$\mathbf{y}_e = \mathbf{X}_{ic}\mathbf{h} - \psi\tilde{\mathbf{X}}(t_a, f_d)\mathbf{q}. \quad (5.27)$$

Under the assumption of Gaussian noise and interference [dRHdG12] with autocorrelation  $\hat{\Phi}_{\tilde{n}\tilde{n}}$  according to (5.25), a maximum likelihood estimate of  $\mathbf{h}$  can be computed as

$$\begin{aligned} \hat{\mathbf{h}} &= \arg \min_{\mathbf{h}} (\mathbf{y} - \mathbf{X}_{ic}\mathbf{h})^H \hat{\Phi}_{\tilde{n}\tilde{n}}^\dagger (\mathbf{y} - \mathbf{X}_{ic}\mathbf{h}) \\ &= \left( \mathbf{X}_{ic}^H \hat{\Phi}_{\tilde{n}\tilde{n}}^\dagger \mathbf{X}_{ic} \right)^\dagger \mathbf{X}_{ic}^H \hat{\Phi}_{\tilde{n}\tilde{n}}^\dagger \mathbf{y}. \end{aligned} \quad (5.28)$$

IC updates the observation vector as  $\mathbf{y}_{new} = \mathbf{y} - \mathbf{X}_{ic}\hat{\mathbf{h}}$ , or equivalently,  $\mathbf{y}_{new} = \mathbf{C}\mathbf{y}$ , where  $\mathbf{C}$  is the cancellation matrix,

$$\mathbf{C} = \left( \mathbf{I} - \mathbf{X}_{ic} \left( \mathbf{X}_{ic}^H \hat{\Phi}_{\tilde{n}\tilde{n}}^\dagger \mathbf{X}_{ic} \right)^\dagger \mathbf{X}_{ic}^H \hat{\Phi}_{\tilde{n}\tilde{n}}^\dagger \right). \quad (5.29)$$

Note that the eigenvalues of  $\mathbf{C}$  are either one or zero. The space orthogonal to the columns of  $\hat{\Phi}_{\tilde{n}\tilde{n}}^\dagger \mathbf{X}_{ic}$  is the eigenspace associated with the eigenvalue 1, while the columns of  $\mathbf{X}_{ic}$  span the nullspace of  $\mathbf{C}$ . This means that  $\mathbf{C}$  removes all energy from the cancellation subspace of the decoded message. Due to this, multiplication with  $\mathbf{C}$  may be seen as a generalized form of blanking, where a certain linear subspace of the space of all possible received signals is blanked. Moreover, by inserting  $\hat{\mathbf{h}}$  from (5.28) in (5.27), the error term can be written as

$$\mathbf{y}_e = (\mathbf{I} - \mathbf{C})(\mathbf{y} - \psi\tilde{\mathbf{X}}(t_a, f_d)\mathbf{q}) - \mathbf{C}\psi\tilde{\mathbf{X}}(t_a, f_d)\mathbf{q}. \quad (5.30)$$

The first term in (5.30) is independent of the received power of the canceled message. Apart from thermal noise, it contains the distortion of other messages overlapping with  $\mathbf{y}$ , which occurs when such messages are not completely orthogonal to the columns of  $\hat{\Phi}_{\tilde{n}\tilde{n}}^\dagger \mathbf{X}_{\text{ic}}$ . The second term in (5.30) is proportional to the canceled message and describes its suppression. We can thus define the suppression factor  $\varepsilon$  as

$$\varepsilon = \frac{\|\mathbf{C}\tilde{\mathbf{X}}(t_a, f_d)\mathbf{q}\|^2}{\|\tilde{\mathbf{X}}(t_a, f_d)\mathbf{q}\|^2}. \quad (5.31)$$

Under idealized conditions,  $\varepsilon$  vanishes [Gal97]. Then, only the first term in (5.30) remains and  $\mathbf{y}_e$  becomes independent of the power of the message to be canceled. As shown by Monte-Carlo simulations in Section 6.3.7,  $\varepsilon$  can be practically very small so that the remaining power of a canceled message may be neglected.

## 5.4 Implementation Aspects and System Parameter Selection for ICBT

### 5.4.1 Introduction

To complete the design of ICBT, practical implementations and parameter choices are required for the functional blocks of the system concept introduced in Section 5.2 and Section 5.3. To this end, we discuss appropriate settings of symbol rate and message length in Section 5.4.2, before focusing on transmitted waveform and receiver filter in Section 5.4.3. Subsequently, Section 5.4.4 specifies coding and modulation. To select the sparsity and the coding and modulation rate, we employ the semi-analytical results from Section 4.5.5. Finally, we optimize the distribution of synchronization symbols in Section 5.4.5 and the detection threshold for coarse synchronization in Section 5.4.6.

### 5.4.2 Symbol Rate and Message Length

ICBT uses a symbol rate of  $1/T_s = 1$  MHz, which leads to a bandwidth comparable to the state of the art aeronautical beaconing system UAT (cf. Section 4.2). Whether  $T_s$  could be increased to decrease the bandwidth depends on the beaconing data traffic and is further analyzed in Section 6.5. To select the message length  $T_{\text{msg}}$ , we look at the semi-analytical results of Section 4.5.5. Figure 4.11 shows that with optimized sparsity, the spectral efficiency grows with  $T_{\text{msg}}$ , but also indicates that this growth

diminishes for long  $T_{\text{msg}}$ . For optimized sparsity, the spectral efficiency increases by only 3% when increasing the message length from  $T_{\text{msg}}W_{\text{sys}} = 3 \cdot 10^4$  to  $T_{\text{msg}}W_{\text{sys}} = 10^5$ . Note that we have  $T_{\text{msg}}W_{\text{sys}} = N_{\text{all}}$  under the assumption that  $W_{\text{sys}} = 1/T_s$ . While we do not consider the transmission delay in detail, it appears questionable whether the transmission delay would still be acceptable at a message length of more than  $10^5 \cdot T_s = 100$  ms, which is already 10% of the critical data age of  $T_{\text{u,crit}} = 1$  s (cf. Section 2.2). For the purposes of this work, we assume that  $T_{\text{msg}} \approx 30$  ms would still be acceptable in terms of transmission delay. Since the spectral efficiency could only be marginally increased by selecting  $T_{\text{msg}} \in (30 \text{ ms}, 100 \text{ ms}]$ , we select  $T_{\text{msg}} \approx 30$  ms in ICBT, i.e.,  $N_{\text{all}} \approx 3 \cdot 10^4$  symbols. The exact  $N_{\text{all}}$  is determined in later sections after appropriately designing the synchronization sequences  $\mathbf{s}_m$ .

### 5.4.3 Transmitted Waveform and Receiver Filter

The elementary waveform  $u_{\text{tx}}(t)$  used in ICBT is a root raised-cosine pulse with Nyquist rate  $1/T_s$  and roll-off factor  $1/2$  [Rap01]. A window function is applied to limit its length to  $4T_s$ . The transmitted power spectral density (PSD) results from the squared magnitude of the spectrum of  $u_{\text{tx}}(t)$  and is shown in Figure 5.6. The PSD in Figure 5.6 is normalized such that 0 dB corresponds to the average PSD within the nominal bandwidth of  $1/T_s$ , i.e., in the frequency range  $|f|T_s \leq 0.5$ . Note that  $W_{\text{sys}} = 1/T_s = 1$  MHz is the 3 dB bandwidth, and recall that the setting  $W_{\text{sys}} = 1$  MHz was already used in Chapter 4 (cf. Table 4.1). The parameters of  $u_{\text{tx}}(t)$  selected above are a good trade-off between the shape of the PSD and the signal duration. Outside of the nominal bandwidth, the PSD should ideally exhibit both a steep decay and low side lobes. A roll-off factor below  $1/2$  would lead to a steeper decay for  $|f|T_s \in [0.5, 1]$ , but would also increase the side lobes due to the limited duration of  $u_{\text{tx}}(t)$ . Increasing the duration of  $u_{\text{tx}}(t)$  would increase the number of samples blanked during an own transmission according to (5.6).

As explained in Section 5.2.1, the receiver filter  $u_{\text{rx}}(t)$  serves only as an anti-aliasing low-pass. To prevent excessive blanking, its duration should be short. Therefore, we employ  $u_{\text{rx}}(t) = (\kappa/T_s)u_{\text{tx}}(\kappa t)$ , which has a duration of only  $4T_s/\kappa$ , due to the limited length of  $u_{\text{tx}}(t)$ . According (5.6), around each nonzero symbol of an outgoing message, the received signal is blanked for the duration of (5.10), which is  $(4 + 4/\kappa)T_s$ . Note also that for  $\kappa \geq 2$ , the transfer function of  $u_{\text{rx}}(t)$  is approximately flat within the nominal signal bandwidth  $|f|T_s \leq 0.5$ . The desired signal spectrum will thus be only marginally distorted by  $u_{\text{rx}}(t)$ , especially for  $\kappa > 2$ .



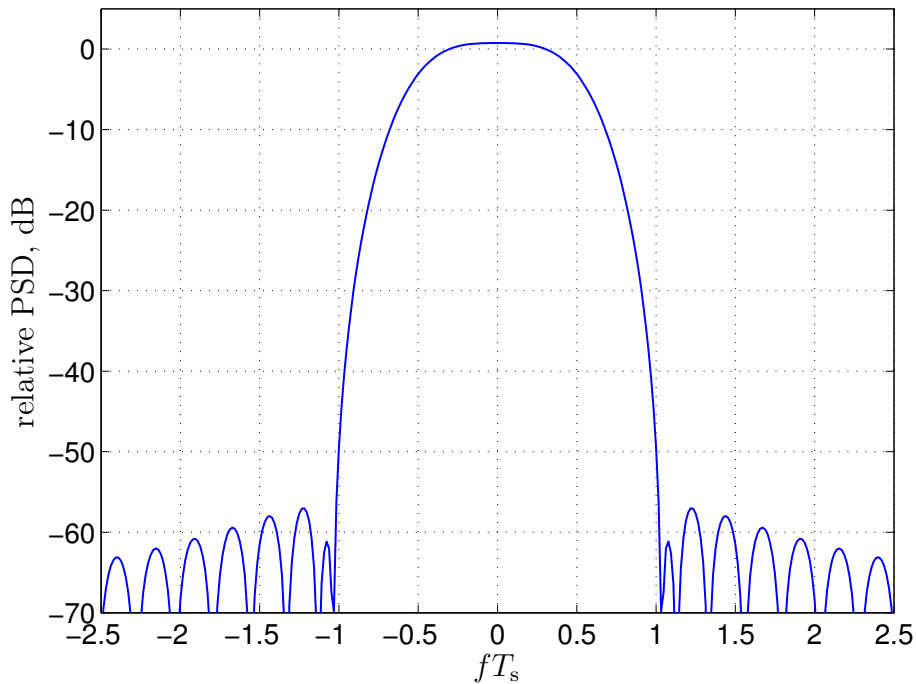


Figure 5.6. Power spectral density of the ICBT transmitted waveform  $u_{\text{tx}}(t)$ , relative to mean value in domain  $|f|T_s \leq 0.5$ .

#### 5.4.4 Coding and Modulation

For forward error correction, we employ a non-binary low-density parity check (LDPC) code with multiplicative repetition according to [KDPS11, PFD08]. The Galois field order is selected as  $2^8$ . The overall code may be seen as a serial concatenation of an outer and an inner code. The non-binary LDPC code serves as the outer code and the multiplicative repetition code represents the inner code. The non-binary LDPC code is regular, with a check node degree of 3 and variable node degree of 2 (code rate  $1/3$ ). Each codeword contains 40 bytes of information, which correspond to  $L = 320$  bits (cf. Section 2.2). The multiplicative repetition code multiplies each of the  $3 \cdot 40$  output bytes of the outer code with  $T_{\text{rep}} \in \mathbb{N}$  nonzero elements of the Galois field. This is equivalent to a binary  $(8T_{\text{rep}}, 8)$  block code. After coding, the bits are modulated onto quadrature phase shift keying (QPSK) symbols. The coding and modulation rate is thus  $a = 2/(3T_{\text{rep}})$ .

To select  $T_{\text{rep}}$ , we consider the results of Section 4.5.5 for our targeted message length of  $3 \cdot 10^4$  symbols and  $W_{\text{sys}} = 1/T_s$ . Ignoring the  $N_{\text{sync}}$  synchronization symbols, the sparsity is  $S = N_{\text{all}} \cdot a/L = 2N_{\text{all}}/(3T_{\text{rep}}L)$ . According to Figure 4.13, the optimum sparsity lies between the sparsities obtained with  $T_{\text{rep}} = 6$  and  $T_{\text{rep}} = 7$ , which are

$S = 10.4$  and  $S = 8.9$ , respectively. We use  $T_{\text{rep}} = 7$  in the following, which results in  $a = 2/21$  bits per data symbol and  $L/a = 3360$  data symbols per message.

To compute the likelihood  $\mathcal{L}(\mathbf{d}_{\text{pr}})$  of some pseudo-randomized symbol vector  $\mathbf{d}_{\text{pr}}$ , we assume that the fine synchronization estimates  $\hat{\mathbf{X}} = \tilde{\mathbf{X}}(\hat{t}_a, \hat{f}_d)$ ,  $\hat{\psi}$  and  $\hat{\Phi}_{\tilde{\mathbf{n}}\tilde{\mathbf{n}}}$  are correct and that  $\tilde{\mathbf{n}}$  is Gaussian. By subtracting the synchronization sequence from  $\mathbf{y}$ , we obtain  $\mathbf{y}' = \mathbf{y} - \hat{\psi}\hat{\mathbf{X}}\mathbf{s}_{\tilde{\mathbf{n}}}$ . Then, we have  $\mathcal{L}(\mathbf{d}_{\text{pr}}) \sim \exp\left(-(\mathbf{y}' - \hat{\psi}\hat{\mathbf{X}}\mathbf{d}_{\text{pr}})^{\text{H}}\hat{\Phi}_{\tilde{\mathbf{n}}\tilde{\mathbf{n}}}^{\dagger}(\mathbf{y}' - \hat{\psi}\hat{\mathbf{X}}\mathbf{d}_{\text{pr}})\right)$ . Neglecting inter-symbol interference (ISI) and exploiting the fact that all QPSK symbols have the same magnitude, we obtain

$$\log \mathcal{L}(\mathbf{d}_{\text{pr}}) = 2\text{Re}\left\{\mathbf{d}_{\text{pr}}^{\text{H}}(\hat{\psi}^*\hat{\mathbf{X}}^{\text{H}}\hat{\Phi}_{\tilde{\mathbf{n}}\tilde{\mathbf{n}}}^{\dagger}\mathbf{y}')\right\} + \tilde{c}, \quad (5.32)$$

where  $\tilde{c} \in \mathbb{R}$  stands for some constant independent of  $\mathbf{d}_{\text{pr}}$ . Finally, decoding is realized as in [KDPS11]. The required likelihood vectors for the encoded bytes can be obtained by inserting (5.1) into (5.32). Note that (5.32) applies a whitening matched filter to  $\mathbf{y}'$  in order to extract the data symbols of the desired message, thus performing the filtering required for decoding, as initially mentioned in Section 5.2.

Figure 5.7 shows the MER of the described code on an AWGN channel over  $E_s/N_0$ , where  $E_s$  refers to the energy received per modulated symbol. Note that the MER including fine-synchronization errors and the labels  $\xi$  and  $\gamma$  shown in Figure 5.7 will be discussed in Section 5.4.5. For the AWGN MER, perfect knowledge of all channel parameters and absence of ISI is assumed. The MER is displayed after 50 and 1000 belief propagation (BP) decoder iterations. As the MER reduction by the additional iterations is insignificant, a maximum of 50 BP iterations is used in the following. In Figure 5.7, we also show  $\Psi(E_s/N_0, 2/21)$  according to (4.2), which is an approximation of the smallest error rate achievable with the selected coding and modulation rate. The loss in  $E_s/N_0$  with respect to this fundamental limit is about 0.7 dB at  $\text{MER} = 10^{-3}$ .

Finally, let us explain why we do not use spreading, i.e., repeat each modulation symbol  $N_{\text{spread}}$  times, followed by scrambling. When the theoretically optimum  $a$  is low, using an increased coding and modulation rate  $a' = aN_{\text{spread}}$  together with spreading is a computationally inexpensive way to transmit  $a$  bits per symbol. In some cases, this strategy can reduce the computational effort of the decoder, at the expense of a small loss in  $E_s/N_0$ . For example, with the code design presented here, one could try to use only the inner, non-binary LDPC code to obtain  $a' = 2/3$  and additionally repeat each modulation symbol  $N_{\text{spread}} = T_{\text{rep}}$  times. Comparing the minimum achievable error rates  $\Psi(E_s/N_0, 2/21)$  and  $\Psi(7E_s/N_0, 2/3)$  shown in Figure 5.7, we observe that at  $T_{\text{rep}} = 7$ , the  $E_s/N_0$  required to achieve a certain MER would rise by about

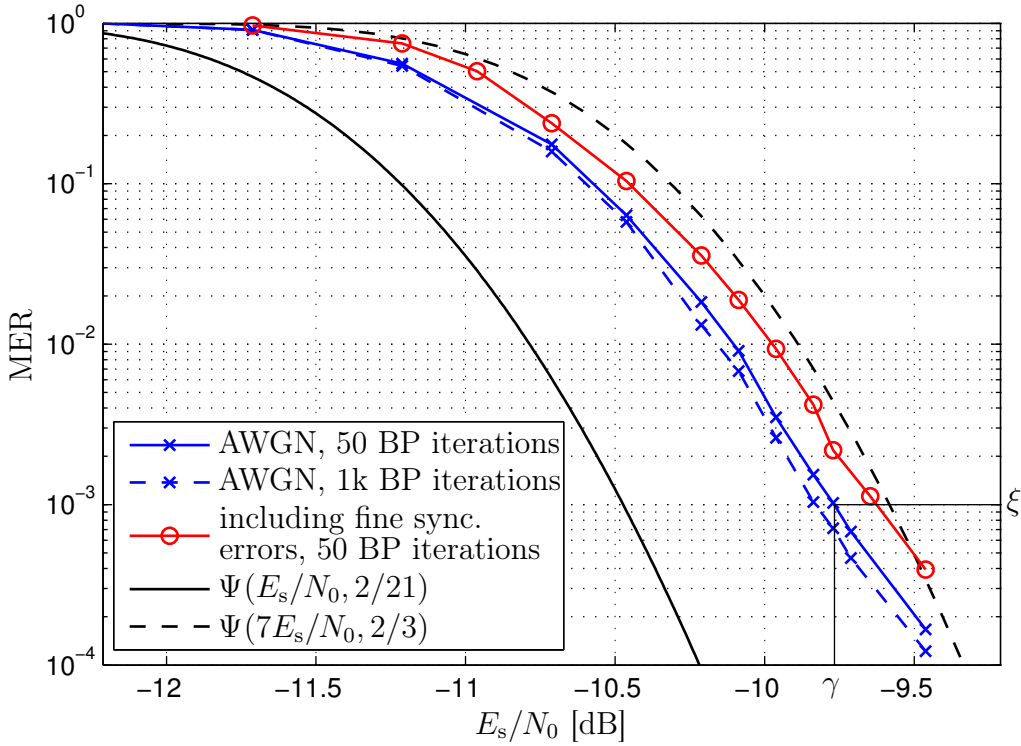


Figure 5.7. MER of the channel code used in ICBT, and approximation  $\Psi(E_s/N_0, 2/21)$  of the minimum possible MER for the AWGN channel, cf. (4.2).

0.9 dB if an ideal code of rate  $a = 2/21$  was replaced by an ideal code of rate  $a' = 2/3$  combined with  $N_{\text{spread}} = 7$ . While this loss in  $E_s/N_0$  may be seen as small, we do not use spreading for two reasons. First, for the combination of non-binary LDPC code and multiplicative repetition described above, the computational effort is almost independent of  $T_{\text{rep}}$  [KDPS11]. In fact, the computational effort for first despreading a spreading factor of  $N_{\text{spread}} = T_{\text{rep}}$  and then decoding only the inner code would not be much lower than the computational effort for decoding the original, multiplicatively repeated non-binary LDPC code. Second, to compensate the loss of 0.9 dB in decoding performance, the SINR must be increased by 0.9 dB. Since in ICBT, the SINR is dominated by interference, this can only be achieved by lowering the number of interfering nodes by  $1 - 10^{-0.09} = 19\%$ . The spectral efficiency would thus be reduced by 19%.

### 5.4.5 Synchronization Structure Optimization

In this section, we minimize  $N_{\text{sync,main}}$  for a given total number of synchronization symbols  $N_{\text{sync}}$ . This maximizes the SINR at the coarse synchronization filter outputs (5.13) and, with respect to Doppler shift, narrows the peak in the fine synchronization metric (5.19). The former facilitates message detection, the latter improves the Doppler

estimation accuracy [WLJ93]. Note that with  $N_{\text{sync,main}} = 0$ , the phase of an incoming message can only be observed during BSS and ESS. This gives rise to ambiguous frequencies, i.e., side lobes in (5.13), located at offsets from the true Doppler shift  $f_d$  which are integer multiples of  $1/\Delta T_{\text{BE}}$ , where  $\Delta T_{\text{BE}} = (N_{\text{all}} - N_{\text{ds}})T_s$  is the time difference between BSS and ESS. To avoid such Doppler ambiguities in fine synchronization,  $N_{\text{sync,main}} > 0$  synchronization symbols must be transmitted in the main section of each message. Thus, we intend to select the minimum  $N_{\text{sync,main}}$  for which the impact of ambiguities is acceptable. To quantify this impact, we consider the probability  $p_{\text{lfe}}$  (“large frequency error”) that the frequency estimate  $\hat{f}_d$  is closer to an ambiguous frequency than to the true  $f_d$  of the incoming message, computed as

$$p_{\text{lfe}} = \Pr\left(\left|f_d - \hat{f}_d\right| > (2\Delta T_{\text{BE}})^{-1}\right). \quad (5.33)$$

According to Section 4.5.5, an Aloha beaconing system with SIC should use the lowest possible beaconing rate  $\lambda' = 1/T_{\text{u,crit}}$ . In this case, the beaconing system must achieve  $\text{MER} \leq \xi$  for all messages from distances  $r \leq r_b$ . As a heuristic approach, we require that  $p_{\text{lfe}} \leq \xi/10$ , which ensures that only a small fraction of the MER is caused by large frequency synchronization errors. The smallest  $N_{\text{sync,main}}$  for which the condition  $p_{\text{lfe}} \leq \xi/10$  is fulfilled can be searched numerically.

For given synchronization sequences  $\mathbf{s}_m$ , the probability  $p_{\text{lfe}}$  can be determined by a simplified Monte-Carlo simulation of fine synchronization, which averages over message parameters  $(t_a, f_d, m)$  and noise realizations  $\tilde{\mathbf{n}}$ . The desired message is transmitted over the largest relevant distance  $r_b$  and the covariance  $\Phi_{\tilde{\mathbf{n}}\tilde{\mathbf{n}}}$  is adjusted to a certain SINR  $\gamma$ . From the AWGN results in Figure 5.7, we determine  $\gamma$  as the  $E_s/N_0$  for which  $\text{MER} = \xi$ . For messages from distances  $r \leq r_b$ , this choice of  $\gamma$  is the minimum acceptable SINR, as for  $\text{SINR} < \gamma$ , the channel code is not able to meet the error rate requirement anymore. We assume  $\hat{\Phi}_{\tilde{\mathbf{n}}\tilde{\mathbf{n}}} = \Phi_{\tilde{\mathbf{n}}\tilde{\mathbf{n}}}$  for the computation of  $p_{\text{lfe}}$ .

With  $\tilde{\mathbf{x}}_{k'}$  denoting column  $k'$  of  $\tilde{\mathbf{X}}(t_a, f_d)$ , the SINR on symbol  $k'$  can be computed as

$$\text{SINR}_{k'} = \left(\frac{r_{\text{ref}}}{r_b}\right)^\alpha \tilde{\mathbf{x}}_{k'}^H \Phi_{\tilde{\mathbf{n}}\tilde{\mathbf{n}}}^\dagger \tilde{\mathbf{x}}_{k'}, \quad (5.34)$$

where we assume perfect synchronization and no inter-symbol interference. Note that (5.34) varies with  $k'$  mainly due to blanking. By ignoring blanking in the Monte-Carlo simulation of  $p_{\text{lfe}}$ , we can use  $\Phi_{\tilde{\mathbf{n}}\tilde{\mathbf{n}}} = P_{\text{int}}\Phi_{ii,0} + \Phi_{nn}$  as a simplification of (5.25). Under this condition,  $\text{SINR}_{k'}$  is approximately constant in  $k'$ . With the known matrices  $\Phi_{ii,0}$  and  $\Phi_{nn}$ , we determine  $P_{\text{int}}$  such that  $\text{SINR}_{k'} = \gamma$ .

Table 5.1. Input Parameters for Optimization of Sync. Distribution.

Parameter	Symbol	Value
Number of information bits per message	$L$	320
Number of information bits per modulated symbol	$a$	2/21
Total number of synchronization symbols	$N_{\text{sync}}$	670
Sparsity factor in BSS & ESS	$S_{\text{ds}}$	5
Sparsity factor in main section	$S_{\text{main}}$	8
Min. number of symbols per burst in BSS & ESS	$N_{\text{B,ds}}$	32
Min. number of symbols per burst in main section	$N_{\text{B,main}}$	16
Number of randomization options	$M$	16
Time oversampling factor	$\kappa$	4
Frequency oversampling factor in fine sync.	$\kappa_{\text{fs}}$	8
Tolerable outage probability	$\xi$	$10^{-3}$
SNR at $r_b$	$\text{SNR}_b$	10 dB
Lowest SINR for decoding	$\gamma$	-9.77 dB

In the following, we discuss  $N_{\text{sync,main}}$  as determined for the parameters given in Table 5.1 and the waveforms  $u_{\text{tx}}(t)$  and  $u_{\text{rx}}(t)$  described in Section 5.4.3. The selected value of  $N_{\text{sync}} = 670$  corresponds to an overhead of 20% with respect to the 3360 data symbols. As simulation results in Section 6.3.6 will show, such a large value is required to achieve acceptable performance of coarse synchronization. According to the semi-analytical model of Section 4.5, which does not consider synchronization symbols, the optimal sparsity for our targeted message length of  $30 \cdot 10^3$  symbols is 9.8, cf. Figure 4.12. To accommodate the  $N_{\text{sync}} = 670$  synchronization symbols, we use a reduced sparsity of  $S_{\text{main}} = 8$  and  $S_{\text{ds}} = 5$ . The thermal noise is specified by the signal to noise ratio  $\text{SNR}_b$  (cf. Chapter 4). For the practical implementation considered here, it can be computed as

$$\text{SNR}_b = \left( \frac{r_{\text{ref}}}{r_b} \right)^\alpha \tilde{\mathbf{x}}_{k'}^H \mathbf{\Phi}_{nm}^\dagger \tilde{\mathbf{x}}_{k'}, \quad (5.35)$$

which corresponds to (5.34) with  $P_{\text{int}} = 0$ . With the chosen settings, we obtained  $N_{\text{sync,main}} = 190$ , which leads to a message length of  $N_{\text{all}} = 30800$ . For this solution, the complementary cumulative distribution function (CCDF) of the frequency error magnitude computed in a Monte-Carlo simulation is shown in Figure 5.8. It is represented as the phase error that accumulates over the time difference between BSS and ESS, i.e.,  $360^\circ |f_d - \hat{f}_d| \Delta T_{\text{BE}}$ . The probability  $p_{\text{ife}}$  is equivalent to the probability that this phase error exceeds  $180^\circ$ . As can be seen, this value is below  $\xi/10 = 10^{-4}$ .

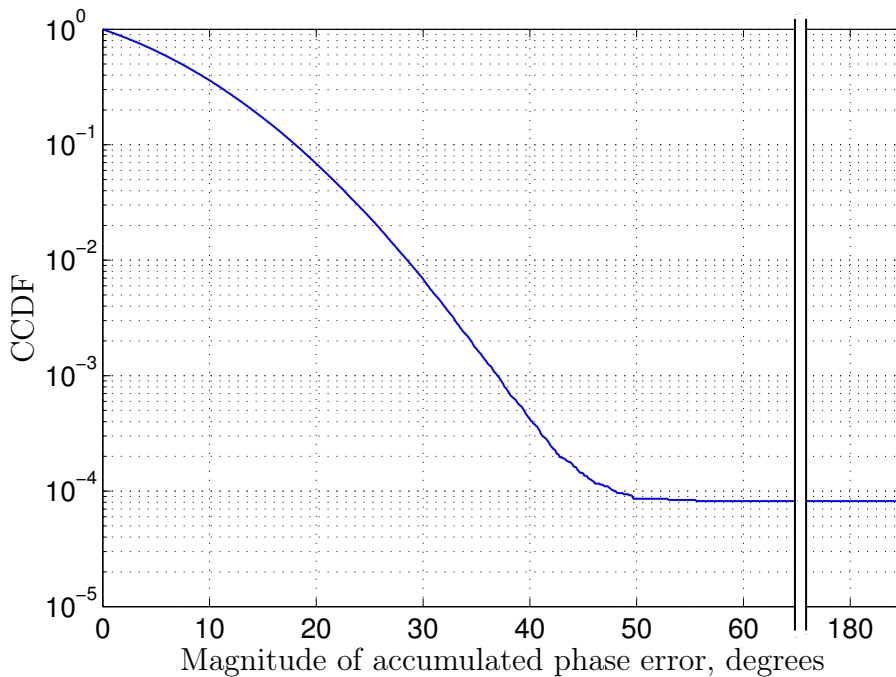


Figure 5.8. CCDF of the fine synchronization frequency error magnitude, represented as accumulated phase error over  $\Delta T_{\text{BE}}$ .

Finally, to show that the choice of  $N_{\text{sync}}$  is sufficiently large for parameter estimation in fine synchronization, fine synchronization and decoding have been jointly simulated to obtain the coded MER under realistic fine synchronization errors in  $\hat{t}_a$ ,  $\hat{f}_d$  and  $\hat{\psi}$ . In this simulation, we simplifyingly assumed that  $\Phi_{\tilde{n}\tilde{n}}$  was known to the receiver and that coarse synchronization (message detection) worked perfectly. The results are plotted in Figure 5.7, where the value of  $E_s/N_0$  on the horizontal axis indicates the SINR for which the results are valid. The loss with respect to the pure AWGN case is reasonably small.

#### 5.4.6 Initial Detection Threshold for Coarse Synchronization

We define the initial detection threshold for coarse synchronization (cf. Section 5.2.2) as

$$\Theta_{\text{ini}}[k] = \Theta_{\text{b}} \max \left\{ 1; 1 + \frac{k - L_{\text{win}} + 1 + L_{\text{rise}}}{L_{\text{rise}}} \right\}, \quad (5.36)$$

where  $\Theta_{\text{b}}$  is the threshold baseline and  $L_{\text{rise}}$  is the length of the threshold rise interval at the end of the processing window. The increased threshold at the end of the processing window ensures that weaker messages in this region are only processed after advancing to the next processing window. These messages are typically corrupted by

strong messages from the following processing window, which can only be decoded and canceled once the processing window is advanced. Increasing the threshold at the end of the processing window merely saves processing resources by minimizing unsuccessful decoding attempts.

The threshold baseline  $\Theta_b$  must be carefully selected such that the rate of undetected messages from sources closer than  $r_b$  is acceptable and the rate of false alarms stays low. As a theoretical analysis of the optimal  $\Theta_b$  is challenging, here we use a simplified Monte-Carlo simulation to determine the probability of a message miss in coarse synchronization. To this end, an incoming message is simulated with arrival time  $t_a = T_\Delta/2$  and with Doppler shift  $f_d = \Delta f_{cs}/2$ , i.e., with the largest possible offset to the time and frequency grid used in coarse synchronization. No blanking is assumed and the same assumptions about noise and interference as in Section 5.4.5 are used, albeit with SINR = -9.62 dB. At this SINR, the MER including errors of fine synchronization and channel estimation reaches  $\xi = 10^{-3}$ , cf. Figure 5.7. Under these conditions, we determine the probability that the coarse synchronization metric stays below  $\Theta_b$  at all four sampling points surrounding the true  $t_a$  and  $f_d$ . This means that for  $(k, l) \in \{0, 1\} \times \{0, 1\}$ , we simulate the missed detection probability  $p_{\text{md}} = \Pr(\max_{k,l} \beta_{cs}(k, l\Delta f_{cs}, m) \leq \Theta_b)$ . Then, we minimize  $\Theta_b$  subject to  $p_{\text{md}} \leq \xi/10$  in order to limit the impact of missed messages on the system performance. For the parameters given in Section 5.4.5 and a coarse synchronization frequency oversampling of  $\kappa_{cs} = 4$ , this leads to  $\Theta_b = 3.51$  (or, in dB:  $20 \log_{10} \Theta_b = 10.9$ ).

Figure 5.9 exemplifies message detection in a processing window. The parameters used here are  $L_{\text{rise}} = 2N_{\text{all}}\kappa$  and a window length of  $L_{\text{win}} = 9N_{\text{all}}\kappa$ . Figure 5.9a shows the arrival time of all incoming messages and the distance to the transmitter of each message. Some messages have already been decoded, while others are yet to be processed. The high number of decoded messages at the beginning of the processing window is mainly due to messages already decoded in the preceding processing window, in the region where both windows overlap. In the example shown, the communication range  $r_b$  is  $0.3r_s$ . The product of user density  $\rho$  and message transmission rate  $\lambda'$  is so high that the receiver cannot typically “see” further away than  $r_b$  due to interference. Figure 5.9b shows the coarse synchronization metric for the current situation, maximized over frequency and randomization option, i.e.,  $\max_{l,m} \beta_{cs}(k, l\Delta f_{cs}, m)$ . The synchronization threshold  $\Theta_{\text{ini}}[k]$  computed according to (5.36) is shown as well. In the considered processing window, the receiving node transmitted one message, which is marked by a gray bar in the background of Figure 5.9. Due to time hopping, the received signal is only partially lost during this own transmission, which is why overlapping messages can be decoded.

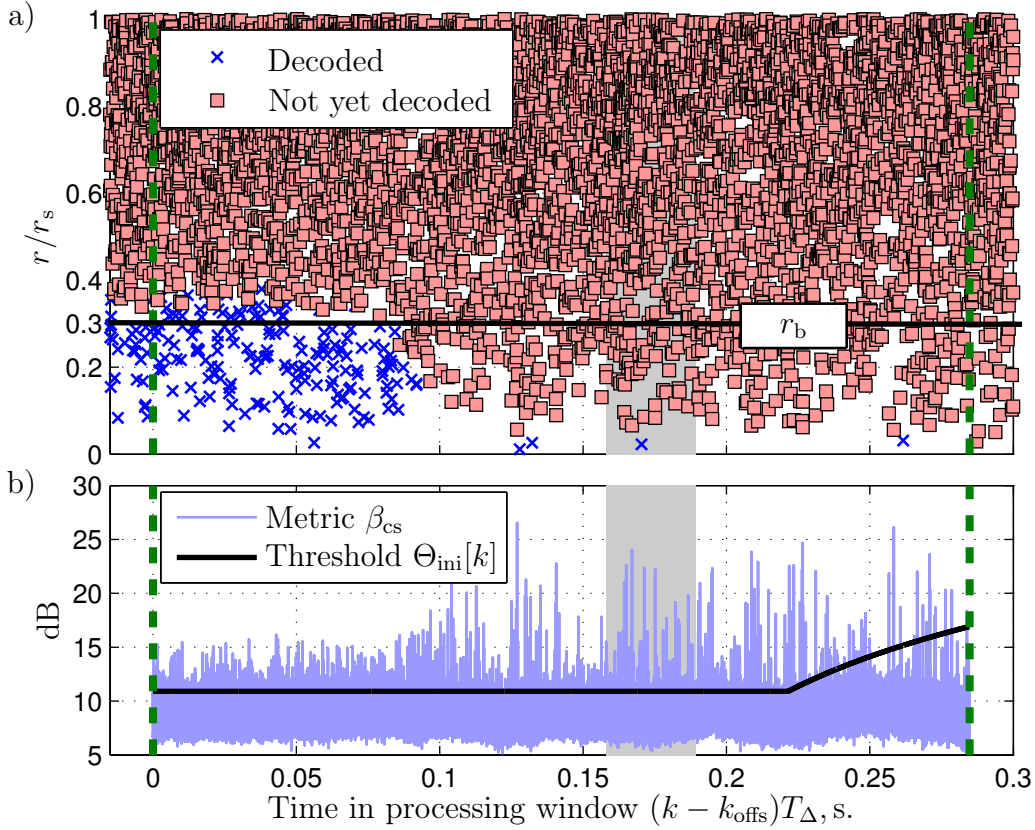


Figure 5.9. (a) Typical ICBT receiver progress, (b) corresponding coarse synchronization metric. Gray bar: blanks due to outgoing transmission. Vertical broken lines: current processing window. a), b) share horizontal axis.

#### 5.4.7 ICBT System Parameter Summary

The system parameters we propose for ICBT are summarized in Table 5.2. As explained in the previous sections, the message generation rate  $\lambda'$ , the coding and modulation rate  $a$ , the number  $N_{\text{all}}$  of symbols per message, as well as the sparsity  $S$  could be selected to maximize the spectral efficiency according to the semi-analytical model from Section 4.5. Note that the parameter choices for the detection threshold baseline  $\Theta_b$ , the number of processing passes  $p_{\text{max}}$  and the number of synchronization symbols  $N_{\text{sync}}$  will be verified by simulations in Chapter 6.



Table 5.2. ICBT System Parameters

## (a) Transmitter Parameters

Parameter	Symbol	Value
Message generation rate	$\lambda'$	$T_{u,\text{crit}}^{-1} = 1 \text{ Hz}$
Number of information bits per message	$L$	320
Number of information bits per modulated symbol	$a$	2/21
Symbol interval	$T_s$	1 $\mu\text{s}$
Total number of synchronization symbols	$N_{\text{sync}}$	670
Number of synchronization symbols in main section	$N_{\text{sync,main}}$	190
Sparsity factor in BSS & ESS	$S_{\text{ds}}$	5
Sparsity factor in main section	$S_{\text{main}}$	8
Overall sparsity factor	$S$	7.6
Total number of symbols per message, incl. zeros	$N_{\text{all}}$	30800
Min. number of symbols per burst in BSS & ESS	$N_{\text{B,ds}}$	32
Min. number of symbols per burst in main section	$N_{\text{B,main}}$	16
Number of randomization options	$M$	16

## (b) Receiver Parameters

Parameter	Symbol	Value
Time oversampling factor	$\kappa$	4
Frequency oversampling factor in coarse sync.	$\kappa_{\text{cs}}$	4
Frequency oversampling factor in fine sync.	$\kappa_{\text{fs}}$	8
Doppler search range	$W_d$	4 kHz
Processing window length (in samples)	$L_{\text{win}}$	$9N_{\text{all}}\kappa$
Processing window overlap (in samples)	$K_{\text{win}}$	$3N_{\text{all}}\kappa$
Detection threshold baseline	$\Theta_b$	10.9 dB
Threshold rise interval (in samples)	$L_{\text{rise}}$	$2N_{\text{all}}\kappa$
Holdoff after decoding failure (in samples)	$\Delta k_h$	$4\kappa$
Number of processing passes	$p_{\text{max}}$	2
IC frequency step size	$\Delta f_{\text{ic}}$	$(4N_{\text{all}}T_s)^{-1}$
IC max. time offset (in samples)	$\Delta k_{\text{ic}}$	3
IC max. frequency offset (in multiples of $\Delta f_{\text{ic}}$ )	$\Delta l_{\text{ic}}$	3



---

## Chapter 6

# Simulation of ICBT under Real-World Effects

### 6.1 Introduction

This chapter focuses on Monte-Carlo simulations computing the MER and the spectral efficiency of the beaconing system ICBT designed in Chapter 5. Under the 2-D aircraft distribution and movement model according to Section 2.5, we analyze the influence of selected system parameters on the spectral efficiency of ICBT. Additionally, the MER and the spectral efficiency of ICBT are compared to the MER and the spectral efficiency predicted by the semi-analytical model of Aloha with SIC. Finally, we investigate the performance of ICBT under a realistic 3-D model of future air traffic.

In Section 6.2, we explain how certain realistic effects relevant to the performance of ICBT can be included in the semi-analytical model of Aloha with SIC developed in Section 4.5. In Section 6.3, we compute the MER and the spectral efficiency of ICBT under the 2-D model, compare ICBT to the semi-analytical model, and analyze the influence of selected system parameters on ICBT. In Section 6.4, we derive a realistic 3-D model of air traffic from flight schedules and predictions of future air traffic growth available from the literature. Monte-Carlo simulations of the MER in the realistic 3-D air traffic model are presented in Section 6.5 to demonstrate that ICBT can fulfill the demands of future air traffic.

### 6.2 Extended Semi-Analytical Model of Aloha with SIC

One goal of this chapter is to compare the semi-analytical model of Aloha with SIC (cf. Section 4.5) to the results of Monte-Carlo simulations of ICBT. For the sake of comparability to the other semi-analytical models discussed in Chapter 4, the semi-analytical model of Aloha with SIC neglects certain effects. In the following, the semi-analytical model of Aloha with SIC is extended to include the following three effects, which have a significant impact on the performance of ICBT:

- The use of a whitening matched filter in the receiver, which takes into account the frequency-dependent power spectral density of the interference.

- The loss in  $E_s/N_0$  of the realistic channel code (cf. Section 5.4.4) as compared to the theoretically optimum coding and modulation assumed in the semi-analytical model.
- The additional interference introduced by the  $N_{\text{sync}}$  synchronization symbols contained in each message.

The aforementioned effects can be integrated into the semi-analytical model of Aloha with SIC merely by modifying some underlying equations, i.e., without any changes to the algorithm shown in Figure 4.10.

To account for the use of a whitening matched filter in the receiver, we derive the SINR at the correct sampling time behind such a filter for a symbol which is not affected by blanking. For this derivation, the receiver input signal  $\tilde{w}(t)$  (cf. Figure 5.1 and Figure 2.4) is assumed to be  $\tilde{w}(t) = \sqrt{P_{\text{rx},m}}u_{\text{tx}}(t) + i(t) + n(t)$ , where  $\sqrt{P_{\text{rx},m}}u_{\text{tx}}(t)$  is a single symbol of a desired message received at  $t = 0$  with power  $P_{\text{rx},m}$ , and  $i(t)$  denotes the multiple-access interference. Since the power spectral density  $\Phi_{ii}(f)$  of the interference must be proportional to  $|U_{\text{tx}}(f)|^2$ , where  $U_{\text{tx}}(f)$  denotes the Fourier transform of  $u_{\text{tx}}(t)$ , and since  $\int_{-\infty}^{\infty} |U_{\text{tx}}(f)|^2 df = T_s$  follows from (5.5), we have

$$\Phi_{ii}(f) = P_{\text{int}} \frac{|U_{\text{tx}}(f)|^2}{T_s}, \quad (6.1)$$

where  $P_{\text{int}}$  stands for the interference power. Inserting  $W_{\text{sys}} = 1/T_s$  into (4.1), we obtain  $\text{SNR}_{\text{b}} = P_{\text{rx}}(r_{\text{b}}, r_{\text{s}})T_s/N_0$ , which is equivalent to the SNR at the correct sampling time at the output of a matched filter for a single symbol transmitted from a sender at distance  $r_{\text{b}}$  to the receiver. The power spectral density of the AWGN can thus be written as  $N_0 = \text{SNR}_{\text{b}}^{-1}P_{\text{rx}}(r_{\text{b}}, r_{\text{s}})T_s$ . The SINR behind a whitening matched filter without blanking can be computed as

$$\text{SINR}_{\text{wf}}(P_{\text{rx},m}, P_{\text{int}}, \text{SNR}_{\text{b}}) = \int_{-\infty}^{\infty} \frac{P_{\text{rx},m}|U_{\text{tx}}(f)|^2}{\text{SNR}_{\text{b}}^{-1}P_{\text{rx}}(r_{\text{b}}, r_{\text{s}})T_s + P_{\text{int}} \frac{|U_{\text{tx}}(f)|^2}{T_s}} df. \quad (6.2)$$

The loss in  $E_s/N_0$  of the realistic channel code is accounted for by dividing the SINR by a loss factor  $\delta_{\text{code}}$ . To consider both the whitening matched filter and the coding loss in the extended semi-analytical model (ESAM) of Aloha with SIC, we reformulate  $\text{MER}_{\text{cnd}}^{(p)}[l, m|k]$  given by (4.41). Instead of the original  $\text{MER}_{\text{cnd}}^{(p)}[l, m|k]$ , the ESAM uses  $\text{MER}_{\text{cnd,esam}}^{(p)}[l, m|k]$ , computed as

$$\text{MER}_{\text{cnd,esam}}^{(p)}[l, m|k] \approx \Psi_{\text{bl}} \left( \frac{\text{SINR}_{\text{wf}}(P_{\text{rx},m}, kP_{\text{int,s}}^{(p)}[l, m], \text{SNR}_{\text{b}})}{\delta_{\text{code}}}, a, p_{\text{bl}}[l] \right). \quad (6.3)$$

Note that (6.3) simplifies to (4.41) for  $\delta_{\text{code}} = 0$  dB and  $U_{\text{tx}}(f) = T_s \text{rect}(fT_s)$ . To take into account the additional interference caused by synchronization symbols in the ESAM of Aloha with SIC, we calculate  $T_{\text{msg}}$  according to (5.3) and  $S$  according to (5.9). This replaces the more simple equation (4.31). By selecting  $\delta_{\text{code}}$  such that  $\Psi(\text{SINR}/\delta_{\text{code}}, a = 2/21)$  fits the MER shown in Figure 5.7 for the case with fine synchronization errors, we determined that the combined imperfections of coding and synchronization in ICBT can be described by  $\delta_{\text{code}} \approx 0.8$  dB.

For comparability to ICBT, all ESAM results reported in the following assume the elementary waveform  $u_{\text{tx}}(t)$  presented in Section 5.4.3, the ICBT system parameters given in Table 5.2, and  $\delta_{\text{code}} = 0.8$  dB. For the 2-D node distribution and movement model,  $\text{SNR}_b = 10$  dB and  $\alpha = 2$  (cf. Table 4.1), we calculated a spectral efficiency of  $\eta_{\text{SICesam}} = 0.53$  bits/s/Hz using the ESAM with  $p_{\text{max}} = 6$  processing passes (cf. Section 4.5). The reason why this value exceeds the corresponding value of  $\eta_{\text{SIC}} = 0.47$  bits/s/Hz from Table 4.3 is the use of a whitening matched filter together with a realistic elementary waveform which is nonzero outside of its 3 dB bandwidth of  $1/T_s$ .

## 6.3 Simulation Results in the 2-D Scenario

### 6.3.1 Monte-Carlo Simulation of the ICBT Message Error Rate

To compute  $\text{MER}(r, \rho)$  for ICBT in the 2-D aircraft distribution and movement model (cf. Section 2.5), we perform Monte-Carlo simulations as explained in the following. As discussed in Sections 4.3 and 4.5, it is sufficient to simulate the receiver of a single aircraft, since  $\text{MER}(r, \rho)$  is independent of the receiver location. The time arrival process of all messages generated within the radio horizon  $r_s$  of the simulated receiver can be well approximated by a Poisson process, since aircraft transmission instants are independent and uniformly distributed. For each message, we randomly generate a new transmitter location and direction of movement according to Section 2.5. This method is equivalent to the 3-D PPP described in Section 4.3 and may be seen as averaging over all possible aircraft arrangements. To simulate blanking as per (5.6), the aircraft whose receiver is simulated transmits messages at regular intervals of  $1/\lambda'$ . The combined message generation rate of all other aircraft is  $\lambda' \rho \pi r_s^2$ . Finally, to approximate  $\text{MER}(r, \rho)$ , messages originating from different distances are grouped into intervals and the average error rate is then computed within each distance interval. The intervals are determined such that a message from the lower end of the interval is received with

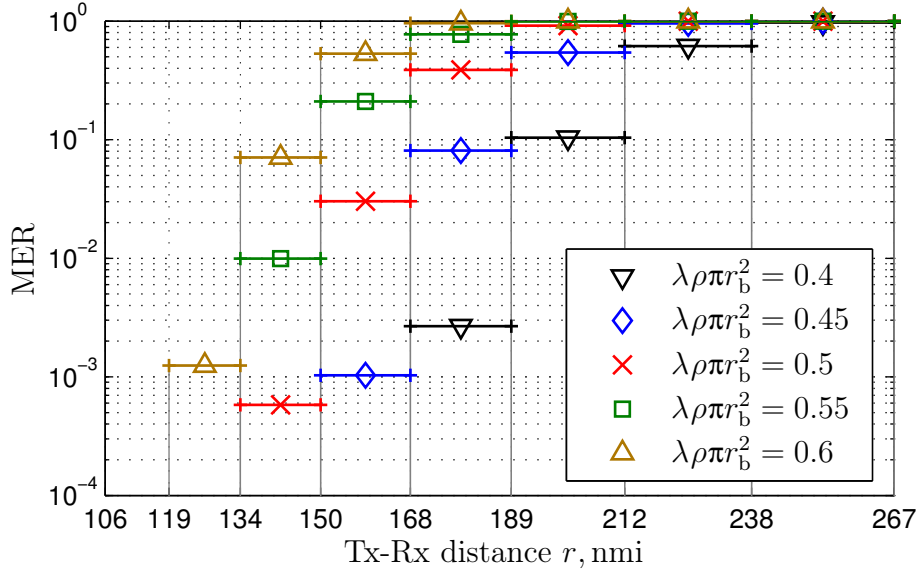


Figure 6.1. ICBT MER at various traffic loads  $\lambda\rho\pi r_b^2$ .

exactly 1 dB more power than a message from the upper end. Messages from the first processing window are ignored.

Unless explicitly stated otherwise, the parameters given in Table 5.2 were assumed for the following simulation results, together with an SNR at distance  $r_b$  of  $\text{SNR}_b = 10$  dB and a channel loss exponent of  $\alpha = 2$  (cf. Table 4.1).

### 6.3.2 Spectral Efficiency of ICBT

To determine the spectral efficiency of ICBT in the 2-D scenario, we have performed Monte-Carlo simulations with various beaconing traffic loads  $\lambda\rho\pi r_b^2$  as shown in Figure 6.1. The ticks on the horizontal axis indicate the distance intervals described in Section 6.3.1 and the horizontal bars indicate the MER inside of each interval. One of the interval boundaries was set to  $r_b = 150$  nmi. According to the results,  $\lambda\rho\pi r_b^2 = 0.5$  is the highest traffic load for which the MER in the distance bin directly below  $r_b = 150$  nmi is below  $\xi = 10^{-3}$ . Note that here, we have  $\lambda_{\text{nom}} = \lambda$ , as ICBT uses  $\lambda' = 1/T_{u,\text{crit}}$ . Hence, following the argumentation of Section 2.3, the nominal spectral efficiency of ICBT is approximately  $\eta_{\text{ICBT}} = 0.5$  bits/s/Hz. This agrees well with the spectral efficiency  $\eta_{\text{SICesam}} = 0.53$  bits/s/Hz predicted by the ESAM (cf. Section 6.2).

For each curve plotted in Figure 6.1, except for  $\lambda\rho\pi r_b^2 = 0.5$ , approximately 5.3 s of simulated receiver operation were evaluated. Depending on the traffic load, between

7500 and 10000 messages from transmitters within the beaconing range  $r_b$  arrived at the receiver during this time, together with a much larger number of messages from the distance interval  $r_b < r \leq r_s$ . Around 1500 to 2000 messages originated from the distance bin between 134 nmi and 150 nmi. For the most interesting case  $\lambda \rho \pi r_b^2 = 0.5$ , the simulation runtime was increased sixfold in order to increase the accuracy. In this case, the intervals below 134 nmi altogether contained about 40100 messages which could all be detected and decoded. The first interval with errors was the one between 134 nmi and 150 nmi. It contained 10339 messages, of which 6 could not be decoded.

### 6.3.3 Message Error Rate with ICBT Compared to the Extended Semi-Analytical Model

To compare ICBT to the ESAM of Aloha with SIC, the MER according to Monte-Carlo simulations of ICBT and according to the ESAM is plotted in Figure 6.2. For better comparability, the ESAM MER is averaged over the same distance bins as used for evaluation of the ICBT MER. Both for ICBT and for the ESAM, we assumed a beaconing traffic load of  $\lambda \rho \pi r_b^2 = 0.5$ . The evaluated receiver runtime for the ICBT simulation is the same as reported in Section 6.3.2 for  $\lambda \rho \pi r_b^2 = 0.5$ . Results are shown for  $p_{\max} \in \{1, 2, 4\}$  to demonstrate the influence of the number of processing passes for both ICBT and ESAM. The results show that for both ICBT and ESAM, the MER reduction between  $p_{\max} = 2$  and  $p_{\max} = 4$  is only moderate, which justifies the choice of  $p_{\max} = 2$  in Table 5.2. The distance  $r$  at which the MER first exceeds the required value  $\xi = 10^{-3}$  seems to be slightly larger for the ESAM than for ICBT, which had to be expected due to the idealized assumptions contained in the ESAM. The main effect making the ICBT MER worse than the ESAM MER appears to be the non-ideal IC in ICBT. This is revealed by another simulation of a hypothetical ICBT, in which the realistic IC of ICBT is replaced by perfect subtraction of the decoded messages (green curve labeled “pIC”). The average MER determined for ICBT with perfect IC in the distance bins above  $r_b = 150$  nmi almost matches the ESAM MER. Note that the simulated receiver runtime for ICBT with perfect IC was only 5.3 s, and that no message from a distance bin below  $r_b = 150$  nmi was lost. As a consequence, no MER is plotted in Figure 6.2 for ICBT with perfect IC at distances below  $r_b = 150$  nmi. In the two distance bins between 168 nmi and 212 nmi, the MER for ICBT with perfect IC is slightly lower than the ESAM MER. This is due to the fact that the model for the channel code MER in the ESAM is only approximate. As described in Section 6.2, the ESAM assumes that the realistic channel code from Section 5.4.4 behaves like the theoretical optimum shifted by  $\delta_{\text{code}} = 0.8$  dB. While this assumption is quite accurate for  $10^{-3} < \text{MER} < 10^{-2}$ , it is slightly pessimistic for larger error rates.

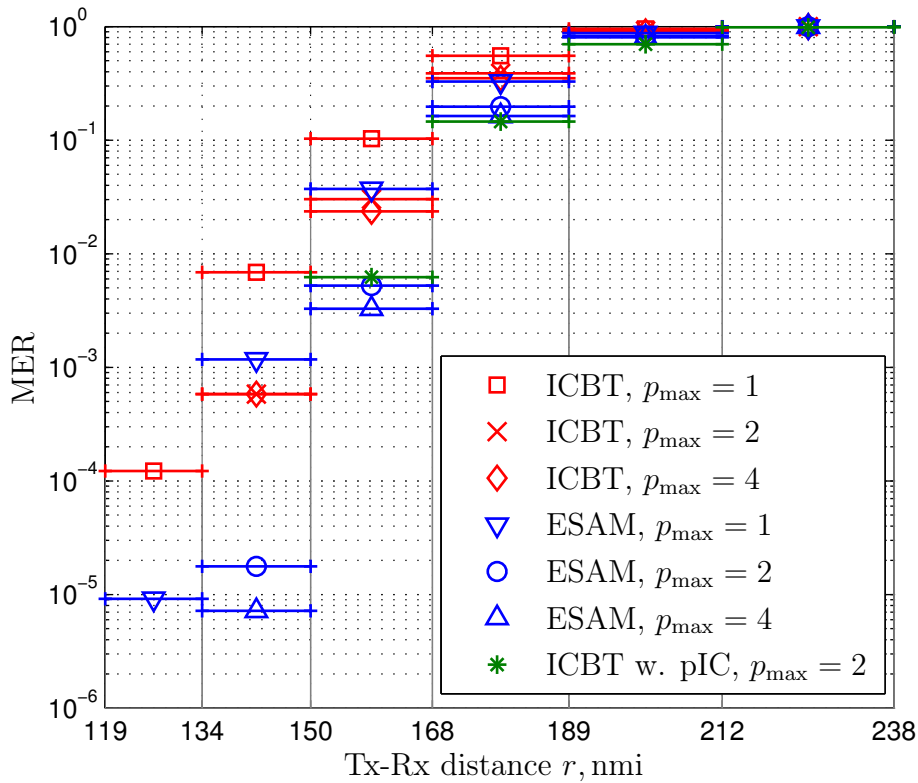


Figure 6.2. ICBT MER compared to ESAM MER;  $\lambda\rho\pi r_b^2 = 0.5$ .

### 6.3.4 Influence of Blanking on the Message Error Rate of ICBT

How much the ICBT MER is impaired by blanking can be analyzed using the output of the ICBT simulation with  $\lambda\rho\pi r_b^2 = 0.5$  already presented in Section 6.3.2. Only the time intervals between outgoing transmissions are evaluated to obtain the MER without blanking. The MER without blanking is plotted in Figure 6.3 together with the MER in the case with blanking already shown in Figure 6.1. Recall that  $\lambda' = 1$  Hz was used for the result in Figure 6.1 (as per Table 5.2). It becomes apparent from Figure 6.3 that at  $\lambda' = 1$  Hz, the influence of blanking is not very large, mainly because it occurs quite infrequently. As an extreme example, the result of another simulation with  $\lambda' = 1/(2N_{\text{all}}T_s) \approx 16$  Hz is shown in Figure 6.3. The beaconing traffic load  $\lambda\rho\pi r_b^2$  is kept constant by assuming that the aircraft density decreases to compensate the increase of  $\lambda'$ . The gaps between outgoing messages are now just as long as the messages themselves, meaning that every message is to some extent affected by blanking. In the simulation with  $\lambda' = 1/(2N_{\text{all}}T_s)$ , about 10.6 s of receiver operation were evaluated. Of the 13400 messages from  $r \leq 134$  nmi, only one was lost (not shown in Figure 6.3). This low MER shows that time hopping is effective even when blanking occurs frequently. Without time hopping, a significantly higher number of messages from close transmitters would have been lost due to the half-duplex constraint.



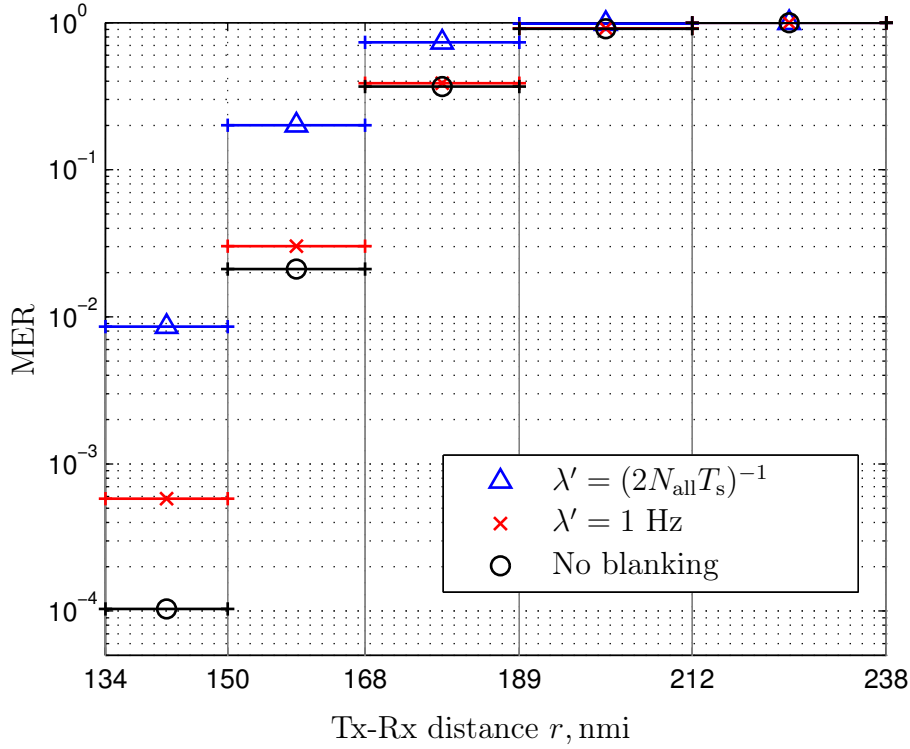


Figure 6.3. MER with blanking according to different  $\lambda' > 0$  compared to no blanking;  $\lambda\rho\pi r_b^2 = 0.5$  in all cases.

### 6.3.5 Influence of Undetected Messages on the Message Error Rate of ICBT

Here we verify our choice of the detection threshold baseline  $\Theta_b$ . To this end, we plot the ICBT MER together with the ratio of undetected messages in Figure 6.4. The beaconing traffic load is  $\lambda\rho\pi r_b^2 = 0.5$ . To decide whether a certain message was detected, we consider all solutions  $(\hat{k}, \hat{l}, \hat{m})$  of (5.7) found by the detection stage of the receiver algorithm (cf. Figure 5.3) during the whole simulation. Then, we restrict attention to only those solutions which were found for the same randomization option as that used by the message under question. If any of these solutions comes closer than  $T_s$  to the true time of arrival of the message, then it is considered as detected. As can be seen from Figure 6.4, the missed detection ratio is by more than an order of magnitude below the MER in the distance interval above  $r_b = 150$  nmi, and no messages were missed in any closer interval. This suggests that undetected messages do not have a significant impact on the MER for  $r \leq r_b$ . Thus, the value of  $\Theta_b$  has been chosen appropriately.

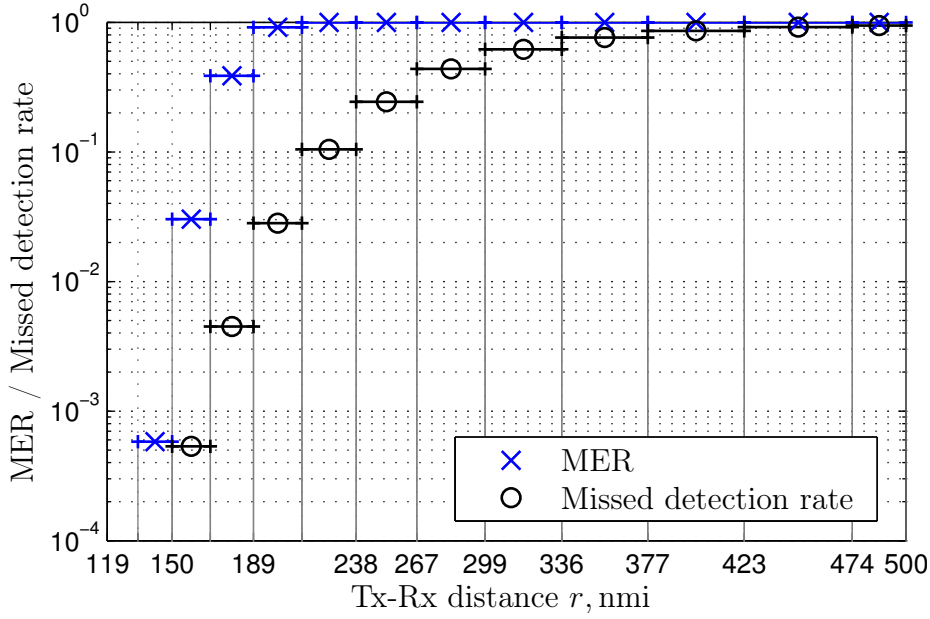


Figure 6.4. ICBT MER, compared to missed detection rate;  $\lambda\rho\pi r_b^2 = 0.5$ .

### 6.3.6 ICBT Performance with Reduced Number of Synchronization Symbols

To determine the influence of the number of synchronization symbols on the system performance, we consider the alternative setting  $N_{\text{sync}}^{\text{alt}} = 504$ , which corresponds to an overhead of 15% relative to the 3360 data symbols. Recall that ICBT uses an overhead of 20% according to Section 5.4.5. Applying the design procedures described in Sections 5.4.5 and 5.4.6 to the setting  $N_{\text{sync}}^{\text{alt}} = 504$ , we determined that  $N_{\text{sync,main}}^{\text{alt}} = 194$  synchronization symbols have to be used in the main section of each message and computed a detection threshold baseline of  $\Theta_b^{\text{alt}} = 7.71$  dB.

To reveal the main effect of reducing  $N_{\text{sync}}$ , we look at the number of receiver iterations. Each time the receiver algorithm enters the decoding stage (cf. Figure 5.3, line number 6 in the pseudo-code) is equivalent to a receiver iteration. Simulations with a beaconing traffic load of  $\lambda\rho\pi r_b^2 = 0.5$  show that the unmodified ICBT decodes on average one message per 28.1 receiver iterations, while with the alternative setting  $N_{\text{sync}}^{\text{alt}} = 504$ , one message is on average decoded per 1478.9 iterations. Hence, when the synchronization overhead is reduced from 20% to 15%, the number of unsuccessful receiver iterations increases by a factor of 52.6. This is mainly due to false alarms in message detection (coarse synchronization), which are caused by the reduced number of synchronization symbols in BSS and ESS. The relatively high synchronization overhead of 20% is thus required in ICBT to avoid the excessive number of unnecessary message decoding attempts at lower values of  $N_{\text{sync}}$ .

### 6.3.7 Interference Suppression Achieved by ICBT

In the simulation of ICBT with traffic load  $\lambda\rho\pi r_b^2 = 0.5$  (cf. Section 6.3.2), the interference suppression  $\varepsilon$  according to (5.31) is below  $-60$  dB except for 0.17% of all decoded messages. This shows that the remaining energy of a message after cancellation can be negligible in a practical situation. Note that  $(2\Delta k_{ic} + 1)(2\Delta l_{ic} + 1) = 49$  cancellation subspace taps are used in ICBT, cf. section 5.3.6 and Table 5.2.

## 6.4 Future Air Traffic Scenario

### 6.4.1 Air Traffic in Europe 2035

To evaluate the ICBT MER in a realistic 3-D aircraft distribution, we have developed a simulation of air traffic over Europe in the year 2035. This simulation is in the following called the Europe 2035 air traffic scenario. It is shortly summarized here, while a complete description is given in Appendix A.2. The distribution of air traffic was derived from a commercially available database of flight schedules from 2007 [Inn07]. By applying the average annual air traffic growth predicted in [Eur10] to the air traffic volume derived from the database, we obtained a prediction for the air traffic in Europe in the year 2035. Additionally, we increased the aircraft density in the vicinity of major airports such that this density matches corresponding estimates reported in [Eur07c] for the 2035 time frame.

Each aircraft in the Europe 2035 air traffic scenario travels along a 3-D trajectory. For the computation of distances and trajectories, we assume a spherical earth of the radius  $R_E = 6370$  km already introduced in Section 2.4.2. Flights departing or landing at an airport within the simulated area include a climb or descent phase for the transition between ground level and a cruise altitude of  $h_{cr} = 45000$  ft. The line of sight range between aircraft at cruise altitude slightly exceeds the value of  $r_s = 500$  nmi assumed in the 2-D model according to Section 2.5. From (2.11), we obtain  $r_{s,3D}(h_{cr}, h_{cr}) = 521$  nmi. As explained in Section 2.5, the assumption of such a high cruise altitude leads to worst-case multiple-access interference. However, in contrast to the 2-D model, we do not use a constant line of sight range in the Europe 2035 air traffic scenario, but apply (2.11) to the actual aircraft altitudes. For a transmitter at  $\mathbf{x}_{tx} \in \mathbb{R}^3$  and a receiver at  $\mathbf{x}_{rx} \in \mathbb{R}^3$ , we insert (2.11) into (2.10) to obtain the received power  $P_{rx}(\|\mathbf{x}_{tx} - \mathbf{x}_{rx}\|, r_{s,3D}(\|\mathbf{x}_{tx}\| - R_E, \|\mathbf{x}_{rx}\| - R_E))$ . The channel loss exponent is  $\alpha = 2$ .

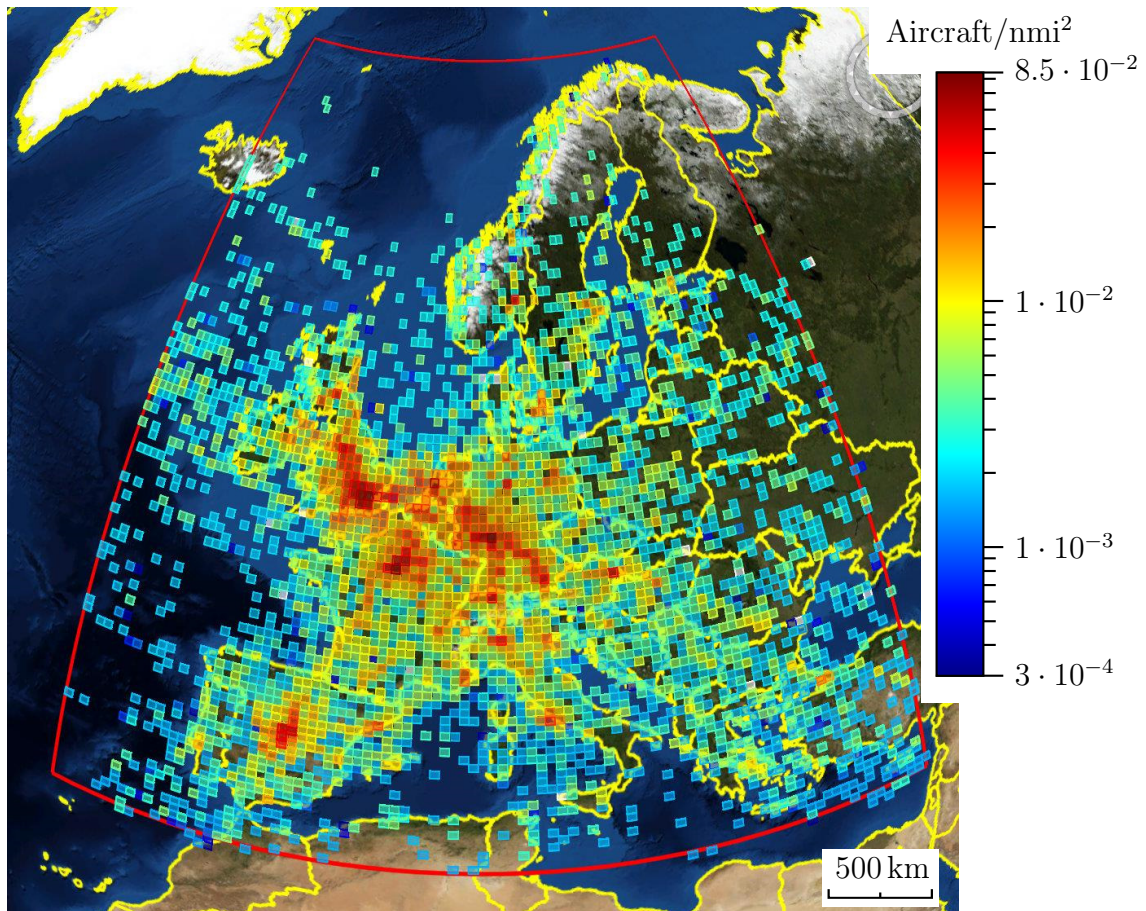


Figure 6.5. Aircraft density in the Europe 2035 air traffic scenario. Red rectangle delimits the area considered by the scenario. Satellite imagery: NASA World Wind, Blue Marble 2004 [BKM<sup>+</sup>07].

We now consider the aircraft distribution during the 10 s interval with the highest aircraft count from a longer simulation of aircraft movements according to the Europe 2035 air traffic scenario (cf. Appendix A.2.5.2). This 10 s interval of simulated air traffic will later be used for the Monte-Carlo simulations of the ICBT MER, and is therefore termed the MER simulation interval. The obtained aircraft distribution is shown in Figure 6.5. The highest air traffic density is observed in the surrounding of Brussels, which is located in between the large airports at London, Paris, Frankfurt and Amsterdam. Within a circle of 150 nmi radius centered at Brussels, 1267 aircraft can be found, which translates into an average density of 0.018 aircraft per nmi<sup>2</sup>. Within large parts of Europe, the average aircraft density in a circle of 150 nmi radius lies between 0.01/nmi<sup>2</sup> and 0.02/nmi<sup>2</sup>. This justifies the assumption  $\rho_{\text{typ}} = 0.015/\text{nmi}^2$  introduced in Section 2.5.

### 6.4.2 Worst-Case Receiver Location

Since the aircraft distribution is inhomogeneous in the Europe 2035 air traffic scenario, the ICBT MER depends on the receiver location. We therefore seek the worst-case location, where reception is most difficult. As an approximative criterion, we maximize the interference to signal ratio (ISR). To this end, let  $\mathbb{M}_{\text{tx}}$  denote the set of all aircraft locations in the Europe 2035 air traffic scenario, at the beginning of the 10s MER simulation interval. Note that in the Europe 2035 air traffic scenario, only transmitters within line of sight from the receiver are considered when computing the MER. This is in line with [RTC02, §3.3.3.1.1]. The distances to all aircraft within line of sight from some receiver location  $\mathbf{x}_{\text{rx}}$  are the elements of the set  $\mathbb{M}_{\text{dst}}$ , which is given by

$$\mathbb{M}_{\text{dst}} = \left\{ \|\mathbf{x}_{\text{rx}} - \mathbf{x}_{\text{tx}}\| : \mathbf{x}_{\text{tx}} \in \mathbb{M}_{\text{tx}} \cap r_{\text{s,3D}}(\|\mathbf{x}_{\text{tx}}\| - R_{\text{E}}, \|\mathbf{x}_{\text{rx}}\| - R_{\text{E}}) \geq \|\mathbf{x}_{\text{rx}} - \mathbf{x}_{\text{tx}}\| \right\}. \quad (6.4)$$

Let  $N_{\text{tx}}(\mathbf{x}_{\text{rx}}) = |\mathbb{M}_{\text{dst}}|$  denote the number of aircraft visible from  $\mathbf{x}_{\text{rx}}$ . Let the sequence of distances  $r_i(\mathbf{x}_{\text{rx}})$ ,  $1 \leq i \leq N_{\text{tx}}(\mathbf{x}_{\text{rx}})$ , be equal to the elements of  $\mathbb{M}_{\text{dst}}$  ordered in ascending order. We now hypothetically assume that all aircraft transmit at the same time, that the receiver processes messages in descending order of power, and that perfect SIC is employed. Under these conditions, the ISR for transmitter  $i$  can be computed as

$$\text{ISR}_i(\mathbf{x}_{\text{rx}}) = \sum_{n=i+1}^{N_{\text{tx}}(\mathbf{x}_{\text{rx}})} \left( \frac{r_i(\mathbf{x}_{\text{rx}})}{r_n(\mathbf{x}_{\text{rx}})} \right)^\alpha. \quad (6.5)$$

Since the receiver is only interested in messages from transmitters closer than  $r_{\text{b}}$ , the maximum ISR the receiver has to operate at is

$$\text{ISR}_{\text{max}}(\mathbf{x}_{\text{rx}}) = \max \left\{ \text{ISR}_i(\mathbf{x}_{\text{rx}}) : r_i(\mathbf{x}_{\text{rx}}) \leq r_{\text{b}} \right\}. \quad (6.6)$$

The worst-case receiver location  $\mathbf{x}_{\text{WC}} \in \mathbb{R}^3$  is determined by solving

$$\mathbf{x}_{\text{WC}} = \arg \max_{R_{\text{E}} \leq \|\mathbf{x}_{\text{rx}}\| \leq R_{\text{E}} + h_{\text{cr}}} \text{ISR}_{\text{max}}(\mathbf{x}_{\text{rx}}), \quad (6.7)$$

where  $\mathbf{x}_{\text{WC}}$  is restricted to locations above the earth and not exceeding an altitude of  $h_{\text{cr}}$ . We employ a regular grid in spherical coordinates to numerically solve (6.7). The grid spacing is  $0.02^\circ$  in latitude,  $0.025^\circ$  in longitude and 5000 ft in altitude. The worst-case receiver location is found at  $48.95^\circ$  north,  $4.3875^\circ$  east, and at the highest considered altitude of  $h_{\text{cr}} = 45000$  ft. It can be observed that  $\text{ISR}_{\text{max}}(\mathbf{x}_{\text{rx}})$  is generally larger at higher altitude, due to the increased line of sight range.

Figure 6.6 shows  $\text{ISR}_{\text{max}}(\mathbf{x}_{\text{rx}})$  for  $\mathbf{x}_{\text{rx}}$  at an altitude of  $h_{\text{cr}} = 45000$  ft. The determined solution for  $\mathbf{x}_{\text{WC}}$  is marked, as well as the locations of the major airports at London



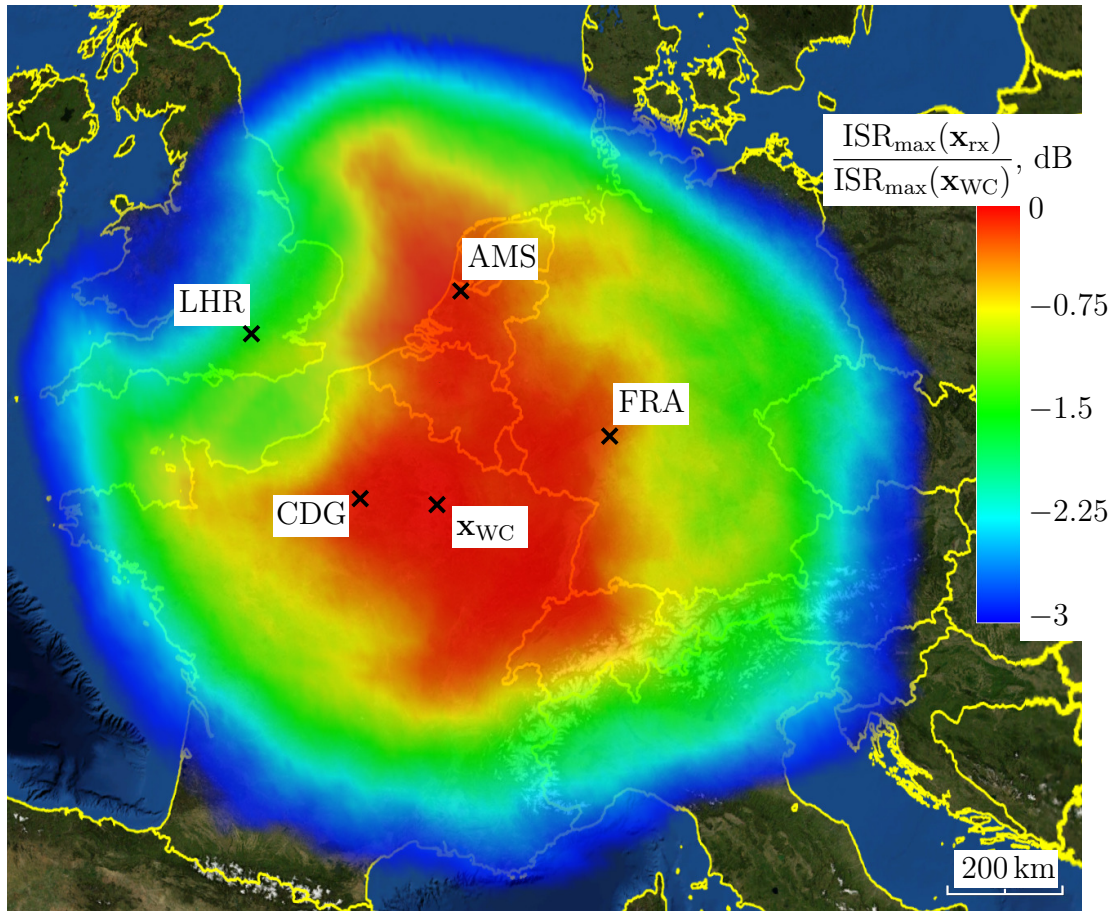


Figure 6.6.  $\text{ISR}_{\max}(\mathbf{x}_{\text{rx}})$  for receiver location  $\mathbf{x}_{\text{rx}}$  at an altitude of 45000 ft. Satellite imagery: NASA World Wind, Blue Marble 2004 [BKM<sup>+</sup>07].

(LHR), Paris (CDG), Frankfurt (FRA) and Amsterdam (AMS). Note that  $\text{ISR}_{\max}(\mathbf{x}_{\text{rx}})$  is plotted only in locations where it is not more than 3 dB below the maximum at  $\mathbf{x}_{\text{WC}}$ . It can be seen that for the chosen receiver altitude, the value of  $\text{ISR}_{\max}(\mathbf{x}_{\text{rx}})$  varies by less than 3 dB within a very large area.

The geographical density of aircraft within line of sight from  $\mathbf{x}_{\text{WC}}$  is plotted in Figure 6.7, where we consider the time average of this density during the 10 s MER simulation interval. Figure 6.8 considers the distances of the aircraft to  $\mathbf{x}_{\text{WC}}$  and shows how many aircraft visible from  $\mathbf{x}_{\text{WC}}$  are on average located within distance bins of 25 nmi width. As can be seen, a large number of aircraft are clustered in the distance bins directly above  $r_b = 150$  nmi. When a SIC receiver is decoding a message received from  $r_i(\mathbf{x}_{\text{rx}}) = r_b$ , interfering transmitters from distances directly above  $r_b$  create the largest possible contribution to (6.5). This explains why the clustering of transmitters at distances close to  $r_b$  typically leads to a high  $\text{ISR}_{\max}(\mathbf{x}_{\text{rx}})$ .

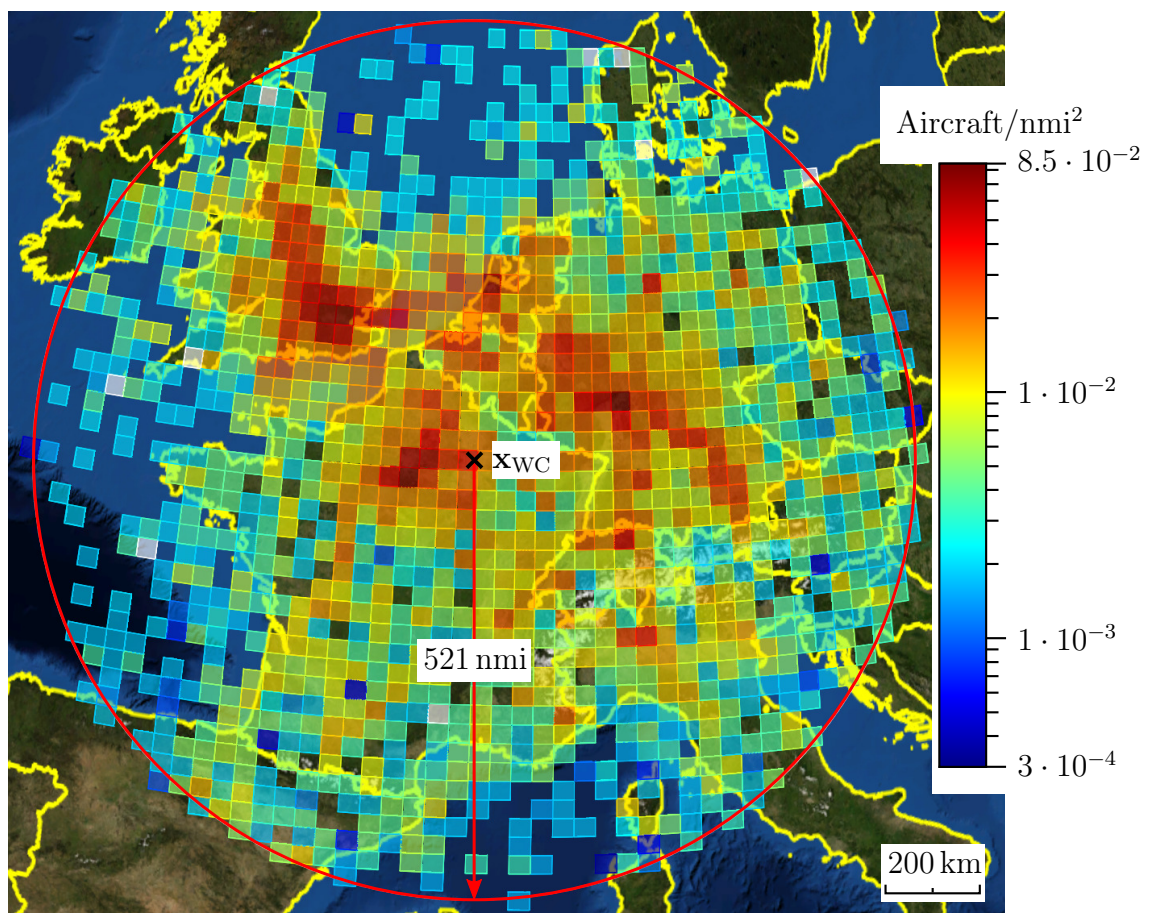


Figure 6.7. Aircraft density visible from  $x_{WC}$  in the Europe 2035 air traffic scenario. Satellite imagery: NASA World Wind, Blue Marble 2004 [BKM<sup>+</sup>07].

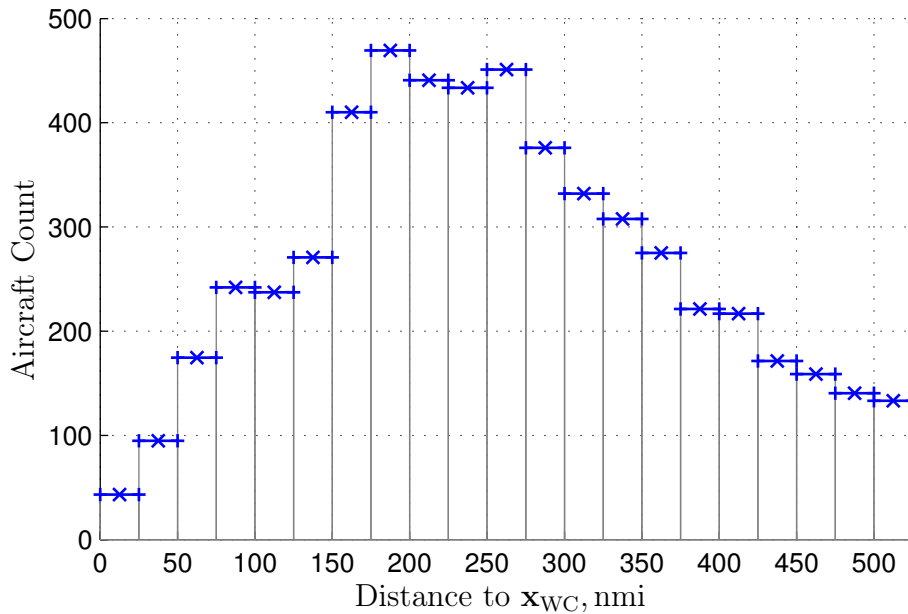


Figure 6.8. Number of aircraft visible from  $x_{WC}$  in the Europe 2035 air traffic scenario. Aircraft are counted in distance bins of 25 nmi width.

## 6.5 Simulation Results in the Future Air Traffic Scenario

### 6.5.1 ICBT Message Error Rate

We simulated the ICBT MER in the Europe 2035 air traffic scenario for a receiver located at  $x_{WC}$ , system parameters as per Table 5.2, and  $\text{SNR}_b = 10$  dB (cf. Section 6.3.1). In total,  $5.6 \cdot 10^4$  messages arrived at the receiver during the 10 s MER simulation interval. In the MER simulation, all messages could be decoded correctly, irrespective of distance, as long as the transmitter was within line of sight of  $x_{WC}$ . This shows that ICBT is perfectly able to fulfill the beaconing requirements stated in Section 2.2 for the beaconing traffic in the Europe 2035 air traffic scenario. Since ICBT performs even better than required, further air traffic growth or an increased data traffic per aircraft could be supported. The reason for this result is that the number of aircraft visible from  $x_{WC}$  in the Europe 2035 air traffic scenario is considerably less than the number of aircraft in the 2-D scenario with  $\lambda \rho \pi r_b^2 = 0.5$ . Although the corresponding aircraft density in the 2-D scenario of  $\rho = 0.022/\text{nmi}^2$  is significantly lower than the peak density in the Europe 2035 air traffic scenario (cf. Figure 6.7), the density in the latter, more realistic scenario is not constant, but decreases significantly at larger distances to  $x_{WC}$  (cf. Figure 6.8).



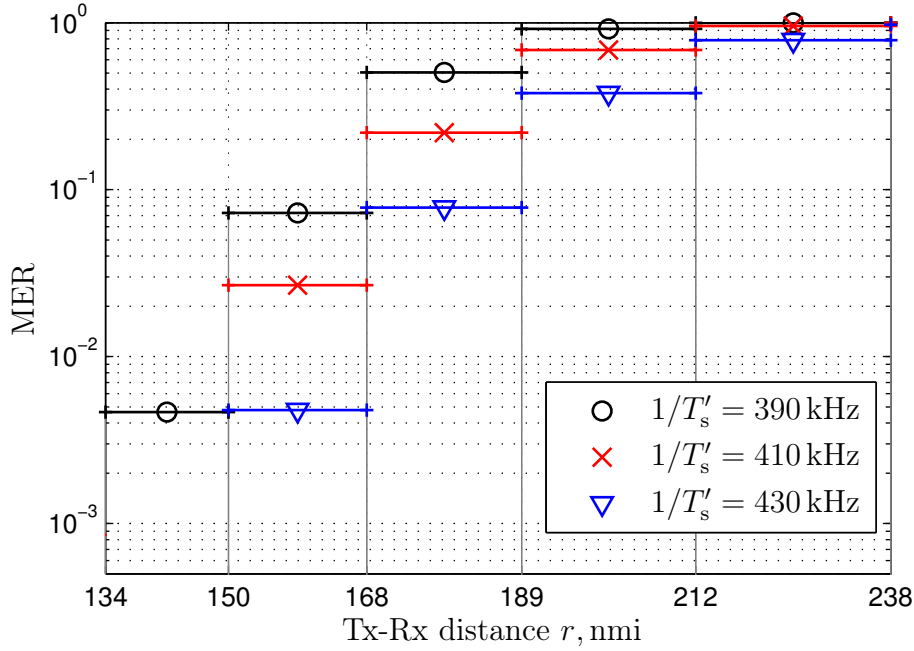


Figure 6.9. ICBT MER, various bandwidths, Europe 2035 air traffic scenario.

### 6.5.2 Bandwidth Required by ICBT in the Future Air Traffic Scenario

The fact that ICBT performs even better than required leads to the question for the minimum bandwidth needed to fulfill the beaconing requirements in the Europe 2035 air traffic scenario. Here, we look at a modification of ICBT where the symbol duration is  $T'_s > T_s$ , while all other parameters remain as per Table 5.2. For a fair comparison, we assume that the same transmit powers are used in the original and in the modified ICBT, which means that the SNR is now  $\text{SNR}'_b = \text{SNR}_b \cdot T'_s/T_s$ . In Figure 6.9, the MER is shown for three different values of  $T'_s$ . While the MER in the distance interval directly below  $r_b = 150$  nmi exceeds  $\xi = 10^{-3}$  for the lowest considered bandwidth  $1/T'_s = 390$  kHz, no errors occurred in the same distance interval for the two larger bandwidths  $1/T'_s = 410$  kHz and  $1/T'_s = 430$  kHz. These results suggest that the beaconing requirements (2.3) are still fulfilled for  $T'_s \approx (410 \text{ kHz})^{-1}$ , which means that less than half of the original bandwidth of  $1/T_s = 1$  MHz could be sufficient for the beaconing traffic generated in the Europe 2035 air traffic scenario. Note, however, that this result is achieved with an increased message length of  $N_{\text{all}}T'_s = 75.1$  ms. If this is not acceptable in reality, the design procedure described in Chapter 5 would have to be repeated for lower  $N_{\text{all}}$ , and the semi-analytical model of Section 4.5 could again be used to determine the optimum  $S$  and  $a$  for the chosen message length.

## 6.6 Summary

We have shown in this chapter that ICBT achieves a spectral efficiency of  $\eta_{\text{ICBT}} = 0.5$  bits/s/Hz in the 2-D scenario, which is only slightly less than the value of  $\eta_{\text{SICesam}} = 0.53$  bits/s/Hz predicted by the ESAM. The discrepancy is mainly due to the assumption of perfect IC in the ESAM. The validity of key parameter choices in ICBT, such as the number of processing passes  $p_{\text{max}}$ , the detection threshold baseline  $\Theta_b$ , and the number of synchronization symbols  $N_{\text{sync}}$ , could be verified by simulations.

Going beyond the 2-D scenario, we have employed published predictions of future air traffic growth [Eur10] to develop a model of air traffic over Europe in 2035. The most critical receiver location was found and selected for Monte-Carlo simulations of the ICBT MER in the Europe 2035 air traffic scenario. The results show that with a bandwidth of  $1/T_s = 1$  MHz, ICBT offers more capacity than actually needed, and that even a bandwidth of approximately 410 kHz would be sufficient for ICBT to fulfill all beaconing requirements stated in Section 2.2.

---

## Chapter 7

### Summary and Outlook

In this work, we addressed the problem of spectrally efficient aeronautical surveillance beaconing. As explained in Chapter 1, future aeronautical surveillance beaconing will require a system which provides increased surveillance capabilities to each aircraft in a situation of increased air traffic density. At the same time, the radio spectrum allocated to aeronautical communications is already congested today. For this reason, the spectral efficiency was used as the primary performance metric in this work.

In Chapter 2, the fundamentals needed for the quantitative analysis of beaconing schemes were explained. The surveillance beaconing problem was formalized by the required beaconing range  $r_b$ , the critical data age  $T_{u,crit}$ , the tolerable probability of outdated information  $\xi$ , and the beacon message size  $L$ . The multiple-access channel was explained, including the effects of signal propagation and received signal outage during own transmissions. Subsequently, a two-dimensional aircraft distribution and movement model was introduced. Due to its simplicity, the 2-D model is a suitable benchmark for the comparison of beaconing schemes. Concluding Chapter 2, we established a mathematical definition of the spectral efficiency of surveillance beaconing and discussed important aspects and challenges to be tackled in aeronautical surveillance beaconing.

In Chapter 3, PHY and MAC layer techniques known from the literature were reviewed. We considered the suitability of such techniques to an aeronautical surveillance beaconing scheme, in order to identify the most promising schemes for quantitative analysis in later chapters. The transmission schemes were categorized according to their use of either coordinated or uncoordinated MAC. The main advantages of uncoordinated MAC are (i) the lack of control data exchange and corresponding overhead, and (ii) the possibility to transmit without time synchronization, which removes the need to synchronize nodes and makes the spectral efficiency independent of propagation delays. The main disadvantage of uncoordinated MAC are the collisions of transmissions at the receiver. The main advantage of coordinated MAC is the possibility to control the SINR at the receiver by appropriate transmission scheduling, while the main disadvantages are the control data overhead, the need for time synchronization between nodes, and possible stability issues with the scheduling algorithm. We found unslotted Aloha with SIC to be the most promising uncoordinated beaconing scheme, due to the aforementioned advantages of uncoordinated, asynchronous transmissions

and due to literature reporting that in satellite communications, the poor spectral efficiency of unslotted Aloha could be mitigated through SIC. Additionally, we identified CB-SOTDMA as the most promising coordinated beacons scheme, since it is able to solve the hidden node problem of SOTDMA without increasing the control data overhead.

In Chapter 4, we developed semi-analytical mathematical models to compute the spectral efficiency of three aeronautical surveillance beacons schemes: unslotted Aloha with single-user receivers, CB-SOTDMA and unslotted Aloha with SIC. The latter two schemes were found to be promising candidates in Chapter 3. Unslotted Aloha with single-user receivers was considered since it is the most important surveillance beacons scheme used in aviation today and no suitable model of its spectral efficiency is known from the literature. The models we derived may be seen as semi-analytical, since we made suitable simplifications which permit the application of analytical expressions as far as possible, but still require the numerical evaluation of integrals and expected values in some cases. In this way, the computational complexity of the semi-analytical models could be kept sufficiently low to numerically search for the optimum PHY and MAC parameters which maximize the spectral efficiency of each beacons scheme.

Since both CB-SOTDMA and unslotted Aloha with SIC had not previously been used for aeronautical surveillance beacons, additional measures had to be devised to overcome challenges specific to aeronautical surveillance beacons. To apply CB-SOTDMA to aeronautical beacons, we introduced a novel subchannel reuse concept, which tackles the large power differences between signals from near and far transmitters when a concurrent multiple-access scheme is used. The exclusive use of sequential transmissions (TDMA) would lead to problems in aeronautics, due to transmit power limitations and necessary guard times. To utilize unslotted Aloha with SIC for beacons, we proposed the use of time hopping. Our semi-analytical model reveals that without time hopping, the spectral efficiency of unslotted Aloha with SIC suffers significantly from received signal outage during own transmissions. Through time hopping, the spectral efficiency loss incurred by such signal outage can be compensated in large parts. Concluding Chapter 4, we found that the spectral efficiency of both advanced schemes significantly surpasses that of unslotted Aloha without multi-user detection. The semi-analytical models predict that CB-SOTDMA has the highest spectral efficiency. However, as already reported in Chapter 3, CB-SOTDMA has the disadvantage of requiring time synchronization between aircraft. Since the spectral efficiency of unslotted Aloha with SIC is not by a large factor lower than the spectral efficiency of CB-SOTDMA, we argued that unslotted Aloha with SIC is the better choice for aeronautical surveillance beacons.

---

In Chapter 5, we designed the ICBT, an aeronautical beaconing system using unslotted Aloha with SIC. To enable simulations of the system behavior under real-world effects (cf. Chapter 6), the design of ICBT addresses multiple issues which were treated in a simplified way in the semi-analytical model from Chapter 4. For message detection and channel estimation, we proposed a novel structure of known synchronization symbols. This structure enables a hierarchical coarse-fine concept, which reduces the size of the Doppler filter bank needed for message detection, and at the same time achieves the Doppler estimation accuracy required for the coherent demodulation of data. The parameters of the synchronization structure were selected to maximize the SINR during message detection and maximize the Doppler estimation accuracy, while avoiding Doppler ambiguities. For IC, we described a scheme which achieves negligible residual interference for realistic time of arrival and Doppler shift estimation errors and for received messages which are asynchronous to the sampling clock. For channel estimation, message decoding and IC, the non-white correlation of the interference was taken into account. The coding and modulation rate, as well as the sparsity introduced by time hopping, were selected according to the optimum values which maximize the spectral efficiency predicted by the semi-analytical model from Chapter 4. A realistic channel code was selected for ICBT and its MER performance was compared to the idealized assumptions of the semi-analytical models (cf. Chapter 4).

Chapter 6 focused on Monte-Carlo simulations of the MER in our system design proposal ICBT. The simulation results reveal the spectral efficiency of ICBT, allow a comparison with the semi-analytical model, and enable the verification of parameter choices in the design. For a meaningful comparison, the semi-analytical model of Aloha with SIC from Chapter 4 had to be extended to take into account the non-white interference correlation, the imperfections of the realistic channel code used in ICBT, and the synchronization symbol overhead. This led to the ESAM of unslotted Aloha with SIC. For the 2-D aircraft distribution and movement model (cf. Chapter 2), we computed the spectral efficiency of ICBT and demonstrated that the ICBT MER and the ESAM MER are in good agreement. The remaining MER loss of ICBT with respect to the ESAM was shown to be mainly due to the fact that ICBT uses a realistic IC method, while perfect IC is assumed in the ESAM. The MER reduction achieved between receiver processing passes two and four was found to be small, justifying the use of only two processing passes in ICBT. The rate of undetected messages was shown to be negligible, which verifies the detection threshold selected in the ICBT design. The synchronization symbol overhead of 20% in ICBT was found to be necessary to control the number of false alarms in message detection.

Concluding Chapter 6, we described a realistic scenario of future air traffic over Europe, which is based on published traffic predictions for the year 2035 and takes into account

three dimensional flight paths. The ICBT MER was simulated in this Europe 2035 air traffic scenario. The results reveal that with its bandwidth of 1 MHz, which is similar to the bandwidth used by the existing UAT system, ICBT significantly exceeds the requirements (cf. Chapter 2). It was shown that the bandwidth of ICBT could be reduced to around 410 kHz in the Europe 2035 scenario, although both the beaconing range and the packet size are larger in ICBT than in state of the art aeronautical surveillance beaconing systems.

In future work, the suitability of the beaconing schemes considered herein could be investigated for beaconing applications other than surveillance. As remarked in Chapter 1, beaconing is also used in MANETs to exchange control data. Exactly how this control data exchange can be implemented is left open in [MHRR12, Grö03]. The semi-analytical models developed in this work could help to determine the best solution, which may be a system similar to ICBT. Furthermore, future work could investigate the performance of ICBT for non-aeronautical applications, where non-line of sight conditions and node mobility cause severe multipath and fading.

# Appendix

## A.1 Derivation of the Message Error Rate Equations

### A.1.1 AWGN Without Blanking

Here, we derive (4.2) from [PPV10, eq. (296)], which approximates the maximum codebook size  $M^*$  at which a MER of  $\epsilon$  can be achieved on a real-valued AWGN channel with  $n_R$  channel uses per codeword. According to [PPV10, eq. (296)], we have

$$\log_2 M^* \approx n_R C_{\text{awgn,R}} - \sqrt{n_R V_{\text{awgn,R}}} Q^{-1}(\epsilon) + \frac{1}{2} \log_2 n_R, \quad (\text{A.1})$$

where  $Q(\epsilon)$  is the CCDF of the standard normal distribution,  $C_{\text{awgn,R}}$  denotes the capacity of the real-valued AWGN channel,

$$C_{\text{awgn,R}} = \frac{1}{2} \log_2(1 + \text{SINR}), \quad (\text{A.2})$$

and  $V_{\text{awgn,R}}$  is the dispersion of the real-valued AWGN channel, given by [PPV10, eq. (293)]

$$V_{\text{awgn,R}} = \frac{\text{SINR}}{2} \frac{\text{SINR} + 2}{(1 + \text{SINR})^2} (\log_2 e)^2. \quad (\text{A.3})$$

Note that while the base of the logarithm is arbitrary in [PPV10], we have used a base of 2 in (A.1) - (A.3), whereby information is measured in bits. To bring (A.1) to the form (4.2), we note that

- In our context, one message carries one codeword. Hence, the number of information bits per message is  $L = \log_2 M^*$ .
- We consider a complex AWGN channel with  $L/a$  channel uses per codeword. This is equivalent to a real-valued AWGN channel with  $n_R = 2L/a$  channel uses per codeword.
- We have  $Q(\epsilon) = \frac{1}{2} \text{erfc}\left(\frac{\epsilon}{\sqrt{2}}\right)$ , where  $\text{erfc}(\cdot)$  is the complementary error function [AS64].

Inserting the aforementioned relationships into (A.1) and solving for  $\epsilon$ , (4.2) is obtained in a straightforward way.

### A.1.2 AWGN With Blanking

In this section, we derive the MER model (4.29) for the case of AWGN and symbol-wise blanking from the results of [PV11]. To this end, we describe blanking by multiplying each symbol of a message with a fading coefficient. The coefficient for symbol  $k'$  is  $H_{k'} \in \mathbb{C}$ . For simplicity, we assume the coefficients  $H_{k'}$  to be i.i.d. random variables, which assume either the value  $H_{k'} = 1$  with probability  $1 - p_{\text{bl}}$ , or the value  $H_{k'} = 0$  with probability  $p_{\text{bl}}$ . With fading,  $n_C$  complex channel uses are not equivalent anymore to  $n_R = 2n_C$  real-valued channel uses, since in the complex case, the same fading coefficient applies to real and imaginary part of each symbol, while in the real-valued case, each channel use has its own, independent fading coefficient. From [PV11, eq. (34)], we obtain the expression

$$\log_2 M^* = n_C C_{\text{fad,C}} - \sqrt{n_C V_{\text{fad,C}}} Q^{-1}(\epsilon) + o(\sqrt{n_C}), \quad (\text{A.4})$$

where, in our case,  $C_{\text{fad,C}}$  is the capacity and  $V_{\text{fad,C}}$  is the dispersion of the complex AWGN fading channel. In our case, the receiver knows the fading coefficients, since it knows which received symbols are affected by its own transmissions. Yet, this knowledge is not available at the transmitter. Under these conditions, the capacity  $C_{\text{fad,C}}$  can be computed as [BPS98, eq. (3.3.10)]

$$\begin{aligned} C_{\text{fad,C}} &= E \left\{ \log_2(1 + |H_{k'}|^2 \cdot \text{SINR}) \right\} \\ &= (1 - p_{\text{bl}}) \log_2(1 + \text{SINR}). \end{aligned} \quad (\text{A.5})$$

The dispersion is given by [PV11, eq. (36)]

$$\begin{aligned} V_{\text{fad,C}} &= \mathbb{L} + (\log_2 e)^2 \left( 1 - \left( E \left\{ \frac{1}{1 + |H_{k'}|^2 \cdot \text{SINR}} \right\} \right)^2 \right) \\ &= \mathbb{L} + (\log_2 e)^2 \left( 1 - \left( \frac{1 + p_{\text{bl}} \text{SINR}}{1 + \text{SINR}} \right)^2 \right), \end{aligned} \quad (\text{A.6})$$

where

$$\begin{aligned} \mathbb{L} &= \lim_{m \rightarrow \infty} \frac{1}{m} \text{Var} \left\{ \sum_{k'=1}^m \log_2(1 + |H_{k'}|^2 \cdot \text{SINR}) \right\} \\ &= p_{\text{bl}}(1 - p_{\text{bl}}) (\log_2(1 + \text{SINR}))^2. \end{aligned} \quad (\text{A.7})$$

The base-2 logarithm is used in (A.4) - (A.7) in order to express information in bits, while the corresponding equations in [PV11, BPS98] use an arbitrary logarithmic base. The second line in (A.7) can be explained by noting that the sum term in the first line is proportional to a binomially distributed random variable of variance  $mp_{\text{bl}}(1 - p_{\text{bl}})$ . To obtain (4.29), we insert (A.5) - (A.7) into (A.4), use  $L = \log_2 M^*$  and  $n_C = L/a$ , and solve for  $\epsilon$ . The  $o(\sqrt{n_C})$  term is neglected.



## A.2 Development of the Europe 2035 Air Traffic Scenario

### A.2.1 Methodology

As part of the simulations of beaconing in Section 6.5, a realistic simulation of future air traffic is required. Such a simulation is also referred to as an air traffic scenario [Int09, ADS01]. The procedure we use to derive such a scenario can be broken down into the following steps:

1. selection of an appropriate simulation area,
2. evaluation of available data to obtain the current air traffic volume in the simulation area,
3. up-scaling of the air traffic according to predictions of future traffic growth,
4. simulation of the up-scaled air traffic and extraction of all aircraft trajectories during a time interval which is suitable for the beaconing MER simulations in Section 6.5,
5. insertion of additional aircraft to make up for remaining discrepancies between the simulated air traffic and the air traffic density close to major airports reported in the literature.

The steps 1 to 5 are addressed in the following Sections A.2.2 - A.2.6.

### A.2.2 Simulation Area

The simulation area is depicted in Figure A.1. Within Europe, the highest air traffic densities, and hence the most critical situations for aeronautical communications, are found over France and Germany [Eur10]. However, based on the line of sight range discussed in Section 6.4.1, the simulation area must be selected significantly larger to ensure that all airborne transmitters are considered, which are picked up by a receiver at high altitude. For this reason, we choose as simulation area a rectangle in latitude and longitude, defined by the following intervals:

- latitude between  $34^\circ$  north and  $72^\circ$  north,
- longitude between  $18^\circ$  west and  $35^\circ$  east.

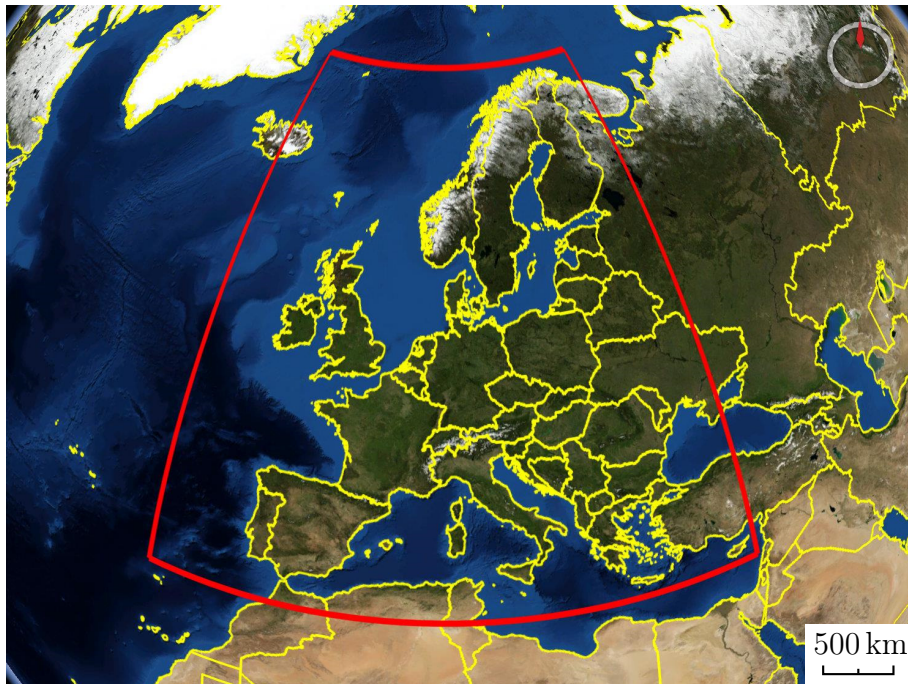


Figure A.1. Simulation area of the Europe 2035 air traffic scenario. Satellite imagery: NASA World Wind, Blue Marble 2004 [BKM<sup>+</sup>07].

### A.2.3 Flight Database Evaluation

The volume of air traffic is often summarized by the total number of flights per year within large geographical regions [Eur10]. However, to correctly assess the interference in the MER simulations, the spatial and temporal distribution of air traffic needs to be known in more detail. In this section, the required air traffic parameters for a time period in the past are obtained from a database of flights. We determine both the spatial distribution of air traffic during a suitable period of peak traffic, and the total number of flights per year within the simulation area. The spatial distribution is described by the matrix  $\mathbf{\Lambda}_{\text{db}}$ , where  $[\mathbf{\Lambda}_{\text{db}}]_{k,l}$  is the average number of aircraft which are at the same time flying from location  $k$  to location  $l$ . These locations are either airports, or points on the border of the simulation area where flights enter or exit the simulation area. The total number of annual flights is required in the following section to up-scale  $\mathbf{\Lambda}_{\text{db}}$  according to predictions of annual flight movements in the future.

The database we evaluated contains worldwide flight schedules from the year 2007, as well as a corresponding list of airport coordinates [Inn07]. The database fields of relevance here are the origin and destination airports of a flight, as well as its departure and arrival time. In this section, we assume that each aircraft moves along a great circle on the ground, and with constant speed according to the departure and arrival

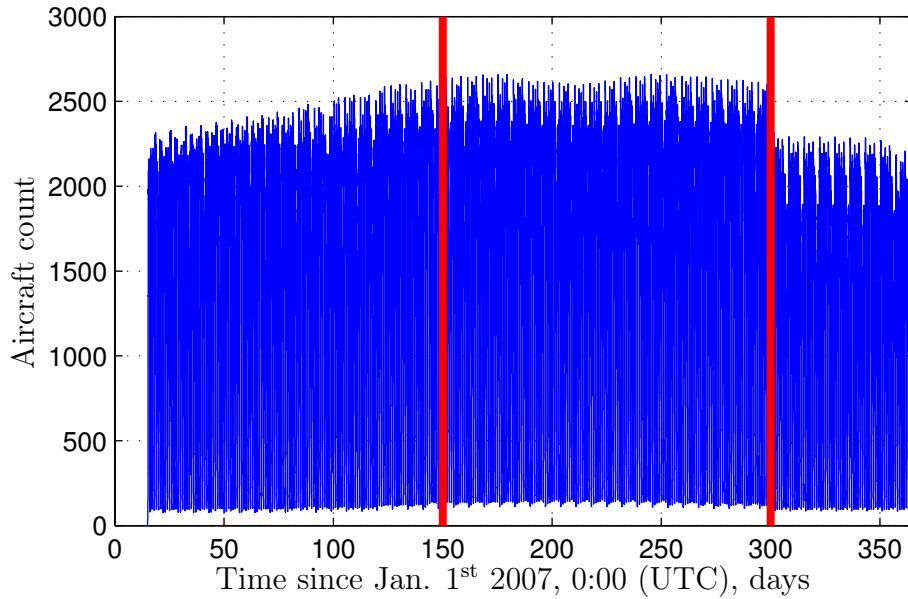


Figure A.2. Instantaneous aircraft count over the simulation area as per the database. Red bars mark the time frame used to estimate the yearly number of flights.

times indicated in the database. The altitude profile is considered later in Section A.2.5.1. Only flights with great circle routes that intersect with the simulation area are considered. This includes flights inside of the simulation area, flights going to or coming from the simulation area, as well as overflights of the simulation area. If a flight departs or lands at an airport outside the simulation area, its path is truncated to begin or end at the point of entry into or exit from the simulation area. Likewise, the time of departure or arrival is set to the time of entry or exit.

The described process yields a list of flights, where each flight begins and ends at a location in the simulation area or on its border. From the departure and arrival times of these flights, the instantaneous number of aircraft in the simulation area is derived as a function of time. It is plotted in Figure A.2. For our simulations, it is sufficient to consider a suitable time period of maximum traffic. To this end, the busiest hour in 2007 is determined by finding the maximum of a running average of the instantaneous number of aircraft in the simulation area. With an average of 2584 aircraft in the simulation area, the hour from 8:45 to 9:45 (UTC) on June 29<sup>th</sup> is found to be the busiest hour. Accordingly, we set  $[\Lambda_{\text{db}}]_{k,l}$  to the average number of aircraft en route from location  $k$  to location  $l$  during this hour.

As can be seen from Figure A.2, no flights occur during the first days of the year, and the number of flights drops significantly after day 300. Since this appears implausible, we use only the time frame between the days 150 and 300 to estimate the annual

number of flights. During this time frame,  $3.29 \cdot 10^6$  flights took place, which, upscaled to one year, corresponds to  $N_{\text{db}2007} = 8.01 \cdot 10^6$  flights in 2007 according to the database.

## A.2.4 Air Traffic Upscaling According to Predicted Growth

To determine the traffic matrix  $\mathbf{\Lambda}_{\text{sim}}$ , which is used in our simulation of future air traffic, we employ growth predictions published by Eurocontrol [Eur10]. We extrapolate the predicted air traffic growth until the year 2035 to obtain  $\mathbf{\Lambda}_{\text{sim}}$  for the Europe 2035 air traffic scenario. In [Eur10], the number of annual flight movements in the Eurocontrol Statistical Reference Area 2008 (ESRA08) is discussed. Although ESRA08 follows national borders and is not entirely identical with our simulation area, we employ data applicable to ESRA08 in the following. In areas where our simulation area differs from ESRA08, the air traffic volume is significantly less than in areas of high air traffic such as France or Germany. Therefore, the error introduced by applying figures published for ESRA08 to our simulation area is limited. For the years 2007 and 2009, [Eur10] reports  $N_{\text{ECTL}2007} = 10.043 \cdot 10^6$  and  $N_{\text{ECTL}2009} = 9.413 \cdot 10^6$  flight movements, respectively. Several scenarios of future growth making different assumptions about influencing factors are discussed in [Eur10]. In the scenario with the highest growth, the average annual air traffic growth factor between 2009 and 2030 is estimated as  $\Gamma = 1.039$ . Accordingly,  $\mathbf{\Lambda}_{\text{sim}}$  is computed as

$$\mathbf{\Lambda}_{\text{sim}} = \mathbf{\Lambda}_{\text{db}} \frac{N_{\text{ECTL}2007}}{N_{\text{db}2007}} \frac{N_{\text{ECTL}2009}}{N_{\text{ECTL}2007}} \Gamma^{2035-2009}. \quad (\text{A.8})$$

The first term represents the mismatch between the database and [Eur10]. It amounts to  $N_{\text{ECTL}2007}/N_{\text{db}2007} = 1.25$ . The second term,  $(N_{\text{ECTL}2009}/N_{\text{ECTL}2007})\Gamma^{2035-2009} = 2.53$ , describes the growth factor between 2007 and 2035.

## A.2.5 Air Traffic Simulation

### A.2.5.1 Aircraft Trajectories

To simulate aircraft movement, trajectories need to be specified in three spatial dimensions and in time. Here, a trajectory is characterized by *(i)* its departure time, *(ii)* its path in the three spatial dimensions, and *(iii)* a set of movement speeds applicable to different sections of the path. The departure times used in the simulation are described later. In the following, the procedure used to construct the path and set the movement speeds of each flight is described.

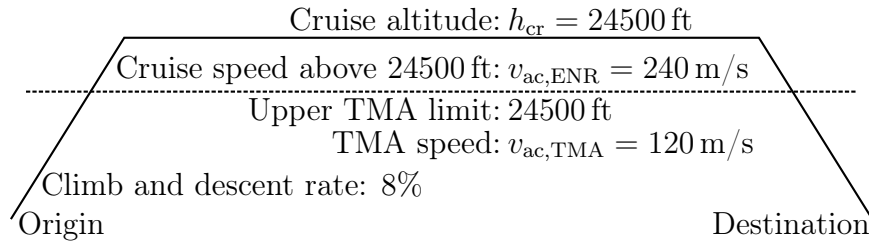


Figure A.3. Trajectory altitude and speed profile.

The flight path is broken down into a path on the ground and an altitude profile. The altitude profile is shown in Figure A.3. According to [Eur07c], a special airspace domain called the terminal maneuvering area (TMA) exists at every airport for the transition of traffic between the airport domain close to the ground and the en-route domain at higher altitudes. Typically, the TMA has a radius of 50 nmi and is located between 5000 ft and 24500 ft altitude. Accordingly, we set the climb and descent rate to  $(24500 \text{ ft}) / (50 \text{ nmi}) = 8\%$ . Once the aircraft is in the en-route airspace above 24500 ft, we assume it to move with  $v_{ac,ENR} = 240 \text{ m/s}$  (467 kts). Below 24500 ft, the movement speed is reduced to  $v_{ac,TMA} = 120 \text{ m/s}$ . For a given average number of aircraft on a certain route, reducing the speed of air traffic in the TMA increases the density of aircraft in the TMA and reduces the density of aircraft in the en-route domain. With the selected setting of  $v_{ac,TMA} = v_{ac,ENR}/2$ , the peak aircraft density in the en-route domain in our simulation matches the en-route peak instantaneous aircraft count reported in [Eur07c] for the time after 2030. As explained in Section 6.4.1, the cruise altitude is  $h_{cr} = 45000 \text{ ft}$ . The cruise altitude is maintained during the cruise phase of the trajectory, which connects the climb and the descent phases. If the distance between origin and destination of a flight is too short to reach  $h_{cr}$ , i.e., shorter than  $2h_{cr}/0.08 = 185 \text{ nmi}$ , then the cruise phase is omitted, such that the altitude profile describes an isosceles triangle. If either origin or destination is on the border of the simulation area, then the corresponding climb or descent phase is omitted, such that the trajectory begins or ends at cruise altitude. Recall that origins and destinations on the border of the simulation area are merely the points where flights enter or exit the simulation area, not the actual locations of departure or landing.

The path on the ground can be determined in two different ways [HESF12]. First, the shortest path along a graph of air traffic routes can be used. For this, we employ air traffic routes obtained from the software Eurocontrol SkyView. Second, the path can follow a great circle between origin and destination. Great-circle routing is randomly selected for 50% of the flights in our simulation in order to model future improvements of air traffic routes. The remaining flights follow the route graph. Figure A.4 shows the climb phase of a trajectory originating at Vienna and flying along the route graph.

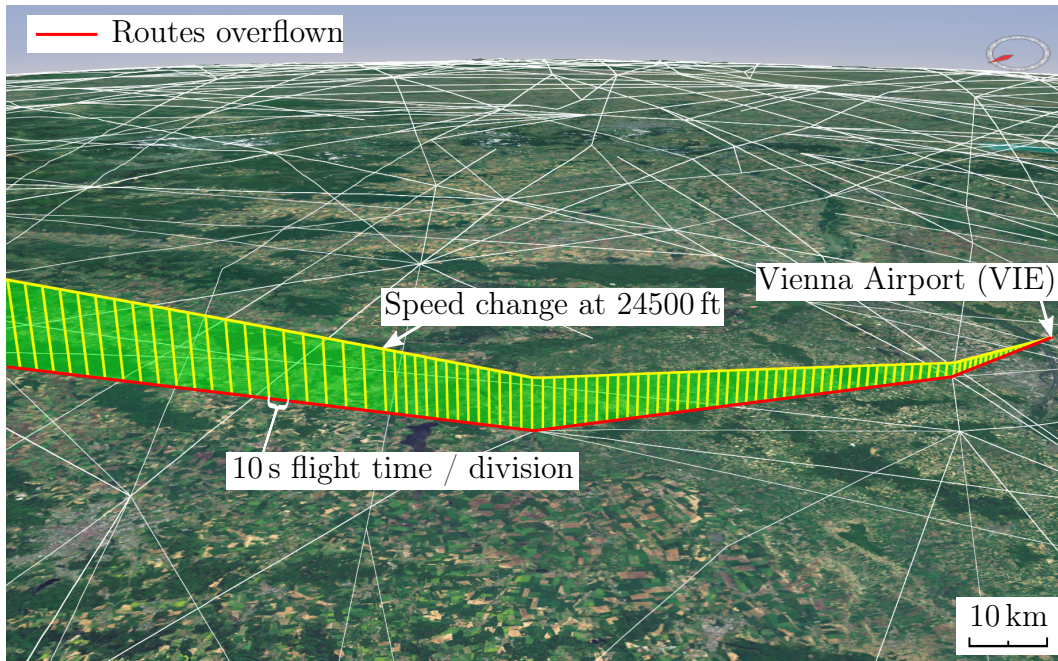


Figure A.4. Climb phase of a trajectory over the route graph. Satellite imagery: NASA World Wind, Landsat [BKM<sup>+</sup>07].

The vertical lines delimit sections of 10 seconds flight time, thus illustrating the speed change at 24500 ft.

#### A.2.5.2 Simulation Procedure and Selection of Time Interval for Beaconing Simulations

To simulate air traffic, we employ the Future Aeronautical Communications Traffic Simulator (FACTS) [HBMA08], which we extended by the altitude-dependent aircraft speeds explained in Section A.2.5.1. Aircraft flying from location  $k$  to location  $l$  are generated according to a Poisson process with mean inter-arrival time  $T_{k,l}^{\text{flt}} / [\Lambda_{\text{sim}}]_{k,l}$ , where  $T_{k,l}^{\text{flt}}$  is the flight time according to our trajectory model. In this way, we have simulated air traffic in the simulation area for 17.5 h. From this simulation, we have selected the interval of 10s duration with the highest average number of aircraft. All aircraft trajectories during this interval are used for the beaconing MER simulations in Section 6.5, which is why we refer to this interval as the MER simulation interval.



## A.2.6 Additional TMA Traffic

As discussed in Section A.2.5.1, the aircraft speed is reduced in TMA airspace such that the aircraft density in the en-route domain is consistent with [Eur07c]. In the following, we additionally match the aircraft counts in some major TMAs of the Europe 2035 air traffic scenario to peak values found in [Eur07c]. We do not consider a detailed model of the TMA boundaries at any specific airport, but merely look at the number of aircraft which can be found within a radius of 100 nmi around any airport, between 5000 ft and 24500 ft altitude. According to [Eur07c], the peak instantaneous aircraft count within a radius of 100 nmi in TMA airspace can be as high as 400 in the time frame after 2030. The highest TMA aircraft count of our simulation is found at London Heathrow (LHR), with an average of 225 aircraft during the MER simulation interval. A further reduction of  $v_{ac,TMA}$  would increase this value, but would also decrease the en-route aircraft density further, which is not desired. Instead, to match our simulated aircraft count in the largest TMA to the peak value from [Eur07c], we insert additional aircraft at the five airports with the highest aircraft generation rates according to  $\Lambda_{sim}$ . These are the airports at London (LHR), Paris (CDG), Frankfurt (FRA), Amsterdam (AMS) and Madrid (MAD). At each airport, 175 additional aircraft are randomly placed, following a uniform distribution within a circle of 100 nmi radius around the airport and between 5000 ft and 24500 ft altitude. This increases the TMA aircraft count at LHR to 400. The additional aircraft remain at the same position during the MER simulation interval. However, the Doppler shifts in the MER simulation are calculated as if each of them was moving into a random direction with a speed of 240 m/s. The density of the additional TMA traffic is displayed in Figure A.5. The aircraft densities discussed in Section 6.5 already include the additional TMA traffic. Note that for better comparability, Figure A.5 uses the same color scale as Figure 6.5, which shows the entire aircraft density.

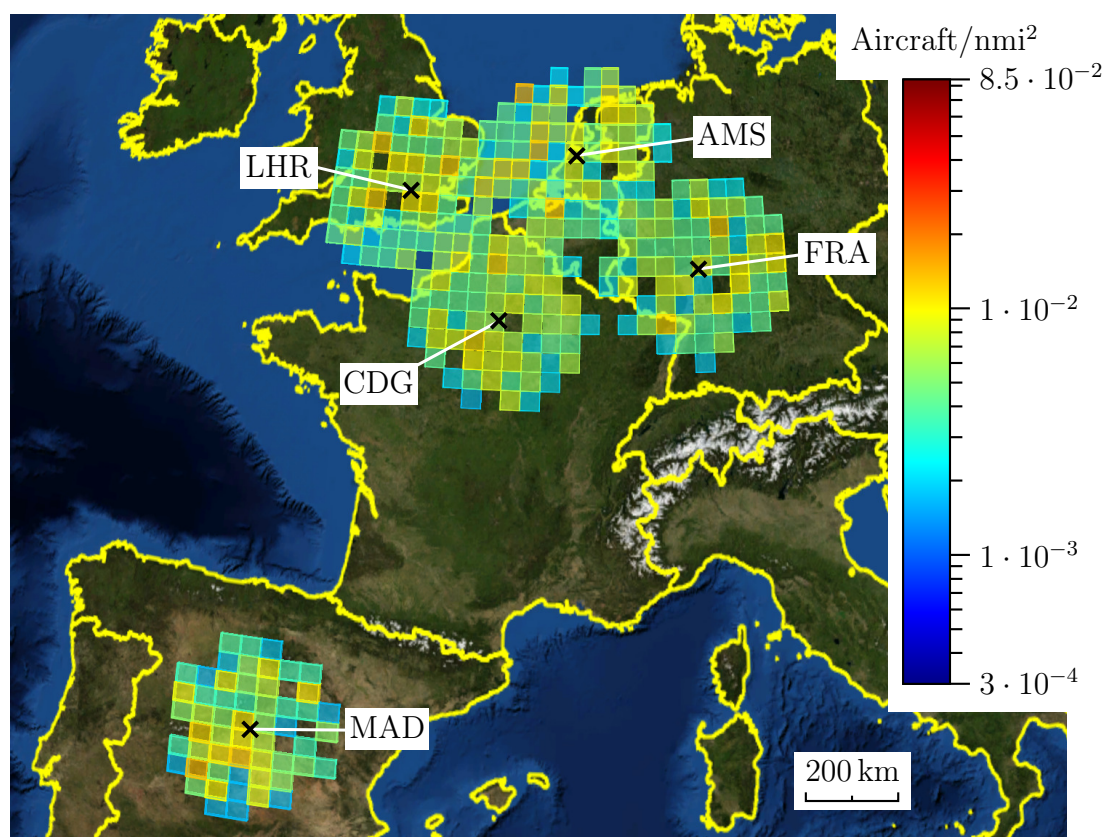


Figure A.5. Density of additional aircraft in large TMAs. Satellite imagery: NASA World Wind, Blue Marble 2004 [BKM<sup>+</sup>07].



# List of Acronyms

1090ES	SSR Mode S Extended Squitter transmitted on 1090 MHz	3, 29
ADS-B	Automatic Dependent Surveillance Broadcast	2
AIS	Automatic Identification System	34
AWGN	Additive white Gaussian noise	20
BP	Belief propagation	90
BPBT	Broadcast Protocol with Busy Tone	40
BSS	Begin synchronization section	80
CB-SOTDMA	Cell-based self-organizing TDMA	6, 36
CCDF	Complementary cumulative distribution function	93
CDF	Cumulative distribution function	48
CDMA	Code-division multiple-access	20
COMB	Cell-Based Orientation Aware MAC Broadcast	36
CRA	Contention Resolution Aloha	30
CRDSA	Contention Resolution Diversity Slotted Aloha	32
CSMA	Carrier sense multiple-access	32
DME	Distance Measuring Equipment	3
E-SSA	Enhanced Spread Spectrum Aloha	30
ECRA	Enhanced Contention Resolution Aloha	30
ESAM	Extended semi-analytical model	100
ESRA08	Eurocontrol Statistical Reference Area 2008	124
ESS	End synchronization section	80
FACTS	Future Aeronautical Communications Traffic Simulator	126
FDMA	Frequency-division multiple-access	20
GNSS	Global navigation satellite system	26
i.i.d.	Independent and identically distributed	16
IC	Interference cancellation	61
ICBT	Interference Canceling Beacon Transceiver	10, 73
IRSA	Irregular Repetition Slotted Aloha	32
ISI	Inter-symbol interference	90
ISR	Interference to signal ratio	109
ITU	International Telecommunication Union	3
LCA	Location-Based Channel Access	37
LDPC	Low-density parity check	89
MAC	Medium access control	4

---

MANET	Mobile ad-hoc network.....	1
MER	Message error rate.....	14
MUD-MAC	Multi-User Detection MAC.....	40
PHY	Physical.....	4
PPP	Poisson point process.....	22
PSD	Power spectral density.....	88
QPSK	Quadrature phase shift keying.....	89
R-Aloha	Reservation Aloha.....	38
RTS/CTS	Request to send, clear to send.....	39
Rx	Receiver	
SDMA	Space-division multiple-access.....	37
SIC	Successive interference cancellation.....	6, 30
SINR	Signal to interference and noise ratio.....	6
SNR	Signal to noise ratio.....	44
SOTDMA	Self-organizing time-division multiple-access.....	4, 34
SSR	Secondary surveillance radar.....	3
STDMA	Spatial reuse TDMA.....	42
TDMA	Time-division multiple-access.....	21
TLAT	Technical Link Assessment Team.....	4
TMA	Terminal maneuvering area.....	125
TPCPC	Two-Phase Coding with Power Control.....	37
Tx	Transmitter	
UAT	Universal Access Transceiver.....	4, 29
VDL4	VHF Digital Link Mode 4.....	4, 34
VHF	Very high frequency.....	3

# List of Symbols

General Notation	
$j$	Imaginary unit; $j^2 = -1$
$\text{Re}\{\cdot\}; \text{Im}\{\cdot\}$	Real and imaginary part of a complex argument, respectively
$(\cdot)^*$	Complex conjugate
$a(t) * b(t)$	Convolution of the functions $a(t)$ and $b(t)$
$\delta(t)$	Dirac delta distribution; $a(t) * \delta(t) = a(t)$
<b>a</b>	Vectors are denoted by lowercase letters in bold print. Unless noted otherwise, <b>a</b> is a column vector
<b>A</b>	Matrices are denoted by uppercase letters in bold print
$(\cdot)^T$	Transpose of a vector or matrix
$(\cdot)^H$	Hermitian transpose of a vector or matrix; $(\cdot)^H = ((\cdot)^*)^T$
$[\mathbf{a}]_k$	Element $k$ of vector <b>a</b>
$[\mathbf{A}]_{l,k}$	Element at row $l$ and column $k$ of matrix <b>A</b>
<b>I</b>	Identity matrix
$\text{diag}(\mathbf{a})$	Diagonal matrix with the elements of <b>a</b> on its main diagonal
$\ \cdot\ $	Euclidean vector norm; $\ \mathbf{a}\  = \sqrt{\mathbf{a}^H \mathbf{a}}$
$\mathbf{A}^\dagger$	Moore-Penrose pseudoinverse of matrix <b>A</b>
$\text{supp}(f(t))$	Support of the function $f(t)$
$ \mathbb{M} $	Cardinality of the set $\mathbb{M}$
$E\{\cdot\}$	Expected value of a random variable
$\text{Pr}(C)$	Probability that the boolean expression $C$ is true
$\mathbf{1}\{C\}$	Indicator function. Yields 1 if the boolean expression $C$ is true, zero otherwise
$\text{sup}(\mathbb{M})$	Supremum (least upper bound) of the set $\mathbb{M}$

$a$	Coding and modulation rate, i.e., number of bits per complex symbol . . . . .	46
$a_{\text{cl}}[M_{\text{cl}}]$	Coding and modulation rate when $M_{\text{cl}}$ nodes share the resources of one cell in CB-SOTDMA, see (4.20) . . . . .	53
$a_{\text{opt,asu}}$	Optimal $a$ in semi-analytical model of Aloha with single-user receivers, see (4.12) . . . . .	48
$A_{\text{cl}}$	Area of hexagonal network cell, see (4.21) . . . . .	53
$\mathcal{A}_{\text{rx}}$	Area of receiver locations to consider in semi-analytical model of CB-SOTDMA . . . . .	56
$\mathcal{A}'_{\text{rx}}$	Discrete set of points used to approximate $\mathcal{A}_{\text{rx}}$ in numerical evaluation of semi-analytical model of CB-SOTDMA . . . . .	57
$b[k]$	Blanking sequence, indicates which samples are blanked in the ICBT receiver, see (5.6) . . . . .	76
<b>B</b>	Diagonal matrix describing the blanking of the received vector $\mathbf{y}$ , see (5.18) . . . . .	84
<b>C</b>	Cancellation matrix for interference cancellation, see (5.29) . . . . .	86
$c$	Speed of light . . . . .	17
$\mathbf{c}_m$	Scrambling sequence for randomization option $m$ , see (5.1) . . . . .	74
$D[N]$	Reuse distance in cellular reuse pattern, see (4.14) . . . . .	49
$D_{\text{tot}}$	Total reuse distance in nested reuse pattern . . . . .	51
$d_{k,l}$	Number of interfering transmitters in co-channel cell (either zero or one) . . . . .	54
$\mathbf{d}_0$	Vector of $L/a$ complex modulation symbols . . . . .	74
$\mathbf{d}_{\text{pr}}$	Pseudo-randomized vector of complex modulation symbols after scrambling, interleaving and time hopping, see (5.1) . . . . .	74
$E_s$	Received energy per modulation symbol . . . . .	90
$F_{\text{dB}}$	Receiver noise figure, in dB . . . . .	20
$f_c$	Carrier frequency . . . . .	17
$f_d$	Doppler shift . . . . .	15
$\hat{f}_d$	Doppler shift estimate from fine synchronization, see (5.21) . . . . .	85

$g_i(t)$	Transmit signal of message $i$ .....	15
$G_{\text{msg}}$	Expected number of overlapping messages prior to SIC in semi-analytical model of Aloha with SIC, see (4.42) .....	64
$g_{\text{own}}(t)$	Own transmit signal .....	19
$g_{\text{pwr}}[m]$	Received power distribution in semi-analytical model of Aloha with SIC .....	61
$g_{\text{toa}}[\Delta l]$	Distribution of arrival times of interfering messages in semi-analytical model of Aloha with SIC, see (4.36) .....	62
$\mathcal{G}_{\text{rx}}$	Isotropic receive antenna gain, see (2.12) .....	17
$\mathcal{G}_{\text{tx}}$	Isotropic transmit antenna gain, see (2.12) .....	17
$h_{\text{cr}}$	Cruise altitude assumed in the Europe 2035 air traffic scenario .....	107
$\hat{\mathbf{h}}$	Estimated channel coefficient vector for interference cancellation, see (5.28) .....	86
$i$	Cellular reuse pattern parameter .....	49
$i_{\text{tot}}$	Parameter $i$ of nested reuse pattern .....	54
$i_{\text{tot}}^{\text{opt}}$	Optimal parameter $i$ of nested reuse pattern according to semi-analytical model of CB-SOTDMA, see (4.28) .....	57
$\mathbf{i}$	Interference contribution in received vector $\mathbf{y}$ , before blanking, see (5.18) .....	84
$k_{\text{cl}}$	Integer coordinate of $\mathbf{x}_{\text{cl}}$ , see (4.23) .....	54
$k_{\text{E}}$	Effective earth radius factor; $k_{\text{E}} = 4/3$ , see (2.11) .....	17
$\hat{k}$	Sample index at which message was detected, see (5.7) .....	77
$k_{\text{offs}}[n]$	Offset of $n$ 'th processing window within sequence of received samples $y[k]$ , see (5.8) .....	78
$\tilde{k}$	Number of messages a single aircraft transmits per $T_{\text{u,crit}}$ .....	14
$\tilde{k}_{\text{opt,asu}}$	Optimal $\tilde{k}$ in semi-analytical model of Aloha with single-user receivers, see (4.12) .....	48
$K_{\text{win}}$	Processing window overlap, in samples, see (5.8) .....	78
$L$	Bits of information per message .....	13

$l_{\text{cl}}$	Integer coordinate of $\mathbf{x}_{\text{cl}}$ , see (4.23) . . . . .	54
$\hat{l}$	Coarse synchronization frequency index at which message was detected, see (5.7) . . . . .	77
$L_{\text{rise}}$	Length of the detection threshold rise interval, in samples, see (5.36) . . . . .	94
$L_{\text{win}}$	Processing window length, in samples, see (5.8) . . . . .	78
$M$	Number of randomization options in ICBT . . . . .	74
$M_{\text{cl}}$	Number of nodes in a single cell . . . . .	53
$\hat{m}$	Randomization option for which message was detected (Chapter 5), see (5.7) . . . . .	77
$\mathbb{M}$	Set of all interfering messages . . . . .	46
$\mathbb{M}_{\text{own}}$	Set of indices of all own messages . . . . .	19
$\text{MER}_{\text{asu}}(r)$	MER in semi-analytical model of Aloha with single-user receivers, see (4.10) . . . . .	48
$\text{MER}_{\text{cl}}(\mathbf{x}_{\text{rx}}, \mathbf{x}_{\text{tx}})$	MER for specific transmitter and receiver locations $\mathbf{x}_{\text{rx}}$ and $\mathbf{x}_{\text{tx}}$ in semi-analytical model of CB-SOTDMA, see (4.25) . . . . .	56
$\overline{\text{MER}}_{\text{cl}}(\mathbf{x}_{\text{rx}}, r)$	MER for specific $\mathbf{x}_{\text{rx}}$ , averaged over all $\mathbf{x}_{\text{tx}}$ at distance $r$ to $\mathbf{x}_{\text{rx}}$ in semi-analytical model of CB-SOTDMA, see (4.26) . . . . .	56
$\text{MER}_{\text{end}}^{(p)}[l, m k]$	MER conditioned on number of overlapping messages prior to SIC in semi-analytical model of Aloha with SIC, see (4.41) . . . . .	64
$\text{MER}_{\text{SIC}}^{(p)}[l, m]$	MER after processing pass $p$ in semi-analytical model of Aloha with SIC . . . . .	63
$\overline{\text{MER}}_{\text{SIC}}^{(p)}[m]$	MER after processing pass $p$ in semi-analytical model of Aloha with SIC, averaged over message arrival time, see (4.44) . . . . .	64
$N_0$	One-sided power spectral density of thermal noise at the receiver . . . . .	20
$n(t)$	Thermal noise at receiver input . . . . .	20
$n_{\text{own}}(t)$	Noise impairing receiver due to own transmissions . . . . .	19
$\mathbf{n}$	Noise contribution in received vector $\mathbf{y}$ , before blanking, see (5.18) . . . . .	84

$\tilde{\mathbf{n}}$	Effective noise vector, i.e., combined noise and interference contribution in received vector $\mathbf{y}$ , after blanking, see (5.18) ..	84
$N[i, q]$	Reuse pattern size, see (4.13) .....	49
$N_{\text{all}}$	Total number of complex symbols per ICBT message, including zero symbols (time hopping) .....	74
$N_{\text{B,ds}}$	Burst size (in symbols) used in the dedicated synchronization sections BSS and ESS .....	81
$N_{\text{B,main}}$	Burst size (in symbols) used in the main section of a message	81
$N_{\text{ds}}$	Total number of symbols per dedicated synchronization section .....	80
$N_{\text{F}}$	Number of FDMA subchannels in nested reuse pattern .....	51
$N_{\text{pwr}}$	Number of discrete received power levels used in semi-analytical model of Aloha with SIC .....	61
$\mathcal{N}_{\text{reuse}}$	Set of possible reuse pattern sizes $N[i, q]$ , see (4.15) .....	50
$\mathcal{N}'_{\text{reuse}}$	Set of TDMA reuse pattern sizes $N_{\text{T}}$ which can be used for reuse pattern nesting, see (4.17) .....	51
$N_{\text{sync}}$	Total number of synchronization symbols per message .....	74
$N_{\text{sync,ds}}$	Number of synchronization symbols per dedicated synchronization section .....	80
$N_{\text{sync,main}}$	Number of synchronization symbols in the main section of a message .....	80
$N_{\text{T}}$	Number of TDMA subchannels in nested reuse pattern .....	50
$N_{\text{toa}}$	Number of discrete message arrival times in semi-analytical model of Aloha with SIC .....	62
$N_{\text{tot}}$	Total number of combined TDMA-FDMA subchannels in nested reuse pattern .....	50
$N_{\text{tot}}^{\text{opt}}$	Total number of combined TDMA-FDMA subchannels in nested reuse pattern with optimal parameters $(i_{\text{tot}}^{\text{opt}}, q_{\text{tot}}^{\text{opt}})$ .....	58
$N_{\mathbf{y}}$	Length of $\mathbf{y}$ , see (5.16) .....	84
$p_{\text{bl}}$	Probability that a single modulation symbol is blanked in semi-analytical model of Aloha with SIC .....	59

$p_{\text{bl,msg}}$	Probability that a received message is affected by blanking in semi-analytical model of Aloha with single-user receivers, see (4.7) . . . . .	48
$\hat{P}_{\text{BSS}}[k, m]$	Estimated power at correlator output $\mu_{\text{BSS}}(k, f, m)$ , see (5.14) . . . . .	83
$\hat{P}_{\text{ESS}}[k, m]$	Estimated power at correlator output $\mu_{\text{ESS}}(k, f, m)$ , see (5.14) . . . . .	83
$P_{\text{int}}[\hat{k}]$	Interference power in received symbol vector $\mathbf{y}$ cut out around coarse synchronization maximum at $\hat{k}$ . . . . .	85
$\hat{P}_{\text{int}}[\hat{k}]$	Estimate of $P_{\text{int}}[\hat{k}]$ used in fine synchronization, see (5.24) . . . . .	85
$P_{\text{int,asu}}$	Interference power in semi-analytical model of Aloha with single-user receivers, see (4.9) . . . . .	48
$P_{\text{int,cl}}$	Interference power in semi-analytical model of CB-SOTDMA, see (4.24) . . . . .	54
$P_{\text{int,s}}^{(p)}[l, m]$	Interference power in semi-analytical model of Aloha with SIC, see (4.40) . . . . .	64
$p_{\text{lfe}}$	Probability for a large frequency error in fine synchronization, see (5.33) . . . . .	92
$p_{\text{max}}$	Number of processing passes in Aloha with SIC . . . . .	63
$p_{\text{out}}(B, t, r)$	Probability that at time $t$ , the information available at aircraft $B$ about another aircraft at distance $r$ from $B$ is outdated, see (2.2) . . . . .	12
$P_{\text{rx}}(r, r_s)$	Received power for aircraft distance $r$ and line of sight range $r_s$ , see (2.10) . . . . .	17
$P_{\text{rx},m}$	Discrete received power levels in semi-analytical model of Aloha with SIC . . . . .	61
$P_{\text{tx}}$	Transmit power, see (2.9) . . . . .	16
$q$	Cellular reuse pattern parameter . . . . .	49
$q_{\text{tot}}$	Parameter $q$ of nested reuse pattern . . . . .	54
$q_{\text{tot}}^{\text{opt}}$	Optimal parameter $q$ of nested reuse pattern according to semi-analytical model of CB-SOTDMA, see (4.28) . . . . .	57
$\mathbf{q}$	Vector of transmitted symbols, see (5.2) . . . . .	74



$q[k']$	Element $k'$ of $\mathbf{q}$ , see (5.4).....	74
$r$	Transmitter-receiver distance.....	15
$r_b$	Required beaconing range.....	1
$R_{cl}$	Cell radius: radius of the circumscribed circle of a cell.....	49
$R_E$	Radius of the earth; $R_E = 6370$ km, see (2.11).....	17
$\text{rect}(t)$	Rectangular function, see (4.6).....	47
$r_{\text{ref}}$	Hypothetical distance for 0 dB transmission loss, see (2.9) ...	16
$r_s$	Line of sight range.....	17
$r_{s,3D}(h_1, h_2)$	Line of sight range between two aircraft at altitudes $h_1$ and $h_2$ , see (2.11).....	17
$r_{\text{sense}}$	Sensing range in CDMA.....	32
$S$	Sparsity factor for time hopping.....	60
$\tilde{s}_{\text{BSS}}(k, f, m)$	Sequence of received samples for the BSS of randomization option $m$ with a Doppler shift of $f$ , see (5.11).....	82
$S_{\text{ds}}$	Sparsity factor of the dedicated synchronization sections BSS and ESS.....	81
$\tilde{s}_{\text{ESS}}(k, f, m)$	Sequence of received samples for the ESS of randomization option $m$ with a Doppler shift of $f$ , see (5.12).....	82
SINR	Signal to interference and noise ratio (SINR).....	46
$\mathbf{s}_m$	Vector of synchronization symbols for randomization option $m$ .....	74
$s_m[k']$	Element $k'$ of $\mathbf{s}_m$ , see (5.11).....	82
$S_{\text{main}}$	Sparsity factor of the main section of a message.....	81
$\text{SNR}_b$	SNR for transmitter-receiver distance $r = r_b$ , see (4.1).....	44
$S_{\text{opt}}(T_{\text{msg}})$	Optimal sparsity according to semi-analytical model of Aloha with SIC, see (4.48).....	66
$t_a$	Time of arrival of a message at the considered receiver.....	46
$\hat{t}_a$	Time of arrival estimate from fine synchronization, see (5.21)	85
$T_\Delta$	Sampling interval.....	76

$t_l$	Discrete arrival times in semi-analytical model of Aloha with SIC, see (4.32) . . . . .	62
$\mathbf{T}_m$	Time-hopping matrix for randomization option $m$ , see (5.1) . .	74
$T_{\text{msg}}$	Nominal message duration . . . . .	15
$T_{\text{rep}}$	Repetition factor of non-binary multiplicative repetition code	89
$T_s$	Symbol interval, i.e., the modulation symbol rate is $1/T_s$ . . . .	74
$T_{\text{toa}}$	Spacing of discrete arrival times in semi-analytical model of Aloha with SIC, see (4.33) . . . . .	62
$t_{\text{tx}}$	Channel access time . . . . .	15
$T_u(t, A, B)$	Data age at time $t$ , defined as age of the most recently received information from aircraft $A$ at receiving aircraft $B$ . . . .	12
$T_{u,\text{crit}}$	Critical data age . . . . .	12
$u_{\text{rx}}(t)$	Receiver filter in complex baseband . . . . .	76
$u_{\text{tx}}(t)$	Elementary waveform in complex baseband . . . . .	74
$\mathbf{v}_1[i, q]$	Co-channel cell offset vector 1, see (4.16) . . . . .	50
$\mathbf{v}_1^{\text{tot}}$	Co-channel cell offset vector 1 for nested reuse pattern . . . . .	54
$\mathbf{v}_2[i, q]$	Co-channel cell offset vector 2, see (4.16) . . . . .	50
$\mathbf{v}_2^{\text{tot}}$	Co-channel cell offset vector 2 for nested reuse pattern . . . . .	54
$v_{\text{ac}}$	Aircraft speed, 2-D model . . . . .	22
$v_{\text{rel}}$	Relative speed of transmitter and receiver . . . . .	15
$w_i(t)$	Channel response for message $i$ , see (2.4) . . . . .	15
$\tilde{w}(t)$	Signal at receiver input, see (2.17) . . . . .	20
$W_d$	Doppler search range . . . . .	16
$W_{\text{sys}}$	Bandwidth of the beaconing system . . . . .	23
$x(t)$	Transmitted waveform filtered with receiver input filter, see (5.10) . . . . .	82
$\mathbf{x}_{\text{cl}}$	Center of the cell the transmitter is located in, see (4.22) . . . .	54
$\mathbf{x}_{\text{ic}}[k, l]$	Response of the channel tap at time $\hat{t}_a + kT_\Delta$ and with Doppler shift $\hat{f}_d + l\Delta f_{\text{ic}}$ to the message $\mathbf{q}$ , see (5.26) . . . . .	86

$\mathbf{X}_{\text{ic}}$	Cancellation subspace matrix. Its columns are the vectors $\mathbf{x}_{\text{ic}}[k, l]$ which span the cancellation subspace . . . . .	86
$\mathbf{X}(t, f)$	Matrix describing the channel response to the transmitted symbols $\mathbf{q}$ of a message received at time $t$ and with Doppler shift $f$ , see (5.17) . . . . .	84
$\tilde{\mathbf{X}}(t, f)$	Matrix describing the blanked channel response to the transmitted symbols $\mathbf{q}$ of a message received at time $t$ and with Doppler shift $f$ , see (5.18) . . . . .	84
$x_{\text{ov}}$	Relative overlap between desired message and own transmission . . . . .	47
$\mathbf{x}_{\text{rx}}$	Receiver location . . . . .	54
$\mathbf{x}_{\text{tx}}$	Transmitter location . . . . .	54
$\mathbf{x}_{\text{WC}}$	Worst-case receiver location in the Europe 2035 air traffic scenario, see (6.7) . . . . .	109
$y[k]$	Sequence of received samples . . . . .	76
$\mathbf{y}$	Vector of $\mathbf{N}_y$ received samples cut out from $y[k]$ , see (5.16) . . . . .	84
$\mathbf{y}_e$	Interference cancellation error vector, see (5.27) . . . . .	86
$\mathbf{z}_{k,l}$	Normalized position of interfering node relative to co-channel cell center . . . . .	54
$\alpha$	Channel loss exponent, see (2.9) . . . . .	16
$\beta_{\text{cs}}(k, f, m)$	Coarse synchronization metric for sample index $k$ , Doppler shift $f$ and randomization option $m$ . . . . .	77
$\beta_{\text{fs}}(t, f, \hat{m})$	Fine synchronization metric for arrival time $t$ , Doppler shift $f$ and randomization option $\hat{m}$ , see (5.19) . . . . .	84
$\gamma$	SINR assumed in the synchronization structure optimization . . . . .	92
$\delta_{\text{code}}$	Loss in $E_s/N_0$ of the realistic channel code as compared to the theoretically optimum coding assumed in the semi-analytical model . . . . .	100
$\Delta f_{\text{cs}}$	Coarse synchronization frequency step size, see (5.15) . . . . .	83
$\Delta f_{\text{fs}}$	Fine synchronization frequency step size, see (5.20) . . . . .	84
$\Delta f_{\text{ic}}$	Frequency step size of the cancellation subspace, see (5.26) . . . . .	86

$\Delta k_h$	Detection hold-off time, in samples . . . . .	78
$\Delta k_{ic}$	Maximum cancellation tap time offset, in samples . . . . .	86
$\Delta l$	Integer time offset in semi-analytical model of Aloha with SIC	62
$\Delta l_{\max}$	Maximum relevant $\Delta l$ , see (4.35) . . . . .	62
$\Delta l_{ic}$	Maximum cancellation tap frequency offset, in multiples of $\Delta f_{ic}$ . . . . .	86
$\Delta N_y$	Excess samples at beginning and end of $\mathbf{y}$ , see (5.16) . . . . .	84
$\Delta T_{BE}$	Time difference between BSS and ESS . . . . .	92
$\varepsilon$	Interference suppression factor, see (5.31) . . . . .	87
$\eta$	Nominal spectral efficiency . . . . .	24
$\eta_{\text{asu}}(a, \tilde{k})$	Nominal spectral efficiency in semi-analytical model of Aloha with single-user receivers . . . . .	48
$\eta_{\text{cl}}(i_{\text{tot}}, q_{\text{tot}}, R_{\text{cl}})$	Nominal spectral efficiency according to semi-analytical model of CB-SOTDMA . . . . .	57
$\eta_{\text{SIC}}(T_{\text{msg}}, S, \tilde{k})$	Nominal spectral efficiency in semi-analytical model of Aloha with SIC . . . . .	66
$\eta_{\text{ICBT}}$	Spectral efficiency of the Interference Canceling Beacon Transceiver (ICBT) . . . . .	102
$\eta_{\text{SICesam}}$	Spectral efficiency predicted by the extended semi-analytical model (ESAM) of Aloha with SIC . . . . .	101
$\Theta[k, m]$	Detection threshold for sample index $k$ and randomization option $m$ . . . . .	77
$\Theta_b$	Detection threshold baseline, see (5.36) . . . . .	94
$\Theta_{\text{ini}}[k]$	Initial value of detection threshold for sample index $k$ . . . . .	78
$\kappa$	Time oversampling factor of ICBT receiver . . . . .	76
$\kappa_{\text{cs}}$	Frequency oversampling factor used in coarse synchroniza- tion, see (5.15) . . . . .	83
$\kappa_{\text{fs}}$	Frequency oversampling factor used in fine synchronization, see (5.20) . . . . .	84

$\Lambda(t, x_{ov})$	Degree of overlap between desired and interfering message in semi-analytical model of Aloha with single-user receivers, see (4.5) . . . . .	47
$\Lambda[\Delta l]$	Average overlap between desired and interfering message at integer time offset $\Delta l$ in semi-analytical model of Aloha with SIC, see (4.34) . . . . .	62
$\lambda$	Normalized beacon transmission rate of a single aircraft . . . . .	23
$\Lambda_{db}$	Air traffic matrix obtained from database evaluation . . . . .	122
$\lambda_{nom}$	Nominal normalized beacon transmission rate of a single aircraft . . . . .	24
$\lambda'$	Beacon generation rate of a single aircraft . . . . .	14
$\Lambda_{sim}$	Upscaled air traffic matrix used for the Europe 2035 air traffic scenario, see (A.8) . . . . .	124
$\mu_{BSS}(k, f, m)$	Correlation filter output for the BSS, randomization option $m$ and Doppler shift $f$ , see (5.13) . . . . .	83
$\mu_{ESS}(k, f, m)$	Correlation filter output for the ESS, randomization option $m$ and Doppler shift $f$ , see (5.13) . . . . .	83
$\nu[l, m]$	Processing order of time of arrival $t_l$ and received power $P_{rx,m}$ in semi-analytical model of Aloha with SIC, see (4.38) . . . . .	63
$\xi$	Tolerable probability for outdated information . . . . .	12
$\Pi_m$	Permutation matrix for randomization option $m$ , see (5.1) . . . . .	74
$\rho$	Aircraft per area (2-D aircraft density) . . . . .	22
$\rho_{max}$	Maximum possible aircraft density . . . . .	24
$\rho_{max,asu}(a, \tilde{k})$	Maximum possible aircraft density in semi-analytical model of Aloha with single-user receivers, see (4.11) . . . . .	48
$\rho_{max,cl}(i_{tot}, q_{tot}, R_{cl})$	Maximum possible aircraft density according to semi-analytical model of CB-SOTDMA, see (4.27) . . . . .	56
$\rho_{max,SIC}(T_{msg}, S, \tilde{k})$	Maximum possible aircraft density in semi-analytical model of Aloha with SIC, see (4.47) . . . . .	66
$\rho_{typ}$	Typical aircraft density to be expected in the future in busy continental airspace . . . . .	23

$\tau$	Propagation delay . . . . .	15
$\varphi$	Phase of $\psi$ , see (2.8) . . . . .	16
$\Phi_{ii,0}$	Normalized autocorrelation matrix of interference vector $\mathbf{i}$ under the simplifying assumption that it is a Toeplitz matrix, see (5.23) . . . . .	85
$\Phi_{ii}$	Autocorrelation matrix of interference vector $\mathbf{i}$ . . . . .	85
$\Phi_{nn}$	Autocorrelation matrix of noise vector $\mathbf{n}$ . . . . .	85
$\Phi_{\tilde{n}\tilde{n}}$	Autocorrelation matrix of effective noise vector $\tilde{\mathbf{n}}$ . . . . .	84
$\hat{\Phi}_{\tilde{n}\tilde{n}}$	Estimate of $\Phi_{\tilde{n}\tilde{n}}$ from fine synchronization, see (5.25) . . . . .	85
$\Psi(\text{SINR}, a)$	Approximation of the minimum possible MER in case of no blanking, see (4.2) . . . . .	46
$\psi$	Complex channel coefficient describing path loss and phase rotation, see (2.8) . . . . .	16
$\Psi_{\text{bl}}(\text{SINR}, a, p_{\text{bl}})$	Approximation of the minimum possible MER with symbol blanking probability $p_{\text{bl}}$ , see (4.29) . . . . .	60
$\hat{\psi}$	Channel coefficient estimate from fine synchronization, see (5.22) . . . . .	85

---

## Bibliography

- [Abr70] N. Abramson, “The aloha system: Another alternative for computer communications,” in *Proc. AFIPS Fall Joint Computer Conf.*, Nov. 1970, pp. 281–285. [Online]. Available: <http://doi.acm.org/10.1145/1478462.1478502>
- [ADS01] *Technical Link Assessment Report*, ADS-B Technical Link Assessment Team, RTCA/Eurocontrol, Mar. 2001.
- [AS64] M. Abramowitz and I. A. Stegun, *Handbook of Mathematical Functions with Formulas, Graphs, and Mathematical Tables*. US Government Printing Office, Washington, DC, 1964.
- [AWH07] J. G. Andrews, S. Weber, and M. Haenggi, “Ad hoc networks: To spread or not to spread?” *IEEE Communications Magazine*, vol. 45, no. 12, pp. 84–91, Dec. 2007.
- [BB99] M. Bossert and M. Breitbach, *Digitale Netze*. Stuttgart: B.G. Teubner, 1999, in German.
- [BCCF02] F. Borgonovo, A. Capone, M. Cesana, and L. Fratta, “RR-aloHa , a reliable R-aloHa broadcast channel for ad-hoc inter-vehicle communication networks,” in *Proc. Med-Hoc-Net*, Baia Cia, Italy, 2002.
- [Bel63] P. Bello, “Characterization of randomly time-variant linear channels,” *IEEE Transactions on Communications Systems*, vol. 11, no. 4, pp. 360–393, 1963.
- [BKM<sup>+</sup>07] D. G. Bell, F. Kuehnel, C. Maxwell, R. Kim, K. Kasraie, T. Gaskins, P. Hogan, and J. Coughlan, “NASA world wind: Opensource GIS for mission operations,” in *Proc. IEEE Aerospace Conf.*, Mar. 2007, pp. 1–9.
- [BM10] B. Błaszczyszyn and P. Mühlethaler, “Stochastic analysis of non-slotted aloha in wireless ad-hoc networks,” in *Proc. IEEE INFOCOM*, San Diego, CA, Mar. 2010, pp. 1–9.
- [BPS98] E. Biglieri, J. Proakis, and S. Shamai, “Fading channels: Information-theoretic and communications aspects,” *IEEE Transactions on Information Theory*, vol. 44, no. 6, pp. 2619–2692, 1998.
- [BV01] S. Bana and P. Varaiya, “Space division multiple access (SDMA) for robust ad hoc vehicle communication networks,” in *Proc. IEEE Intelligent Transportation Systems*, 2001, pp. 962–967.
- [CK13] F. Clazzer and C. Kissling, “Enhanced contention resolution aloha – ECRA,” in *Proc. 9th Internat. ITG Conf. on Systems, Communication and Coding (SCC)*, Munich, Germany, Jan. 2013, pp. 1–6.

- [CVMK11] C. Campolo, A. Vinel, A. Molinaro, and Y. Koucheryavy, “Modeling broadcasting in iee 802.11p/WAVE vehicular networks,” *IEEE Communications Letters*, vol. 15, no. 2, pp. 199–201, Feb. 2011.
- [CWC07] C.-Y. Chiu, E. H.-K. Wu, and G.-H. Chen, “A reliable and efficient MAC layer broadcast protocol for mobile ad hoc networks,” *IEEE Transactions on Vehicular Technology*, vol. 56, no. 4, pp. 2296–2305, Jul. 2007.
- [dRHdG09] O. del Rio Herrero and R. de Gaudenzi, “A high efficiency scheme for large-scale satellite mobile messaging systems,” in *Proc. 27th IET and AIAA Internat. Communications Satellite Systems Conf.*, Edinburgh, UK, Jun. 2009.
- [dRHdG12] ———, “High efficiency satellite multiple access scheme for machine-to-machine communications,” *IEEE Transactions on Aerospace and Electronic Systems*, vol. 48, no. 4, pp. 2961–2989, Oct. 2012.
- [Ebn05] A. Ebner, “Selbstorganisierende Datenfunknetze für Anwendungen im Straßenverkehr,” Ph.D. dissertation, Technische Universität Hamburg-Harburg, Hamburg, Germany, May 2005, in German.
- [ES11] U. Epple and M. Schnell, “Overview of interference situation and mitigation techniques for LDACS1,” in *Proc. 30th IEEE/AIAA Digital Avionics Systems Conf. (DASC)*, 2011, pp. 4C5–1 – 4C5–12.
- [Eur07a] *Future Communications Infrastructure – Step 2: Technology Assessment Results*, 1st ed., Eurocontrol, Oct. 2007.
- [Eur07b] *Action Plan 17 Future Communications Study: Final Conclusions and Recommendations Report*, Eurocontrol/FAA, Nov. 2007, version 1.1.
- [Eur07c] *Communications Operating Concept and Requirements for the Future Radio System*, Eurocontrol/FAA, 2007, version 2.0.
- [Eur10] *Eurocontrol Long-Term Forecast: IFR Flight Movements 2010-2030*, 1st ed., Eurocontrol STATFOR, Dec. 2010, CND/STATFOR Doc415.
- [FEB09] R. J. F. Fang, M. Eroz, and N. Becker, “Data collection and SCADA over GEO-MSS satellites using spread SCMA,” in *Proc. Internat. Workshop on Satellite and Space Communications*, Siena, Italy, Sep. 2009, pp. 441–445.
- [Fra11] N. Franzen, “Advanced aloha with SIC for beaconing in a MANET,” in *Proc. 73rd IEEE Vehicular Technology Conf. (VTC Spring)*, Budapest, Hungary, May 2011, pp. 1–5.
- [Fra12] ———, “Comparison of coordinated and uncoordinated PHY/MAC schemes for beaconing,” in *Proc. 31st IEEE/AIAA Digital Avionics Systems Conf. (DASC)*, Williamsburg, VA, Oct. 2012, pp. 5D1–1–5D1–12.
- [Fra14] ———, “Zellulares Kommunikationsnetzwerk,” German Patent DE102 010 035 729B4, Oct. 9, 2014.



- [FS15] N. Franzen and D. Shutin, “Successive interference cancellation for aeronautical surveillance beaconing,” *IEEE Transactions on Aerospace and Electronic Systems*, submitted for publication in Aug. 2015.
- [FWD<sup>+</sup>03] A. Fort, J.-W. Weijers, V. Derudder, W. Eberle, and A. Bourdoux, “A performance and complexity comparison of auto-correlation and cross-correlation for OFDM burst synchronization,” in *Proc. IEEE Internat. Conf. on Acoustics, Speech, and Signal Processing (ICASSP)*, vol. 2, Apr. 2003, pp. II–341–344.
- [Gal97] R. Gallager, “Residual noise after interference cancellation on fading multipath channels,” in *Communications, Computation, Control, and Signal Processing*, A. Paulraj, V. Roychowdhury, and C. Schaper, Eds. Springer US, 1997, pp. 67–77. [Online]. Available: [http://dx.doi.org/10.1007/978-1-4615-6281-8\\_3](http://dx.doi.org/10.1007/978-1-4615-6281-8_3)
- [Grö03] J. Grönkvist, “Distributed STDMA algorithms for ad hoc networks,” Swedish Defence Research Agency (FOI), Tech. Rep. FOI-R-1059-SE, Dec. 2003.
- [HBE<sup>+</sup>01] H. Hartenstein, B. Bochow, A. Ebner, M. Lott, M. Radimirsch, and D. Vollmer, “Position-aware ad hoc wireless networks for inter-vehicle communications: The fleetnet project,” in *Proc. 2nd ACM Internat. Symposium on Mobile Ad Hoc Networking & Computing (MOBIHOC)*, Long Beach, CA, 2001, pp. 259–262.
- [HBMA08] F. Hoffmann, C. Bauer, D. Medina, and S. Ayaz, “FACTS: An OMNeT++ based simulator for aeronautical communications,” in *Proc. 1st Internat. Conf. on Simulation Tools and Techniques for Communications, Networks and Systems & Workshops (SimuTools)*, Marseille, France, Mar. 3–7, 2008, p. 85.
- [HBWB07] M. Heissenbüttel, T. Braun, M. Wälchli, and T. Bernoulli, “Evaluating the limitations of and alternatives in beaconing,” *Ad Hoc Networks*, vol. 5, no. 5, pp. 558 – 578, Jul. 2007.
- [HESF12] F. Hoffmann, U. Epple, M. Schnell, and U.-C. Fiebig, “Feasibility of LDACS1 cell planning in european airspace,” in *Proc. 31st IEEE/AIAA Digital Avionics Systems Conf. (DASC)*, Williamsburg, VA, Oct. 2012, pp. 5E1–1–5E1–13.
- [Hof14] F. Hoffmann, “Routing and internet gateway selection in aeronautical ad hoc networks,” Ph.D. dissertation, Technische Universität Berlin, Berlin, Germany, Dec. 2014.
- [Hug14] D. Hughes, “ADS-B essentials: Part 2 – frequently asked questions about ADS-B avionics installations,” *Avionics News*, pp. 59–61, Jun. 2014. [Online]. Available: <http://www.brightcopy.net/allen/avne/51-6/#/60>

- [IEE10] IEEE 802.11p, *IEEE Standard for Information technology–Telecommunications and information exchange between systems–Local and metropolitan area networks–Specific requirements–Part 11: Wireless LAN Medium Access Control (MAC) and Physical Layer (PHY) Specifications–Amendment 6: Wireless Access in Vehicular Environments*, 2010, IEEE Std. 802.11p, version 2010.
- [IEE12] IEEE 802.11, *IEEE Standard for Information technology–Telecommunications and information exchange between systems–Local and metropolitan area networks–Specific requirements–Part 11: Wireless LAN Medium Access Control (MAC) and Physical Layer (PHY) Specifications*, 2012, IEEE Std. 802.11, version 2012.
- [Inn07] *Flight Schedule Database*, Innovata, LLC, 2007, <http://www.innovata-llc.com>.
- [Inta] *Annex 10 to the Convention on International Civil Aviation, Vol. I: Radio Navigation Aids*, International Civil Aviation Organization.
- [Intb] *Annex 10 to the Convention on International Civil Aviation, Vol. III: Communication Systems*, International Civil Aviation Organization.
- [Int04] *Manual on VHF Digital Link (VDL) Mode 4*, 1st ed., International Civil Aviation Organization, 2004.
- [Int09] *Manual on the Universal Access Transceiver (UAT)*, International Civil Aviation Organization, 2009.
- [Int10] *Technical characteristics for an automatic identification system using time-division multiple access in the VHF maritime mobile band*, International Telecommunication Union, Recommendation ITU-R M.1371-4, Apr. 2010. [Online]. Available: <http://www.itu.int/rec/R-REC-M.1371>
- [Int12a] *Radio Regulations*, International Telecommunication Union, 2012, edition of 2012.
- [Int12b] *Propagation curves for aeronautical mobile and radionavigation services using the VHF, UHF and SHF bands*, International Telecommunication Union, Recommendation ITU-R P.528-3, Feb. 2012. [Online]. Available: <http://www.itu.int/rec/R-REC-P.528>
- [JM13] C. Jayaram and C. R. Murthy, “Noncoherent integration for signal detection: Analysis under model uncertainties,” *IEEE Transactions on Aerospace and Electronic Systems*, vol. 49, no. 4, pp. 2413–2430, 2013.
- [KAE<sup>+</sup>11] G. Karagiannis, O. Altintas, E. Ekici, G. Heijenk, B. Jarupan, K. Lin, and T. Weil, “Vehicular networking: A survey and tutorial on requirements, architectures, challenges, standards and solutions,” *IEEE Communications Surveys & Tutorials*, vol. 13, no. 4, pp. 584–616, Apr. 2011.

- [KDPS11] K. Kasai, D. Declercq, C. Poulliat, and K. Sakaniwa, “Multiplicatively repeated nonbinary LDPC codes,” *IEEE Transactions on Information Theory*, vol. 57, no. 10, pp. 6788–6795, 2011.
- [Kis11] C. Kissling, “Performance enhancements for asynchronous random access protocols over satellite,” in *Proc. IEEE Internat. Conf. on Communications (ICC)*, 2011, pp. 1–6.
- [KJO11] M. Kaynia, N. Jindal, and G. E. Oien, “Improving the performance of wireless ad hoc networks through MAC layer design,” *IEEE Transactions on Wireless Communications*, vol. 10, no. 1, pp. 240–252, Jan. 2011.
- [KMR<sup>+</sup>03] S. Katragadda, G. Murthy CNS, R. Rao MS, M. Kumar S, and R. Sachin, “A decentralized location-based channel access protocol for inter-vehicle communication,” in *Proc. 57th IEEE Vehicular Technology Conf. (VTC Spring)*, vol. 3, Apr. 2003, pp. 1831–1835.
- [KVM<sup>+</sup>09] K. Kusume, R. Vilzmann, A. Müller, C. Hartmann, and G. Bauch, “Medium access in spread-spectrum ad hoc networks with multiuser detection,” *EURASIP Journal on Advances in Signal Processing*, vol. 2009, 2009, article ID 156247.
- [Lam80] S. Lam, “Packet broadcast networks – a performance analysis of the R-aloah protocol,” *IEEE Transactions on Computers*, vol. C-29, no. 7, pp. 596–603, Jul. 1980.
- [Lan96] H. Lans, “Position indicating system,” U.S. Patent 5 506 587, Apr. 9, 1996.
- [LHSR01] M. Lott, R. Halfmann, E. Schultz, and M. Radimirsch, “Medium access and radio resource management for ad hoc networks based on UTRA TDD,” in *Proc. 2nd ACM Internat. Symposium on Mobile Ad Hoc Networking & Computing (MOBIHOC)*, Long Beach, CA, 2001, pp. 76–86.
- [LIT<sup>+</sup>09] M. Lenoble, K. Ito, Y. Tadokoro, M. Takanashi, and K. Sanda, “Header reduction to increase the throughput in decentralized TDMA-based vehicular networks,” in *Proc. IEEE Vehicular Networking Conf. (VNC)*, Oct. 2009, pp. 1–4.
- [Liv11] G. Liva, “Graph-based analysis and optimization of contention resolution diversity slotted aloha,” *IEEE Transactions on Communications*, vol. 59, no. 2, pp. 477–487, Feb. 2011.
- [Ma07] X. Ma, “Transient solutions of sliding frame R-aloah for real-time ad hoc wireless networks in a fading environment,” *IEEE Communications Letters*, vol. 11, no. 4, pp. 354–356, Apr. 2007.
- [MB11] I. Mallett and J. Bollard, “The need for an alternative PNT,” Working Paper, International Civil Aviation Organization, Navigation Systems Panel Working Group of the Whole 10th Meeting, May 9–20, 2011.

- [MHRR12] D. Medina, F. Hoffmann, F. Rossetto, and C.-H. Rokitansky, “A geographic routing strategy for north atlantic in-flight internet access via airborne mesh networking,” *IEEE/ACM Transactions on Networking*, vol. 20, no. 4, pp. 1231–1244, 2012.
- [MJ14] S. Malik and P. Jacquet, “An overview of local capacity in wireless networks,” *Telecommunication Systems*, vol. 55, no. 2, pp. 225–240, 2014.
- [MKK01] M. Marina, G. Kondylis, and U. Kozat, “RBRP: A robust broadcast reservation protocol for mobile ad hoc networks,” in *Proc. IEEE Internat. Conf. on Communications (ICC)*, vol. 3, 2001, pp. 878–885.
- [NA02] T. Nadeem and A. Agrawala, “Efficient time-based topology-dependent scheduling for radio packet networks,” in *Proc. IASTED Internat. Conf. on Communications and Computer Networks (CCN)*, Cambridge, USA, Nov. 2002.
- [Par00] J. D. Parson, *The Mobile Radio Propagation Channel*, 2nd ed. John Wiley & Sons Ltd, 2000.
- [PFD08] C. Poulliat, M. Fossorier, and D. Declercq, “Design of regular  $(2, d_c)$ -LDPC codes over  $GF(q)$  using their binary images,” *IEEE Transactions on Communications*, vol. 56, no. 10, pp. 1626–1635, 2008.
- [PPV10] Y. Polyanskiy, H. Poor, and S. Verdú, “Channel coding rate in the finite blocklength regime,” *IEEE Transactions on Information Theory*, vol. 56, no. 5, pp. 2307–2359, 2010.
- [Pro01] J. G. Proakis, *Digital Communications*, 4th ed. McGraw Hill, 2001.
- [PV11] Y. Polyanskiy and S. Verdú, “Scalar coherent fading channel: Dispersion analysis,” in *Proc. IEEE Internat. Symposium on Information Theory (ISIT)*, Jul. 2011, pp. 2959–2963.
- [Rap01] T. Rappaport, *Wireless Communications: Principles and Practice*, 2nd ed. Upper Saddle River, NJ, USA: Prentice Hall PTR, 2001.
- [Ras01] K. Rascher, “Untersuchungen zum Kanalzugriff in selbstorganisierenden Datenfunknetzen,” Ph.D. dissertation, Technische Universität Braunschweig, Braunschweig, Germany, Apr. 2001, in German.
- [RG12] C. Rico García, “Medium access control protocols in mobile ad-hoc networks using beaconing,” Ph.D. dissertation, Universität Ulm, Ulm, Germany, Sep. 2012.
- [RGLS08] C. Rico García, A. Lehner, and T. Strang, “COMB: Cell based orientation aware MANET broadcast MAC layer,” in *Proc. IEEE Global Communications Conf. (GLOBECOM)*, New Orleans, LO, Nov. 2008, pp. 1–5.
- [RTC02] *Minimum Aviation System Performance Standards For Automatic Dependent Surveillance Broadcast (ADS-B)*, RTCA, Inc., Washington, DC, USA, Jun. 2002, RTCA DO-242A.

- [RTC09] *Minimum Operational Performance Standards for 1090 MHz Extended Squitter Automatic Dependent Surveillance – Broadcast (ADS-B) and Traffic Information Services – Broadcast (TIS-B)*, RTCA, Inc., Washington, DC, USA, Dec. 2009, RTCA DO-260B.
- [SC97] T. M. Schmidl and D. C. Cox, “Robust frequency and timing synchronization for OFDM,” *IEEE Transactions on Communications*, vol. 45, no. 12, pp. 1613–1621, 1997.
- [SC09] R. Scopigno and H. A. Cozzetti, “Mobile slotted aloha for VANETs,” in *Proc. 70th IEEE Vehicular Technology Conf. (VTC Fall)*, Sep. 2009, pp. 1–5.
- [SD99] M. Schnell and T. Dorsch, “Future VHF systems – architecture implementation study WP5000: VDL mode 4 evaluation – ADS-B,” Eurocontrol, Tech. Rep., Dec. 1999, edition 1.1.
- [SEH11] M. Schnell, U. Epple, and F. Hoffmann, “Using the future L-band communication system for navigation,” in *Proc. Integrated Communications, Navigation and Surveillance Conf. (ICNS)*, Herndon, VA, 2011.
- [SS90] E. S. Sousa and J. A. Silvester, “Optimum transmission ranges in a direct-sequence spread-spectrum multihop packet radio network,” *IEEE Journal on Selected Areas in Communications*, vol. 8, no. 5, pp. 762–771, Jun. 1990.
- [SSLM14] M. Strohmeier, M. Schäfer, V. Lenders, and I. Martinovic, “Realities and challenges of NextGen air traffic management: The case of ADS-B,” *IEEE Communications Magazine*, vol. 52, no. 5, pp. 111–118, May 2014.
- [Sta08] D. Stacey, *Aeronautical Radio Communication Systems and Networks*. John Wiley & Sons Ltd, 2008.
- [TGLA99] Z. Tang and J. Garcia-Luna-Aceves, “A protocol for topology-dependent transmission scheduling in wireless networks,” in *Proc. IEEE Wireless Communications and Networking Conf. (WCNC)*, 1999, pp. 1333–1337.
- [TL94] G. Tziritas and C. Labit, *Motion Analysis for Image Sequence Coding*, ser. Advances in Image Communication. Amsterdam: Elsevier Science B.V., 1994, vol. 4.
- [Vit90] A. J. Viterbi, “Very low rate convolutional codes for maximum theoretical performance of spread-spectrum multiple-access channels,” *IEEE Journal on Selected Areas in Communications*, vol. 8, no. 4, pp. 641–649, May 1990.
- [VT01] H. L. Van Trees, *Detection, Estimation, and Modulation Theory, Part III: Radar-Sonar Signal Processing and Gaussian Signals in Noise*. John Wiley & Sons Inc., Oct. 2001.

- [WAJ10] S. P. Weber, J. G. Andrews, and N. Jindal, "An overview of the transmission capacity of wireless networks," *IEEE Transactions on Communications*, vol. 58, no. 12, pp. 3593–3604, Dec. 2010.
- [WAYdV07] S. P. Weber, J. G. Andrews, X. Yang, and G. de Veciana, "Transmission capacity of wireless ad hoc networks with successive interference cancellation," *IEEE Transactions on Information Theory*, vol. 53, no. 8, pp. 2799–2814, Aug. 2007.
- [WFS10] M. Walter, N. Franzen, and M. Schnell, "New concepts for a decentralized, self-organizing air-to-air radio link," in *Proc. 29th IEEE/AIAA Digital Avionics Systems Conf. (DASC)*, Salt Lake City, UT, Oct. 2010, pp. 3.D.1-1 – 3.D.1-12.
- [WLJ93] K. M. Wong, Z.-Q. Luo, and Q. Jin, "Design of optimum signals for the simultaneous estimation of time delay and doppler shift," *IEEE Transactions on Signal Processing*, vol. 41, no. 6, pp. 2141–2154, Jun. 1993.
- [ZC01] C. Zhu and M. S. Corson, "A five-phase reservation protocol (FPRP) for mobile ad hoc networks," *Wireless Networks*, vol. 7, no. 4, pp. 371–384, Sep. 2001.
- [Zhi08] S. V. Zhidkov, "Analysis and comparison of several simple impulsive noise mitigation schemes for OFDM receivers," *IEEE Transactions on Communications*, vol. 56, no. 1, pp. 5–9, Jan. 2008.
- [ZSX03] L. Zhang, B.-H. Soong, and W. Xiao, "A new multichannel MAC protocol for ad hoc networks based on two-phase coding with power control (TPCPC)," in *Proc. 2003 Joint Conf. of the 4th Internat. Conf. on Information, Communications and Signal Processing, and 4th Pacific Rim Conf. on Multimedia*, vol. 2, Dec. 2003, pp. 1091–1095.

# Lebenslauf

Name: Nico Franzen  
Anschrift: Irmonherstraße 13, 81241 München  
Geburtsdatum: 13.04.1982  
Geburtsort: Weingarten (Württemberg)  
Familienstand: ledig

## Schulbildung

08/1988 – 07/1992      Grundschule in Weingarten  
08/1992 – 06/2001      Gymnasium Weingarten

## Studium

08/2002 – 03/2008      Studium der Elektrotechnik an der  
Universität Ulm,  
Studienabschluss: Diplom

## Berufstätigkeit

06/2008 – 06/2015      wissenschaftlicher Mitarbeiter in der  
Abteilung Nachrichtensysteme,  
Institut für Kommunikation und Navigation,  
Deutsches Zentrum für Luft- und Raumfahrt e.V. (DLR)